

The Production and Characterization of Ceramic Carbon Electrode Materials for CuCl-HCl Electrolysis

By

Patrick Edge

A Thesis Submitted in Partial Fulfillment
of the Requirements for the Degree of

Master of Science

In

The Faculty of Science

Materials Science

University of Ontario Institute of Technology

July 2013

© Patrick Edge, 2013

Abstract

Current H₂ gas supplies are primarily produced through steam methane reforming and other fossil fuel based processes. This lack of viable large scale and environmentally friendly H₂ gas production has hindered the wide spread adoption of H₂ fuel cells. A potential solution to this problem is the Cu-Cl hybrid thermochemical cycle. The cycle captures waste heat to drive two thermochemical steps creating CuCl as well as O₂ gas and HCl from CuCl₂ and water. The CuCl is oxidized in HCl to produce H₂ gas and regenerate CuCl₂, this process occurs at potentials well below those required for water electrolysis.

The electrolysis process occurs in a traditional PEM fuel-cell. In the aqueous anolyte media Cu(I) will form anionic complexes such as CuCl₂⁻ or CuCl₃²⁻. The slow transport of these species to the anode surface limits the overall electrolysis process. To improve this transport process we have produced ceramic carbon electrode (CCE) materials through a sol-gel method incorporating a selection of amine containing silanes with increasing numbers of primary and secondary amines. When protonated these amines allow for improved transport of anionic copper complexes.

The electrochemical and physical characterization of these CCE materials in a half and full-cell electrolysis environment will be presented. Electrochemical analysis was performed using cell polarization, cyclic voltammetry, and electrochemical impedance spectroscopy.

Keywords: CuCl-HCl electrolysis, ceramic carbon electrode, sol-gel, amine functionalization

Acknowledgements

I would like to give my deepest thanks to my supervisor Dr. Brad Easton for the opportunity to work with him on my master's thesis. You have been a tremendous help to me in my studies for both my graduate and undergraduate schooling. I would also like to thank Dr. Ranganathan Santhnam for the help he has given me in starting my research as well as the foundations of the project which he laid before I started. Thank you to the rest of my supervisory committee Dr. Igor Svishchev and Dr. Liliana Trevani as well as my external supervisor Dr. Brian Ikeda for your input and comments; this is a far better document as a result. To the rest of the faculty of the UOIT science department, thank you for making the last three years of my life fly by. You have certainly made my graduate school experience memorable.

Thank you to the members of the Easton research group past and present. You have been exceptionally helpful to me either through insightful comments or simply listening to me ramble until I sort out the answer to my own problem. Specifically, thank you to Jennie Eastcott for your continued help and expertise.

To my friends and family I would like to thank you for your overwhelming love and support over the years. To my parents in particular, in any moment of doubt you have kept me on the straight and narrow. Tremendous thanks to my wonderful fiancée Stephanie Mavilla who has been wonderfully understanding while I have been slogging away and my work. I can only hope to repay her in kind when she needs it. Additionally, thank you Aunt Tori for your advice and encouragement.

Finally, I would like to acknowledge our research collaborators in the faculty of Engineering and at AECL. I am only a small corner of this massive project and I am very happy to have been a part of it.

Contents

| | |
|---|-----|
| Abstract | i |
| Acknowledgements..... | ii |
| Table of Tables..... | vi |
| Table of Figures..... | vii |
| Common Abbreviations..... | xvi |
| Chapter 1 : Introduction to Hydrogen Production and Electrochemical Characterization | |
| Techniques | 1 |
| 1.1: Current H ₂ Production Methods | 2 |
| 1.1.1: Production from fossil fuels. | 2 |
| 1.1.2 Hydrogen production from water electrolysis. | 4 |
| 1.2: Introduction to Thermochemical Cycles..... | 7 |
| 1.2.1: Conventional Thermochemical Cycles | 8 |
| 1.2.2: Hybrid Thermochemical Cycles | 9 |
| 1.2.3: Three Step Hybrid CuCl-HCl Thermochemical Cycle..... | 10 |
| 1.2.4: Research Targets for the Hybrid CuCl-HCl Thermochemical Cycle..... | 14 |
| 1.3: CCE Materials | 14 |
| 1.3.1: Sol-Gel Method | 15 |
| 1.3.2: Ceramic Carbon Electrodes | 18 |
| 1.4: Electrochemical Characterization Techniques..... | 21 |
| 1.4.1: DC Voltammetry Techniques | 22 |
| 1.4.2: AC Electrochemical Impedance Spectroscopy | 23 |
| 1.5: Thesis Objectives..... | 26 |
| Chapter 2 : Experimental Methods and Instrumentation..... | |
| 2.1: Electrode Preparation | 29 |
| 2.1.1: Sol Gel Production | 29 |
| 2.1.2: Half-Cell Electrode Production | 29 |
| 2.1.3: Full-Cell Electrode Production..... | 29 |
| 2.1.4: Cathode Pt/C Electrode Production | 30 |
| 2.2: Materials Characterization | 31 |
| 2.2.1: TGA Weight Characterization..... | 31 |
| 2.2.2: SEM Imaging..... | 31 |

| | |
|---|-----|
| 2.2.3: TEM Imaging..... | 31 |
| 2.3: Full-Cell Production and Design | 31 |
| 2.3.1: Original Design | 32 |
| 2.3.2: Iterative Designs | 32 |
| 2.3.3: Catholyte/Anolyte Preparation | 35 |
| 2.3.4: Membrane Electrode Assembly Fabrication and Full-Cell Construction | 35 |
| 2.4: Electrochemical Characterization | 36 |
| 2.4.1: Half-Cell Electrochemical Techniques..... | 36 |
| 2.4.2: Full-Cell Electrochemical Techniques | 37 |
| 2.4.3: Ultra Micro Electrode Measurements | 37 |
| Chapter 3 : Materials for Half Cell Electrolysis | 38 |
| 3.1: Materials Characterization Results | 39 |
| 3.2: Electrochemical Characterization Results | 41 |
| 3.2.1: Electrochemical Results for 1N Materials | 42 |
| 3.2.2: Electrochemical Results for 2N Materials | 47 |
| 3.2.3: Electrochemical Results for 3N Materials | 52 |
| 3.3: Discussion of Half-Cell Materials..... | 57 |
| 3.3.1: 1N Materials..... | 57 |
| 3.3.2: 2N Materials..... | 58 |
| 3.3.3: 3N Materials..... | 59 |
| 3.3.4: Comparison of Varied Silane Types | 60 |
| Chapter 4 : Materials for Full-Cell Electrolysis..... | 62 |
| 4.1: Results | 66 |
| 4.1.1: Results for 1N Materials | 66 |
| 4.1.2: Results for Varied CCE Loadings (1N) | 81 |
| 4.1.3: Results for Varied Silanes..... | 92 |
| 4.2: Discussion | 112 |
| 4.2.1: 1N Materials..... | 112 |
| 4.2.2: Varied CCE Loadings (1N)..... | 115 |
| 4.2.3: 2N Materials..... | 117 |
| 4.2.4: 3N Materials..... | 118 |
| 4.2.5: Comparison of Varied Silane Types | 120 |

| | |
|--|-----|
| Chapter 5 : Materials Durability and Copper Crossover Resistance | 130 |
| 5.1: Copper Crossover Identification | 132 |
| 5.2: Comparison of materials crossover resistances..... | 133 |
| 5.3: Cell Regeneration | 136 |
| 5.4: Ultra-Micro Electrode Measurements | 138 |
| Chapter 6 : Conclusions and Future Directions | 141 |
| 6.1: Conclusions | 142 |
| 6.2: Future Directions..... | 144 |
| Chapter 7 : References..... | 146 |
| Chapter 8 : Appendices | 153 |

Table of Tables

| | |
|---|-----|
| Table 1-1: General Half-Cell reactions for the electrolysis of water in alkaline and acidic liquid environments ⁵ | 4 |
| Table 1-2: The general Half-Cell reactions for the electrolysis of water for high temperature solid oxide electrolysis cells with O ²⁻ as the mobile ion | 6 |
| Table 1-3: The stepwise chemical reactions for the production of H ₂ and O ₂ gas in the Sulfur-Iodine thermochemical cycle | 8 |
| Table 1-4: The stepwise chemical reactions and electrochemical half-cell reactions for the Hybrid Sulfur thermochemical cycle ¹³ | 9 |
| Table 1-5: The stepwise chemical and electrochemical half-cell equations for the three, four, and five step hybrid CuCl-HCl thermochemical cycle ⁴ | 11 |
| Table 3-1: Compositions of CCE materials for half-cell testing produced with 1N, 2N, and 3N silane precursors | 41 |
| Table 3-2: Total Resistance of 1N CCE materials. As determined from Warburg region of impedance plots. | 43 |
| Table 3-3: Total Resistance of 2N CCE materials. As determined from Warburg region of impedance plots. | 49 |
| Table 3-4: Total Resistance of 3N CCE materials. As determined from Warburg region of impedance plots. | 55 |
| Table 4-1: 1N CCE materials for full-cell electrolysis compositional information. | 66 |
| Table 4-2: 1N CCE materials with varied total mass loadings for full-cell electrolysis: compositional information | 82 |
| Table 4-3: 2N and 3N CCE materials for full-cell electrolysis: compositional Information. | 92 |
| Table 5-1: Bare CFP and CCE materials for full-cell electrolysis: Cu crossover resistance and sample compositional information | 134 |

Table of Figures

| | |
|---|----|
| Figure 1-1: Schematic Diagram of PEM Electrolyzer with associated half-cell equations. | 6 |
| Figure 1-2: Schematic of general thermochemical cycle processes. | 7 |
| Figure 1-3: Schematic Diagram for the electrolysis of SO ₂ and production of H ₂ gas in a PEM style electrolyzer for the Hybrid Sulfur thermochemical cycle. Diagram based on work of Staser JA and Weidner JW ¹³ | 9 |
| Figure 1-4: Schematic Diagram for the electrolysis of CuCl in the presence of HCl and the production of H ₂ gas in a PEM style electrolyzer Hybrid three step CuCl-HCl thermochemical cycle ¹⁸ | 12 |
| Figure 1-5: An overview of the sol-gel process and the reaction pathways to the various products ³⁰ . Reproduced with permission of TAYLOR & FRANCIS GROUP LLC in the format Republish in a thesis/dissertation via Copyright Clearance Center. | 16 |
| Figure 1-6: The base catalyzed hydrolysis of a silane monomer. | 16 |
| Figure 1-7: The acid catalyzed hydrolysis of a silane precursor. | 17 |
| Figure 1-8: The base catalyzed condensation reaction between two silane monomers..... | 17 |
| Figure 1-9: The acid catalyzed condensation reaction between two silane monomers. | 17 |
| Figure 1-10: Silane monomers from top to bottom: (3-Aminopropyl)triethoxysilane, N-[3-(Trimethoxysilyl)propyl]ethylenediamine, and N ¹ -(3-Trimethoxysilylpropyl)diethylenetriamine. 1N, 2N, 3N respectively..... | 20 |
| Figure 1-11: The Finite Transmission Line Model Circuit for modeling a PEM electrode. Diagram based on work of Li, G. and Pickup, P. ⁴¹ | 24 |
| Figure 1-12 : Nyquist plot at 0 V vs. OCV of ceramic carbon electrode with Warburg region detailed and $R_{\text{Membrane}} = 0$ | 25 |
| Figure 2-1: Serpentine flow path for the spray coating of CCE materials onto CFP backings..... | 30 |
| Figure 2-2: Initial Electrolysis Cell Design with analogue pump, 5 cm ² cell, and barbed fittings (Not Pictured: Recirculated Flow Lines). | 32 |
| Figure 2-3: Iterative Electrolysis Cell Design with digital peristaltic pump, 5 cm ² cell, barbed fittings, and recirculated electrolyte flow. | 33 |
| Figure 2-4: Full Electrolysis Cell Schematic Diagram. Coloured lined are included to identify individual flow paths..... | 34 |
| Figure 2-5: Current Electrolysis Cell Design with digital peristaltic pump, 5 cm ² cell, barbed fittings, and recirculated electrolyte flow (temperature controller not pictured). | 35 |

| | |
|---|----|
| Figure 3-1: Example TGA spectra of 1N CCE Materials under flowing air with temperatures ramped from 20-1000 °C at 20 °C min ⁻¹ . Mass percent normalized at 200 °C. | 39 |
| Figure 3-2: Capacitive CV of CCE materials with varied 1N silane loading and normalized for geometric surface area (SA). Experiment performed in 1.5 M HCl under N ₂ atmosphere. Scan from 0.15 to 0.85 V vs. RHE at 50 mv s ⁻¹ | 42 |
| Figure 3-3: Impedance and capacitance plots of CCE materials with varied 1N silane content. Collected in 1.5 M HCl under N ₂ atmosphere. (A) Nyquist plot (B) High frequency region (C) Capacitance plot normalized for the total mass of carbon present in the CCE sample..... | 44 |
| Figure 3-4: Potential stair step measurement of CCE materials with varied 1N silane compositions. Scanned from 0.35-0.85 V vs. RHE with 10 mV steps and 3 s dwell times. Electrochemical measurement were collected in 1 mM CuCl in 1.5 M HCl under N ₂ atmosphere electrolyte. | 45 |
| Figure 3-5: Potentiostatic measurements of CCE materials with varied 1N silane compositions. Potential held at 0.6 V vs. RHE. Collected in 1 mM CuCl in 1.5 M HCl under N ₂ atmosphere electrolyte. | 46 |
| Figure 3-6: Relationship between 1N silane composition and current response from potentiostatic holds. Value taken from current at 150 s. | 47 |
| Figure 3-7: Capacitive CV of CCE materials with varied 2N silane loading and normalized for Geometric SA. Collected in 1.5 M HCl under N ₂ atmosphere. Scan from 0.15 to 0.85 V vs. RHE at 50 mv s ⁻¹ | 48 |
| Figure 3-8: Impedance and Capacitance plots of CCE materials with varied 2N silane content. Tests were performed in 1.5 M HCl under N ₂ atmosphere at 0 V vs. OCV. (A) Nyquist plot (B) High frequency region (C) Capacitance plot..... | 50 |
| Figure 3-9: Potential stair step measurement of CCE materials with varied 2N silane compositions. Scanned from 0.35-0.85 V vs. RHE with 10 mV steps and 3 s dwell times. Collected in 1 mM CuCl in 1.5 M HCl under N ₂ atmosphere electrolyte. (A) Working plots (B) Transient current plot included. | 51 |
| Figure 3-10: Potentiostatic measurements of CCE materials with varied 2N silane compositions. Potential held at 0.6 V vs. RHE. Experiments performed in 1 mM CuCl in 1.5 M HCl under N ₂ atmosphere electrolyte. (A) Scaled to show difference between materials (B) Scaled to keep the same maximum current as shown in Figure 3-5 for comparison. | 52 |

| | |
|---|----|
| Figure 3-11: Capacitive CV of CCE materials with varied 3N silane loading and normalized for geometric SA. Collected in 1.5 M HCl under N ₂ atmosphere. Scan from 0.15 to 0.85 V vs. RHE at 50 mv s ⁻¹ . | 53 |
| Figure 3-12: Impedance and capacitance plots of CCE materials with varied 3N silane content. Tests were performed in 1.5 M HCl under N ₂ atmosphere at 0 V vs. OCV. (A) Nyquist plot (B) High frequency region (C) Capacitance plot. | 54 |
| Figure 3-13: Potential stair step Measurement of CCE materials with varied 3N silane compositions. Scanned from 0.35-0.85 V vs. RHE with 10 mV steps and 3 s dwell times. Collected in 1 mM CuCl in 1.5 M HCl under N ₂ atmosphere electrolyte. (A) Working plots (B) Transient current plot included. | 56 |
| Figure 3-14: Potentiostatic measurements of CCE materials with varied 3N silane compositions. Potential held at 0.6 V vs. RHE. Tests were performed in 1 mM CuCl in 1.5 M HCl under N ₂ atmosphere electrolyte. | 57 |
| Figure 3-15: Potentiostatic measurements of CCE materials produced with 1N, 2N and 3N silane precursors. Potential held at 0.6 V vs. RHE. Tests were performed in 1 mM CuCl in 1.5 M HCl under N ₂ atmosphere electrolyte. | 61 |
| Figure 4-1: Comparison of CuCl and H ₂ O electrolysis with a Pt/C anode and cathode catalyst. CuCl electrolysis collected in 0.2 M CuCl in 2 M HCl anolyte and DI H ₂ O catholyte both under N ₂ atmosphere at 14 mL min ⁻¹ electrolyte flow rate. Water electrolysis collected in DI H ₂ O electrolyte at cathode and anode under N ₂ atmosphere at 14 mL min ⁻¹ flow rate. | 64 |
| Figure 4-2: Comparison of linear sweep and potential stair step measurements at equivalent scan rates. Tests were performed in 0.2 M CuCl in 2 M HCl anolyte and DI H ₂ O catholyte both under N ₂ atmosphere at 60 mL min ⁻¹ electrolyte flow rate. | 65 |
| Figure 4-3: SEM images taken of CCE samples B1P73S2, B1P69S1, B1P69S2, and B1P69S3 at 100 and 2500 x magnification. | 68 |
| Figure 4-4: Capacitive CV of CCE materials with varied 1N silane loading. 10 mV s ⁻¹ scan rate from 0.2 to 1.0 V vs. RHE. Current normalized for geometric SA and for mass of carbon. In 2 M HCl under N ₂ atmosphere at 60 mL min ⁻¹ anolyte flow rate. (A) Area specific (B) Carbon mass normalized. | 70 |
| Figure 4-5: Nyquist plots of varied 1N silane content CCEs. Collected at 0 V vs. OCV in 2 M HCl anolyte under N ₂ atmosphere at 60 mL min ⁻¹ anolyte flow rate and 25 mL min ⁻¹ H ₂ gas provided to the cathode. (A) Nyquist plot (B) High frequency region. | 71 |

| | |
|--|----|
| Figure 4-6: Capacitance plots of varied 1N silane content CCEs. Tests were performed at 0 V vs. OCV in 2 M HCl anolyte under N ₂ atmosphere at 60 mL min ⁻¹ anolyte flow rate and 25 mL min ⁻¹ H ₂ gas provided to the cathode. (A) Area specific capacitance (B) Mass of carbon normalized (C) Capacitance normalized to 1. | 72 |
| Figure 4-7: Potential stair step measurements of 27.2 wt% CCE at varied flow rates. Scanned from 0.2 to 1.2 V with 5 mV steps and 0.5 s dwell time per step. Tests were performed in 0.2 M CuCl in 2 M HCl anolyte and DI H ₂ O catholyte both under N ₂ atmosphere at 60 mL min ⁻¹ electrolyte flow rate. | 73 |
| Figure 4-8: Potential stair step measurements of CCE's with varied 1N silane composition. Scanned from 0.2-1.2 V with 5 mV steps and 0.5 s dwell time per step. Experiment performed in in 0.2 M CuCl in 2M HCl anolyte and DI H ₂ O catholyte both under N ₂ atmosphere at 60 mL min ⁻¹ electrolyte flow rate. (A) Enlarged onset potential region from 0.3 to 0.5 V vs. RHE. | 74 |
| Figure 4-9: Current Trends of CCEs with varied 1N silane content at 0.7 and 1.1 V and varied flow rates. The experiments were performed in 0.2 M CuCl in 2 M HCl anolyte and DI H ₂ O catholyte both under N ₂ atmosphere at 40, 60, 80, and 100 mL min ⁻¹ electrolyte flow rate. Scanned from 0.2 to 1.2 V vs. RHE with 5 mV steps and 0.5 s dwell time per step. (A) Current density at 0.7 V vs. RHE (B) Current density at 1.1 V vs. RHE..... | 76 |
| Figure 4-10: Potentiostatic Holds of the 27.18 wt% CCE at 0.7 V. The experiments were performed in 0.2 M CuCl in 2 M HCl anolyte and DI H ₂ O catholyte both under N ₂ atmosphere at 40, 60, 80, and 100 mL min ⁻¹ electrolyte flow rate..... | 77 |
| Figure 4-11: Comparison of current response dependence on flow rate at 0.7 V for 27.18 wt% Si CCE. Both experiments were performed in 0.2 M CuCl in 2 M HCl anolyte and DI H ₂ O catholyte both under N ₂ atmosphere at 40, 60, 80, and 100 mL min ⁻¹ electrolyte flow rate. | 78 |
| Figure 4-12: Potentiostatic holds at 0.7 V for the 32.4 wt% Si CCE. Experiments performed in 0.2 M CuCl in 2 M HCl anolyte and DI H ₂ O catholyte both under N ₂ atmosphere at 40 and 60 mL min ⁻¹ electrolyte flow rate. Copper crossover visible after approximately 400 s. | 79 |
| Figure 4-13: Potentiostatic hold current trends of CCEs with varied 1N silane content at 0.7 V and varied flow rates. The experiments were performed in 0.2 M CuCl in 2 M HCl anolyte and DI H ₂ O catholyte both under N ₂ atmosphere at 40, 60, 80, and 100 mL min ⁻¹ electrolyte flow rate. Potential held at 0.7 V vs. RHE, current value taken at 150 s. (A) Area specific (B) Carbon mass normalized..... | 80 |

| | |
|--|----|
| Figure 4-14: Relationship of 1N silane composition to current response in potentiostatic holds taken at 0.7 V. Experiment was performed in 0.2 M CuCl in 2 M HCl anolyte and DI H ₂ O catholyte both under N ₂ atmosphere at 40 mL min ⁻¹ electrolyte flow rate..... | 81 |
| Figure 4-15: Capacitive CV of CCE materials with 30±3% 1N silane loading and varied total CCE mass loadings. 10 mV s ⁻¹ scan rate from 0.2 to 1.0 V vs. RHE. Current normalized for geometric SA and for mass of carbon. In 2 M HCl under N ₂ atmosphere at 60 mL min ⁻¹ anolyte flow rate. (A) Area specific (B) Carbon mass normalized..... | 84 |
| Figure 4-16: Nyquist plots of CCE's with 30±3% 1N silane content and varied total mass loadings. Experiments were performed in 2 M HCl anolyte under N ₂ atmosphere at 60 mL min ⁻¹ anolyte flow rate and 25 mL min ⁻¹ H ₂ gas provided to the cathode. (A) Nyquist plot (B) High frequency region. | 85 |
| Figure 4-17: Capacitance plots of 30±3% 1N silane content CCEs with varied total mass loadings. Experiment was performed in 2 M HCl anolyte under N ₂ atmosphere at 60 mL min ⁻¹ anolyte flow rate and 25 mL min ⁻¹ H ₂ gas provided to the cathode. (A) Area specific capacitance (B) Mass of carbon normalized. | 86 |
| Figure 4-18: Potential stair step measurements of CCEs with 30±3% 1N silane composition and varied total CCE mass loadings. Scanned from 0.2 to 1.2 V with 5 mV steps and 0.5 s dwell time per step. Experiment performed in 0.2 M CuCl in 2 M HCl anolyte and DI H ₂ O catholyte both under N ₂ atmosphere at 60 mL min ⁻¹ electrolyte flow rate. | 87 |
| Figure 4-19: Current Trends of CCEs with 30±3% 1N silane composition and varied total CCE mass loading at 0.7 and 1.1 V and varied flow rates. Tests performed in 0.2 M CuCl in 2 M HCl anolyte and DI H ₂ O catholyte both under N ₂ atmosphere at 40, 60, 80, and 100 mL min ⁻¹ electrolyte flow rate. Scanned from 0.2-1.2 V vs. RHE with 5 mV steps and 0.5s dwell time per step. (A) Current density at 0.7 V vs. RHE (B) Current density at 1.1 V vs. RHE. | 89 |
| Figure 4-20: Potentiostatic hold current trends of CCEs with 30±3% 1N silane composition and varied total CCE mass loadings at 0.7 V vs. RHE and varied flow rates. Tests performed in 0.2 M CuCl in 2 M HCl anolyte and DI H ₂ O catholyte both under N ₂ atmosphere at 40, 60, 80, and 100 mL min ⁻¹ electrolyte flow rate. Potential held at 0.7 V, current value taken at 150 s. | 90 |
| Figure 4-21: Relationship of total CCE mass loading to current response in potentiostatic holds taken at 0.7 V. Collected in 0.2 M CuCl in 2 M HCl anolyte and DI H ₂ O catholyte both under N ₂ atmosphere at 40 mL min ⁻¹ electrolyte flow rate..... | 91 |

| | |
|---|-----|
| Figure 4-22: Normalized capacitance plot of 30±3% 1N silane content CCEs with varied total mass loadings. Tests performed at 0 V vs. OCV in 2 M HCl anolyte under N ₂ atmosphere at 60 mL min ⁻¹ anolyte flow rate and 25 mL min ⁻¹ H ₂ gas provided to the cathode..... | 91 |
| Figure 4-23: TEM Images of B1P69S1 1N material (A) and B1P83S1 2N material (B) at 92000 and 180000x magnification respectively. | 93 |
| Figure 4-24: SEM images taken of CCE samples B1P81S1, B1P81S2, and B1P83S1 at 100 and 2500 x magnification..... | 94 |
| Figure 4-25: SEM images taken of CCE samples B1P85S2, B1P85S1, and B1P85S3 at 100 and 2500 x magnification..... | 95 |
| Figure 4-26: Capacitive CV of CCE materials with varied 2N silane loading. 10 mV s ⁻¹ scan rate from 0.2 to 1.0 V vs. RHE. Current normalized for geometric SA and for mass of carbon. In 2 M HCl under N ₂ atmosphere at 60 mL min ⁻¹ anolyte flow rate. (A) Area specific (B) Carbon mass normalized..... | 97 |
| Figure 4-27: Nyquist plots of varied 2N silane content CCEs. Tests performed at 0 V vs. OCV in 2 M HCl anolyte under N ₂ atmosphere at 60 mL min ⁻¹ anolyte flow rate and 25 mL min ⁻¹ H ₂ gas provided to the cathode. (A) Nyquist plot (B) High frequency region. | 98 |
| Figure 4-28: Capacitance plots of CCEs with varied 2N silane content. Experiments performed at 0 V vs. OCV in 2 M HCl anolyte under N ₂ atmosphere at 60 mL min ⁻¹ anolyte flow rate and 25 mL min ⁻¹ H ₂ gas provided to the cathode. (A) Area specific capacitance (B) Mass of carbon normalized (C) Capacitance normalized to 1..... | 99 |
| Figure 4-29: Potential stair step measurements of CCE's with varied 2N silane composition. Scanned from 0.2 to 1.2 V with 5 mV steps and 0.5 s dwell time per step. Tests performed in 0.2 M CuCl in 2 M HCl anolyte and DI H ₂ O catholyte both under N ₂ atmosphere at 60 mL min ⁻¹ electrolyte flow rate. | 100 |
| Figure 4-30: Current Trends of CCEs with varied 2N silane content at 0.7 and 1.1 V and varied flow rates. Tests performed in 0.2 M CuCl in 2 M HCl anolyte and DI H ₂ O catholyte both under N ₂ atmosphere at 40, 60, 80, and 100 mL min ⁻¹ electrolyte flow rate. Scanned from 0.2 to 1.2 V vs. RHE with 5 mV steps and 0.5 s dwell time per step. (A) Current density at 0.7 V vs. RHE (B) Current density at 1.1 V vs. RHE. | 101 |
| Figure 4-31: Potentiostatic hold current trends of CCEs with varied 2N silane content at 0.7 V and varied flow rates. Tests performed in 0.2 M CuCl in 2 M HCl anolyte and DI H ₂ O catholyte | |

| | |
|--|-----|
| both under N ₂ atmosphere at 40, 60, 80, and 100 mL min ⁻¹ electrolyte flow rate. Potential held at 0.7 V vs. RHE, current value taken at 150 s. (A) Area specific (B) Carbon mass normalized.. | 102 |
| Figure 4-32: Relationship of 2N silane composition to current response in potentiostatic holds taken at 0.7 V. Experiments performed in 0.2 M CuCl in 2 M HCl anolyte and DI H ₂ O catholyte both under N ₂ atmosphere at 40 mL min ⁻¹ electrolyte flow rate. | 104 |
| Figure 4-33: Capacitive CV of CCE materials with varied 3N silane loading. 50 mV s ⁻¹ scan rate from 0.2 to 1.0 V vs. RHE. Current normalized for geometric SA and for mass of carbon. In 2 M HCl under N ₂ atmosphere at 60 mL min ⁻¹ anolyte flow rate. (A) Area specific (B) Carbon mass normalized..... | 105 |
| Figure 4-34: Nyquist plots of varied 3N silane content CCEs. Experiment performed at 0 V vs. OCV in 2 M HCl anolyte under N ₂ atmosphere at 60 mL min ⁻¹ anolyte flow rate and 25 mL min ⁻¹ H ₂ gas provided to the cathode. (A) High frequency region (B) Full nyquist plot..... | 107 |
| Figure 4-35: Capacitance plots of CCEs with varied 3N silane content. Experiment performed at 0 V vs. OCV in 2 M HCl anolyte under N ₂ atmosphere at 60 mL min ⁻¹ anolyte flow rate and 25 mL min ⁻¹ H ₂ gas provided to the cathode. (A) Area specific capacitance (B) Mass of carbon normalized (C) Capacitance normalized to 1..... | 108 |
| Figure 4-36: Potential stair step measurements of CCEs with varied 3N silane composition. Scanned from 0.2-1.2 V with 5 mV steps and 0.5 s dwell time per step. Collected in 0.2 M CuCl in 2 M HCl anolyte and DI H ₂ O catholyte both under N ₂ atmosphere at 60 mL min ⁻¹ electrolyte flow rate..... | 109 |
| Figure 4-37: Current Trends of CCEs with varied 3N silane content at 0.7 and 1.1 V and varied flow rates. Experiments performed in 0.2 M CuCl in 2 M HCl anolyte and DI H ₂ O catholyte both under N ₂ atmosphere at 40, 60, 80, and 100 mL min ⁻¹ electrolyte flow rate. Scanned from 0.2 to 1.2 V vs. RHE with 5 mV steps and 0.5 s dwell time per step. (A) Current density at 0.7 V vs. RHE (B) Current density at 1.1 V vs. RHE..... | 110 |
| Figure 4-38: Potentiostatic hold current trends of CCEs with varied 3N silane content at 0.7 V and varied flow rates. Experiments performed in 0.2 M CuCl in 2 M HCl anolyte and DI H ₂ O catholyte both under N ₂ atmosphere at 40, 60, 80, and 100 mL min ⁻¹ electrolyte flow rate. Potential held at 0.7 V vs. RHE, current value taken at 150 s. (A) Area specific (B) Carbon mass normalized..... | 111 |

| | |
|---|-----|
| Figure 4-39: Relationship of 3N silane composition to current response in potentiostatic holds taken at 0.7 V. Collected in 0.2 M CuCl in 2 M HCl anolyte and DI H ₂ O catholyte both under N ₂ atmosphere at 40 mL min ⁻¹ electrolyte flow rate..... | 112 |
| Figure 4-40: Nyquist and Capacitance plots of CCEs with representative compositions from 1N, 2N, and 3N silane precursors. Representative compositions of the silanes were used. Collected in 2 M HCl anolyte under N ₂ atmosphere at 60 mL min ⁻¹ anolyte flow rate and 25 mL min ⁻¹ H ₂ gas provided to the cathode. (A) High frequency region Nyquist plot (B) Mass of carbon normalized capacitance plot..... | 121 |
| Figure 4-41: Example of the integrated area for the forward scan integration of capacitive CVs. | 122 |
| Figure 4-42: Total charge from capacitive CV measurements taken at 50 mV s ⁻¹ in relation to the molar loading of silane in the CCE material. | 123 |
| Figure 4-43: Total charge from capacitive CV measurements taken at 50 mV s ⁻¹ in relation to the molar content of amines in the CCE material. | 124 |
| Figure 4-44: Comparison of best potential stair step measurements for 1N, 2N, and 3N CCEs as well as bare CFP and standard Pt/C catalyst materials. Scanned from 0.2 to 1.2 V with 5 mV steps and 0.5 s dwell time per step. Collected in 0.2 M CuCl in 2 M HCl anolyte and DI H ₂ O catholyte both under N ₂ atmosphere at 60 mL min ⁻¹ electrolyte flow rate..... | 125 |
| Figure 4-45: Relationship between silane loading and mass of carbon normalized limiting current taken from potentiostatic measurements. | 126 |
| Figure 4-46: Comparison of CCE capacitance and mass of carbon specific limiting current taken from potentiostatic holds..... | 127 |
| Figure 4-47: Comparison of area normalized current response to potentiostatic holds for all 1N, 2N, and 3N materials. | 128 |
| Figure 4-48: Comparison of best area normalized current responses to potentiostatic holds from 1N, 2N, and 3N CCE materials as well as control electrodes..... | 128 |
| Figure 5-1: 18000x magnification TEM image of Pt/C cathode catalyst before operation (A) and after Cu plating had occurred (B). | 131 |
| Figure 5-2: SEM Images of Cu Dendrites grown on 0.3 mg Pt cm ⁻² catalyst cathode (A) and Cu metal impregnated into the Nafion 115 PEM (B) after electrolysis cell failure. | 132 |

| | |
|---|-----|
| Figure 5-3: Picture of 0.3 mg Pt cm ⁻² catalyst cathode (A) and cathode side of the Nafion 115 PEM (B) for the CuCl-HCl electrolysis process after significant Cu crossover and plating has occurred (Red/brown colour is Cu metal)..... | 132 |
| Figure 5-4 : Examples of transient currents during potentiostatic measurements..... | 133 |
| Figure 5-5: Total charge at time of cell failure for CCE materials and Bare CFP control..... | 136 |
| Figure 5-6: Example crossover and cell regeneration of the 50 wt% 1N CCE (B1P69S2) during 0.7 V potentiostatic holds (Red) with 0 V regeneration holds (Blue). Experiments performed in 0.2 M CuCl in 2 M HCl anolyte and DI H ₂ O catholyte both under N ₂ atmosphere at 60 mL min ⁻¹ electrolyte flow rate. | 138 |
| Figure 5-7: Linear sweep voltammetry from 0.1 to 1.0 V at 20 mV s ⁻¹ scan rate of CuCl at varied concentrations in 2 M HCl under N ₂ atmosphere..... | 139 |
| Figure 5-8: Relationship between Cu concentration in 2 M HCl and current amplitude. Low concentration values expanded and inset. Data taken from Figure 5-7..... | 140 |

Common Abbreviations

1N - (3-Aminopropyl)triethoxysilane,

2N - N-[3-(Trimethoxysilyl)propyl]ethylenediamine

3N - N¹-(3-Trimethoxysilylpropyl)diethylenetriamine

AC – Alternating Current

Ag/AgCl – Silver/Silver Chloride Electrode

CCE – Ceramic Carbon Electrode

CFP – Carbon Fiber Paper

CV – Cyclic Voltammetry

DC – Direct Current

EIS – Electrochemical Impedance Spectroscopy

g_{Carbon} – Grams of Carbon

HER – Hydrogen Evolution Reaction

LSV – Linear Sweep Voltammetry

M – Mols L⁻¹

MEA – Membrane Electrode Assembly

mmol - milimole

OCV/OCP – Open Circuit Voltage / Open Circuit Potential

PEM – Proton Exchange Membrane / Polymer Electrolyte membrane

POX – Partial Oxidation

Pt/C – Platinum on Carbon Support

RHE – Reversible Hydrogen Electrode

R_{Σ} – Sum of Ionic and Electronic Resistance

SCE – Saturated Calomel Electrode

SEM – Scanning Electron Microscopy

SHE – Standard Hydrogen Electrode

TEM – Transmission Electron Microscopy

TGA – Thermogravimetric Analysis

Z' – Real Impedance

Z'' – Imaginary Impedance

Chapter 1 : Introduction to Hydrogen Production and Electrochemical Characterization Techniques

Currently the bulk of the world's power demands are met by non-renewable technologies such as gas or coal fire power plants^{1,2}. In the case of distributed power supplies such as vehicles and generators, gasoline consumption creates a considerable amount of volatile organic compounds as well as nitrous oxide and carbon monoxide¹. This is combined with the consumption of a non-renewable resource. The overall energy demands of the world are also expected to increase by an amount more than double the projected population increase by 2050². Compounding this, in America alone, it has been shown that pollutants could be affecting the lives and/or the surrounding environment of half of the population¹.

There is an obvious need for a renewable energy technology to replace existing non-renewables and to meet growing demands. While this would in essence free us from non-renewable fuels, there is also need to develop technologies to carry the energy produced². Hydrogen gas has potential as a fuel for distributed power sources, as it can be produced from a wide variety of fuel sources both through the consumption of renewable products such as biomass or through various electrolysis procedures^{1,2}. In the interim, hydrogen can also be produced from fossil fuels in a non-renewable manner. When consumed within a standard PEM fuel cell or combusted, the sole product is water (Equation 1-1)³.



Additionally, hydrogen gas can be reacted with carbon dioxide to produce liquid hydrocarbons, alcohols, or other high value products via the Fisher-Tropsch process amongst others¹.

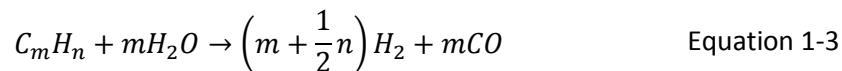
1.1: Current H₂ Production Methods

There are a variety of technologies that allow for the production of hydrogen gas, though there are associated drawbacks with each. The most widely adopted method is the steam reforming of fossil fuels. In addition to this method there is the gasification of biomass, the production of biological hydrogen, and finally the electrolysis of water.

1.1.1: Production from fossil fuels.

Conversion of fossil fuels to H₂ gas currently accounts for approximately 97% of the world's H₂ production⁴. For most of the fossil fuel conversion, steam reforming is used. The reforming process can use a wide variety of fossil fuel products, but most often simple methane is used, accounting for more than half of the world's reforming process⁵. In its most basic sense

the steam methane reforming reaction proceeds as shown in Equation 1-2 and Equation 1-3 below^{1,2,5}.



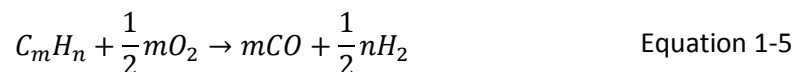
The reforming reaction is endothermic and only takes place at elevated temperatures, typically around 700 – 1000 °C^{1,2,5}. Additionally, the reaction requires the presence of a transition metal catalyst which is typically nickel¹. Finally, the carbon monoxide produced is subsequently reacted in a water-gas shift reaction to produce carbon dioxide and hydrogen gas as follows:¹.

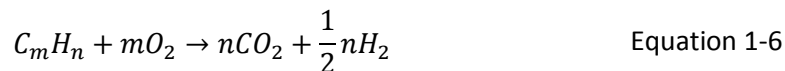


The entire process allows for the production of a gas mixture that is approximately 75% H₂ with the balance mainly comprised of CO₂ and CO¹. As a final step, inline gas purification is required to produce a commercially pure product.

Steam methane reforming is easily the most widely researched and adopted technology for the production of H₂ gas². The process benefits from good conversion efficiency as well as the production of commercially beneficial byproduct gasses. Higher weight hydrocarbons can be used for the production of H₂ in place of the methane, but they do require a higher operating temperature and are generally less efficient^{1,2}. There are a few main drawbacks to the steam methane reforming process. The first and most significant is that it is a currently a nonrenewable process. There has been research into the use of ethanol and methanol, chemicals that can be produced renewably, for reforming, but the technologies are less efficient than, for pure methane^{1,2}. In addition to the nonrenewable nature of the process, the steam methane reforming reaction also readily deactivates and corrodes the catalysts used in the process¹.

Similarly to the steam reforming reaction, fossil fuels can be partially oxidized to produce H₂ gas. By limiting the amount of O₂ gas present during combustion the products can be shifted towards H₂ gas with CO and CO₂ as opposed to H₂O. The reaction is exothermic and can be performed without the aid of a catalyst. Generally the reaction proceeds as follows^{1,5}.





While exothermic, the partial oxidation reaction must be carried out at high temperatures between 1200 and 1450°C, to drive the formation of H₂ gas. The reaction produces H₂ in a lower concentration than the steam methane reforming reaction, but can easily use heavier hydrocarbons for the oxidation. The partial oxidation reaction also uses nonrenewable resources, relying on the consumption of fossil fuels^{1,5}. Building on this technology, the gasification of biomass products also works in the same way as partial oxidation. In the case of biomass gasification a biological feed stock is used in place of the fossil fuel to produce H₂ through a similar partial oxidation reaction and subsequent water-gas shift reaction¹. While this process can tackle some of the nonrenewable aspects of the partial oxidation process, the associated thermal efficiency of biomass gasification is much lower at 35 – 50% compared to 60-75% efficiencies from the POX process¹.

1.1.2 Hydrogen production from water electrolysis.

In contrast to the conversion of fossil fuels, the electrolysis of water provides a renewable method to produce H₂ gas. The electrolysis of water is an established process, with commercial production as far back as the 1890's⁵. There are two main methods of performing water electrolysis; alkaline electrolysis and proton exchange membrane electrolysis (in an acidic environment). In both cases H₂ gas is the primary product with a byproduct of O₂ gas. The two methods of electrolysis typically operate at temperatures under 80 °C⁶. The primary difference between the two methods is simply which type of intermediate ion is produced during the reaction. The intermediate ion is what will travel between the anode and cathode to produce the H₂ and O₂ gas separately. The anode and cathode reactions associated with both types of electrolysis are shown below.

Table 1-1: General Half-Cell reactions for the electrolysis of water in alkaline and acidic liquid environments⁵.

| Reaction Location | Alkaline Reactions | E° (V) | Acidic Reactions | E° (V) |
|-------------------|--|--------|---|--------|
| Anode | $2OH^- \rightarrow H_2O + \frac{1}{2}O_2 + 2e^-$ | -0.40 | $H_2O \rightarrow 2H^+ + \frac{1}{2}O_2 + 2e^-$ | -1.23 |
| Cathode | $2H_2O + 2e^- \rightarrow H_2 + 2OH^-$ | -0.83 | $2H^+ + 2e^- \rightarrow H_2$ | 0.00 |

Alkaline water electrolysis is a process that was first developed in the 1980's⁵. The anode and cathode are both held in an alkaline electrolyte solution (typically ~30 wt% KOH)⁵.

The electrodes are separated by a porous membrane to allow OH^- anions to flow from the cathode to the anode. To provide sufficient current density the cell voltage in alkaline electrolysis ranges between 1.8 and 2.2 V vs. SHE⁵. This voltage is made up of the redox potential of water at 1.23 V vs. SHE as well as ohmic loss and added anodic and cathodic overpotentials⁶. This overall process has been well developed and is currently a commercial technology¹.

In contrast to alkaline water electrolysis, proton exchange membrane (PEM) electrolyzers perform acidic water electrolysis, with H^+ cations transported from the anode to the cathode. A proton exchange membrane separates the anode and cathode electrodes selectively allowing transport of protons between the electrodes. This is done in place of an anionic liquid electrolyte in alkaline water electrolysis and allows for the separation of the H_2 and O_2 gas products^{1,2,5}. Operating voltages for the acidic PEM electrolysis are also similar in range to that of alkaline electrolysis. This large voltage is again due to the presence of ohmic losses and the overpotentials at the anode and cathode. A particular issue with PEM electrolysis is the transport of protons from the anode to the cathode as they must pass through a solid membrane⁵.

Typically the PEM is made of Nafion polymer. In some cases other heavily sulfonated polymer materials can also be used¹. In PEM electrolysis systems the anode, cathode, and PEM are sandwiched together with high pressures. This creates a zero gap construction providing good contact between the PEM and electrode surfaces. This allows for quick movement of the protons through the PEM¹. This contact can also create a corrosive environment at the surface of the electrode, creating some electrode design constraints⁵. In all, the PEM electrolysis process has similar benefits and draw backs when compared to alkaline water electrolysis. It also produces high purity H_2 gas from a renewable source but also suffers from poorer efficiency when compared to fossil fuel reforming.

In a process that reverses a solid oxide fuel cell, hydrogen can be produced. These solid oxide electrolysis cells (SOEC) are the third and final form of direct hydrogen production through electrolysis. The use of SOEC's allows for the production of the H_2 gas at higher overall temperatures between 750 and 1050 $^\circ\text{C}$ ¹. A SOEC uses a solid electrolyte that allows for the migration of O^{2-} ions to facilitate the production of H_2 gas. The two electrode reactions can be summarized in the following way (Table 1-2)^{1,2}.

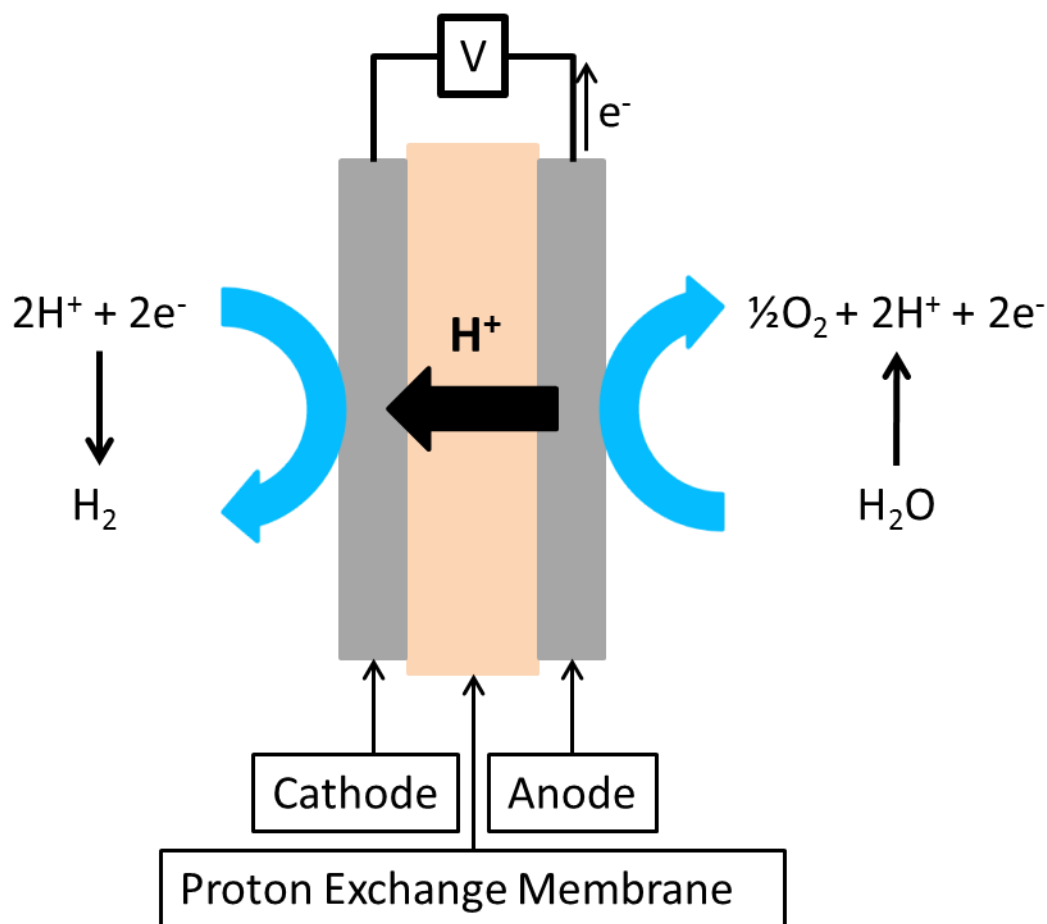


Figure 1-1: Schematic Diagram of PEM Electrolyzer with associated half-cell equations.

Table 1-2: The general Half-Cell reactions for the electrolysis of water for high temperature solid oxide electrolysis cells with O^{2-} as the mobile ion

| Reaction Location | Reaction Equation |
|-------------------|--|
| Cathode | $2\text{H}_2\text{O} + 4\text{e}^- \rightarrow 2\text{H}_2 + 2\text{O}^{2-}$ |
| Anode | $2\text{O}^{2-} \rightarrow \text{O}_2 + 4\text{e}^-$ |

Materials choices for this method of H_2 production are constrained by the high temperatures of reactions¹. In addition to this there is the need for a high temperature heat source. With all this taken into consideration there is still a dramatic increase in efficiency for SOEC's over PEM and alkaline electrolysis systems. This is mainly due to the high temperature of operation decreasing in the anodic and cathodic overpotentials⁷.

Of the processes reviewed the primary industrial installations of these technologies focus on fossil fuel reforming, as well as alkaline electrolysis. Biomass gasification and PEM electrolysis are also being deployed by companies such as Proton Onsite and Hydrogenics^{8,9}. When summarizing the drawbacks of the primary H₂ production methods either a lack of renewability or a low efficiency become the common problems. A notable alternative to the previously mentioned technologies is the use of thermochemical cycles.

1.2: Introduction to Thermochemical Cycles

Thermochemical cycles allow for the production of H₂ and O₂ gas from H₂O through a series of chemical intermediates^{10,11}. Under ideal conditions without catalysis, water will decompose into H₂ and O₂ gas at a 2500 °C¹. The chemical intermediates are chosen to reduce the overall temperature required. In addition to the reduced temperatures for decomposition, the chemical intermediates are selected such that they can be regenerated. Regenerating the chemical intermediates means that the net equation for thermochemical cycles is simply the decomposition of H₂O into H₂ and O₂. There are several potential thermochemical cycles that can be employed in this manner but the general structure of their reactions is shown in Figure 1-2.

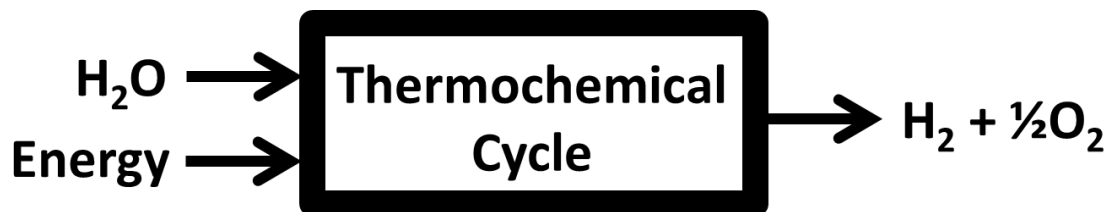


Figure 1-2: Schematic of general thermochemical cycle processes.

The temperature required for uncatalyzed H₂O decomposition for industrial production of H₂ gas has significant materials and power source constraints. These challenges spurred the investigation of thermochemical cycles. There are over 200 potential thermochemical cycles of which a select few have been isolated for research purposes^{4,10,11}. These cycles can be selected for the materials used as well as the overall temperature requirements.

1.2.1: Conventional Thermochemical Cycles

Of the multiple thermochemical cycles only a few have received significant research. The most common cycle is the Sulfur-Iodine cycle. The cycle is comprised of three steps shown below (Table 1-3)^{5,12}.

Table 1-3: The stepwise chemical reactions for the production of H₂ and O₂ gas in the Sulfur-Iodine thermochemical cycle

| # | Reaction Equation |
|---|---|
| 1 | $SO_{2(g)} + I_{2(l)} + 2H_2O_{(l)} \rightarrow H_2SO_{4(aq)} + 2HI_{(aq)}$ |
| 2 | $H_2SO_{4(aq)} \rightarrow SO_{2(g)} + H_2O_{(aq)} + \frac{1}{2}O_{2(g)}$ |
| 3 | $2HI_{(aq)} \rightarrow H_{2(g)} + I_{2(g)}$ |

Only step 1 from the above list occurs at a low temperature and is also exothermic. This highlights a significant hurdle involved in the operation of the sulfur iodine cycle. Both of the remaining two reactions require a high temperature to proceed. Reaction 3 requires a temperature of 400 °C and reaction 2 requires 900 °C⁵. These high temperatures are common throughout the most viable thermochemical cycles. For example, the Ispra Mark 10 reactions requires temperatures of 870 °C and the ZnO/Zn cycle requires 1800 °C temperatures for one step¹. Even with these large thermal requirements the cycles still report reasonable efficiencies. In the case of the Sulfur-Iodine cycle there is a reported total efficiency of 47%¹. This is again comparable to the efficiencies seen for water the electrolysis processes. The advantage that can be gained by thermochemical cycles is the potential for capture of waste heat to at least partly drive the thermochemical cycles. While these additions will not improve the physical efficiency of the reaction the processes will be necessarily more economical, offsetting the poorer reaction efficiency. One final issue with standard thermochemical cycles is the potentially highly corrosive reaction steps. The mixture of high temperatures and strong acids limits the materials choices¹². This extends beyond problems seen with SOEC's. In the case of the Sulfur-Iodine cycle the 2nd reaction takes place in 50-98% H₂SO₄ at the previously mentioned 900 °C. In addition to the specific examples listed for the Sulfur-Iodine cycle, similar problems are common to all thermochemical cycles. There has been a large amount of research into reducing the temperatures and associated corrosive environments with thermochemical cycles. One notable method is through the development of hybrid thermochemical cycles.

1.2.2: Hybrid Thermochemical Cycles

Hybrid thermochemical cycles incorporate one or more electrochemical steps to replace existing reactions that could have proven too challenging or costly to complete traditionally. This brings with it two features. The first is that in many cases the temperature of the electrochemical step is at ambient or only slightly elevated temperatures^{4,11,13}. Additionally, the electrolysis steps allow for the hybrid cycles to draw from existing technologies. It is important to note that the electrical input required does present a potential drawback.

As an example, the Sulfur-Iodine cycle outlined previously (1.2.1: Conventional Thermochemical Cycles) has been altered to include an electrolysis step. In this case the decomposition of H_2SO_4 is maintained, but the electrolysis of SO_2 in the presence of water facilitates the production of H_2 (Figure 1-3). The whole cycle is reduced to only two steps.

Table 1-4: The stepwise chemical reactions and electrochemical half-cell reactions for the Hybrid Sulfur thermochemical cycle¹³.

| # | Reaction Equation | | | |
|---|--|---------------|------------------------------------|---------------|
| 1 | $H_2SO_{4(aq)} \rightarrow SO_{2(g)} + H_2O_{(g)} + \frac{1}{2}O_{2(g)}$ | | | |
| | Anode | E° (V) | Cathode | E° (V) |
| 2 | $SO_{2(aq)} + 2H_2O_{(l)} \rightarrow H_2SO_{4(aq)} + 2H^+ + 2e^-$ | -0.17 | $2H^+ + 2e^- \rightarrow H_{2(g)}$ | 0.00 |

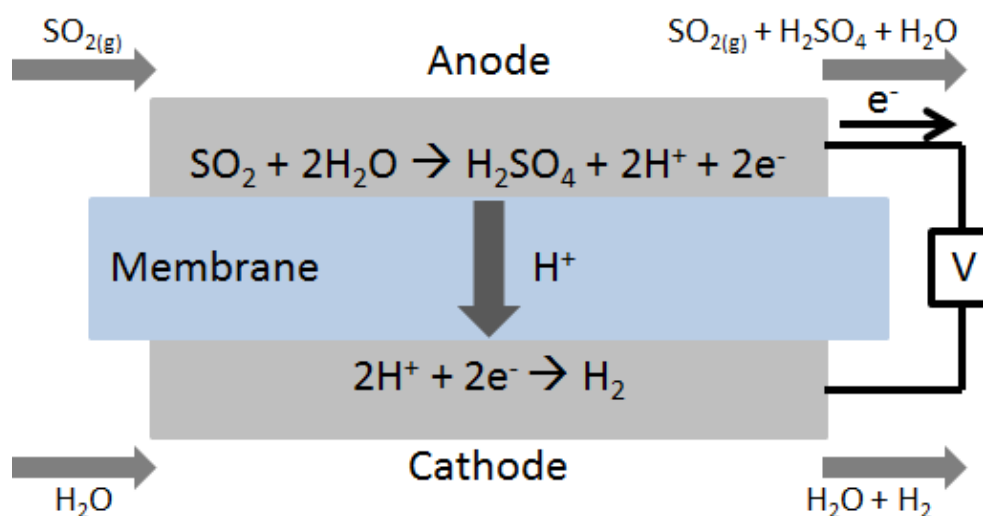


Figure 1-3: Schematic Diagram for the electrolysis of SO_2 and production of H_2 gas in a PEM style electrolyzer for the Hybrid Sulfur thermochemical cycle. Diagram based on work of Staser JA and Weidner JW¹³.

By both eliminating a step and reducing the overall temperature requirement the thermal efficiency of the reaction can be maintained. This reaction does, however, have a direct competition from alkaline electrolysis. This is again a point where the concept of waste heat capture must be considered to account for potential inefficiencies in the hybrid cycle. In particular, when comparing Figure 1-1 and Figure 1-3 it can be seen that the hybrid sulfur cycle electrochemical step is very similar to PEM electrolysis. Where the water would normally be split to produce O_2 and H^+ ions, instead SO_2 , is oxidized to produce the H_2SO_4 and H^+ ions.

Taking advantage of existing technologies, the electrolysis step occurs in a zero gap PEM electrolyzer system (with modification to the electrolyte solutions). There are however restrictions limiting the effectiveness of Nafion over other materials¹³. At the cathode the cycle can benefit from existing technologies as the production of H_2 gas is identical to a standard PEM electrolyzer process. The main advantage of this electrolysis process over water electrolysis is that the thermodynamic onset potential for the oxidation of SO_2 is 0.17 V vs. SHE as opposed to 1.23 V vs. SHE for the oxidation of H_2O ¹. This smaller reversible potential decreases the cell voltage required for operation which allows the Hybrid Sulfur Cycle, as well as other hybrid cycles, to compete with simple water electrolysis. As with the traditional thermochemical cycles, the Hybrid sulfur cycle was provided as an example cycle owing to the significant research on the topic. The problems that were addressed in this example can be expected to carry through to other hybrid cycles. Finally, one additional problem associated with thermochemical cycles is the conversion ratios of the different reactions. With incomplete conversion of the reactants, thermal inefficiencies begin to arise. The removal of steps, streamlining the thermochemical cycle is one method by which to combat this problem^{1,2,5}. There is also potential to gain insight into the electrolysis process by examining redox flow cells. These are power generating systems oxidizing H_2 gas and using a closed loop of reactions to provide a reducible catholyte solution. This is in essence the reverse of hybrid cycles electrochemical steps.¹⁴

1.2.3: Three Step Hybrid CuCl-HCl Thermochemical Cycle

Another hybrid thermochemical cycle is the CuCl-HCl cycle. Specific investigations into this cycle are the total focus of the research presented in this thesis. As such a more in depth description and investigation of this cycle follows. The CuCl-HCl cycle has multiple variations with different numbers of steps as well as varied electrochemical steps. The current cycle

consists of only three steps, a reduction from the original five and four step cycles. Table 1-5 shows the separate reactions for the three, four, and five step CuCl-HCl cycle. Both the four and five step thermochemical cycles are identical chemically with the five step cycle including an additional step for the drying of aqueous CuCl₂ produced in step three. Further specifics of the four step cycle can be found in work performed in our group previously^{4,15}.

Table 1-5: The stepwise chemical and electrochemical half-cell equations for the three, four, and five step hybrid CuCl-HCl thermochemical cycle⁴.

| # | 3 Step Cycle Reaction Equations | | | |
|---|--|--------|---|--------|
| 1 | $2\text{CuCl}_{2(s)} + \text{H}_2\text{O}_{(l)} \rightarrow \text{Cu}_2\text{OCl}_{2(s)} + 2\text{HCl}_{(aq)}$ | | | |
| 2 | $\text{CuOCuCl}_{2(s)} \rightarrow \frac{1}{2}\text{O}_{2(g)} + 2\text{CuCl}_{(s)}$ | | | |
| | Anode | E° (V) | Cathode | E° (V) |
| 3 | $2\text{CuCl}_{(aq)} + 2\text{HCl}_{(aq)} \rightarrow 2\text{CuCl}_{2(aq)} + 2\text{H}^+ + 2\text{e}^-$ | -0.16 | $2\text{H}^+ + 2\text{e}^- \rightarrow \text{H}_{2(g)}$ | 0.00 |

| # | 4 and 5 Step Cycle Reaction Equations | | | |
|---|--|--------|--|--------|
| 1 | $2\text{CuCl}_{2(s)} + \text{H}_2\text{O}_{(l)} \rightarrow \text{Cu}_2\text{OCl}_{2(s)} + 2\text{HCl}_{(aq)}$ | | | |
| 2 | $\text{CuOCuCl}_{2(s)} \rightarrow \frac{1}{2}\text{O}_{2(g)} + 2\text{CuCl}_{(s)}$ | | | |
| 3 | $2\text{Cu}_{(s)} + 2\text{HCl} \rightarrow \text{H}_{2(g)} + 2\text{CuCl}_{(s)}$ | | | |
| | Anode | E° (V) | Cathode | E° (V) |
| 4 | $\text{CuCl}_{(aq)} + \text{HCl}_{(aq)} \rightarrow \text{CuCl}_{2(aq)} + \text{e}^-$ | -0.16 | $\text{CuCl}_{(aq)} + \text{e}^- \rightarrow \text{Cu}_{(s)} + \text{Cl}_{(aq)}^-$ | 0.52 |

One of the main attractions of the CuCl-HCl cycle is that it requires relatively low temperatures to operate. The first and second steps of the reactions require only 400 and 500 °C respectively to drive the reactions. This, coupled with the ambient/low temperature CuCl electrolysis, allows for a lower overall temperature of operation when compared to other thermochemical cycles. These low temperature requirements allow for the system to be coupled to a variety of heat sources; however, the cycle is being investigated specifically for its integration with GEN IV supercritical water nuclear reactors which have a compatible operating temperature^{4,16,17}. As can be seen in Figure 1-4, the third step of the cycle is similar to both standard PEM water electrolysis as well as the SO₂ electrolysis process

associated with the Hybrid Sulfur Cycle^{1,13}. Another advantage of the CuCl-HCl thermochemical cycle is that H₂ gas is produced through the same mechanism at the cathode as SO₂ electrolysis and standard PEM water electrolysis. This allows the CuCl-HCl reaction to borrow from existing H⁺ reduction catalyst technologies.

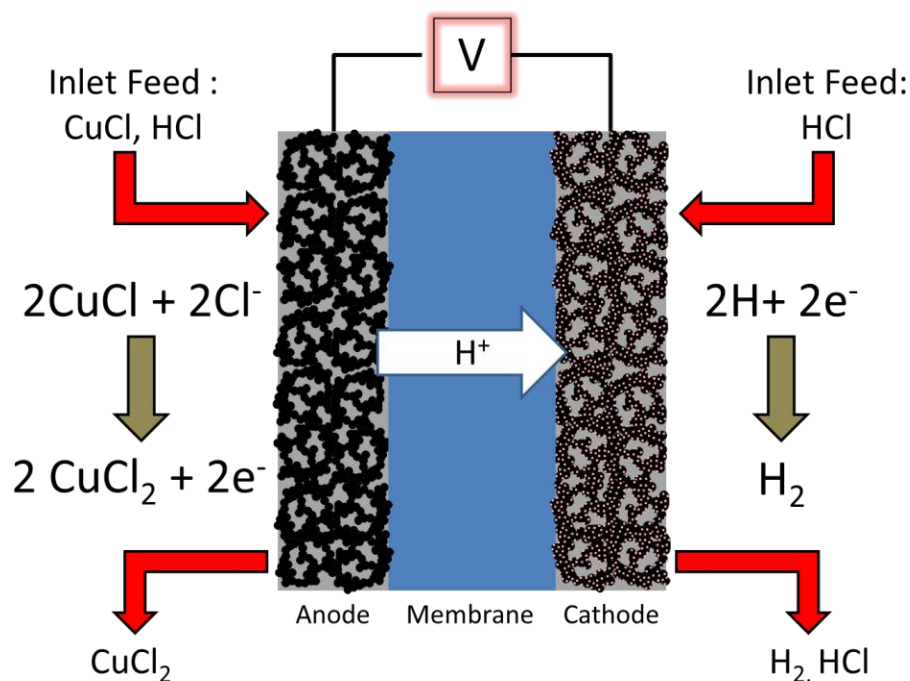


Figure 1-4: Schematic Diagram for the electrolysis of CuCl in the presence of HCl and the production of H₂ gas in a PEM style electrolyzer Hybrid three step CuCl-HCl thermochemical cycle¹⁸.

A distinct difference in the CuCl-HCl cycle when compared to PEM electrolysis and the hybrid sulfur cycle is that the primary oxidation reaction occurs at a transition metal center^{4,16,17}. This inclusion of the Cu atom allows for easy oxidation. Ideally, the onset potential of the Cu(I) oxidation occurs at 0.159 V vs. SHE¹⁹. As with the hybrid sulfur cycle this is a much lower onset potential when compared to H₂O oxidation. Realistically, the onset potential for the cell during testing is actually around 0.4 V vs. SHE which is still more than a volt lower than the average onset potential of 1.5-1.8 V vs. SHE required for water splitting²⁰. This energy difference again translates into a large gain for the CuCl-HCl cycle.

While oxidation can occur easily at a copper center the overall electrolysis process can be limited by the diffusion of the CuCl to the electrode surface. In the case of water electrolysis

the redox species is the electrolyte solution. For CuCl electrolysis the copper species must first diffuse to the surface of the electrode for the oxidation to occur. This diffusion limits the overall rate of the electrolysis process²¹. By comparison the diffusion of H⁺ ions through the PEM and the production of H₂ gas can be considered fast. The other main challenge with the CuCl electrolysis step is the crossover of Cu⁺ to the cathode. If this occurs then the cationic copper can be reduced to copper metal (Equation 1-7)⁴. This parasitic form of the reaction is also present in the hybrid sulfur cycle, where SO₂ can be reduced to sulfur and O₂ gas as seen in Equation 1-8¹³.



The overall negative effects of SO₂ are not fully known. In the case of Cu crossover it has been shown that it causes plating on the cathode electrode as well as negative effects for the overall CuCl-HCl electrolysis process⁴.

Along with the challenges faced in the electrochemical step there are a number of other challenges associated with the CuCl thermochemical cycle. The primary concern is that both steps one and two of the reaction require a solid copper species which must be transported. This is a non-ideal scenario when compared to other cycles such as the Sulfur-Iodine cycle where all the involved reagents are either liquids or gases. In addition to this the molar mass of CuCl is ~99 g mol⁻¹. When considering that two molecules of CuCl must be oxidized to produce one molecule of H₂ gas a reactant to product mass ratio of 100:1. This means that to produce ~1 Kg of H₂ ~100 Kg of CuCl must be moved through the thermochemical cycle. All of these considerations limit the overall heat to hydrogen efficiency of the hybrid CuCl-HCl thermochemical cycle to approximately 43%^{4,22}. While this efficiency is not as high as those listed previously it has been shown to outperform comparable electrolysis from the same nuclear power source. As with other hybrid thermochemical cycles the increase in net efficiency stems from the removal of some intermediate power generation. The inefficiencies associated with the production of electricity for use in direct water electrolysis can be avoided when the direct capture of heat is used to drive some of the cycles' steps.

1.2.4: Research Targets for the Hybrid CuCl-HCl Thermochemical Cycle

The department of energy in the United States outlined a need for high throughput renewable hydrogen production sources. To meet these demands a large scale research project encompassing many research groups as well as industry partners has been developed^{4,20,23,24}. The overall project encompasses many disciplines of chemistry, and engineering. Specific to our research, the eventual goal for the electrochemical step is to produce H₂ gas through CuCl electrolysis with a current density of 500 mA cm⁻² at 0.7 V vs. SHE applied^{4,25}. This is an aggressive goal that is not meant to be met until the year 2025. This is in part to coincide with the deployment of the associated Gen IV Supercritical Water Nuclear reactors which have operating temperatures appropriate for powering the thermochemical cycle. Before this time there are also a series of milestone goals. The most recent of these was to produce a sustained current of 300 mA cm⁻² at 0.7 V vs. SHE²⁶.

1.3: CCE Materials

Within the zero gap PEM electrolyzer there are three main components, the anode and cathode electrodes as well as the proton conducting membrane. For the purposes of most research the membrane is Nafion, a standard PEM material. The Nafion thickness can be altered, however the general material is kept constant across most testing^{18,20,21}. The electrode materials offer more room for modification.

At the cathode of the electrolysis cell the production of H₂ gas behaves similarly to standard electrolysis systems. With this in mind the cathode materials are often comprised of standard platinum on carbon (Pt/C) catalyst materials^{18,20}. At the anode there are a few significant challenges, the first is to provide a large active surface area for the copper oxidation to occur. The second challenge is to produce a durable electrode material to withstand the harsh acidic electrolyte^{21,26}. Currently the anode materials are also derived from standard Pt/C electrolysis electrodes²⁰, however it has been shown that the Pt catalyst is not required for oxidation to occur^{27,28}. The production and characterization of novel anode electrode materials is the primary goal of our work. Specifically our work is done in the absence of a Pt catalyst. To produce durable electrode materials we have examined the use of ceramic carbon electrodes derived from a sol-gel synthesis coupled with a high surface area carbon.

1.3.1: Sol-Gel Method

Sol-Gel chemistry is a process involving the transition from a sol to a gel. A sol is a colloidal suspension of solid particles in a liquid and a gel is a suspension of a liquid inside a solid interlocking structure. The liquid contained in the gel is not at equilibrium and thus pushes outward on the solid structure preventing its collapse. Balancing this outward force, the solid structure pushes in on the liquid keeping it in place²⁹. Through this balance the gel is able to keep its shape that would not exist if the liquid was not present.

The Sol-gel process is used to make metal oxide compounds. They are made by linking together inorganic compounds that can potentially contain organic functional groups. Typically silicon and titanium are used for the production of these compounds, though other atoms such as boron or vanadium can be used²⁹. For our research we produced sol-gels strictly from silicon based precursors. When silicon is added to the solution it is often in the form $\text{Si}(\text{OR})_4$. In this case the R group is an organic group that will either serve a purpose in the characteristics of the gel or be replaced by another functional group later. Two common silicon precursors are tetramethoxysilane and tetraethoxysilane (TMOS and TEOS respectively)²⁹.

The sol-gel process is very broad and can be used for a large number of applications (Figure 1-5). After a gel has been formed it can be dried to form a xerogel or aerogel material. These products can also be heated to form dense ceramics. Before the gel is completely formed the solution can be dried to form a series of uniform colloidal particles. These particles can also be made by grinding xerogels and aerogels. Again before the gel has completely formed the solution can be sprayed or otherwise coated to create thin films, sometimes only a monolayer thick. The solutions can also be pulled into gel fibres. These films and fibres can also be made into dense ceramics fibres and films³⁰. Using a combination of spray coating a not fully formed gel and a subsequent heating we have produced our thin coated ceramic materials¹⁸.

To produce a sol-gel material, silane monomers are condensed into larger polymers. This step cannot be accomplished without the addition of hydroxyl groups to the silane monomers. This is the first step in the production of gels. The addition of hydroxyl groups can be catalyzed either by base or by acid. In the base catalyzed (Figure 1-6) mechanism an OH^- group is added to the silica monomer via an $\text{S}_{\text{N}}2$ reaction²⁹. The OH^- attaches to the silica molecule which then causes an OR^- group to leave.

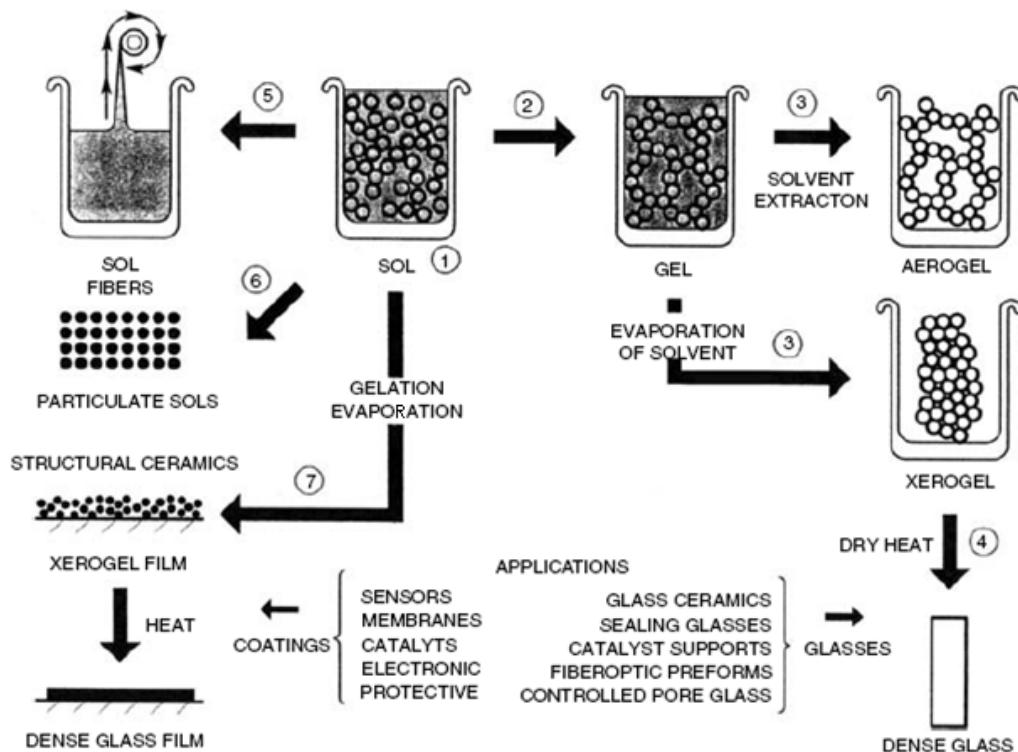


Figure 1-5: An overview of the sol-gel process and the reaction pathways to the various products³⁰. Reproduced with permission of TAYLOR & FRANCIS GROUP LLC in the format Republish in a thesis/dissertation via Copyright Clearance Center.

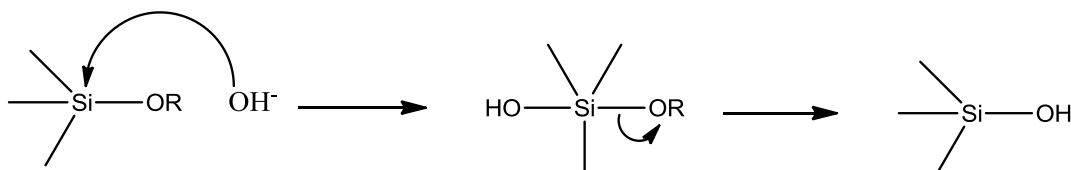


Figure 1-6: The base catalyzed hydrolysis of a silane monomer.

In the acid catalyzed mechanism (Figure 1-7) a hydrogen atom adds to the -OR group, and a water is added to the molecule forming an unstable intermediate. The protonated -ORH group leaves the molecule and a hydrogen is abstracted from the hydronium ion leaving a hydroxyl group attached to the Silane monomer.

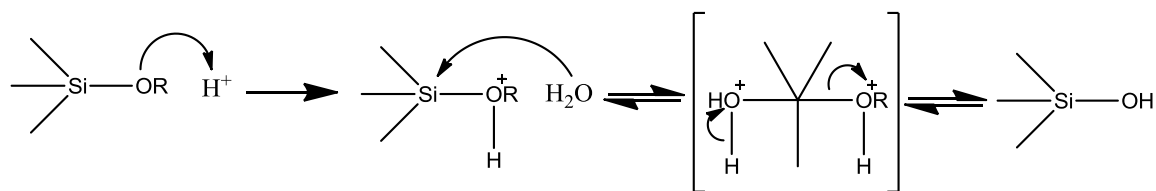


Figure 1-7: The acid catalyzed hydrolysis of a silane precursor.

Importantly, in both mechanisms the acid and base added are simply catalysts. The amount of OR groups that will be replaced is related to the ratio of silica molecules to water molecules, the timeframe of the reaction, as well as the pH, and the concentration of the catalyst. The number of hydroxyl groups on the silica monomer will dictate the overall characteristics of the gel. If there are a large number of hydroxyl groups on the silica there will be more branching than when fewer OH groups are present.

Concurrent with the production of the hydroxyl groups on the silane monomers, condensation reactions between existing hydroxyl groups will cause the gelation of the reaction creating larger polymers. The bonds between the silica monomers are an ether linkage, Si-O-Si, again catalyzed by either base or acid (Figure 1-8 and Figure 1-9 respectively). In the base catalyzed mechanism a proton is abstracted from a hydroxyl group on the silane. This produces a Si-O⁻ group which readily attacks another silicon atom, again in an S_N2 fashion¹ forcing the removal of an OH⁻ group.

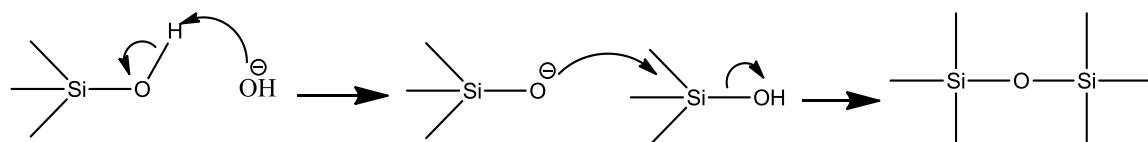


Figure 1-8: The base catalyzed condensation reaction between two silane monomers.

In the acid catalyzed mechanism Si-OH groups are protonated causing them to leave. This stimulates the addition of another Si-OH. With the formation of the Si-O-Si bond, the final hydrogen atom is abstracted to produce the desired product.

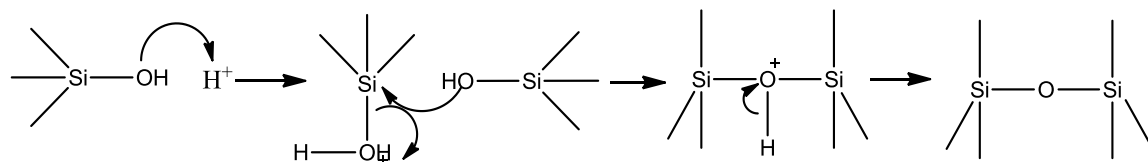


Figure 1-9: The acid catalyzed condensation reaction between two silane monomers.

Once most of the hydroxyl groups have been consumed the condensation reactions can continue as alcoholyses. In this reaction an alcohol molecule is produced instead of water. The use of either an acid or base catalyst can have a large effect on the overall shape of the molecule. The use of a base catalyst gives more condensed, highly branched chains that have a more fractal-like geometry. The use of an acid catalyst will produce gels with longer more randomly branched chains²⁹. Additionally, in the same way the hydrolysis is affected, the condensation reactions are affected by heat, time, pH, concentration of the catalyst, and the ratio of silicon to water. For this research the sol-gel processes were catalysed by the addition of ammonium hydroxide base. This caused cluster aggregation from monomers as seen in base catalysed reactions. The formation of large particles was driven by Ostwald ripening³⁰. This method of aggregation will continue until the difference in the energies of the large and small particles is negligible giving uniform particle size distribution. Overall this leads to very dense structures with a high degree of branching. The cluster aggregation leads to denser gels with a more uniform pore size.

Once the wet gel has been set it can be dried out to form either a xerogel or an aerogel. Only under special circumstances not applicable to our research can an aerogel be formed and as such will not be discussed. The drying process is simply the evaporation of solvent from the gel. As the drying occurs and the solvent is evaporated there will be less liquid to hold the gel in shape causing the structure to shrink. This shrinking will decrease the volume of the gel which will force the liquid to the surface of the gel to be evaporated. This process will continue until the gel is too stiff to shrink any more. During this drying, strain on different parts of the gel can also lead to cracking and breaking of the gel. Ultimately a xerogel structure can be achieved with a high surface area and porosity. It is this feature that allows them to be used as high surface area electrodes. From here the xerogel materials can be sintered to produce ceramic materials. When coupled with high surface area carbons high surface area carbon ceramics are produced. These materials can have a host of interesting properties as well as challenges associated with their production³¹.

1.3.2: Ceramic Carbon Electrodes

Above, the process of creating a variety of basic sol-gel structures was discussed. Of particular interest to us is the use of sol-gels to produce carbon electrodes. Specifically, these ceramic carbon electrodes (CCE) offer good physical and chemical properties for the electrolysis

of $\text{CuCl}^{24,32}$. The production of CCEs is not a new process and a large amount of research exists covering the wide range of areas they can be used³³.

To produce CCEs a procedure similar to that of a generic sol-gel procedure is employed. A solution of high surface area carbon such as Vulcan XC-72 or Black Pearls is mixed with a solvent including water and a catalytic amount of either base or acid. To this mixture a varying amount of the selected silane precursor is added. This solution is then allowed to react and evaporate over a period of hours to days. Techniques such as painting or spray coating can be used to produce a thin coating of the carbon sol-gel mixture on an appropriate backing structure such as carbon fiber paper. With the coating in place the carbon sol-gel mixture can be dried and heated to produce the aforementioned ceramic carbon surface²⁴.

These materials work well together as they allow for the combination of the best features of both the carbon and sol-gel materials. From the carbon a large electrically conducting surface is provided³⁴. A sol-gel material will be naturally resistive making it unsuitable for an electrochemical application³³. From the sol-gel a strong backbone is produced that holds the carbon material in place. This is a feature that could be provided by any number of polymer materials such as Teflon, and in many cases it is^{35,36}. Another feature of the sol-gel material, after conversion to a ceramic, is its high thermal stability³⁷. CCE's can also have their conductive and structural properties modified by simply altering the amounts of silane added. The final advantage of the sol-gel materials is its easy customizability.

Silicon is a tetravalent molecule. TEOS and TMOS, the two most basic silane precursors both have four silyl ether connections made to them. This means that the silane precursors will be able to make four separate Si-O-Si bonds creating a very cross-linked polymer. By replacing only one of the silyl ether linkages with a various functional group the silane monomer can take on an expansive array of properties while still maintaining a good crosslinking characteristic. The stable nature of the Si-C bond also ensures that the functionality that is attached will be stable under thermally and chemically harsh conditions³⁸.

As previously mentioned, the ways in which a silane precursor can be modified are vast. These modifications have led to their use as gas electrodes, hydrophobic surfaces, and even bio sensors^{31,38}. Three materials that we have used are (3-Aminopropyl)triethoxysilane, N-[3-(Trimethoxysilyl)propyl]ethylenediamine, and N^1 -(3-Trimethoxysilylpropyl)diethylenetriamine

which are hereafter referred to as 1N, 2N, and 3N silanes. These three silanes are functionalized with amine groups. All three materials have one primary amine with the second and third silanes having one and two additional secondary amines respectively. The three silanes will be referred to as 1N, 2N, and 3N for the 1, 2, and 3 nitrogen atoms in their amine functionalities (Figure 1-10).

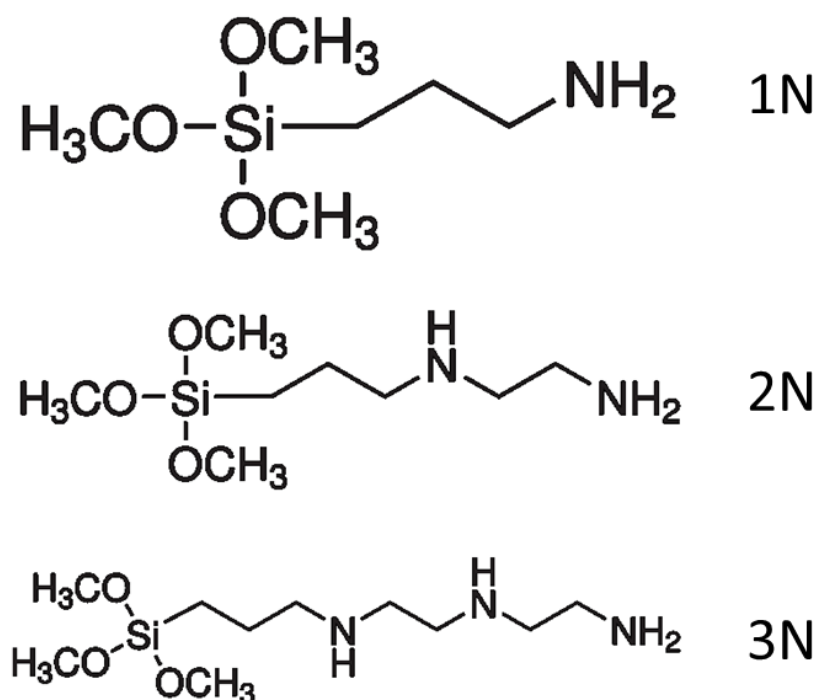


Figure 1-10: Silane monomers from top to bottom: (3-Aminopropyl)triethoxysilane, N-[3-(Trimethoxysilyl)propyl]ethylenediamine, and N¹-(3-Trimethoxysilylpropyl)diethylenetriamine. 1N, 2N, 3N respectively.

The (3-Aminopropyl)triethoxysilane has been previously^{18,24,32} shown to have a positive impact on the activity of a CCE material used in CuCl oxidation.

When producing a normal sol-gel material cracking during drying can be a problem disrupting the otherwise homogeneous surface area. This cracking can be prevented by incorporating a means to slow drying or, alternatively, by lowering the barrier for evaporation with a co solvent. Even with a slow reaction time and a co solvent cracking can occur. In the case of CCEs the relatively low volume of sol-gel limits the large scale cracking that can occur. However, at a smaller scale cracking can still be observed. On a larger scale the low volume of

binder can also lead to unstable CCE materials. The stability of the materials can be improved and controlled by the proper selection of silane precursors as well as the silane to carbon ratio.

1.4: Electrochemical Characterization Techniques

To evaluate the electrolysis properties of the CCE materials and indeed any electrode, there are a suite of standard measurements that can be made. These measurements can be used to determine onset potential, current response, electrode stability, surface area, and other properties of the electrode as well as the electrolysis system as a whole. The measurements can be split into two main groups based on their current type, either direct or alternating current.

Generally speaking electrochemical tests can be performed in either a two or three electrode environment. In the case of the two electrode environment a working and counter electrode are used. Both potential and current are measured between the two electrodes which are directly related to the redox processes happening at the anode and cathode. Two electrode measurement is a direct measurement technique. It has the problem of changing chemical conditions at the two electrodes during testing. If the effective redox potential changes during the experiment then the potential applied at the two electrodes will change. This is given by the following equation.

$$E_{Cell} = (E_{Cathode} - E_{Anode}) + [(\eta_{Cathode} - \eta_{Anode}) - IR] \quad \text{Equation 1-9}$$

If the chemical environment in the cell remains constant then the redox potentials will not change. This is the principle behind full-cell electrolysis measurements. The high flow rate of the electrolyte solutions ensures that there should be no change in redox potentials. In addition, if one electrode can be the reversible hydrogen electrode (RHE) with its associated potential of 0 meV then then it can act as a reference electrode¹⁹. The reference electrode will maintain a fixed potential within the cell allowing for accurate measure of E_{Cell} cell potential is directly related to the potential at the other electrode.

Three electrode systems avoid the problem of shifting redox potentials by adding a third electrode to the system. The three electrode system includes a working electrode where the electrode of interest is located, a counter electrode which will balance the current from the working electrode, and a reference electrode to measure the potential of the working electrode. The reference electrode will have a stable and known redox potential associated with it. This allows the working electrodes potential to be measured in reference to it without causing redox

potential drift. Both the AC and DC techniques can be used in the two and three electrode systems and both electrochemical cells were used for our investigations.

1.4.1: DC Voltammetry Techniques

Direct current measurements are the more straightforward of the two measurement types. The single direction of flow within the system in question ensures that effects from electrode charging, and cell capacitance can be mitigated to allow easier evaluation of solution based processes. Typical DC measurement techniques are cyclic voltammetry or potentiostatic. Both of these measurements examine the current response to an electric potential being applied across the cell.

In cyclic voltammetry a potential is applied from the working to the counter electrode. The cell potential is scanned to larger magnitudes and then reversed back to the original potential value. The potential scan occurs at a constant rate between high and low potential vertices. Once a redox potential is met the current will move to more anodic values as the species is oxidized. Once the concentration near the electrode is depleted the overall anodic current will decrease. This process will give peaks at different potentials for different redox species. As the potential scan is reversed if the redox reaction that occurred was reversible then another peak corresponding to the reduction of the species will be present. From this, CV measurements can be used to determine both the onset potential, and reversibility of a system. If a system is simply scanned in one direction then the measurement can be called linear sweep voltammetry (LSV). This process follows identical behavior to a CV allowing for observation of onset potentials as well as overall current response.

The drop in current as potential is scanned represents a longer time for the analyte to diffuse to the surface of the electrode than the rate of consumption. This is a result of a local drop in analyte concentration near the electrode surface. This depletion creates a diffusion zone which the analytes must cross from the bulk solution to be oxidized or reduced. In the case of normal electrodes the diffusion layer is very small in comparison to the width of the electrode allowing us to treat it as a region with a uniform width. To reduce and remove this change in current, ultra-microelectrode measurements have been developed³⁹. These electrodes are typically 25 μm in diameter. At this electrode width the diffusion layer can no longer be considered linear. Instead a process called hemispherical diffusion can occur. The hemispherical diffusion allows for much faster transport of the analyte to the solution of the

electrode surface, reducing or eliminating a drop off in current as the potential is scanned higher. This allows for additional information about the electrochemical system to be determined by both CV and LSV measurements.

Another useful voltammetry technique is that of potentiostatic and galvanostatic holds. In these measurements either potential or current are held constant over time. These procedures allow for the measurement of either current or potential as the other is held constant over time. For potentiostatic measurements the potential should be applied above a given redox potential to allow for a solution to be reduced or oxidized. In cells where the electrolyte solution is replenished frequently these measurements allow for a long term observation of the cell's behavior.

1.4.2: AC Electrochemical Impedance Spectroscopy

In a standard DC circuit the relationship between potential and current can be modeled by Ohm's law, Equation 1-10. Simply, as potential is increased under a constant electrical resistance the current will also increase.

$$V = IR \quad \text{Equation 1-10}$$

In an alternating current (AC) circuit the direction of current flow is alternated based on a given frequency. As the direction of the current flow changes different elements in the circuit will impede the flow of electrons. This gives us the new term of impedance (Z). By modifying Equation 1-10 we can replace the resistance with impedance to give us Equation 1-11. In this new equation the relationship between current and potential can be seen at constant impedance in the same way that current and potential are related in Equation 1-10.

$$V = IZ \quad \text{Equation 1-11}$$

Apart from DC circuits where the resistance remains constant, the impedance of a system will change dependent on the frequency of the AC signal. Under an AC frequency electronic features such as capacitors and charge transfer processes take on characteristics different than resistors. These features will cause a phase shift (lag) between the potential and the current signal⁴⁰. This variation is dependent upon frequency which, when varied at a known rate, allows for investigations into the electronic properties of materials.

Electrochemical Impedance Spectroscopy (EIS) records the real and imaginary impedance at a fixed DC potential with a super-imposed AC signal. The AC signal has its

frequency modulated from high to low during the measurement. The signals are plotted in a complex plane impedance plot or “Nyquist” plot. Typically an equivalent circuit is used to model the system that is being measured. With this model, the shape of the graph when compared to the idea model can then be used to extract valuable information about the electronic properties of the system. For a PEM electrolysis cell the electrodes are modeled by the “Finite Transmission Line” model⁴¹ (Figure 1-11). In this model two resistive rails are connected to one another across a series of capacitors. The two resistive rails represent the resistance for transmission of electrons through the carbon electrode and the transmission of ions through porous electrode. The capacitors are used to describe the differential capacitance between the electrode and the electrolyte. Finally a resistor representing the electrolyte resistance (e.g. the PEM) is connected in series to the end of the model circuit.

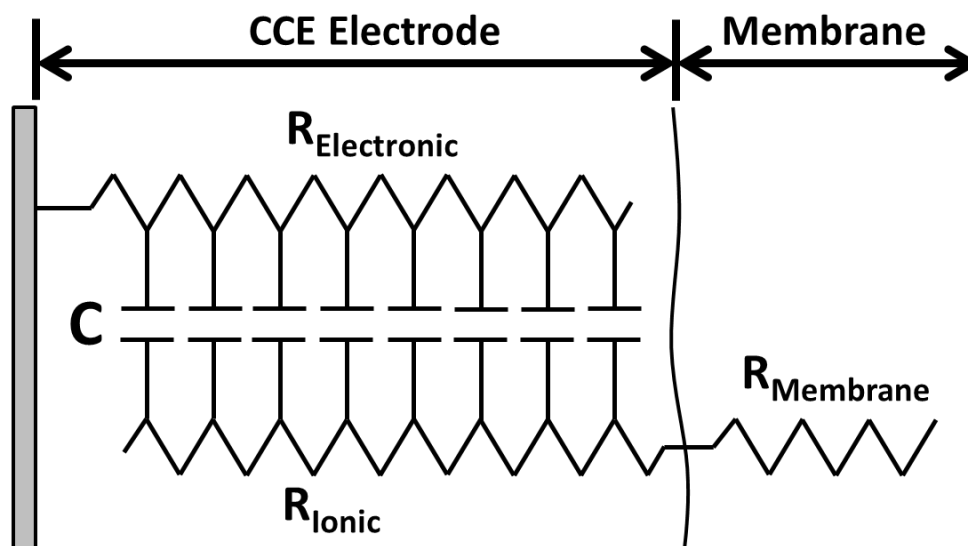


Figure 1-11: The Finite Transmission Line Model Circuit for modeling a PEM electrode. Diagram based on work of Li, G. and Pickup, P.⁴¹

When plotted on a Nyquist plot the impedance spectra for a PEM electrode takes on a distinctive shape. With frequency increasing from right to left in the high frequency region a linear section of the plot follows a 45° slope. This is known as the Warburg region (Figure 1-12). When using the finite transmission line model as an equivalent circuit the length of the Warburg region along the real axis is proportional to 1/3 of the total resistance within the electrode (R_{Σ}). This means that in a general sense, the longer the Warburg region is, the higher the resistance is within the electrode layer⁴². The use of AC electrochemical impedance spectroscopy in

combination with previously mentioned DC electrochemical techniques allow for a full characterization of the electronic properties of CCE electrodes as well as a host of other materials.

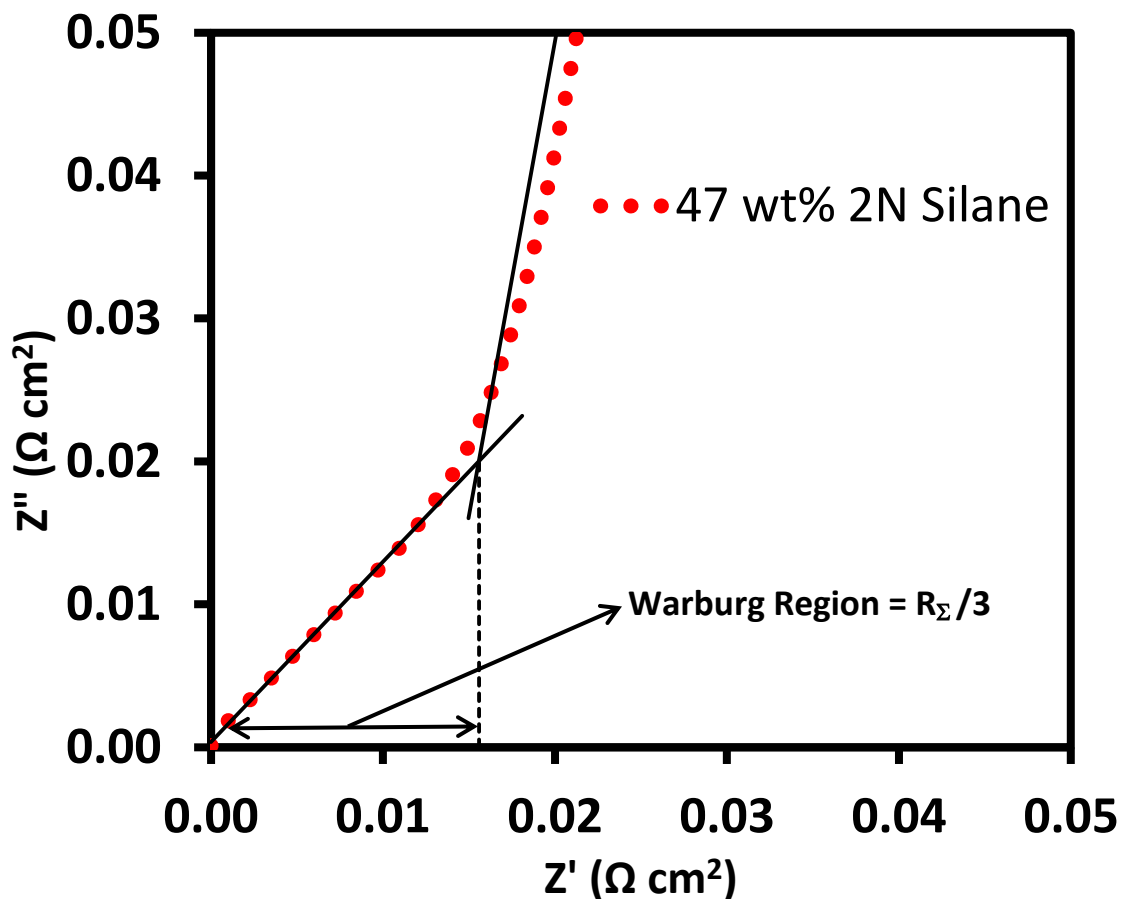


Figure 1-12 : Nyquist plot at 0 V vs. OCV of ceramic carbon electrode with Warburg region detailed and $R_{\text{Membrane}} = 0$.

In addition to traditional Nyquist plots, EIS data can be manipulated into capacitance plots. In these plots the real impedance is plotted with the inverse of the imaginary impedance multiplied by the AC frequency of the measurement ($1/Z''\omega$). Capacitance plots can be used to show the relative total capacitance of the sample. The capacitance can also be normalized with respect to geometric surface area as well as mass of sample. In addition to the total capacitance, the initial charging portion of the capacitance plots can be used to show conductivity within the sample. For these investigations a steeper slope in the charging current region indicates greater conductivity. To better visualize the charging region of capacitance

plots with disparate limiting capacitances' the data can be normalized to a maximum of 1. This normalization better shows which sample has the steepest initial slope and thus the highest conductivity.

1.5: Thesis Objectives

The primary goal of this thesis is to produce and characterize new materials to improve the electrolysis of CuCl in HCl. These will be compared to existing data on CuCl electrolysis, specifically work by Balashov et al who have produced initial testing of Pt containing catalysts at a variety of full-cell conditions²⁰. Additionally, we will construct a full-cell liquid electrolysis test station for the characterization of the produced materials. Specifically we aim to improve the anode electrode for CuCl-HCl electrolysis. This portion of the MEA allows the most room for improvement of the overall conversion rates and efficiencies. The cathode electrode works in a manner identical to those seen in H₂O or SO₂ electrolysis in PEM electrolysis and the hybrid sulfur cycle respectively. These topics among others have provided extensive research into the hydrogen evolution reaction (HER) making it difficult to provide substantial improvements. The CuCl oxidation step is comparatively novel leaving large room for improvements.

We will be producing CCE materials for use in the anode of the electrolysis cell. These materials will be produced in a standard sol-gel method. The silanes used will contain amine functionalities. These amine functional groups when protonated in the acidic electrolyte will provide enhanced ionic conductivity. In addition to the characterization of the electrodes abilities to oxidize CuCl we will also investigate the ability of the electrodes to resist cationic copper crossover within the materials. These investigations will only be preliminary and the crossover resistance can be considered secondary to achieving better overall activity from the electrode materials. The primary source of Cu crossover resistance within the electrolysis cell will likely come from the PEM material. The production and characterization of PEM materials was outside of the scope of this project and as such will not be discussed in this thesis.

Chapter 3 of this thesis outlines the initial testing of the CCE materials in a three electrode half-cell environment. Both traditional voltametric techniques and EIS measurements were used to investigate the properties of these materials. The bulk physical properties were also characterized by thermogravimetric analysis. Chapter 4 details the development of a full-cell test station as well as a standard testing protocol. Materials based on those characterized in

the half-cell are tested in the full-cell. In addition to these tests the materials were also investigated using SEM and TEM microscopy. Finally, in chapter 5, the copper crossover resistances of the materials produced are discussed. As well as diagnostic methods related to copper crossover detection and cell regeneration are discussed in chapter 5. The sum of this investigation is to present our materials as potential candidates for integration into further CuCl electrolysis tests for the three step hybrid CuCl-HCl thermochemical cycle.

Chapter 2 : Experimental Methods and Instrumentation

2.1: Electrode Preparation

Electrodes were prepared through a standard sol-gel method to produce a high surface area CCE material. Three different silane precursors were used during the production of the CCE materials; (3-Aminopropyl)triethoxysilane, N-[3-(Trimethoxysilyl)propyl]ethylenediamine, and N¹-(3-Trimethoxysilylpropyl)diethylenetriamine (All 99% pure Sigma Aldrich). Hereafter the silanes will be referred to as 1N, 2N, and 3N respectively.

2.1.1: Sol Gel Production

The sol-gels were prepared using a base catalyzed method. In a beaker, 400 mg Vulcan XC-72 carbon black (Cabot Corp.) was combined with 2.5 mL of DI H₂O and 13.5 mL of MeOH. To this solution 5.2 μ L of 6 M NH₄OH was added. The solution was allowed to stir uncovered for 15 minutes. Amounts of silane monomer (detailed in 2.1) ranging from 0.2-1.2 mL were added drop wise to the carbon solution. The solutions were stirred, covered, at room temperature for 16 hours. After stirring, the vessels were covered and vented slightly to allow for a slow evaporation of the solvent liquids. The reactions were left at room temperature to stir until a desired consistency was reached.

2.1.2: Half-Cell Electrode Production

The gel was allowed to dry to partial completion until a thick mud consistency was reached. Bare carbon fiber paper (TGP-H-090 Toray Paper, Fuel Cell Earth LLC) (CFP) was cut into strips 1 cm wide and approximately 5 cm long. The gels produced were painted in thin layers onto both sides of a 1 cm² section of the CFP, the coated samples were kept at a mass loading of 3 mg/cm². After coating, the samples were hung and allowed to dry at room temperature for 16 hrs followed by a further 12 hrs at 80 °C. For each sample produced a portion of the gel was reserved for characterization. The characterization samples were subjected to identical drying conditions. The dried electrodes were used as prepared in half-cell testing. The characterization samples were ground into a powder and reserved.

2.1.3: Full-Cell Electrode Production

For full-cell electrodes, the CCE gels were spray coated onto bare CFP. To facilitate this, the gels were allowed to dry to a thick liquid state. If required, the gel solutions were diluted with methanol to the desired milky consistency for spray coating was reached. Unless otherwise noted, the gels were spray coated onto a 90 cm² target of both bare CFP and non-wet proofed

carbon cloth mounted on aluminum foil. An air brush (Primus Arthur) was used with 15 psi N₂ carrier gas. The gels were sprayed in a serpentine pattern at a distance of approximately 20 cm (Figure 2-1). To achieve a homogeneous distribution the spray pattern was rotated 90° for each coating. As with the half-cell electrodes, the samples were allowed to dry at room temperature for 16 hrs and then a further 12 hrs at 80 °C. Gel that was sprayed outside of the electrode target was recovered for further analysis. For full-cell operation, square 5 cm² sections of the electrode were punched out and used without further preparation.

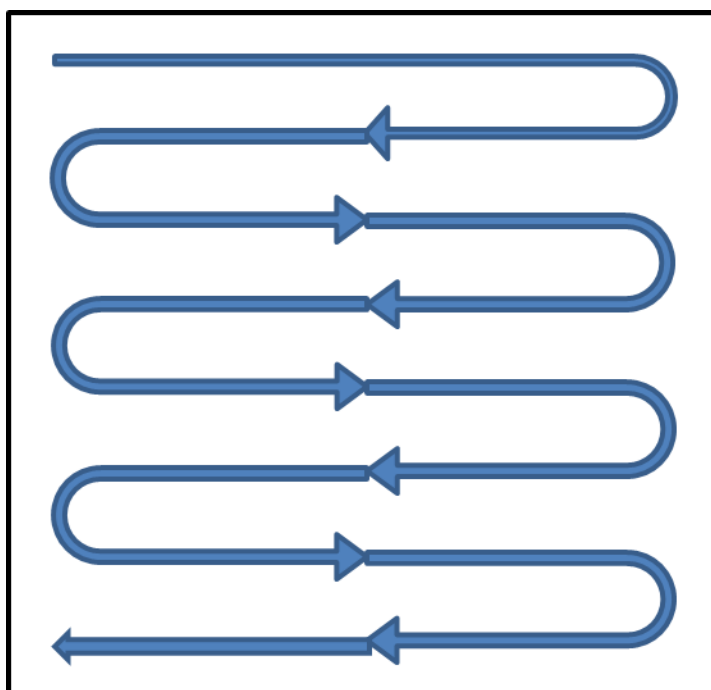


Figure 2-1: Serpentine flow path for the spray coating of CCE materials onto CFP backings

2.1.4: Cathode Pt/C Electrode Production

The preparation method for the Pt containing catalyst was modified from an existing procedure from our lab³³. Vulcan XC-72 Carbon containing 20% Pt (E-Tek) by weight was mixed with 5 wt% Nafion in alcohol and water (Sigma Aldrich) as well as additional water and isopropyl alcohol. The solution was mixed vigorously to prepare the electrode ink. The ink was spray coated onto non wet proofed CFP (TGP-H-090 Toray Paper, Fuel Cell Earth LLC) using the spraying technique detailed above (Section 2.1.3). The electrode was allowed to dry for 30 min at room temperature followed by 30 min at 130 °C.

2.2: Materials Characterization

2.2.1: TGA Weight Characterization

A TA Instruments Q600 SDT-TGA was used for thermogravimetric analysis of our CCE materials. Between 5 and 20 mg of powdered sample was heated in alumina pans in an extra dry air atmosphere flowing at 50 mL min^{-1} (Praxair). The temperature was ramped from 20 to $1000 \text{ }^\circ\text{C}$ at a constant rate of $20 \text{ }^\circ\text{C min}^{-1}$. Data analysis was performed using TA Universal Analysis Software.

2.2.2: SEM Imaging

SEM images were acquired using a JEOL JSM 6400 scanning electron microscope at a working distance of 8 mm and an accelerating voltage of 20 keV. Images were taken to assess porosity, thickness of CCE coatings, and to physically identify microscopic Cu plating.

2.2.3: TEM Imaging

MilliQ 18 M Ω water was sterile filtered through a $0.2 \text{ }\mu\text{M}$ pore size filter to remove contaminants. A small amount of the powdered nanomaterial on the end of a clean weighing spatula was added to $500 \text{ }\mu\text{L}$ of sterile water in a microcentrifuge tube. Each sample was hand mixed to gently stir the particles into the water until the suspension was a uniform grey colour. $10\text{-}20 \text{ }\mu\text{L}$ of sample was immediately transferred onto a Formvar Grid held level by locking forceps. The samples were allowed to settle onto the grid surface for 1-2 minutes. Excess water was then slowly drawn off from above the settled particles using small triangles of filter paper, and the grids were transferred onto clean filter paper and dried under a heat lamp for a minimum of 30 minutes before imaging.

2.3: Full-Cell Production and Design

The full-cell electrolysis system was constructed in house. The electrolysis cell was designed to allow a robust range of operation conditions including those developed by Lvov et al²⁰. In all designs a 5 cm^2 full graphite PEM electrolysis cell was used (FC-05-02 ElectroChem Hardware with Teflon fittings). The particular electrolysis cell was selected because of its full graphite flow channels which resist corrosion in liquid HCl and CuCl. In all iterations of the design 0.2 M CuCl in 2 M HCl liquid electrolyte was used as the anolyte solution and DI H_2O was used as the catholyte solution.

2.3.1: Original Design

The initial design consisted of a Masterflex analogue variable speed peristaltic pump (RK-77240-10), the aforementioned electrolysis cell, and two 2 L glass vessels to contain the anolyte and catholyte (Figure 2-2). The liquid electrolytes were kept under N_2 atmosphere. Liquids were fed using a combination of Masterflex Pt cured silicon tubing and 1/4" OD plastic tubing. The tubing lines were connected to the electrolysis cell using 1/4" barb fitting to male NPT adapters. The electrolyte flow was returned to the electrolyte tanks for a recirculated flow of both liquids.



Figure 2-2: Initial Electrolysis Cell Design with analogue pump, 5 cm^2 cell, and barbed fittings (Not Pictured: Recirculated Flow Lines).

2.3.2: Iterative Designs

A series of iterative changes were made to the original electrolysis system to arrive at the final pump design (Figure 2-3). The electrolyte solutions were stored in two custom fabricated 4 L Pyrex glass tanks with 1/4" OD Chemglass tubing adapters and the ability to purge with N_2 gas. Electrolyte flow was provided by a Materflex L/S digital drive peristaltic pump (RK-

07523-80). The digital control pump was selected for its precision flow rate control as well as a greatly expanded flow rate capability of 4.8-480 mL min⁻¹ vs. 0.8-28 mL min⁻¹ from the analogue pump.



Figure 2-3: Iterative Electrolysis Cell Design with digital peristaltic pump, 5 cm² cell, barbed fittings, and recirculated electrolyte flow.

The pump was used with two Masterflex L/S Easy-Load 3 roller pump heads. Platinum cured silicone L/S-16 tubing calibrated for use with the pump was used to provide flow rates between 4.8 and 480 mL min⁻¹. Outside of the pump head hard 1/4" OD PTFE tubing was used to transport the liquid electrolyte. 1/4" PTFE Swagelok connectors were used to connect the PTFE tubing to the electrolysis cell. For impedance and capacitive CV measurements a 2 M HCl tank and H₂ gas flow were incorporated into the electrolysis system. An H₂ gas line was incorporated into the cathode flow with capacity to switch between H₂ and catholyte flow. To the anode side the ability to interchange H₂O and 2 M HCl flow with the option of washing both cathode and anode with the 2 M HCl feed was included (Figure 2-4 and Figure 2-5). The additional option to flow HCl to the anode and H₂ gas to the cathode allowed for electrochemical surface characterization. The lack of a redox active species in the anolyte isolates non-faradaic charging of the electrode surface with the H₂ gas at the cathode providing a reversible hydrogen

electrode. This allows for capacitive CV measurements and electrical impedance spectroscopy to be performed.

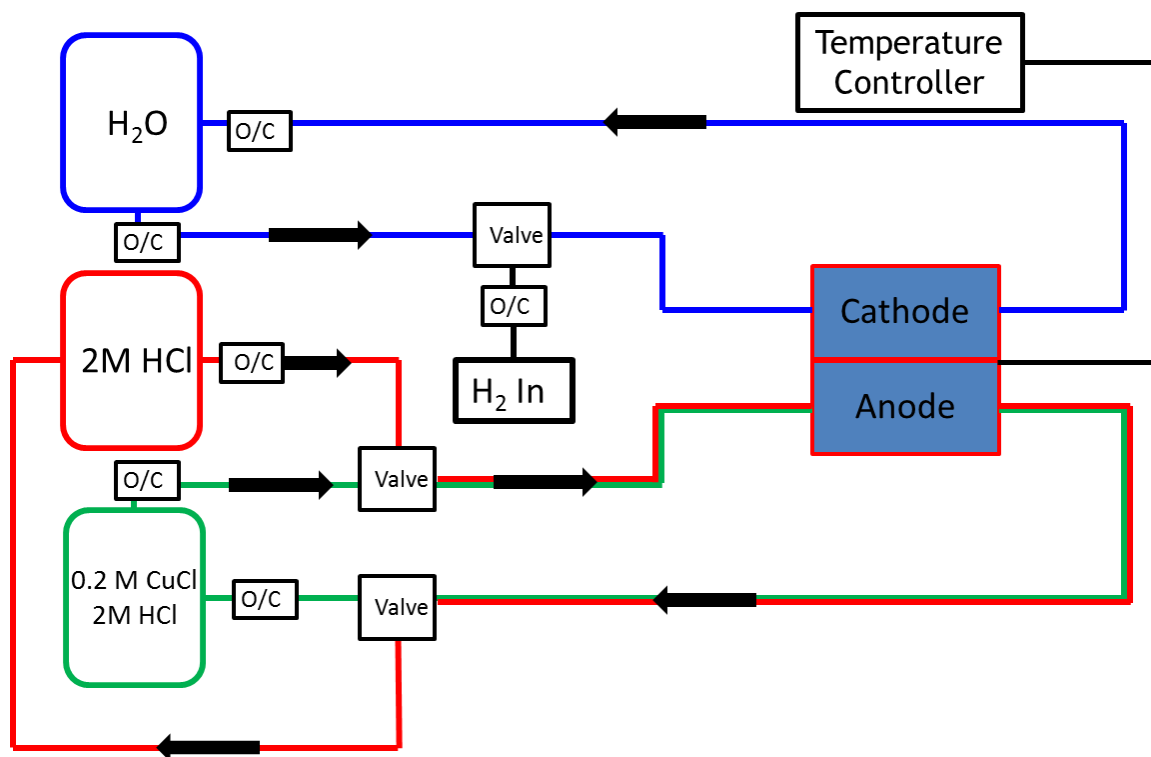


Figure 2-4: Full Electrolysis Cell Schematic Diagram. Coloured lined are included to identify individual flow paths.

The electrolysis cell was kept at a constant temperature of 25.0 ± 0.5 °C using a programmable PID controller (Omega), a K-type thermocouple (Omega), and the existing heating pads on the cell's current collector plates.

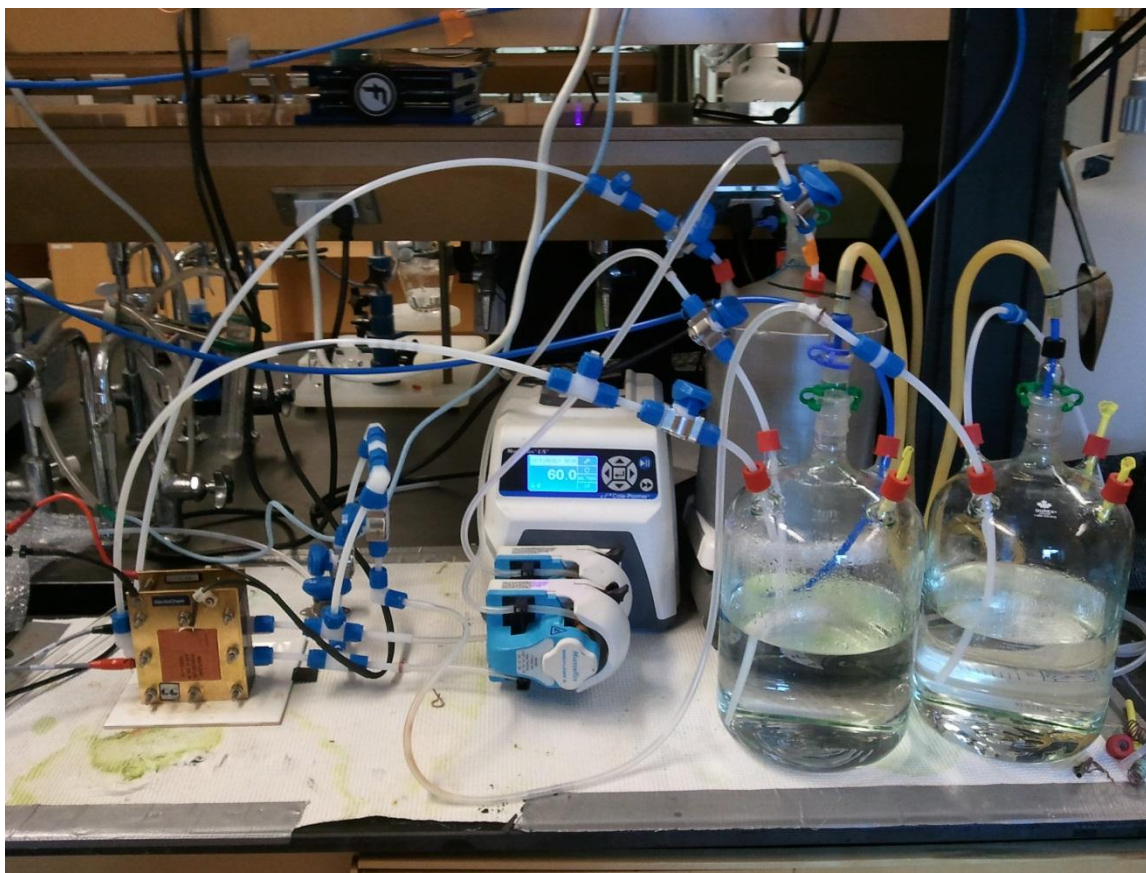


Figure 2-5: Current Electrolysis Cell Design with digital peristaltic pump, 5 cm² cell, barbed fittings, and recirculated electrolyte flow (temperature controller not pictured).

2.3.3: Catholyte/Anolyte Preparation

For the anolyte solution approximately 325 mL of concentrated HCl was diluted to 2 L with DI H₂O to produce 2 M HCl. The solution was sparged with N₂ gas for 30 minutes to remove any dissolved O₂ gas. To the 2 M HCl solution 39.6 g of 97% CuCl (Sigma Aldrich) was added. The solution was stirred under N₂ atmosphere until the CuCl had been completely dissolved. The solution was stored (with stirring) under N₂ atmosphere. When noted, to the solution of CuCl/HCl, 25 g of solid copper wire was added to convert excess Cu²⁺ to Cu⁺. The Catholyte solution was simply 2 L of type 1 deionized water (18 MΩ cm resistance).

2.3.4: Membrane Electrode Assembly Fabrication and Full-Cell Construction

Membrane electrode assemblies (MEA) were fabricated from in house materials. A 5 cm² section of cathode catalyst (detailed in 2.1.4) was combined with a 3.5 cm x 5 cm section of cleaned Nafion 115 in a hot press. The samples were compressed under a load of 200 kg m⁻²

at a temperature of 125 °C for 75 s. The combined cathode and membrane were placed immediately onto a prepared 5 cm² section of anode material in the full-cell.

The full-cell was assembled by placing a 5 cm² section of anode material over the anode flow channels. The anode electrode was surrounded by a piece of 10 mil (1 mil = 0.001") silicone gasket material that completely covered the electrolysis cell's graphite plates. As described above the membrane and cathode materials were placed over the anode electrode. The cathode electrode was also surrounded by a piece of 10 mil silicone gasket material cut to match the existing gasket. The cathode graphite plate was placed on top of the completed MEA and the electrolysis cell bolts were tightened to 30 in lb (3.4 N m) of torque. This compression ensured proper contact between the electrodes and the Nafion 115 membrane.

2.4: Electrochemical Characterization

For both full and half-cell characterizations, solutions of CuCl in HCl were produced. The working electrode/anode in all cases was a high surface CCE material coated onto non-wet proofed CFP (TGP-H-090). In all tests an atmosphere of N₂ gas was used to prevent spontaneous oxidation of Cu⁺ to Cu²⁺. Half and full-cell electrochemical measurements were acquired using a combination of a Solartron 1470 E multichannel potentiostat and Solartron SI 1260 Impedance Analyzer controlled using Multi-Stat software.

2.4.1: Half-Cell Electrochemical Techniques

The half-cell electrochemical tests took place in a standard three electrode cell. A saturated calomel (SCE) reference electrode was used along with a Pt wire counter electrode. The working electrodes in all cases were 2 cm² sections of CCE materials coated onto bare carbon fiber paper as discussed in 2.1.2. Impedance and capacitive CV measurements were taken at ambient temperature in 100 mL of 1.5 M HCl under quiescent conditions and with 380 RPM stirring. Impedance spectra were collected over a range of 100000 Hz to 0.1 Hz at 0.0 V vs. open circuit potential (OCV). Capacitive CV measurements were taken at scan rates of 20, 50, and 100 mv s⁻¹ across a range of 0.15 to 0.85 V vs RHE. Potential stair step and potentiostatic measurements were taken in identical conditions with the addition of CuCl to produce an electrolyte solution of 1 mM CuCl in 1.5 M HCl. Potential stair step measurements were taken from 0.35 to 0.85 V vs RHE with 10 mV steps and varied dwell times at each potential. Potentiostatic measurements were taken at 0.50 V vs. RHE for 600 s.

2.4.2: Full-Cell Electrochemical Techniques

Unless otherwise noted, the electrochemical characterization was performed using DI H₂O as a catholyte, 0.2 M CuCl in 2 M HCl as the anolyte. The electrochemical cell was comprised of a novel 5 cm² anode, a Nafion 115 polymer electrolyte membrane, and a standard 3 mg cm⁻² Pt cathode catalyst. Capacitive CV and impedance measurements were taken at a constant flow rate of 60 mL min⁻¹ of 2 M HCl at the anode and 25 mL min⁻¹ of H₂ gas at the anode. Flow rates were varied between 40 and 200 mL min⁻¹ for all other measurements. Impedance spectra were recorded from 100000 Hz to 0.1 Hz and from 65000 Hz to 0.1 Hz both at 0 V vs OCV. Capacitive CV measurements were taken between 0.2 and 0.8 V vs. RHE at scan rates of 50 and 100 mV s⁻¹. Potential stair step measurements were taken from 0.2 to 1.2 V vs. RHE with stair steps of 10 mV and a dwell time of 0.5 s. Unless otherwise noted, potentiostatic holds were taken at 0.7 V vs RHE at 600 s. During cell regeneration steps the cell was held at 0 V vs. RHE or the catholyte was replaced with 2 M HCl. In both cases the anolyte and catholyte flow rates were held at 60 mL min⁻¹.

2.4.3: Ultra Micro Electrode Measurements

Ultra micro electrode measurements were taken in 2 M HCl with a Silver/Silver Chloride (Ag/AgCl) Reference electrode (0.197 V vs. RHE), a Pt Counter electrode, and a 25 μm Pt working electrode. Concentrations of CuCl were varied from 0.2 M to 0.002 M. Linear sweep voltammetry measurements were taken from -0.1 V to 0.6 V vs. Ag/AgCl at 20 mV s⁻¹. CV measurements were also taken from -0.1 V to 0.6 V vs. Ag/AgCl at 100 mV s⁻¹.

Chapter 3 : Materials for Half Cell Electrolysis

3.1: Materials Characterization Results

After production of the CCE materials the composition of the electrode structure as well as bulk chemical characteristics were examined. To maintain the same physical and chemical composition the excess ceramic carbon materials were processed in the same manner that we used to produce the CCE materials.

Initially thermogravimetric analysis (TGA) analysis was performed on excess ceramic carbon material left over from the production of the CCE materials. The mass of the samples were assessed before and after the combustion of the sample to determine bulk composition. A sample TGA graph is shown in Figure 3-1 where weight percent of the original sample is recorded as a function of temperature.

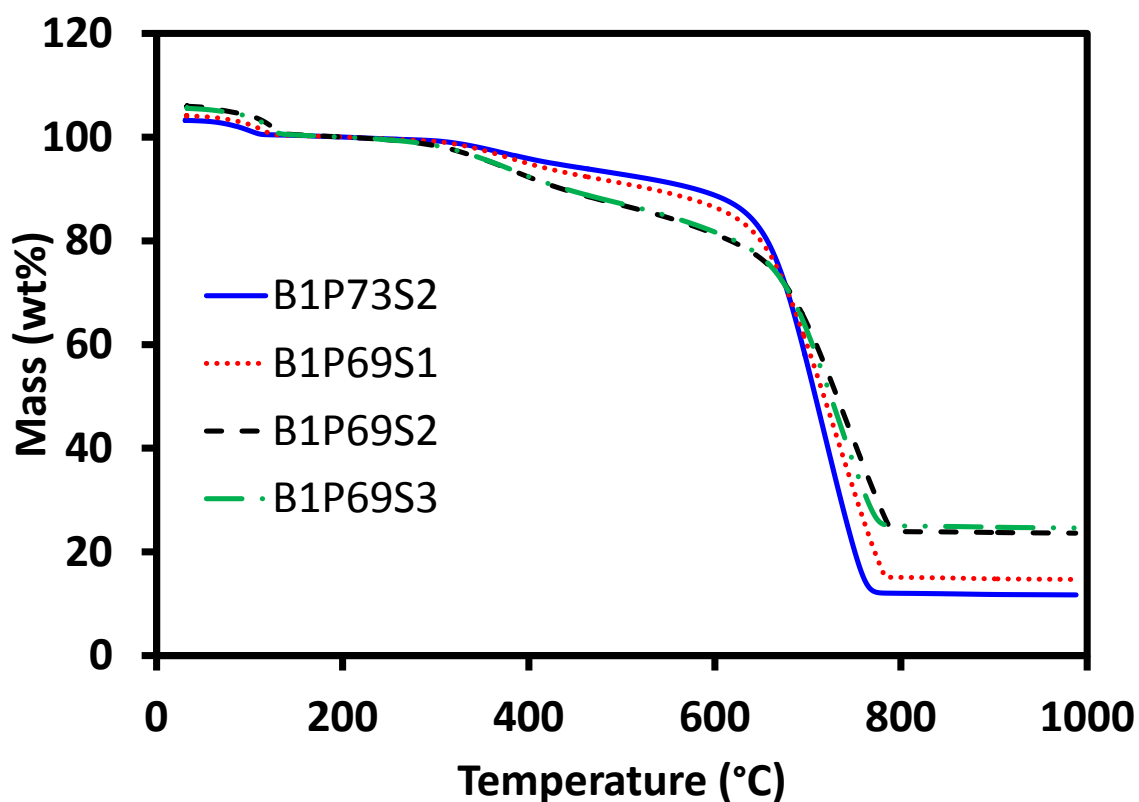


Figure 3-1: Example TGA spectra of 1N CCE Materials under flowing air with temperatures ramped from 20-1000 °C at 20 °C min⁻¹. Mass percent normalized at 200 °C.

During the production of the sol-gel network water is produced as a byproduct. The water produced can become trapped within the sol-gel networks and pores. To account for the

variation in moisture content within the CCE materials the TGA data was normalized to the weight percent at 200 °C, explaining the greater than 100% weight percents shown in Figure 3-1. The CCE's relatively simple chemical composition (silane and carbon only) allowed the mass percent of silane to be determined from the remaining SiO₂ after the sample was combusted in an air environment. Mass percent of SiO₂ gives moles of silicone per gram of CCE (assuming 1 g total). Weight percent of silane in the CCE was taken as the moles per gram of silane multiplied by the silanes polymerized molar mass. The chemical formula of polymerized silane monomer was taken as SiO_{1.5}R where R is the silane monomers side chain. The O_{1.5} is representative of the fact that each of the three bonded oxygen atoms is shared with a neighboring silane monomer within the branched Si-O-Si network.

As mentioned in chapter 2 the half-cell electrodes were prepared by coating them onto strips of bare CFP. This provided us with a CCE working electrode that could be inserted into a standard 3 electrode cell environment for testing. Both the EIS measurements and capacitive CV measurements were taken in the absence of CuCl to assess the electrodes total conductivity and capacitive surface area. It is assumed that if the electrode has a larger capacitive surface area then it should have a larger limiting current when normalized for geometric surface area for the conversion of CuCl to CuCl₂. This rational is supported because there is no catalyst component required for the oxidation of Cu⁺; therefore, it can take place at any free and accessible section of the electrode structure^{27,28}. Additionally, the capacitive CV measurements were used to assess the degassed state of the electrode and the cleanliness of the electrode surface. In an ideal case the capacitive CV measurement will be characterized by steep onset at the initial potential followed by a horizontal scan at a constant current to the upper potential, the reverse scan the shows the mirrored response. Any slope in the CV shape as the potential is scanned will indicate that the sample is resistive and requires a further break in period. Additionally, the appearance of peaks at approximately 0.4 V vs. RHE indicate the presence of surface quinones on the CCE electrode also indicating that further break in is required.

There were only two main measurements made of the actual ability for the CCE's to oxidize Cu, potential stair step measurements and potentiostatic holds. For the full-cell testing, potential stair step measurements were adapted from previous work to replace standard linear sweep voltammetry^{24,32}. At 0.4 V applied vs. RHE the Cu⁺ species will be oxidized to Cu²⁺. This

characterizes the onset of the current response. Onset potentials higher than 0.4 V vs. RHE can indicate a destruction of our anode or a chemical change in our cathode counter electrode in the case of full-cell electrolysis. Ultimately, an onset potential at 0.4 V is expected and larger current responses are favorable.

3.2: Electrochemical Characterization Results

Half-cell measurements were taken to initially characterize the varied silanes effects as well as to compare them to previous work from our lab^{24,32}. The varied silanes were tested in the half cell conditions previously used in our lab. Multiple iterations of the 1N silane were produced initially to validate our testing methods through comparison of the electrochemical test data to previous work^{24,32}. To compliment these samples we produced CCE materials with similar molar loadings of the 2N and 3N silanes. The discussed silane CCE materials produced with the 1N, 2N, and 3N materials are listed in Table 3-1.

Table 3-1: Compositions of CCE materials for half-cell testing produced with 1N, 2N, and 3N silane precursors.

| Sample Code | Silane Type | mMol Silane/g C | Wt% Silane |
|-------------|-------------|-----------------|------------|
| B1P12S1 | 1N | 4.28 | 47.0 |
| B1P12S2 | 1N | 5.56 | 61.2 |
| B1P12S3 | 1N | 6.29 | 69.2 |
| B1P13S1 | 2N | 3.83 | 58.6 |
| B1P13S2 | 2N | 4.92 | 75.4 |
| B1P13S3 | 2N | 5.19 | 79.4 |
| B1P15S1 | 3N | 3.62 | 70.9 |
| B1P15S2 | 3N | 4.26 | 83.4 |
| B1P15S3 | 3N | 4.61 | 90.3 |

All of the composition data was determined using TGA analysis as described above. The CCE structures were comprised of solely Vulcan XC-72 carbon and the silane binders. In all cases only one type of silane monomer precursor was used in each gel reaction. This was done to allow for individual characterization of the different silanes effects on the CCE electrochemical activity.

The CCE materials were prepared as described in section 2.1.2: Half-Cell Electrode Production. The double sided CCE allowed for a 2 cm² area of electrode to be tested. To test only the CCE coated area of the electrodes samples were held partially submerged in the

electrolyte solution for the duration of the testing, the double sided coating additionally prevented an uncoated back of the electrode from being coated.

Each set of CCE materials consisted of three gels, with the aim to produce a “low”, “medium”, and “high” wt% silane CCE. The samples were originally intended to have comparable silane loadings to those produced by our lab previously²⁴. The original target compositions were 22, 36, and 56 wt% silane respectively. As listed above (Table 3-1), all of the samples produced had relative silane compositions above the 22 and 36 wt% samples produced previously in our lab. Across the low, medium, and high loading samples produced with each silane precursor the silane content had a relative standard deviation of 8.6, 13.3, and 16.0% respectively. With these samples we were able to compare the effects of the type and amount each silane precursor on the electrochemical properties of the CCE’s.

3.2.1: Electrochemical Results for 1N Materials

The 1N samples were initially characterized in the absence of CuCl to assess electrochemical impedance characteristics and electrode surface area (Figure 3-2). The surface area was estimated by the magnitude of the capacitive current observed during the CV measurements. The relative sizes of the capacitive CVs were compared to estimate relative surface areas.

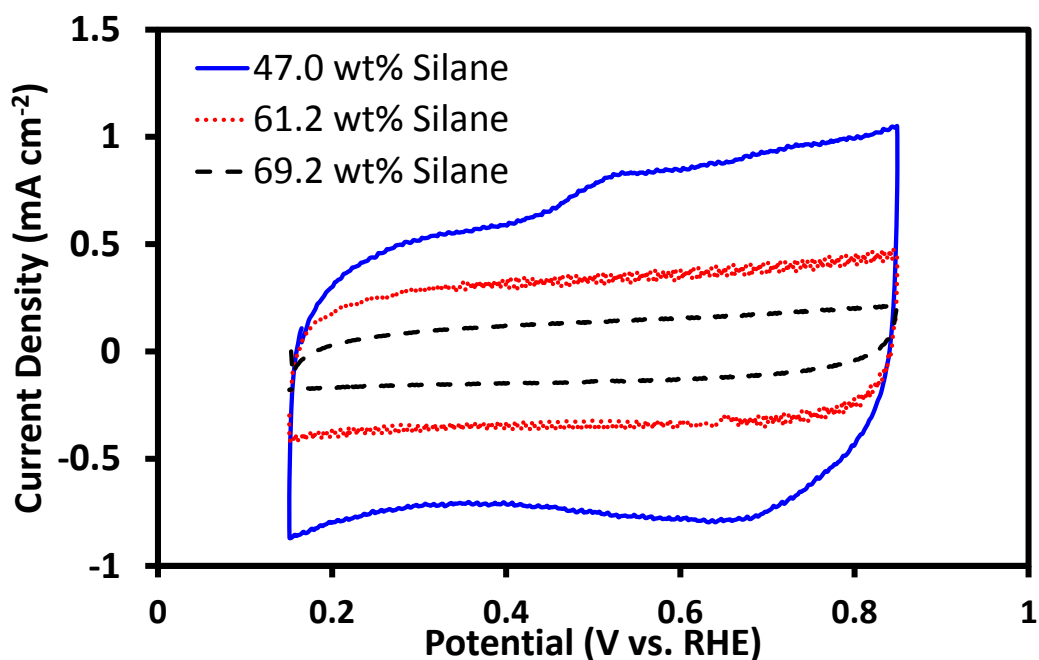


Figure 3-2: Capacitive CV of CCE materials with varied 1N silane loading and normalized for geometric surface area (SA). Experiment performed in 1.5 M HCl under N₂ atmosphere. Scan from 0.15 to 0.85 V vs. RHE at 50 mv s⁻¹.

The capacitive CV's of the CCE materials showed a standard large non-faradaic charging current for all three materials. As these measurements were taken in the absence of CuCl all three CVs showed the expected lack of peaks in both the forward and reverse scan though at 0.45 V vs. RHE there is a small shoulder on the 47 wt% sample. This was attributed to the presence of surface quinones in our sample. The charging current of these samples plateaued from approximately 0.15 to 0.8 mA cm⁻². These values are in good agreement with what we have previously seen produced in our group²⁴. This validates the production method used for these materials from a morphological standpoint.

We further characterized the CCE morphology through electronic impedance spectroscopy (EIS). In the high frequency region of the Nyquist plot we can examine the conductivity of the samples we produced. The Warburg regions of the nyquist plots were determined and used to calculate the total resistance for the 1N materials (R_z) (Table 3-2). The 47.0 wt% silane sample showed the smallest Warburg region and thus the highest conductivity. The capacitance measurements showed a similar behavior, the lower wt% silane samples showed the fastest onset of charging and also the highest plateau. The 69.2 wt% silane sample showed a very low capacitance when compared with the other two samples.

Table 3-2: Total Resistance of 1N CCE materials. As determined from Warburg region of impedance plots.

| Sample | R_z (Ω cm ²) |
|-----------------|------------------------------------|
| 47.0 wt% Silane | 0.3 |
| 61.2 wt% Silane | 2.1 |
| 69.2 wt% Silane | 12.3 |

Following the initial characterization the CCE materials were tested in the presence of CuCl. Initially the 1N materials were tested to compare again to previous samples made with the silane in question³². The potential stair step measurements showed that all three 1N samples had the same onset potential at 0.4 V vs. RHE (Figure 3-4).

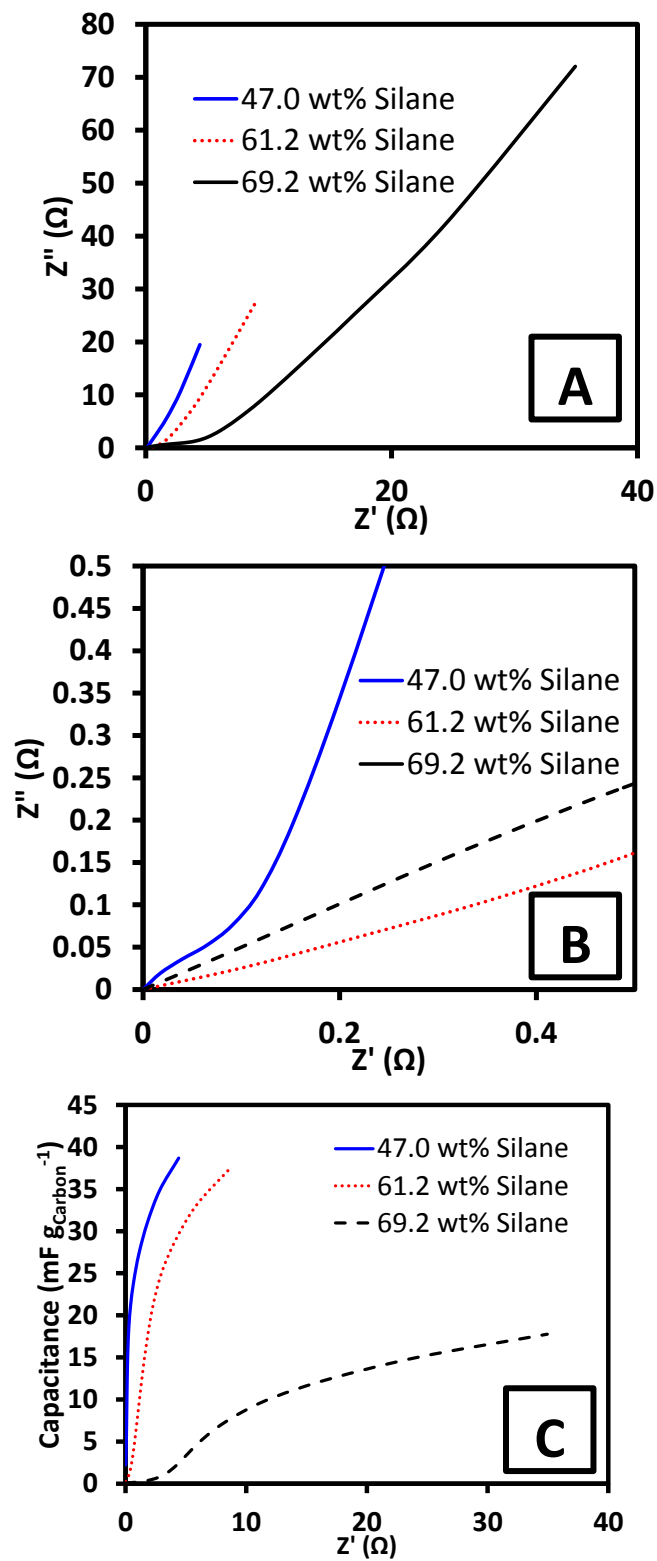


Figure 3-3: Impedance and capacitance plots of CCE materials with varied 1N silane content. Collected in 1.5 M HCl under N_2 atmosphere. (A) Nyquist plot (B) High frequency region (C) Capacitance plot normalized for the total mass of carbon present in the CCE sample.

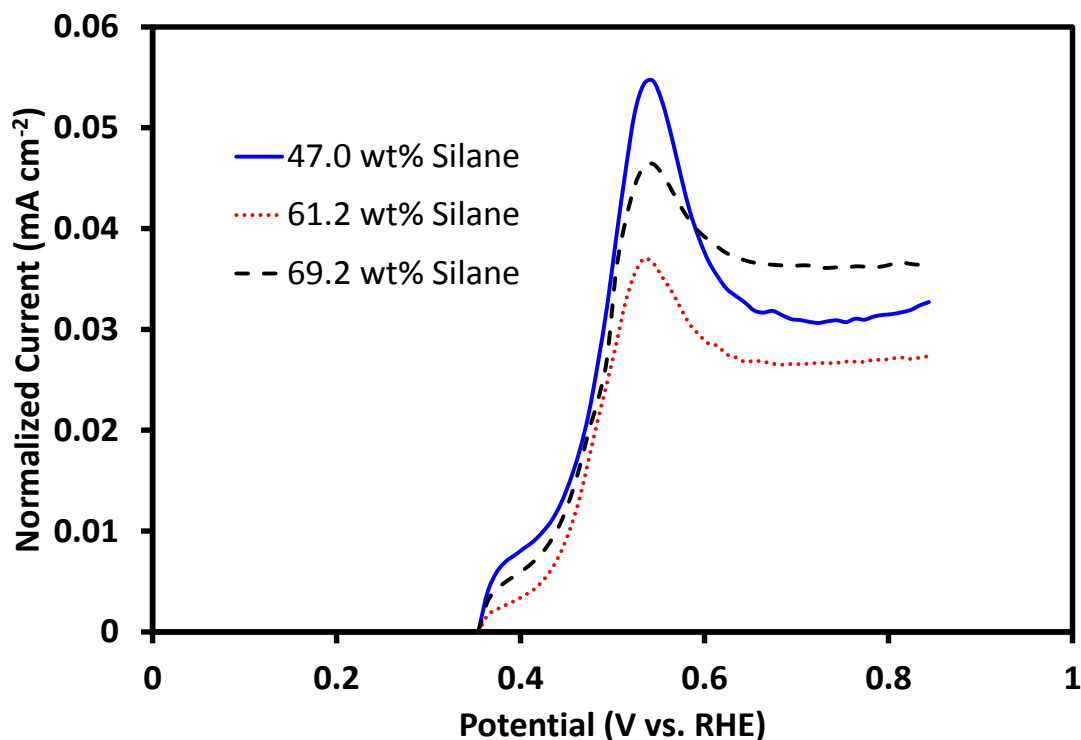


Figure 3-4: Potential stair step measurement of CCE materials with varied 1N silane compositions. Scanned from 0.35-0.85 V vs. RHE with 10 mV steps and 3 s dwell times. Electrochemical measurement were collected in 1 mM CuCl in 1.5 M HCl under N₂ atmosphere electrolyte.

Each of the materials had a similar current response and plateau time. The overall plateau current provides insight into the relative limiting operating currents of the three materials when their currents are controlled by diffusion. In this set we saw that the highest weight percent sample had the highest limiting current while the sample at 61.2 wt% had the lowest limiting current, performing the worst. It was shown that these samples performed comparably to those produced previously in our lab with limiting currents within 0.02 mA cm⁻² of previous values³². The linear shape of the diffusion limited current also indicated that there were no further faradaic processes occurring at the electrode surface.

To better simulate sustained full-cell operation, the 1N materials were held at a constant potential of 0.60 V vs. RHE for 10 min (600 s) (Figure 3-5). At this potential the oxidation of CuCl can occur allowing for the production of H₂ gas at Pt wire counter electrode. This hold was performed to assess each of the different materials abilities to produce H₂ gas over time. The linear shape of the three materials current responses indicate that the electrode materials did not degrade over the time scale of the experiments. This initial stability is

promising as the electrodes will be expected to perform reliably over long time frames when integrated into the full CuCl-HCl electrolysis cycle. The potentiostatic holds showed the same trend in activity that we observed in the potential stair step measurements. Taking the current of the potentiostatic hold at 150 seconds to be representative of each material's current response we can examine the effects of the CCE composition on the electrodes current response (Figure 3-6).

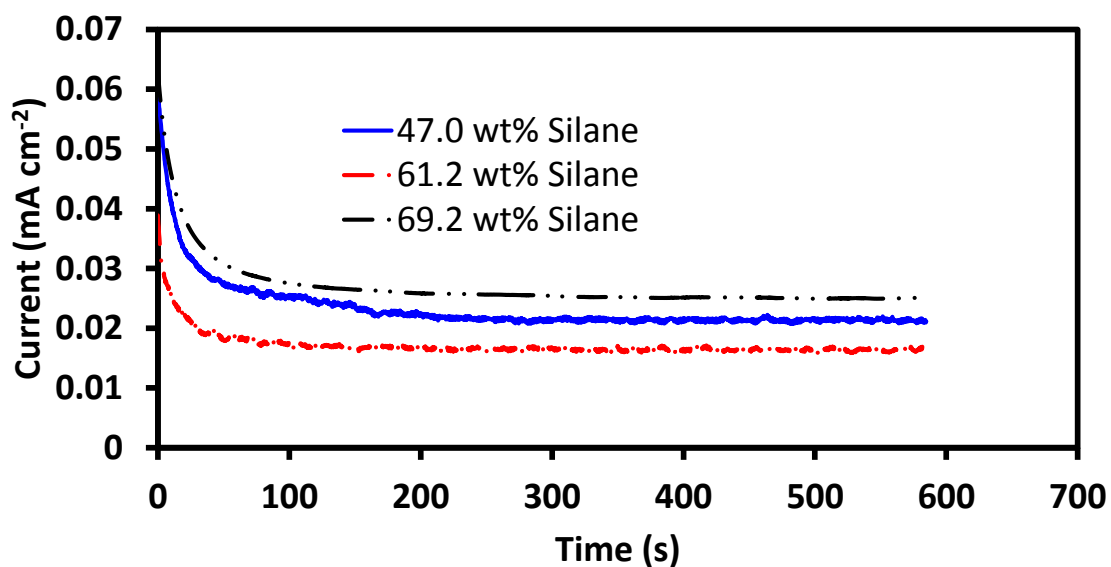


Figure 3-5: Potentiostatic measurements of CCE materials with varied 1N silane compositions. Potential held at 0.6 V vs. RHE. Collected in 1 mM CuCl in 1.5 M HCl under N₂ atmosphere electrolyte.

The current responses were normalized for the mass of carbon in the CCE to better compare electrode performance. As mentioned above there is very little dependence of the current on the composition of the silane outside of a slight positive correlation (Figure 3-6).

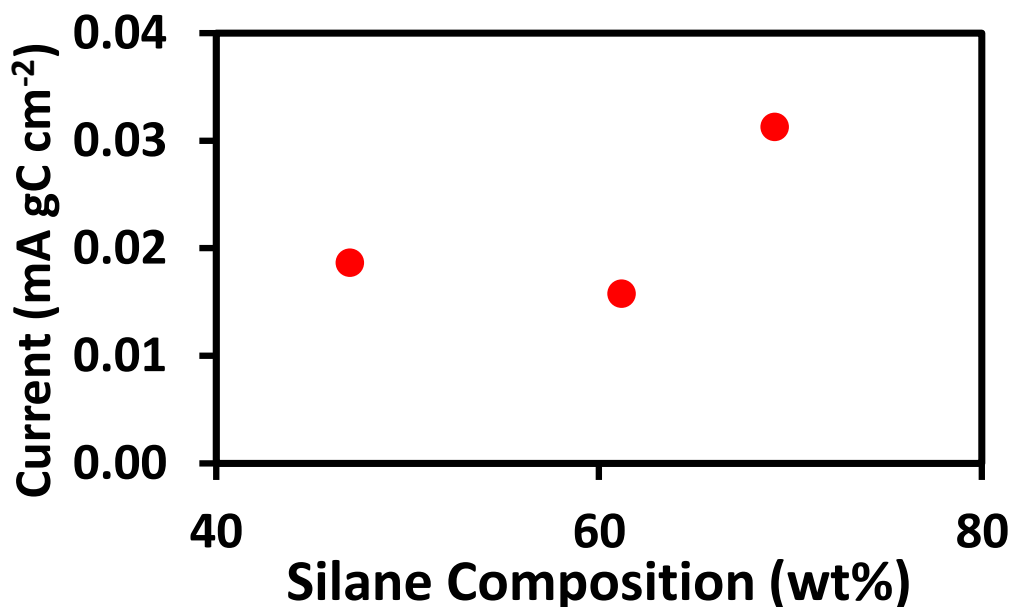


Figure 3-6: Relationship between 1N silane composition and current response from potentiostatic holds. Value taken from current at 150 s.

3.2.2: Electrochemical Results for 2N Materials

The 2N and 3N materials were tested in the same fashion as the 1N materials. We can see in Figure 3-7 that the 2N materials showed a similar trend in capacitive surface area and silane composition to the previously tested 1N materials (Figure 3-2). In our impedance measurements of the samples we once again see that the highest conductivity comes from the lowest wt% silane CCE at 58.6 wt% silane (Figure 3-8 and Table 3-3). In this case we also see a comparable conductivity from the 75.4 wt% silane. After the second sample there is a marked decrease in the conductivity for the 79.4 wt% sample. This indicates that there is a sharp increase in the electronic resistance between 75.4 and 79.4 wt% 2N silane as the only notable change is the increase in the electrically resistive silane. This high electronic resistance in the 79.4 wt% CCE can be seen in the comparatively shallow slope on the initial charging region of the capacitance plot as well. There is a much lower plateau for the 79.4 wt% silane sample than was observed for the other two samples. This is consistent with the capacitive CV measurements shown in Figure 3-7 which showed the same trend in the capacitive surface areas.

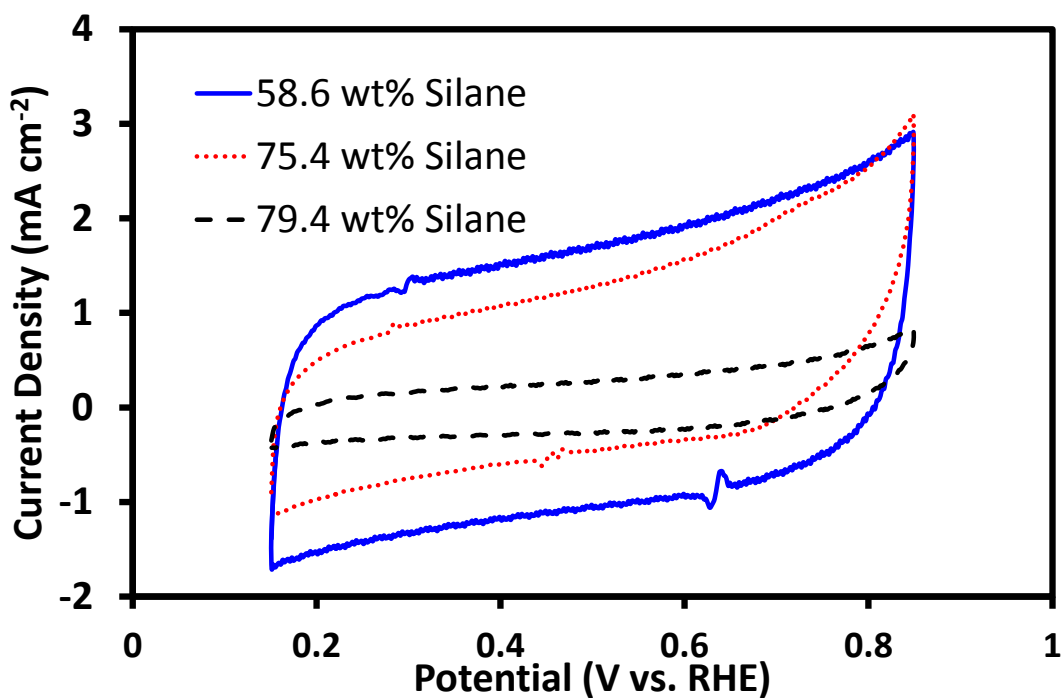


Figure 3-7: Capacitive CV of CCE materials with varied 2N silane loading and normalized for Geometric SA. Collected in 1.5 M HCl under N_2 atmosphere. Scan from 0.15 to 0.85 V vs. RHE at 50 mV s^{-1} .

Under potential stair step measurements there was a significant transient current recorded for the 75.4 wt% 2N sample (Figure 3-9 (B)). For this reason the sample was removed from further examination during comparison between different 2N samples and between different silanes. As with the 1N materials there is a similar shape to the current onset and eventual plateau. Transient currents were observed for the remaining two CCE's shown by the steady increase in current after the expected plateau of the potential stair step. Visual inspection of the Pt counter electrode determined the transient currents to be due to plating of Cu from Cu^+ or Cu^{2+} at the Pt counter electrode. It was assumed that the initial plateau current was still representative of the CCE's performances.

Under potentiostatic holds the 2N materials showed a stable current response (Figure 3-10) as compared with the transient currents shown in the diffusion limited region of the potential stair step measurements (Figure 3-9). In Figure 3-10 only the anodic currents are shown, for approximately the first 100 seconds the 58.6 wt% sample showed a large cathodic current. In both runs the samples were held at the same fixed potential for equal amounts of time.

Table 3-3: Total Resistance of 2N CCE materials. As determined from Warburg region of impedance plots.

| Sample | R_z ($\Omega \text{ cm}^2$) |
|-----------------|---------------------------------|
| 58.6 wt% Silane | 0.3 |
| 75.3 wt% Silane | 0.3 |
| 79.4 wt% Silane | 1.2 |

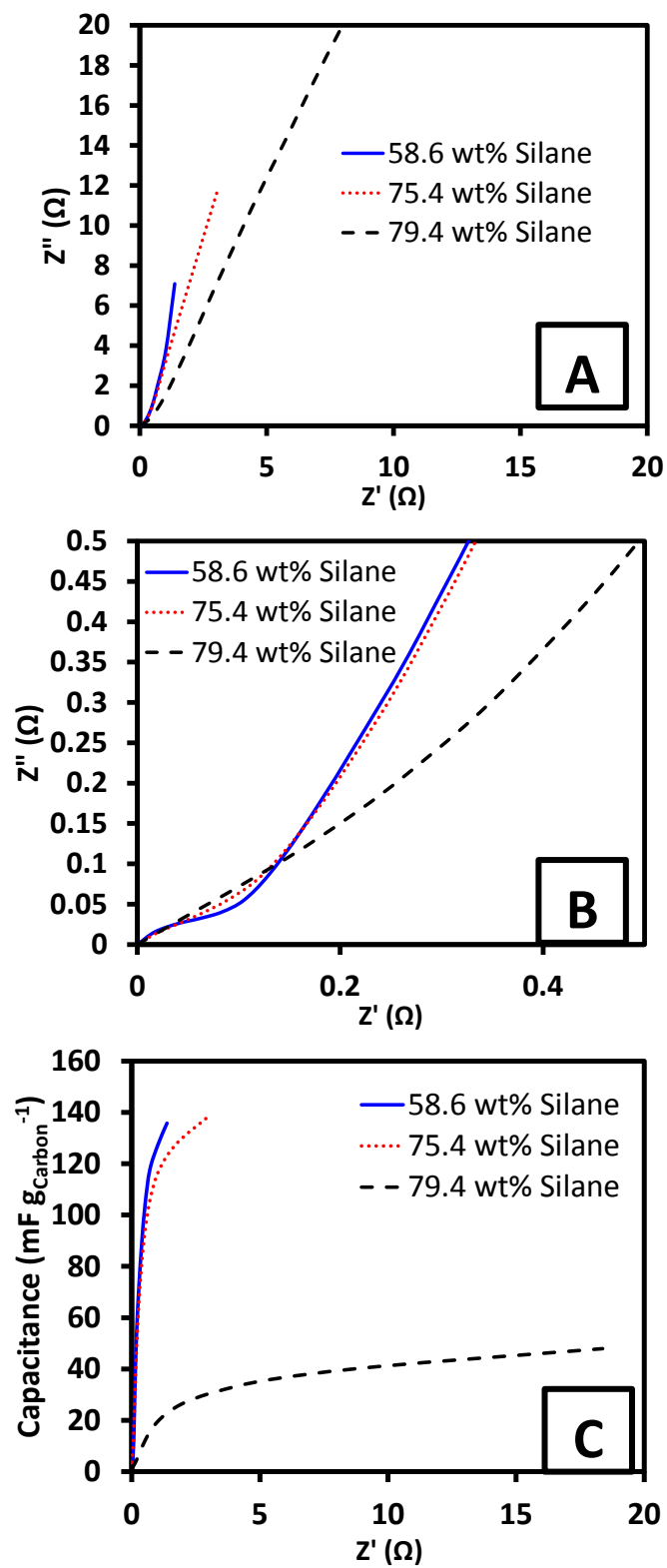


Figure 3-8: Impedance and Capacitance plots of CCE materials with varied 2N silane content. Tests were performed in 1.5 M HCl under N₂ atmosphere at 0 V vs. OCV. (A) Nyquist plot (B) High frequency region (C) Capacitance plot.

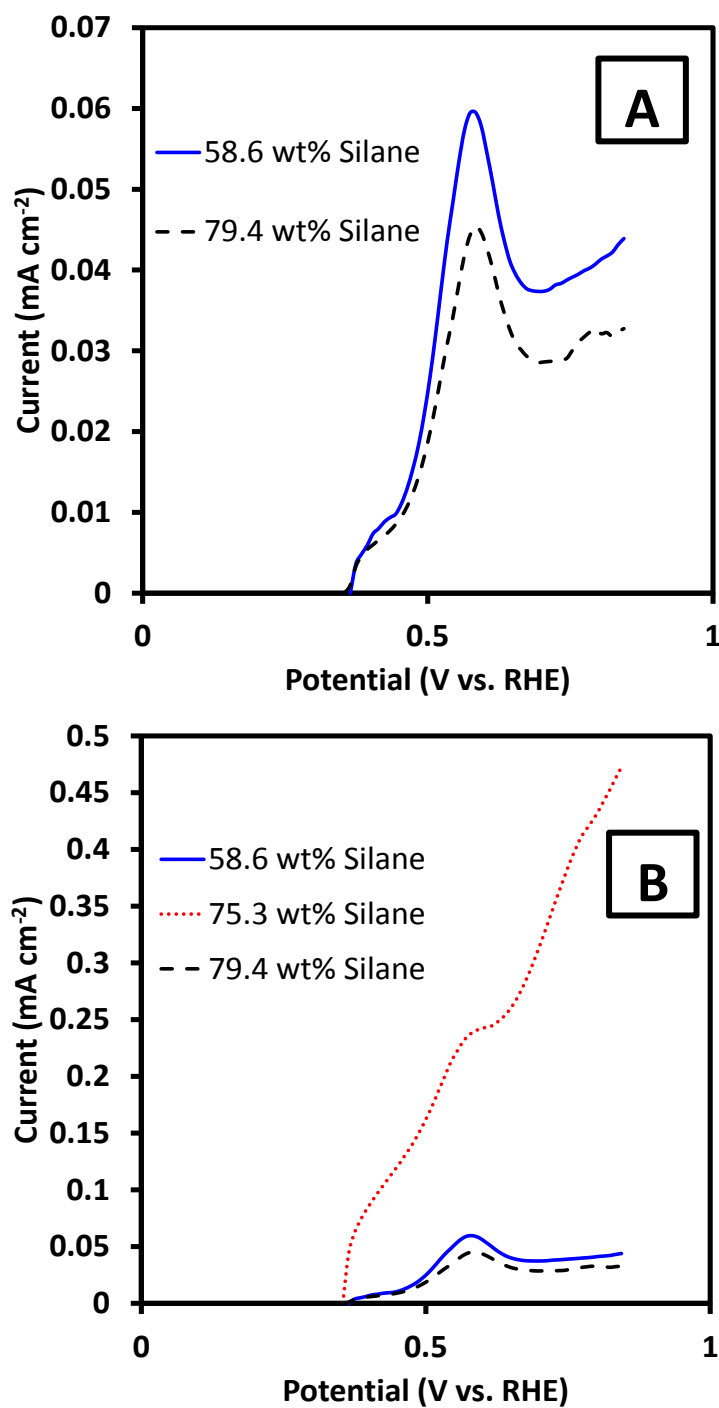


Figure 3-9: Potential stair step measurement of CCE materials with varied 2N silane compositions. Scanned from 0.35-0.85 V vs. RHE with 10 mV steps and 3 s dwell times. Collected in 1 mM CuCl in 1.5 M HCl under N₂ atmosphere electrolyte. (A) Working plots (B) Transient current plot included.

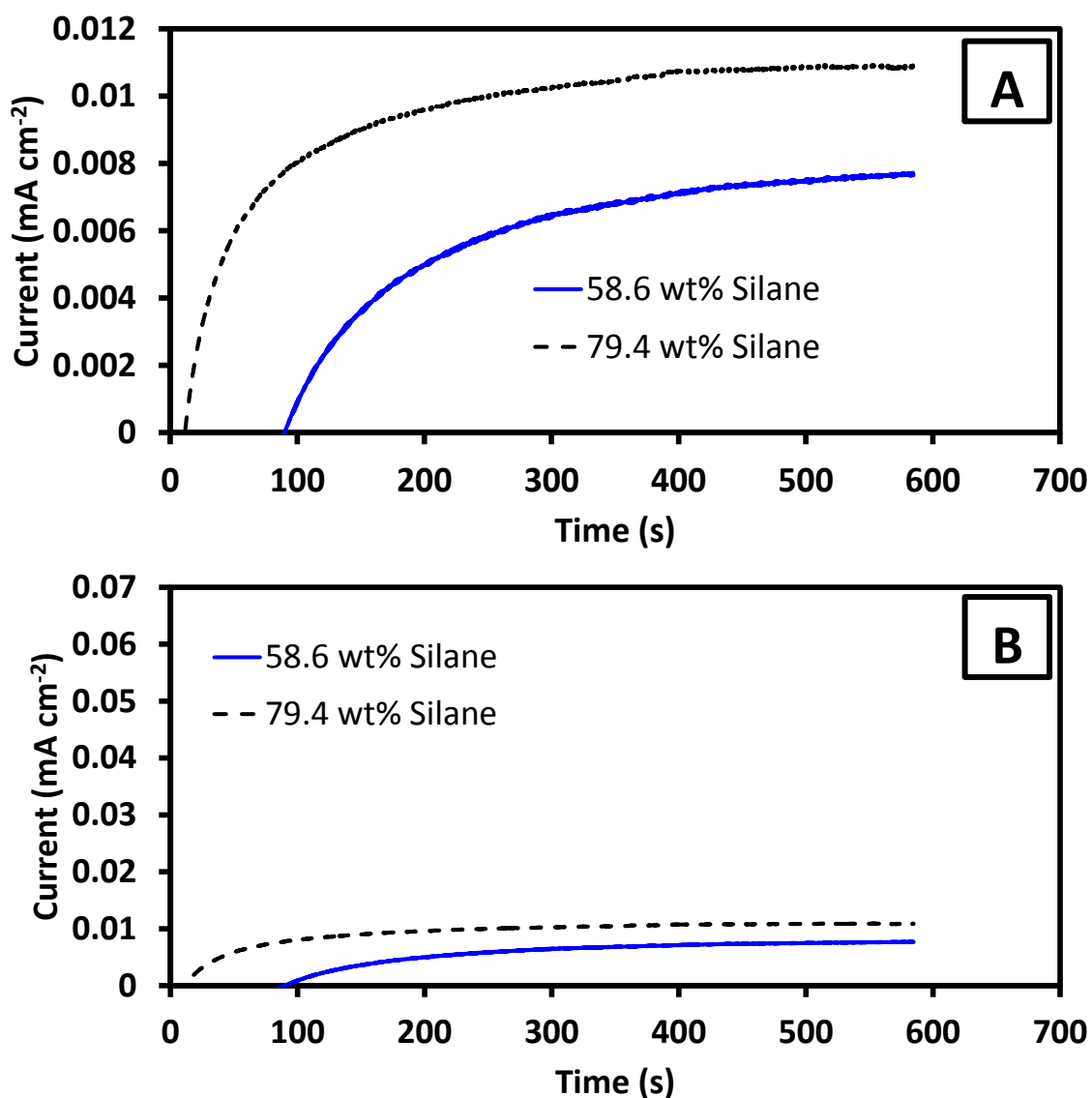


Figure 3-10: Potentiostatic measurements of CCE materials with varied 2N silane compositions. Potential held at 0.6 V vs. RHE. Experiments performed in 1 mM CuCl in 1.5 M HCl under N₂ atmosphere electrolyte. (A) Scaled to show difference between materials (B) Scaled to keep the same maximum current as shown in Figure 3-5 for comparison.

3.2.3: Electrochemical Results for 3N Materials

The 3N materials also showed a decrease in capacitive area with increased silane content (Figure 3-11) similar to what was seen for the 1N and 2N materials). All three CVs showed a lack of significant faradaic processes, though the linear increase in current with potential during the entire CV measurement of the 83.4 wt% sample did display significant

resistance during the measurement. Overall the maximum capacitive charging current of the 3N CCE CV's did not show a significant change from those of the 1N and 2N CCEs.

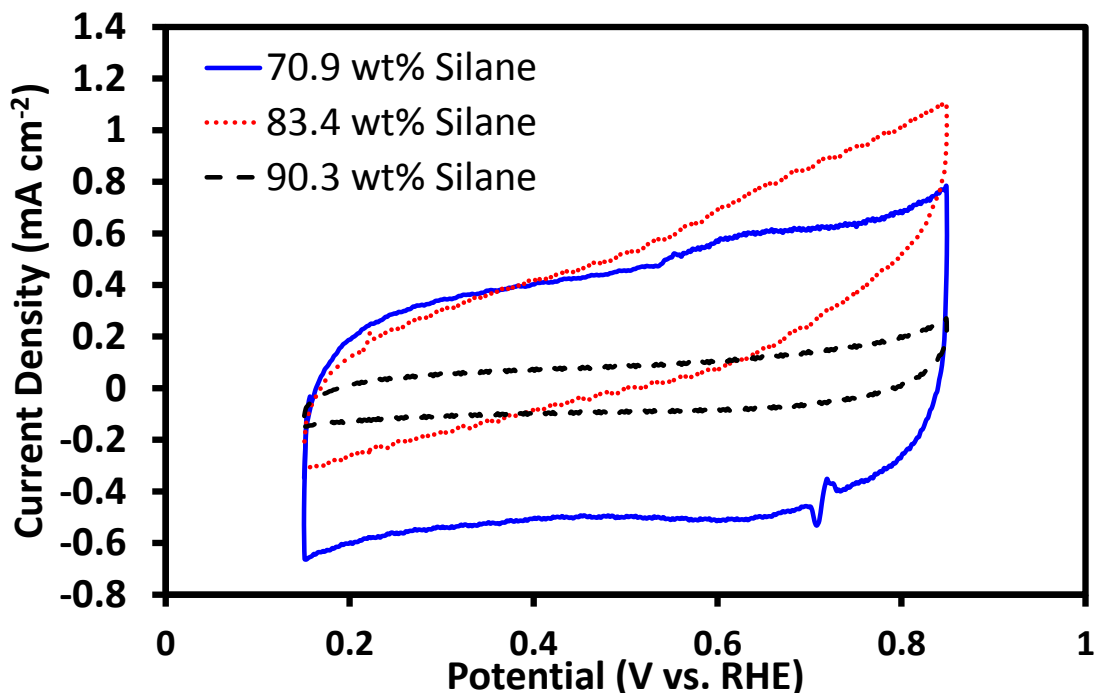


Figure 3-11: Capacitive CV of CCE materials with varied 3N silane loading and normalized for geometric SA. Collected in 1.5 M HCl under N_2 atmosphere. Scan from 0.15 to 0.85 V vs. RHE at 50 mV s^{-1} .

In the impedance measurements (Figure 3-12) of the 3N materials we see the least adherence to our previous trends. While the low loading 70.9 wt% silane sample had the highest conductivity, the other two samples had similar conductivity (Table 3-4). There is still a large decrease in conductivity comparing the 70.9 wt% silane sample to the 83.4 and 90.3 wt% samples. In the capacitance measurements normalized for the mass of carbon we see a different behavior. As expected the 70.9 wt% sample has the highest plateau. The 83.4 wt% sample has the second highest plateau while the 90.3 wt% sample had the lowest plateau. This shows that there is a better utilization of carbon at the lower mass loadings of silane.

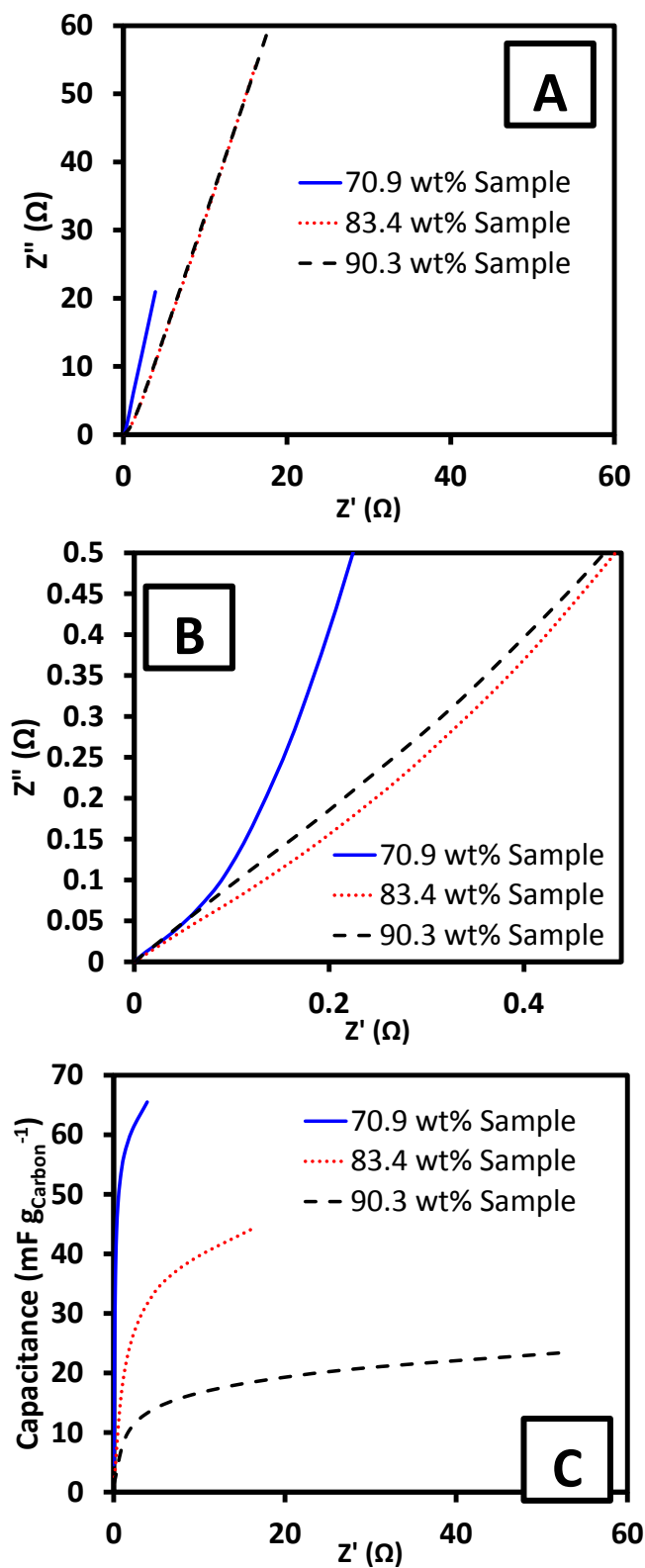


Figure 3-12: Impedance and capacitance plots of CCE materials with varied 3N silane content. Tests were performed in 1.5 M HCl under N_2 atmosphere at 0 V vs. OCV. (A) Nyquist plot (B) High frequency region (C) Capacitance plot.

Table 3-4: Total Resistance of 3N CCE materials. As determined from Warburg region of impedance plots.

| Sample | R_z ($\Omega \text{ cm}^2$) |
|-----------------|---------------------------------|
| 70.9 wt% Silane | 0.3 |
| 83.4 wt% Silane | 1.2 |
| 90.3 wt% Silane | 1.2 |

The potential stair step measurements showed transient currents for the 83.4 wt% 3N sample masking any of the CuCl oxidation current (Figure 3-13 (A)). Again for this reason the 83.4 wt% sample was discarded for comparisons of the potential stair steps. The two samples that were successfully run both show onset potential as well as current response similar to the 1N and 2N materials tested (Figure 3-4 and Figure 3-9 respectively). In these samples there was a flatter current response in the diffusion limited region indicating that there were no non faradaic processes occurring (Figure 3-13(B)). With regards to the diffusion limited current, we can see that the 3N materials behaved in a similar fashion to the 2N materials with the higher wt% silane samples exhibiting a higher current response than the lower ones. The 3N materials did show a lower overall current response in the potential stair step measurements than was observed for the 1N and 2N materials (Figure 3-13).

While the 3N materials did behave in a manner that was consistent with previous measurements the current response in the potentiostatic hold measurements was also seen to be lower. Again for the 3N materials, a potential hold was applied at 0.60 V vs. RHE for a total time of 600 s; however, a cathodic current was recorded for the initial approximately 100 s and was not shown in Figure 3-14.

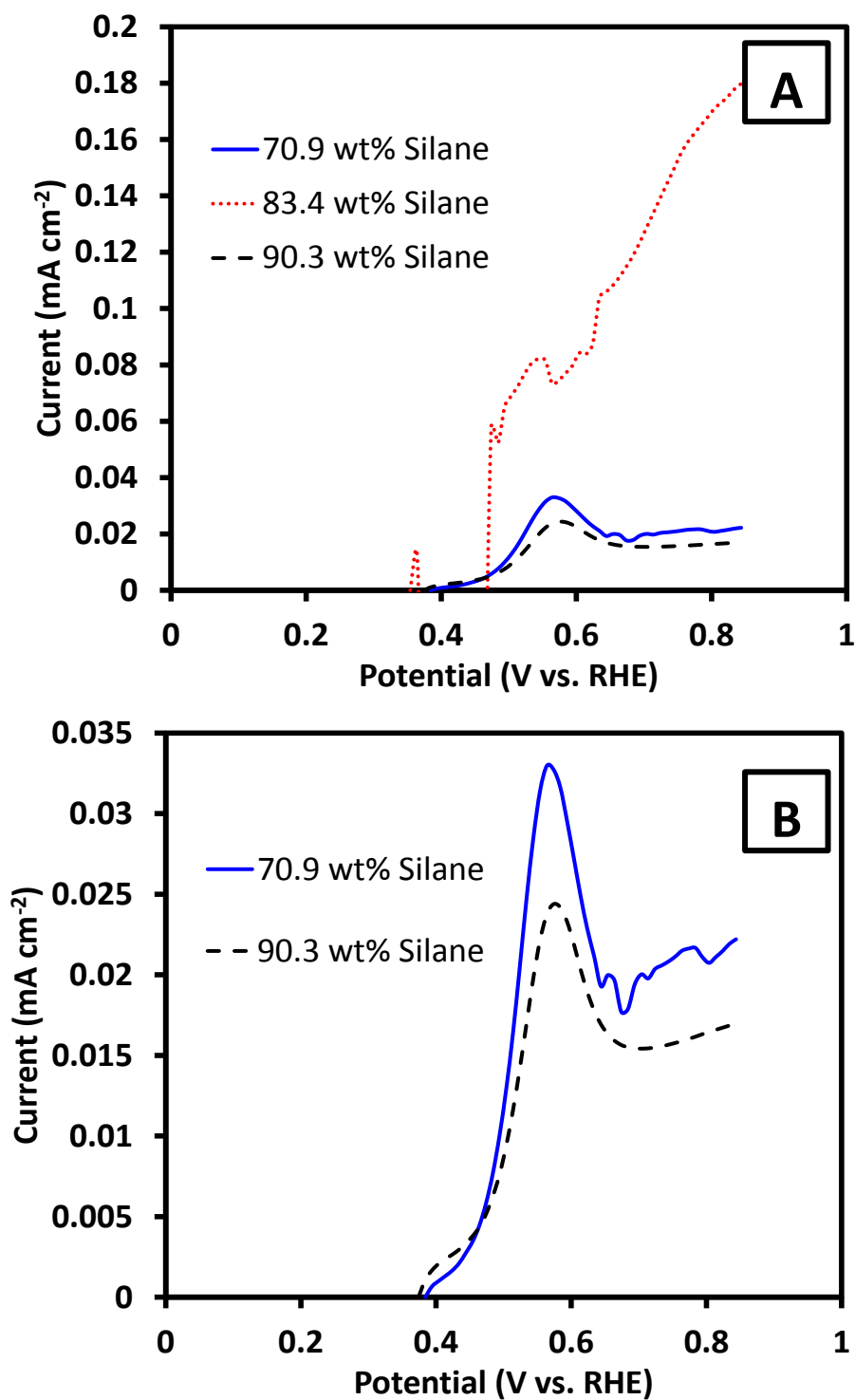


Figure 3-13: Potential stair step Measurement of CCE materials with varied 3N silane compositions. Scanned from 0.35-0.85 V vs. RHE with 10 mV steps and 3 s dwell times. Collected in 1 mM CuCl in 1.5 M HCl under N_2 atmosphere electrolyte. (A) Working plots (B) Transient current plot included.

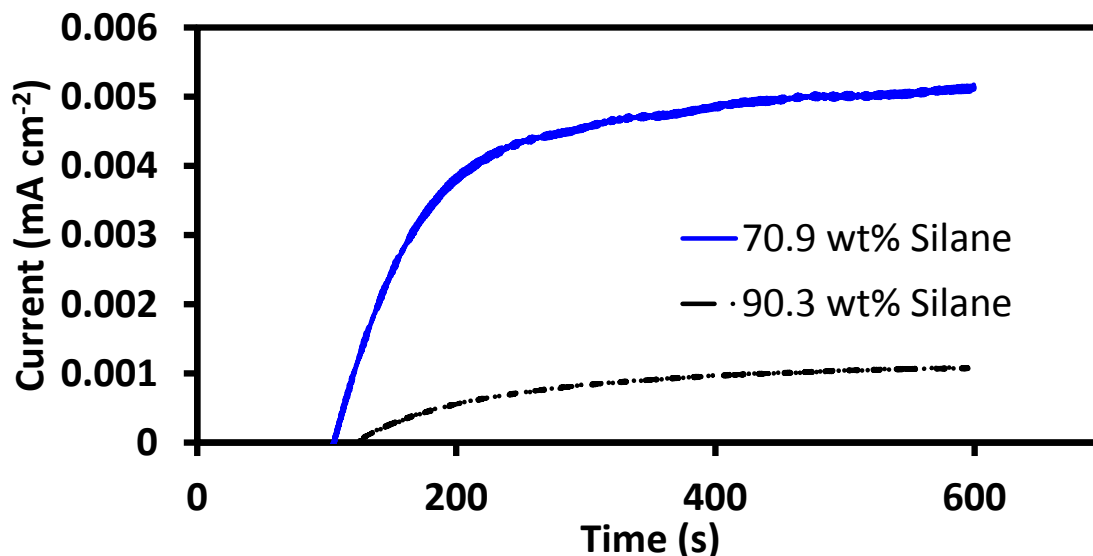


Figure 3-14: Potentiostatic measurements of CCE materials with varied 3N silane compositions. Potential held at 0.6 V vs. RHE. Tests were performed in 1 mM CuCl in 1.5 M HCl under N₂ atmosphere electrolyte.

3.3: Discussion of Half-Cell Materials

As shown in Table 3-1 the various silane materials were all produced with similar molar loadings of the 1N, 2N, and 3N silane materials. This allowed for the easy comparison of the materials to one another to assess their relative electrochemical properties. The standardized testing protocol also allowed for easy comparison between silane materials. Of the actual electrochemical results the most important metric was the ability for the materials to oxidize CuCl. The potentiostatic holds were performed to assess the CCE's performance under conditions as close to approximating the conditions to be used during full-cell testing as can be performed in the half-cell. Potentiostatic holds provided good insight into the under load operation of the CCE working electrodes. Holds made at 0.6V vs. RHE were used to compare the electrodes performance to one another. Observing the drop off in current over time in the potentiostatic holds also gave an insight into the CCE's overall lifetime and stability. While still operating properly the potentiostatic hold gave a linear current response for the oxidation of Cu⁺, deviations from this linear response are related to transient current processes such as the plating of Cu⁺ at the Pt Counter electrode.

3.3.1: 1N Materials

From the initial Capacitive CV measurements (Figure 3-2), a decrease in capacitive current was observed as silane content increased. As the carbon surface area dominates the

CCE structure, the lower capacitive current was attributed to the lower carbon composition in the higher wt% silane samples. Additionally, it was assumed that with the higher resistance from the silicate backbone will also cause a lower rate of capacitive charging on the existing carbon in the higher wt% silane samples. This trend of lower overall capacitance was also displayed in the capacitance plots of the 1N materials (Figure 3-3 (C)). Further confirming the resistive nature of the high silane content materials, the EIS measurements the samples with higher silane content were shown to have a larger Warburg region and therefore a higher resistance (Figure 3-3 (A and B)). The protonated amines present on the silane materials should provide an increased ionic conductivity. With this in mind it would be expected for the sample with the highest silane content (69 wt%) to have the highest ionic conductivity, which was not the case. The explanation for this is that the increased silane content causes the higher wt% silane samples to become more electronically resistive. As the Warburg region can only be used to identify the total resistance, the increased electronic resistance from the silane content was too large for the CCE to benefit from the increased ionic conductivity.

As mentioned above, the potentiostatic measurements were used to examine the under load operation of the different CCEs. Both the potentiostatic and potential stair step measurements showed that there were no transient processes occurring during the CuCl oxidation process (Figure 3-4, Figure 3-5). This was expected as there was no catalytic material present on the electrode to facilitate side reactions. As seen in Figure 3-6 there was a low correlation between the wt% of silane and the mass normalized current response. This indicated that either the limiting current was being reached for the electrodes in question or that there is another factor affecting the current response such as the CCE microstructure.

3.3.2: 2N Materials

As with the 1N samples, the capacitive CV measurements of the 2N materials (Figure 3-7) showed higher capacitive currents were present in the samples with lower wt% of silane. This again indicates that there was a better utilization of the carbon surface area in the samples with a lower silane wt% composition. In addition to this, we can see that the total charging current from the 58 and 75 wt% samples was approximately double that of the associated 1N materials, with the high loading samples also showing increased current. This indicates that the 2N materials are allowing better access to the carbon surface area when compared to 1N materials with similar silane loadings. Additionally, this increased capacitive current should

result in a better electrode performance. Despite this we can see that there is a very poor utilization of the carbon surface from the 79.4 wt% sample which could be indicative of high electronic resistance from the large amount of silane present in the sample, as well as the silane obstructing access to the carbon surface.

During the EIS measurements, an increase in resistance for the 79.4 wt% 2N silane sample was observed (Figure 3-8 (A and B)). This sharp increase can be explained by the silane finally destroying the majority of electron pathways at 79.4 wt% silane while there are still many free electron pathways at 75.4 wt% silane. Regardless, this dramatic increase in resistance also reinforces the notion that the increase in resistance is limiting the charging of the 79.4 wt% silane material during the capacitive CV measurements. Additionally, the capacitance plot (Figure 3-8 (C)) shows the same trend in total capacitance as seen in the capacitive CV measurements (Figure 3-7).

The large transient current observed for the 75.3 wt% 2N CCE during the potential stair step measurement (Figure 3-9) was attributed to a large deposition of copper at the cathode. By discarding this sample from the subsequent testing there was little that could be drawn from the potentiostatic holds (Figure 3-10). What can be observed was that the higher wt% sample outperformed the lower wt% one by a margin similar to the differences between 1N materials (Figure 3-5). The better performance of the 79.4 wt% is opposite of what can be seen in the potential stair step measurements (Figure 3-9). It is assumed that the increase seen in the potential stair step measurements was due to Cu plating artificially increasing the current recorded for the 58.6 wt% sample. The potentiostatic measurements were assumed to be representative of CuCl oxidation as there were no visible transient current regions.

3.3.3: 3N Materials

For the 3N materials there was once again a decrease in capacitive current with increasing silane content (Figure 3-11). This decrease was consistent with the 1N and 2N materials capacitive CV measurements and supports the idea that there is a large increase in electronic resistance for the higher wt% silanes. The EIS measurements (Figure 3-12 (A and B)) also showed an increase in resistance with increasing silane content. This increase also agrees with EIS measurements taken of the 1N and 2N materials (Figure 3-3 and Figure 3-8). From this it was again assumed that while there should be an increase in ionic conductivity from the increased protonated amine content, the increased silane content increased electronic

resistance by a larger margin. As with the 1N and 2N materials the capacitance plots (Figure 3-12 (C)) showed the same trend in capacitance as the capacitive CV measurements. Overall, the 3N materials were shown to have a lower current response during the potential stair step and potentiostatic hold measurements, indicating that the 3N silane was inhibiting the oxidation of the CuCl either chemically or by physically altering the structure of the electrode.

3.3.4: Comparison of Varied Silane Types

CCE materials of the three silane types showed a couple of common trends. The most pronounced was the decrease in the overall capacitive current with increased silane content. This was supported by similar trends being observed in the EIS measurements. It was assumed that in all of these materials that the increased silane content was increasing the electronic resistance. Beyond this, the comparison of the potentiostatic measurements did not show as consistent a trend. It was observed that the 1N materials had the best overall current response. After being normalized for the mass of CCE material deposited on the electrodes surface a distinct increase in current response from the 1N materials was observed while the 2N and 3N materials showed nearly identical current responses (Figure 3-15). From this information it appears that the 2N and 3N CCEs are maximizing the available carbon surface area even though it is not as effective as 1N CCE. Additionally, the 1N CCE has a higher ratio of moles of silane to mass of carbon loading than the best 2N and 3N materials. This should imply that the electronic resistance would decrease the overall current response from the 1N material. The counterintuitive current response indicates that the structure of the CCE material could also affect the limiting current for CuCl oxidation. This new factor in CuCl oxidation also explains why the highest wt% 2N material showed the best CuCl oxidation rate despite an increased electronic resistance.

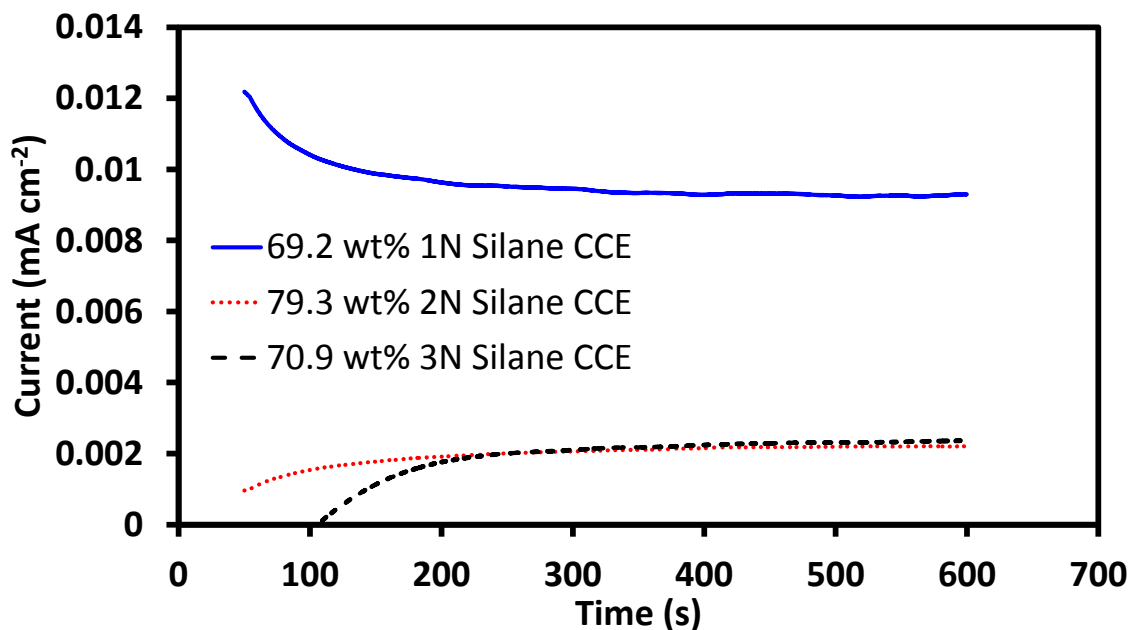


Figure 3-15: Potentiostatic measurements of CCE materials produced with 1N, 2N and 3N silane precursors. Potential held at 0.6 V vs. RHE. Tests were performed in 1 mM CuCl in 1.5 M HCl under N₂ atmosphere electrolyte.

While the 1N materials appeared to be the best option, all three silane types were selected for further testing to examine their effects in a full-cell environment. While the half-cell testing does provide some initial screening of CCE activity and porosity it is in an unrealistic condition to represent full-cell production. The low concentration of the CuCl used in the half cell could inhibit the electrolyte's ability to properly permeate into the CCE structure to allow for a better current response in the underperforming materials. Under full-cell conditions the concentration of the CuCl in the anolyte solution will be much higher to help overcome any blocked anode CCE structures. Further, the high flow rates will allow for reduction of the mass transport phenomenon as seen in the potential stair step measurements (Figure 3-4, Figure 3-9, and Figure 3-13).

Chapter 4 : Materials for Full-Cell Electrolysis

CCE materials with silane and carbon compositions similar to those described in chapter 3 (Table 3-1) were produced for testing in a full-cell environment. This was done to examine the CCE materials in an environment closer in design to what will be required for integration into a full CuCl-HCl cycle. Additionally, the full-cell environment was used to validate the predictive capabilities of the half-cell measurements. The full-cell testing station and test protocol underwent several design revisions through the full extent of testing. Unless noted, the results were produced using the full-cell described in section 2.3.2 as well as the standard full-cell protocol in section 2.4.2.

The initial cell design (Section 2.3.1) was used to verify the electrochemical activity of the CuCl electrolysis and the purity of the prepared anolyte. Both the anode and cathode were composed of 5 cm² sections of standard Pt/C carbon CCE. To test water electrolysis, a solution of deionized water was provided to both the anode and cathode at flow rate of 14 mL min⁻¹ per side. A potential stair step measurement was taken from 1.0 – 2.0 V vs. RHE. An onset potential of 1.75 V vs. RHE was observed, a value expected for water electrolysis when accounting for thermodynamic and resistive losses⁵. Below the onset potential value there was no appreciable current response recorded. To evaluate the CuCl-HCl electrolysis process in our initial full-cell system, deionized water was passed to the cathode and 0.2 M CuCl in 2M HCl was passed to the anode, both at a flow rate of 14 mL min⁻¹. A potential stair step measurement was taken from 0.05-1.4 V vs. RHE. In this case the onset potential was calculated to be 0.41 V vs. RHE. Again, below this value there was no recorded current response (Figure 4-1). Both onset potentials appeared at expected values^{5,27}. From this measurement it can be seen that the CuCl-HCl electrolysis process is performing as expected with a marked drop in onset potential over water electrolysis. Additionally, a drop in current response can be observed at 0.86 V vs RHE for the CuCl-HCl electrolysis process. This can be attributed to mass transport limitations for the electrochemical cell. Beyond this initial testing, the characterization of the CCE materials performed on the initial cell configuration (Section 2.3.1) were discarded in favor of test results collected on the full-cell systems with design improvements (Section 2.3.2).

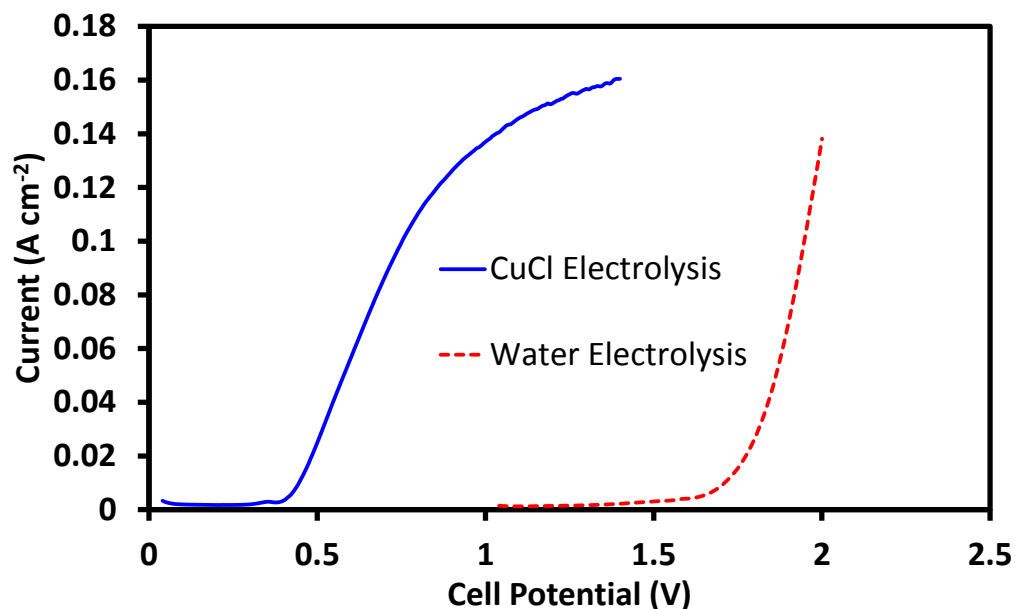


Figure 4-1: Comparison of CuCl and H₂O electrolysis with a Pt/C anode and cathode catalyst. CuCl electrolysis collected in 0.2 M CuCl in 2 M HCl anolyte and DI H₂O catholyte both under N₂ atmosphere at 14 mL min⁻¹ electrolyte flow rate. Water electrolysis collected in DI H₂O electrolyte at cathode and anode under N₂ atmosphere at 14 mL min⁻¹ flow rate.

The primary concern with the initial full-cell design was the low flow rates provided by the analogue pump. At 14 mL per minute maximum flow rate data acquired in the full-cell design was not reasonable comparable data reported in literature which acquired at much higher flow rates^{20,21}. Given this, the pump system was changed to the Masterflex L/S digital drive peristaltic pump (RK-07523-80). With this replacement the full-cell system remained effectively unchanged throughout testing as tubing and electrolyte vessel changes had no discernible impact on the maximum performance of the cell, and only helped to improve electrolyte stability and long term cell operation.

A Potential stair step methodology was validated as a replacement for a linear sweep voltammetry. A potential stair step measurement with 5 mV steps and 0.5 s dwell times at each step (10 mV s⁻¹ effective) was made from 0.2 to 1.2 V vs. RHE. Additionally, an LSV scan from 0.2 to 1.2 V vs. RHE at 10 mV s⁻¹ was taken (Figure 4-2). The two scan methods produced similar current responses. Importantly, the onset potential, when extrapolated, is very similar for both the CV and potential stair step. Both plots also show the onset of the diffusion limited current process at a similar potential. The only notable difference between the two graphs is a broad

peak from approximately 0.2 to 0.65 V vs. RHE on the 10 mV s⁻¹ LSV scan. This peak can be attributed to electrolyte preloading within the highly porous electrode structure.

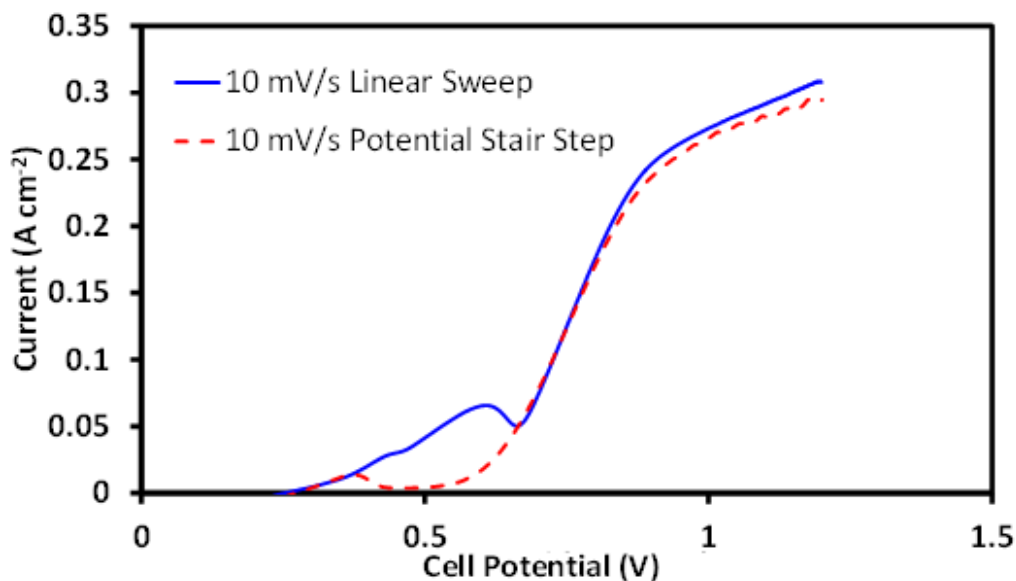


Figure 4-2: Comparison of linear sweep and potential stair step measurements at equivalent scan rates. Tests were performed in 0.2 M CuCl in 2 M HCl anolyte and DI H₂O catholyte both under N₂ atmosphere at 60 mL min⁻¹ electrolyte flow rate.

To electrochemically characterize the CCEs produced a standard series of electrochemical experiments were developed. The electrochemical test parameters were based on the initial work in the half-cell. Impedance and capacitance measurements were taken in the absence of CuCl to assess the conductivity of the MEA as well as the relative electrochemically active surface area. Capacitive CV's were also taken in the absence of CuCl to estimate the overall surface area of the CCE as well as to ensure that electrode surface was clean. Potential stair step measurements were taken to assess the onset potential as well as the onset of the diffusion limited current response. Finally, both galvanostatic and potentiostatic measurements were taken to examine the operational current responses of the MEA's as well as their long term stability and resistance to copper crossover. Standard materials were used for the proton conducting membrane (Nafion 115) and the cathode electrode (0.3 mg cm⁻¹ Pt/C). This was done to isolate the electrochemical changes produced by the varied CCE anode electrodes. Electrolyte flow rate was also varied at both the anode and cathode. At consistent electrochemical parameters varied flow rates can be used to change the effective concentration

of CuCl at the anode electrode, from this we expect to see an increase in current response with higher flow rates.

The method for physical characterization of the CCE materials was also drawn from the half-cell electrode production. The bulk composition of the electrodes was determined through TGA analysis. Excess powder was scraped off of the aluminum foil spray coat backing. This controlled the TGA sample under the same drying conditions used for the CCE electrodes. Additionally this allowed for the TGA sample to be subjected to the same spraying conditions that could potentially contaminate the CCE sample. Finally, after production, the samples were analyzed through SEM to examine bulk surface properties and to provide an insight into potential coating defects.

4.1: Results

4.1.1: Results for 1N Materials

As with the half-cell electrode samples, initial tests were centered on varying the total concentration of the 1N silane within the CCE. This was done to both verify the findings in the half-cell measurements as well as to assess differences in how the full-cell electrodes handled the presence of the electrically insulating sol gel network. Silane composition was targeted at between 20 and 60 wt% silane. This allowed for the examination of lower loading silane samples which were not produced for half-cell testing. The target silane loadings were also chosen to correlate with work published previously in our lab²⁴.

Table 4-1: 1N CCE materials for full-cell electrolysis compositional information.

| Sample Code | wt% Silane | Mass Loading (mg cm ⁻²) | Carbon Loading (mg cm ⁻²) | mMol Si g _{Carbon} ⁻¹ |
|-------------|------------|-------------------------------------|---------------------------------------|---|
| B1P73S2 | 27.18 | 1.78 | 1.30 | 3.39 |
| B1P69S1 | 32.42 | 2.66 | 1.80 | 4.36 |
| B1P69S2 | 50.72 | 2.79 | 1.37 | 9.36 |
| B1P69S3 | 53.45 | 3.65 | 1.70 | 10.44 |
| B1P60S2 | 62.49 | 4.24 | 1.59 | 15.14 |

Many 1N CCE samples were produced and tested; from them the above five were selected to examine the effects of the varied silane content on full-cell electrode properties and performance. The samples were selected because they represented an approximately even spacing of silane content from the lowest to highest amounts. Across the five samples the total

mass loading of the CCE increases with increased silane composition. This is to be expected as the sol-gel binder is denser than the carbon support which it is binding to. The loading of carbon on the electrode has a relative standard deviation of 13.68%. The relatively narrow range of carbon loading ensures that changes in electrode performance can be attributed to the change in silane composition and not to morphological CCE changes from increased carbon loading. The effects of changing carbon loadings are examined in chapter 4.1.2: Results for Varied CCE Loadings (1N). To compare the 1N CCEs to those prepared with other silanes a molar loading of silicon normalized to the mass of carbon was also calculated.

4.1.1.1: Materials Characterization Results

All of the CCEs produced had very similar physical properties. As with the half-cell CCEs the full-cell CCEs were characterized using both TGA analysis and SEM imaging. The samples all showed consistent behavior analyzed through TGA. As with the half-cell CCE materials, the total mass was normalized at 200 °C to account for water loss. After the initial drying the samples were air stable up to approximately 600 °C at which point the carbon structures combusted leaving only SiO₂ at the final temperature of 1000 °C, an example of this degradation can be seen in Figure 3-1. The uniform and simple degradation of the materials indicated that, like the half-cell CCEs, the CCE materials have a standard morphology that is unaltered on a macro scale. This is to be expected as the materials used for the production of the CCEs are largely uniform. Accounting for volume, very little silane is actually present within the CCE with the bulk being comprised of the very high surface area and low density carbon (Vulcan XC-72).

In addition to the TGA analysis performed on the samples SEM images were taken to observe the bulk structural properties (Figure 4-3). All of the CCEs photographed showed a homogeneous morphology. At lower magnifications, near the micrometer range, the samples showed similar structural features; a rough surface featuring mud cracks and small defects. At higher magnifications the differences between the samples become more apparent, where the homogeneous distribution of the CCE appeared to decrease with increased silane content.

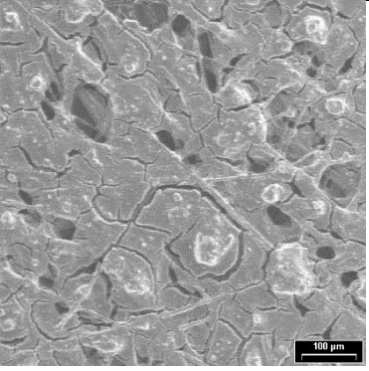
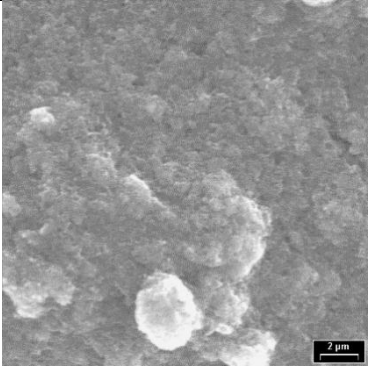
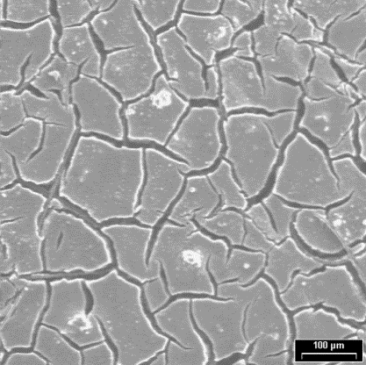
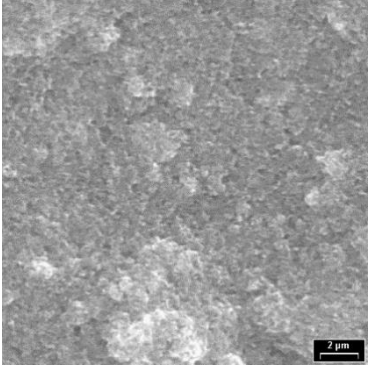
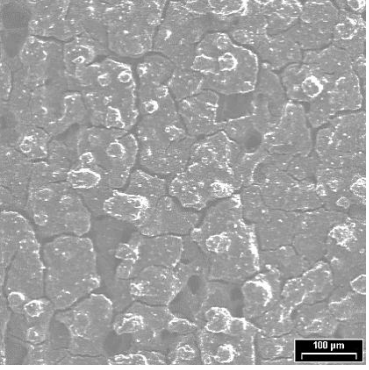
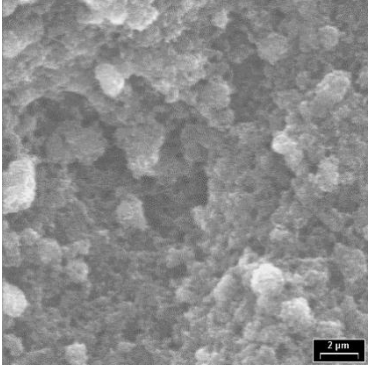
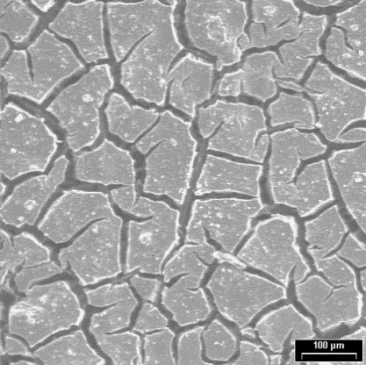
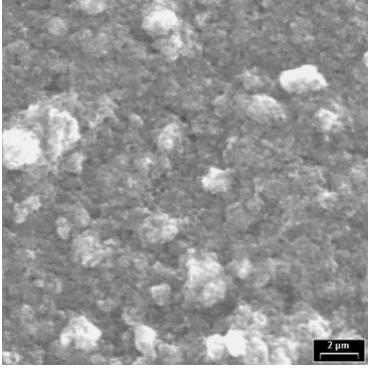
| Sample and Silane wt% | 100 x Magnification | 2500 x Magnification |
|-----------------------|--|---|
| B1P73S2 27.2 wt% |  100 μm |  2 μm |
| B1P69S1 32.4 wt% |  100 μm |  2 μm |
| B1P69S2 50.7 wt% |  100 μm |  2 μm |
| B1P69S3 53.4 wt% |  100 μm |  2 μm |

Figure 4-3: SEM images taken of CCE samples B1P73S2, B1P69S1, B1P69S2, and B1P69S3 at 100 and 2500 x magnification.

4.1.1.2: Electrochemical Results for 1N materials

Similar electrochemical test conditions to those performed in the half-cell were applied in the full-cell testing. Expanding upon the testing done in the half-cell, flow rate was also varied to examine the effects of it on cell performance. During the operation, the evolution of H₂ on Pt at the cathode was used as a reference electrode for the full-cell. From this, all of the electrochemical data was taken as V vs. RHE and was not adjusted for a reference potential.

Capacitive CVs and EIS were collected in the absence of CuCl to analyze the surface area and ionic conductivity of the different anode materials. As stated in chapter 2.3 the anode was supplied with 2 M HCl solution at 60 mL min⁻¹ and the cathode was supplied with H₂ gas at a rate of 25 mL min⁻¹.

The impedance plots of the five CCE materials showed an interesting trend in conductivity. As the silane monomer is functionalized with amines, increased silane content should show a higher ionic conductivity from the increased number of charged amine groups. However, we see a reduction in the overall conductivity with increased silane loading. The two CCEs with the lowest silane content showed effectively nonexistent Warburg regions indicating a high conductivity. The two highest silane containing samples showed the largest Warburg regions (both approximately 0.01 Ω) and, therefore, the lowest conductivity.

In addition to the ionic conductivity, the impedance measurements were also used to examine the capacitance of the CCE samples. There was no apparent trend in the capacitance plots. The two samples with the highest plateau were the 32.42 and 53.45 wt% samples. There was very little difference in the plateaus of these two electrodes. This is consistent with the very similar areas of their capacitive CVs for the same CCE materials (Figure 4-4 (A)). Differing from the capacitive CV measurements, the 27.18 wt% sample shows a higher plateau compared to the 50.72 wt% sample. The 62.5 wt% sample showed a low overall capacitance because of the high mass of silane within the sample.

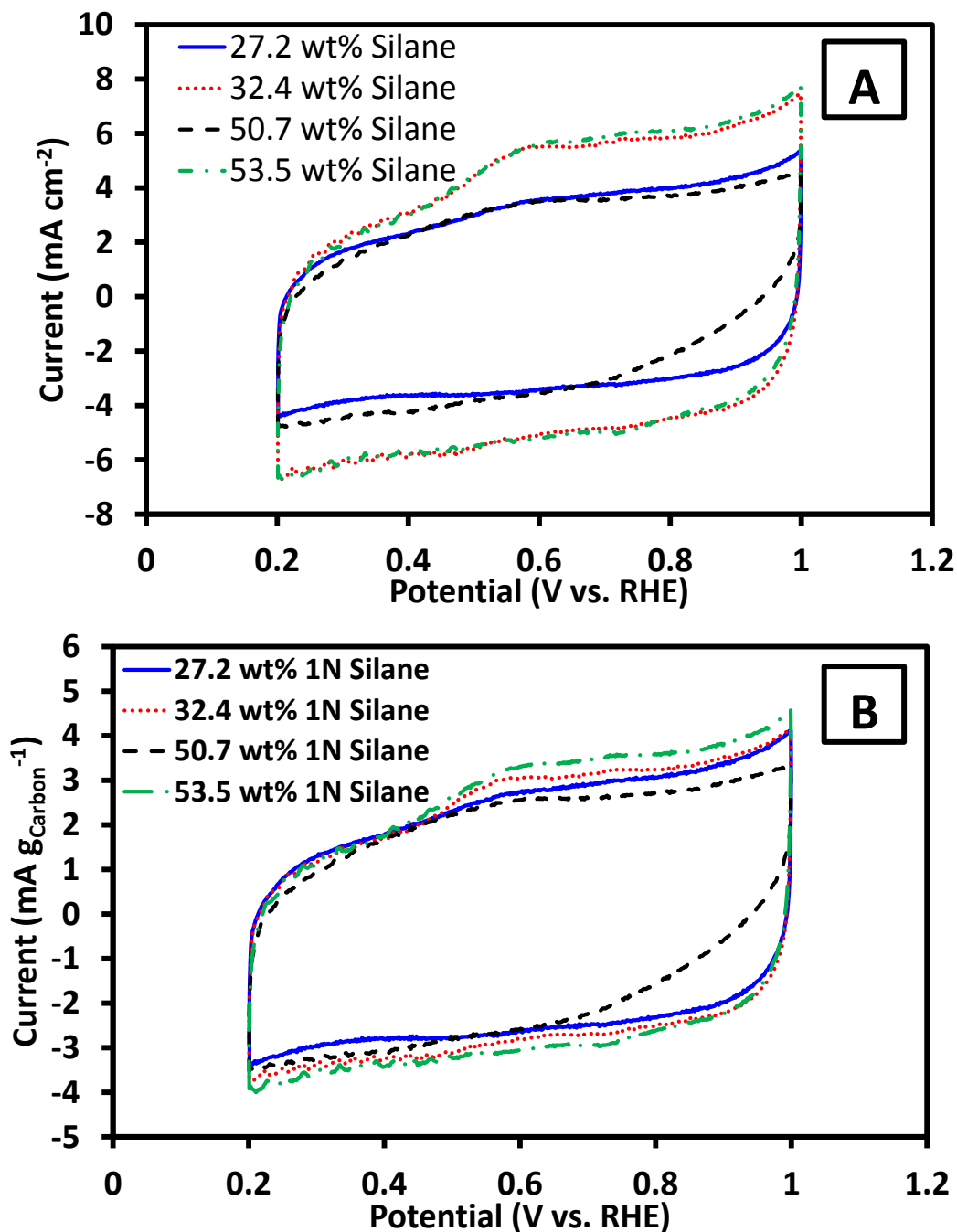


Figure 4-4: Capacitive CV of CCE materials with varied 1N silane loading. 10 mV s^{-1} scan rate from 0.2 to 1.0 V vs. RHE. Current normalized for geometric SA and for mass of carbon. In 2 M HCl under N_2 atmosphere at 60 mL min^{-1} analyte flow rate. (A) Area specific (B) Carbon mass normalized.

There did not appear to be any dependence of the capacitive surface area on the silane loading. When normalized for the mass of carbon present on the CCE the materials showed very similar capacitances (Figure 4-4).

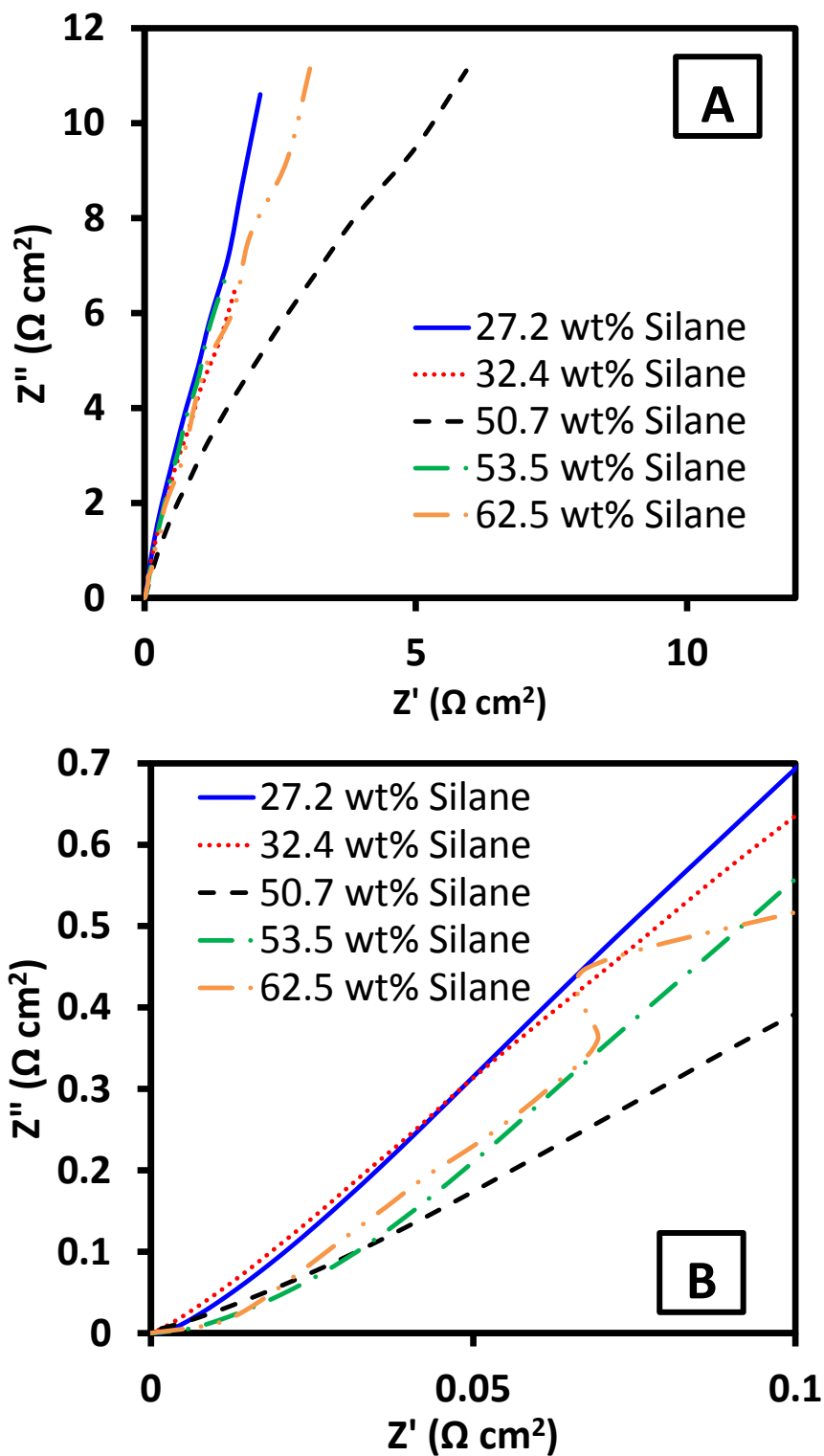


Figure 4-5: Nyquist plots of varied 1N silane content CCEs. Collected at 0 V vs. OCV in 2 M HCl anolyte under N_2 atmosphere at 60 mL min^{-1} anolyte flow rate and 25 mL min^{-1} H_2 gas provided to the cathode. (A) Nyquist plot (B) High frequency region.

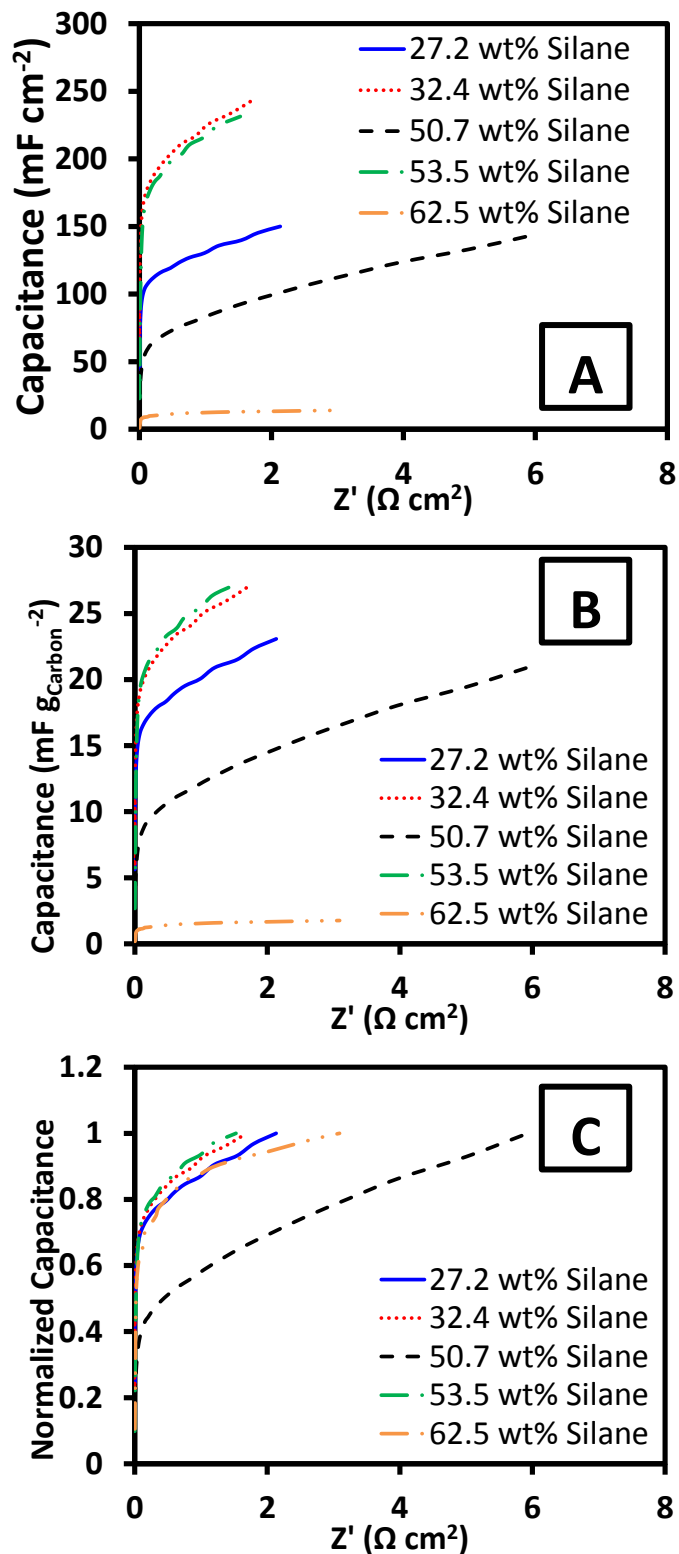


Figure 4-6: Capacitance plots of varied 1N silane content CCEs. Tests were performed at 0 V vs. OCV in 2 M HCl analyte under N_2 atmosphere at 60 mL min^{-1} analyte flow rate and 25 mL min^{-1} H_2 gas provided to the cathode. (A) Area specific capacitance (B) Mass of carbon normalized (C) Capacitance normalized to 1.

Beyond the initial characterization, operational tests were performed to assess the different CCE materials abilities to electrolyze Cu^+ in the full-cell. The anolyte was 0.2 M CuCl in 2M HCl and the catholyte was DI H_2O . Both electrolyte solutions were provided to the cell at flow rates ranging from 40 to 100 mL min^{-1} . The selection was made to compare results with literature, as well as to address initial safety concerns of working with more concentrated acid solutions²⁰. The CCEs were examined with potential stair step voltammetry at a scan rate of 10 mV s^{-1} to assess onset potential, current response, and response to increased flow rate. All of the CCE's were scanned from 0.2 to 1.2 V vs. RHE at flow rates of 40, 60, 80, and 100 mL min^{-1} . A representative example of the current response at different flow rates is shown in Figure 4-7.

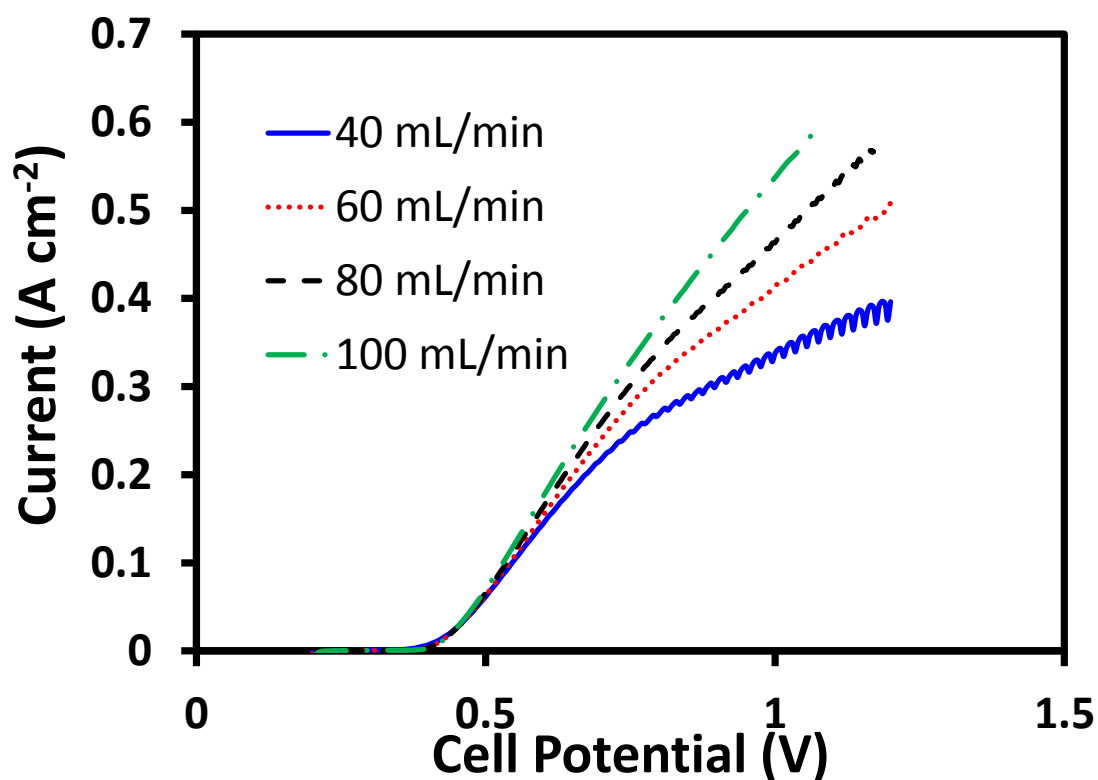


Figure 4-7: Potential stair step measurements of 27.2 wt% CCE at varied flow rates. Scanned from 0.2 to 1.2 V with 5 mV steps and 0.5 s dwell time per step. Tests were performed in 0.2 M CuCl in 2 M HCl anolyte and DI H_2O catholyte both under N_2 atmosphere at 60 mL min^{-1} electrolyte flow rate.

Generally, the CCEs showed an expected onset potential of approximately 0.4 V vs. RHE^{18,20}. The maximum current response varied across the CCEs tested from 0.08 to 0.268 A cm^{-2} at 0.7 V vs. RHE. During the 40 mL min^{-1} flow rate test all of the samples showed signs of a diffusion limited process occurring within the sample. Above approximately

0.9 V vs. RHE the rate at which current increased with potential was reduced. This was particularly noticeable in the highest wt% silane sample (62.5 wt% Silane) which showed the lowest capacitive surface area. For the 62.5 wt% sample the reduction in current response was also noticeable in the 60 mL min⁻¹ run.

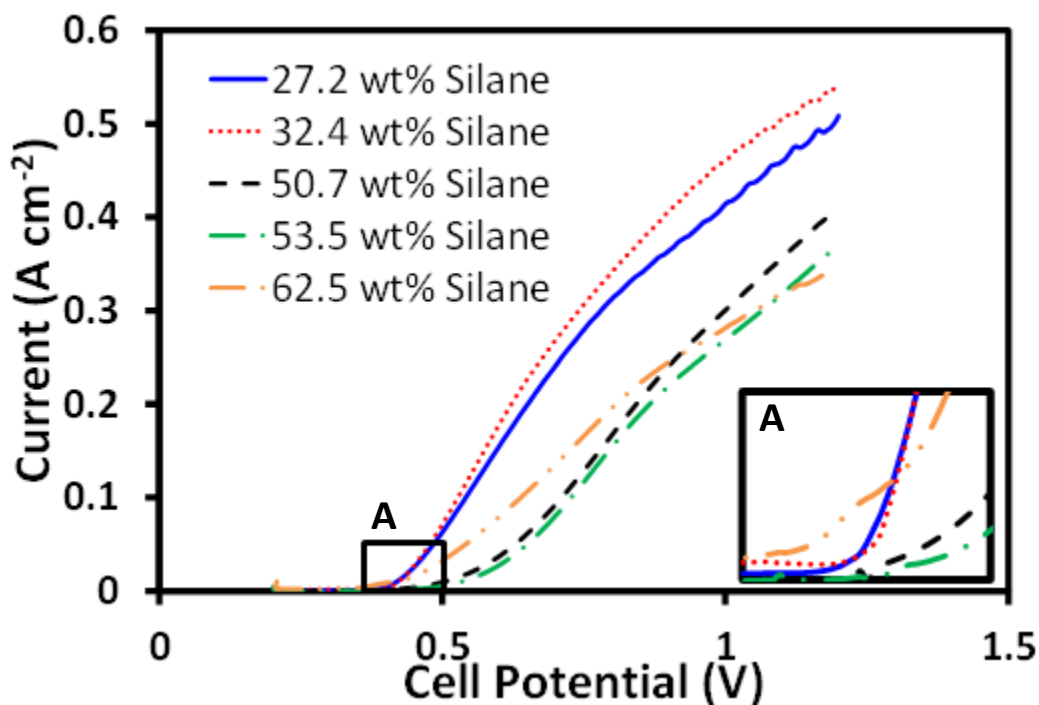


Figure 4-8: Potential stair step measurements of CCE's with varied 1N silane composition. Scanned from 0.2-1.2 V with 5 mV steps and 0.5 s dwell time per step. Experiment performed in in 0.2 M CuCl in 2M HCl anolyte and DI H₂O catholyte both under N₂ atmosphere at 60 mL min⁻¹ electrolyte flow rate. (A) Enlarged onset potential region from 0.3 to 0.5 V vs. RHE.

When compared, the current responses of the different CCE's at the same flow rate show a slight trend towards better performance from the CCE's with lower silane content. The top performing CCE's were the 32.42 and 27.18 wt% samples respectively. The low silane loading CCE's showed a slightly better onset potential than the higher silane content samples. The lower onset potential can be partly attributed to the higher conductivity of the electrodes leading to lower resistive losses within the cell. There was also a clear increase in performance from the lower silane loading CCEs compared to the higher loading samples. Figure 4-8 shows that the higher silane loading CCEs had a varied dependence of the current response on silane content. Regarding the three highest silane content CCEs, at 1.2 V vs. RHE there was a trend of

lower current response with increased silane content. At 0.7 V the 62.48 wt% silane CCE outperformed both the 50.72 and 53.45 wt% silane samples, this can be attributed to the CCE's earlier onset potential. All three samples were still dramatically outperformed by the 27.18 and 32.42 wt% silane samples. This trend is in agreement with work done previously showing the lower loading CCE's to be more active²⁴.

The LSV data was further analyzed by plotting the current at 0.7 and 1.1 V vs. RHE with respect to the flow rate of the electrolyte solutions (Figure 4-9). Using this, the cell's response to increased flow at the anode surface was evaluated. At 1.1 V vs. RHE all of the samples show a linear response to increased flow rate. While the 32.4 wt% silane showed the best current of the samples, the 27.2 wt% sample showed a steeper response to the increased flow rate. Therefore, at even higher flow rates the 27.2 wt% sample may outperform the 32.4 wt% sample. Similar behavior was observed for the 0.7 V vs. RHE comparison. This is particularly important as the DOE target for operation is set at 0.7 V vs. RHE²². The 32.4 wt% sample also showed the highest current response at 0.7 V vs. RHE; however, the 27.3 wt % sample showed comparable currents with a steeper response to the increased flow rates. This shows more conclusively that, while the 27.3 wt% sample showed a slightly lower current response, at higher flow rates or concentrations the 27.3 wt% sample should perform the best of all the tested CCEs. Additionally, the 62.5 wt% sample showed a plateau in the current response to higher flow rates at 0.7 V vs. RHE. This plateau can indicate that its maximum accessible electrochemical surface area has been reached.

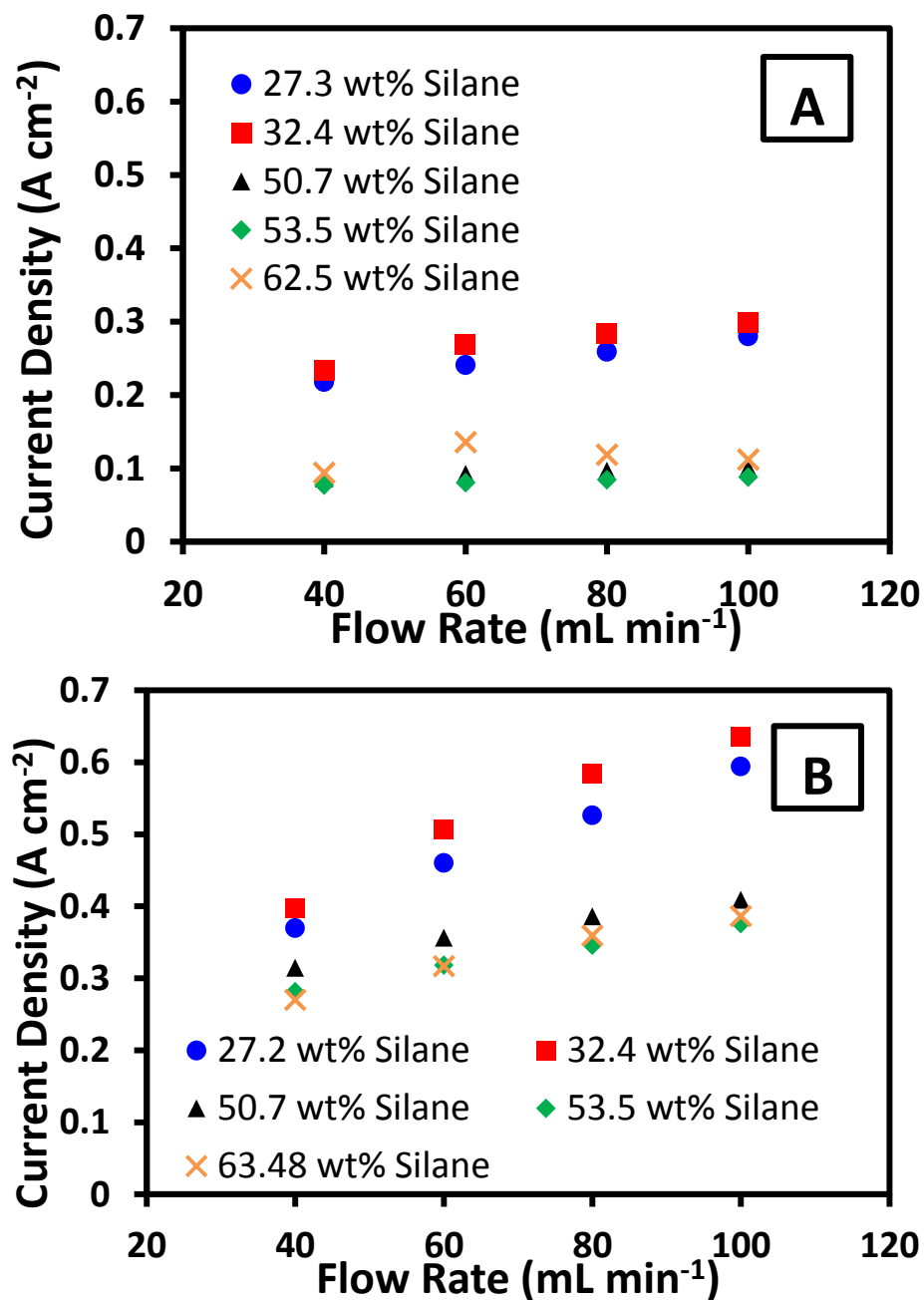


Figure 4-9: Current Trends of CCEs with varied 1N silane content at 0.7 and 1.1 V and varied flow rates. The experiments were performed in 0.2 M CuCl in 2 M HCl anolyte and DI H₂O catholyte both under N₂ atmosphere at 40, 60, 80, and 100 mL min⁻¹ electrolyte flow rate. Scanned from 0.2 to 1.2 V vs. RHE with 5 mV steps and 0.5 s dwell time per step. (A) Current density at 0.7 V vs. RHE (B) Current density at 1.1 V vs. RHE.

Finally, potentiostatic measurements were used to compare the CCE materials. In these measurements the cell was polarized to a constant 0.7 V vs. RHE for extended periods of time. The tests were performed to simulate the operation of the electrolysis cell integrated into the

full thermochemical cycle at the standard DOE target potential of 0.7 V vs. RHE⁴. Generally, there was a constant current response to the potentiostatic holds for extended periods of time. The measurements were also taken at varied flow rates to test the effects of increased flow on the anode's ability to oxidize CuCl. In the absence of external factors such as analyte spoilage or copper crossover, the increased flow rates showed a linear increase in current response.

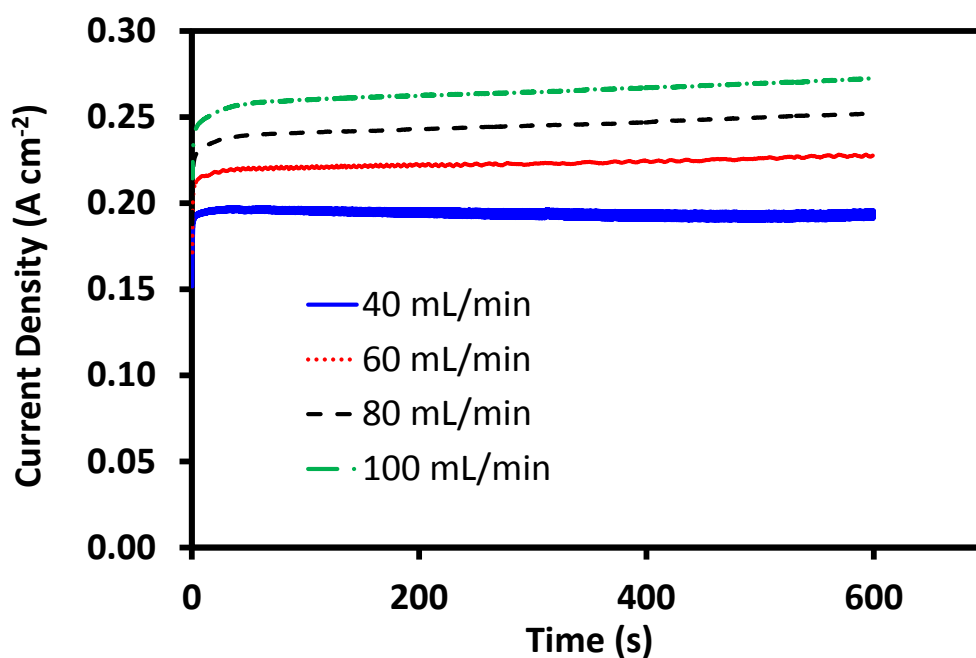


Figure 4-10: Potentiostatic Holds of the 27.18 wt% CCE at 0.7 V. The experiments were performed in 0.2 M CuCl in 2 M HCl anolyte and DI H₂O catholyte both under N₂ atmosphere at 40, 60, 80, and 100 mL min⁻¹ electrolyte flow rate.

Figure 4-10 shows us a normal operation of the full-cell under standard potentiostatic conditions. The four samples with the lowest wt% silane showed relatively stable behavior under the potentiostatic tests. The 62.5 wt% sample showed an inconsistent and low current response when tested. This behavior was consistent with the CuCl analyte spoiling; converting to CuCl₂, reducing the effective concentration of CuCl, and as such was removed from the analysis. At 150 s into the run, the current was recorded as a representative value for the potentiostatic test. These representative points were then plotted with respect to the anolyte flow rate. As seen in Figure 4-2 the trend in current with respect to flow rate also closely resembles that which was observed at 0.7 V vs. RHE during the potential stair step measurements (Figure 4-11). Comparing the current at 0.7 V vs. RHE with respect to analyte

flow rate, the linear regressions of the two data sets show only a 3.5% relative standard deviation indicating that the two current responses to flow rate are equal. There is a slight increase in the overall current observed for the potential stair step data. The increase in current can be explained by increased CuCl concentration from analyte preloading at the CCE surface. In the potentiostatic tests the representative current at 150 s is preceded by consistent operation at 0.7 V vs. RHE, this is not the case for the potential stair step measurements. The lower potentials before the 0.7 V vs. RHE current point is recorded allows for extra CuCl to be built up at the surface of the anode, increasing the CuCl concentration.

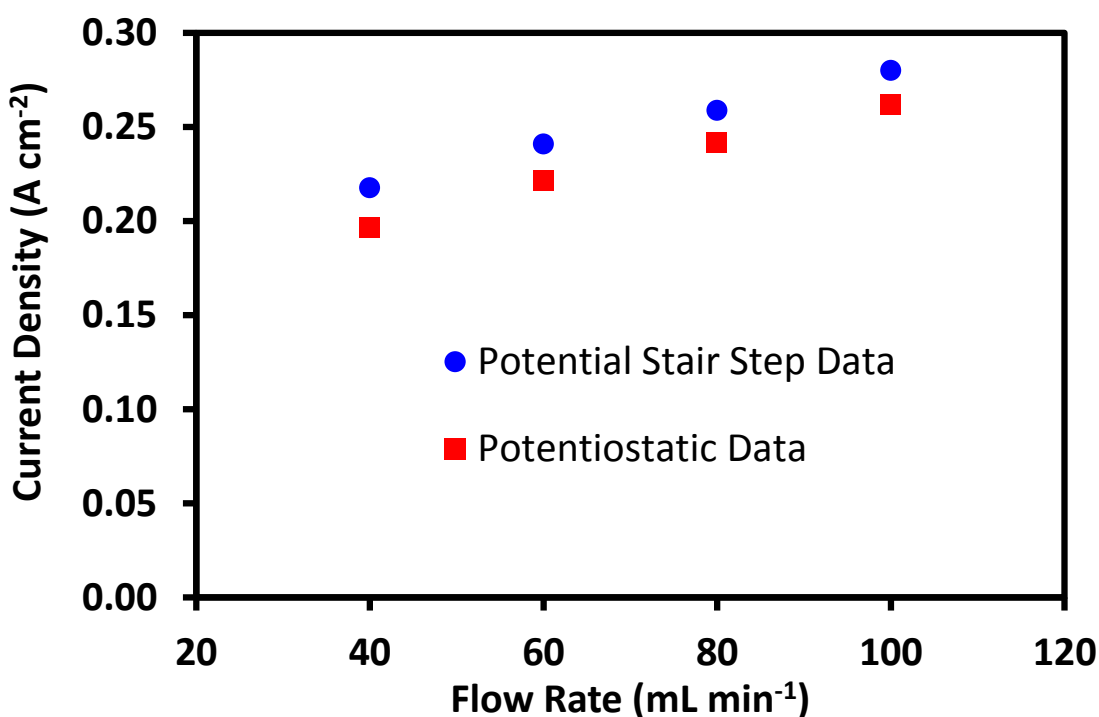


Figure 4-11: Comparison of current response dependence on flow rate at 0.7 V for 27.18 wt% Si CCE. Both experiments were performed in 0.2 M CuCl in 2 M HCl anolyte and DI H₂O catholyte both under N₂ atmosphere at 40, 60, 80, and 100 mL min⁻¹ electrolyte flow rate.

With the exception of the 32.4 wt% silane sample, potentiostatic measurements of all of the samples showed a consistent increase in current with flow rate. The 32.4 wt% silane sample performed well at a flow rate of 40 mL min⁻¹. The representative current recorded corresponded with the current recorded in the potential stair step measurement at the same flow rate and cell potential, 0.188 and 0.233 A cm⁻¹ respectively. During the 40 mL min⁻¹ potentiostatic measurement, at approximately 280 s, a transient current was observed. The

transient current was also observed for the entirety of the subsequent 60 mL min^{-1} measurement (Figure 4-12).

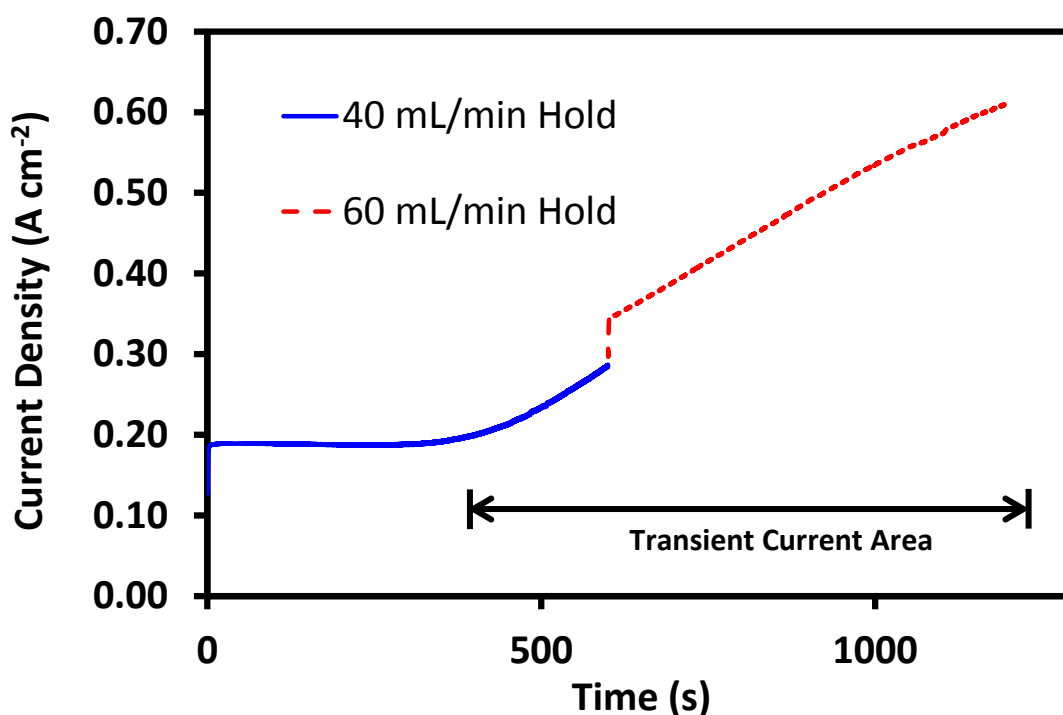


Figure 4-12: Potentiostatic holds at 0.7 V for the 32.4 wt% Si CCE. Experiments performed in 0.2 M CuCl in 2 M HCl anolyte and DI H₂O catholyte both under N₂ atmosphere at 40 and 60 mL min⁻¹ electrolyte flow rate. Copper crossover visible after approximately 400 s.

This current was ascribed to cationic copper crossing the cell membrane and plating as Cu⁰ on the cathode surface (detailed in 5.1). To remove this, an electrode cleaning was performed (detailed in 5.4). This regeneration lowered the cell's current response giving the 32.4 wt% silane an apparent non-linear response to flow rate. The remaining samples did not exhibit transient current and showed reasonable current responses to changes in flow rate. Normalized for total mass of carbon the 27.3 and 32.4 wt% samples still showed the best current response of the four samples tested (32.4 wt% at 40 mL mL⁻¹ only) (Figure 4-13). The 50.7 wt% sample showed a notable increase in its current response with respect to changing flow rate.

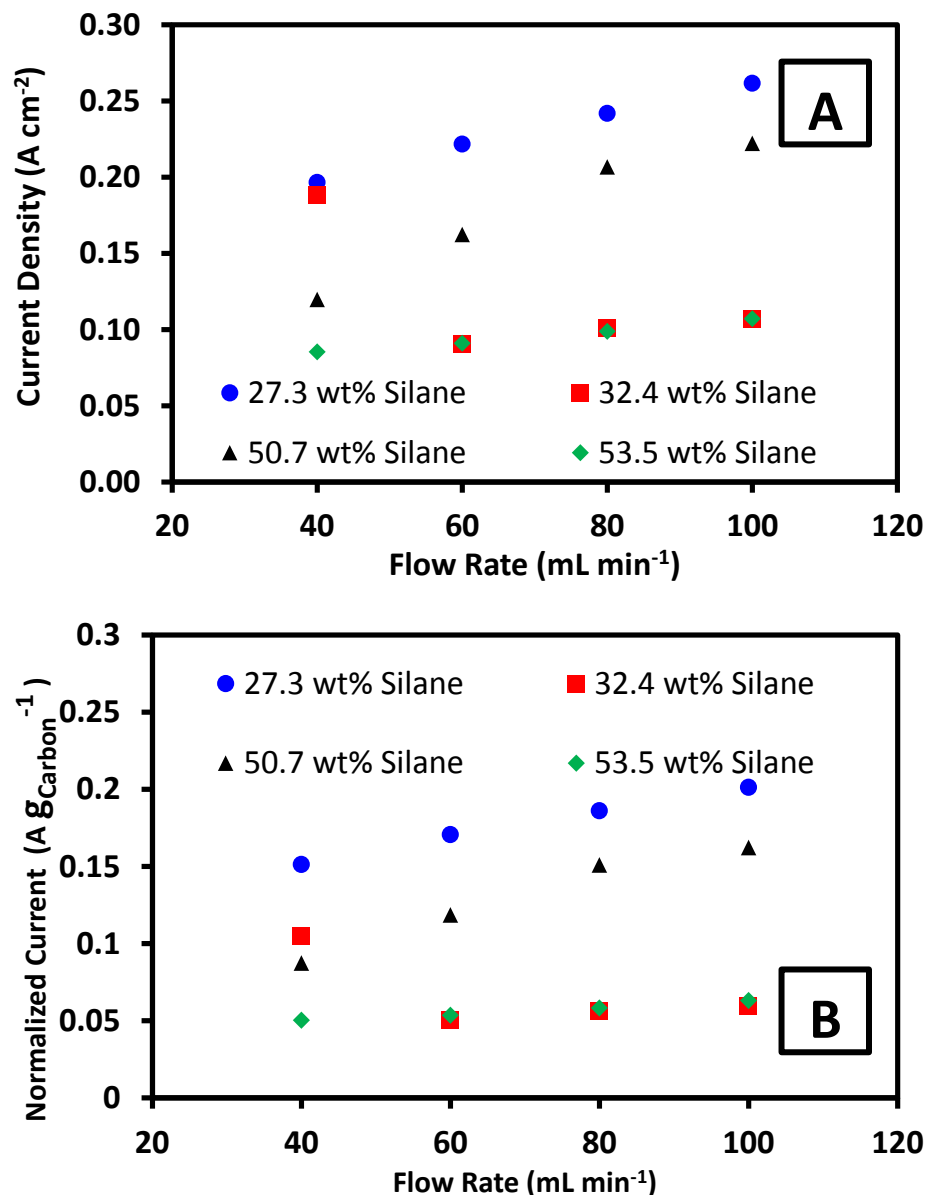


Figure 4-13: Potentiostatic hold current trends of CCEs with varied 1N silane content at 0.7 V and varied flow rates. The experiments were performed in 0.2 M CuCl in 2 M HCl anolyte and DI H₂O catholyte both under N₂ atmosphere at 40, 60, 80, and 100 mL min⁻¹ electrolyte flow rate. Potential held at 0.7 V vs. RHE, current value taken at 150 s. (A) Area specific (B) Carbon mass normalized.

Using the 40 mL min⁻¹ flow rate data the representative current at 0.7 V vs. RHE was related to the amount of silane present in the CCE sample (Figure 4-14). The normalized current showed a slight linear relationship ($r^2 = 0.8178$) between increased silane content and decreased current response. This relationship was expected, carrying forward from our previous half-cell work as well as the work done previously in our group²⁴.

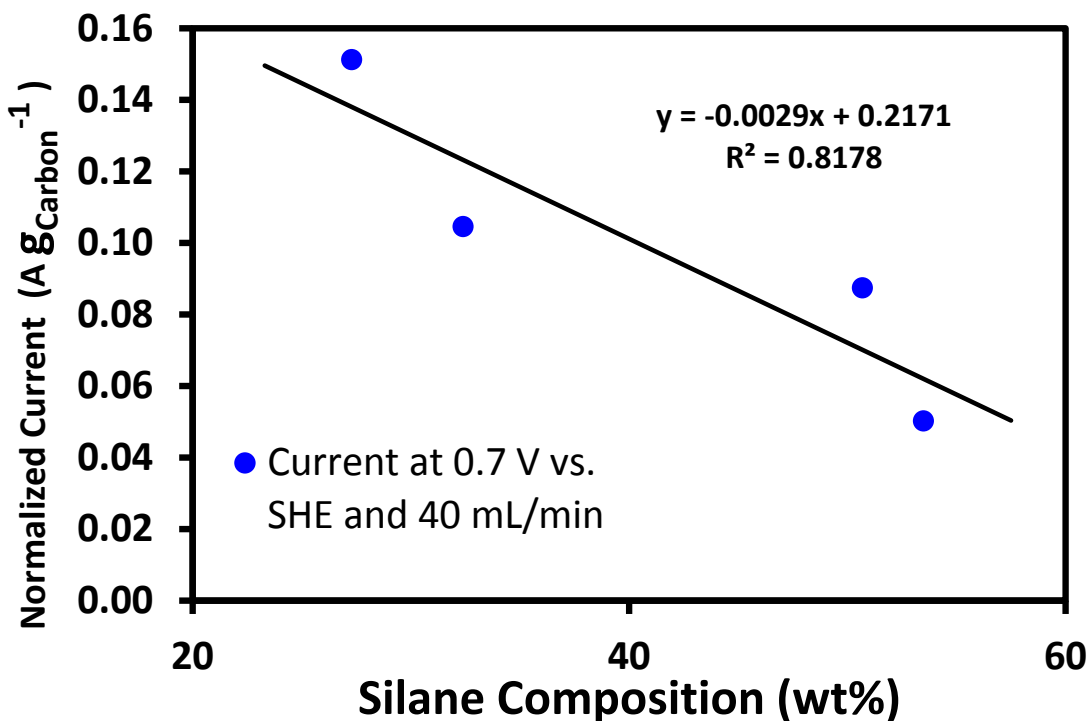


Figure 4-14: Relationship of 1N silane composition to current response in potentiostatic holds taken at 0.7 V. Experiment was performed in 0.2 M CuCl in 2 M HCl anolyte and DI H₂O catholyte both under N₂ atmosphere at 40 mL min⁻¹ electrolyte flow rate.

4.1.2: Results for Varied CCE Loadings (1N)

Beyond varied silane content the effects of total CCE loading were also examined. When normalized for carbon mass the CCEs showed a relationship between silane content and operational current (Figure 4-14). Within this relationship there was significant variance. This variance can potentially be attributed to the different CCE materials varied total mass loading. While the current responses for each of the materials were normalized for mass of carbon present, this does not account for varied utilization of the carbon surface. With increased CCE loading it is possible that areas of the active carbon were not well utilized, lowering the effective electrode surface area per gram of carbon. This is an important factor in the CCE development as high utilization of the materials used is both economical and electrochemically desirable. To examine the effects of increased mass loading, five samples were produced and tested with similar silane compositions and varied total mass loadings. The samples were prepared at 30 ± 3 wt% silane. This target silane content of 30 wt% silane was chosen because

experimentation (Figure 4-13 and Figure 4-14) showed that samples with approximately 30 wt% silane had the best electrochemical performance.

Table 4-2: 1N CCE materials with varied total mass loadings for full-cell electrolysis: compositional information.

| Name | wt% Sample | Mass Loading | g_{Carbon} mass loading | $\text{mMol Si g}_{\text{Carbon}}^{-1}$ |
|---------|------------|--------------|---|---|
| B1P73S1 | 28.83 | 1.11 | 0.8103 | 3.288 |
| B1P73S2 | 27.18 | 1.78 | 1.2962 | 3.393 |
| B1P69S1 | 32.42 | 2.66 | 1.7976 | 4.362 |
| B1P77S3 | 31.11 | 5.24 | 3.6098 | 4.106 |

The samples were produced using the standard method detailed in 2.1.3. Data collected for the 27.18 wt% silane sample was reused from the varied silane content testing. The total mass loading was varied between 1.11 and 5.24 g cm^{-1} with the bulk of the samples mainly produced between 1.11 and 2.61 g cm^{-1} . The range of CCE loadings is dramatically increased from what was tested in 4.1: Results. To account for the silanes altering the CCE's density the mass of carbon was calculated, providing a more standardized idea of the change in CCE loading. The samples compared were not all produced with the intent of varying the mass loading on the CCE but rather the various samples were selected from a stock of samples produced throughout the investigation of the full-cell electrochemical behavior. Two of the samples listed above (B1P73S2 and B1P69S1) were tested previously comparing various silane loadings in chapter 4.1: Results. The two samples were shown to be the best performing of the four materials tested.

4.1.2.1: Physical Electrode Characterization Results

While the electrodes were created with higher ceramic loadings they all behaved similarly under TGA analysis. The samples all underwent the same degradation pattern seen in the samples produced for chapters "3.1: Materials Characterization Result" and "4.1: Results". The samples were all produced with the same ratio of carbon to APTMS with the intent of producing samples of identical composition. The differences in silane loadings (Table 4-2) can be attributed to variance during the gelation and spray coating. To produce samples with a higher total mass loading, larger amounts of carbon and APTMS were gelled and then sprayed onto standard 100 cm^2 sized targets. To produce the samples with lower mass loadings, a standard 400 mg of carbon was gelled and sprayed onto targets of larger sizes.

4.1.2.2: Electrochemical Results for Varied CCE Loadings

Following the procedure developed by the previous half and full-cell testing, the samples were analyzed with; capacitive CV, EIS, LSV, and potentiostatic measurements. In all cases the samples were assessed on the bulk scale and after mass normalization to observe the effects of higher CCE content on the overall electrode performance as well as utilization of the specific carbon surface area.

During capacitive CV measurements, the samples showed an expected increase in surface area with the increased CCE loading (Figure 4-15). The three samples with the lowest CCE loading all showed a normal behavior in their charging and discharging. The fourth sample with the highest CCE loading showed a much more gradual discharging during the cathodic sweep of the CV. Additionally we observed a large peak at approximately 0.4 V vs. RHE on the cathodic sweep. This was attributed surface oxide reduction from an incomplete degassing of the catholyte prior to operation.

Once the samples were normalized for the mass of CCE used the capacitive surface area became much more consistent. There was an apparent decrease in the mass normalized surface area with increased CCE loading.

EIS was performed on the four samples (Figure 4-16). In the high frequency region of the spectra, the three samples with the lowest loadings show a distinct similarity with nearly parallel lines and effectively no Warburg region. This is expected as they have nearly the same silane content and their total loadings fall within a 1 mg cm^{-2} range ($0.8\text{-}1.8 \text{ mg cm}^{-2}$). The 3.6 mg cm^{-2} sample showed a Warburg region of 0.02Ω and a flatter slope overall. This indicated decreased ionic and electronic conductivity.

The capacitance measurements showed a similar trend to what was seen in the capacitive CV measurements (Figure 4-17). As the mass of carbon on the electrode was increased, the maximum capacitance also increased. After normalizing for the mass of carbon present we again see a similar trend in capacitance values when compared with the mass normalized capacitive CV measurements. The three lower loading silanes ($0.8 - 1.8 \text{ mg cm}^{-2}$) showed similar maximum capacitance values while the higher loading CCE showed a lower maximum capacitance value. The 0.8 mg cm^{-2} sample showed the highest mass normalized capacitance indicating the best utilization of the carbon surface. The better utilization of the

carbon surface is expected as the sample has the least silane present to block the carbon's micro-porous structure. The 1.8 mg cm^{-2} sample showed the steepest initial slope indicating that it had a higher ionic conductivity, charging its surface the fastest. This significantly higher ionic conductivity was made with a small loss in the overall utilization of the carbon surface indicating that the 1.8 mg cm^{-2} CCE should perform better than the 0.8 mg cm^{-2} sample.

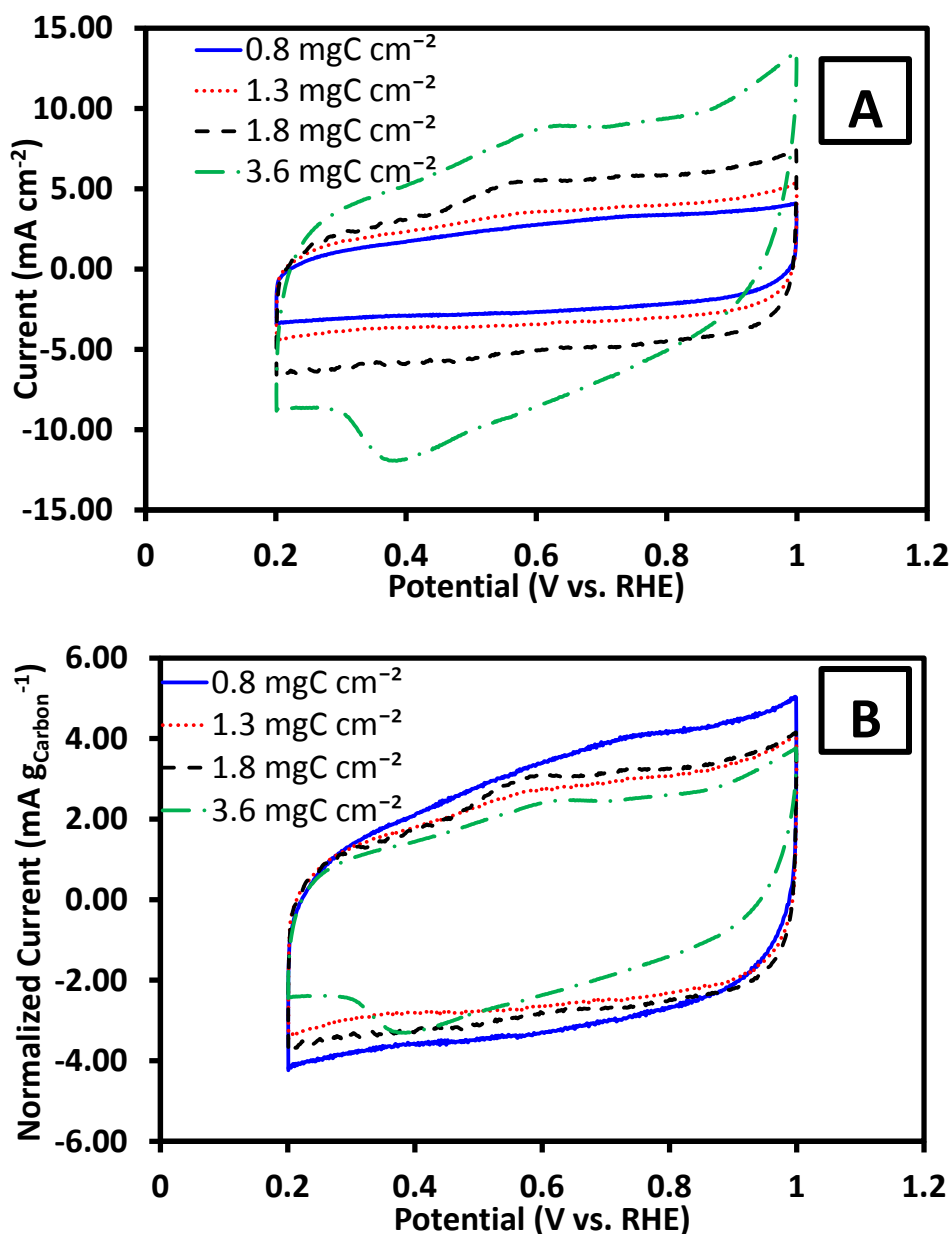


Figure 4-15: Capacitive CV of CCE materials with $30 \pm 3\%$ 1N silane loading and varied total CCE mass loadings. 10 mV s^{-1} scan rate from 0.2 to 1.0 V vs. RHE. Current normalized for geometric SA and for mass of carbon. In 2 M HCl under N_2 atmosphere at 60 mL min^{-1} analyte flow rate. (A) Area specific (B) Carbon mass normalized.

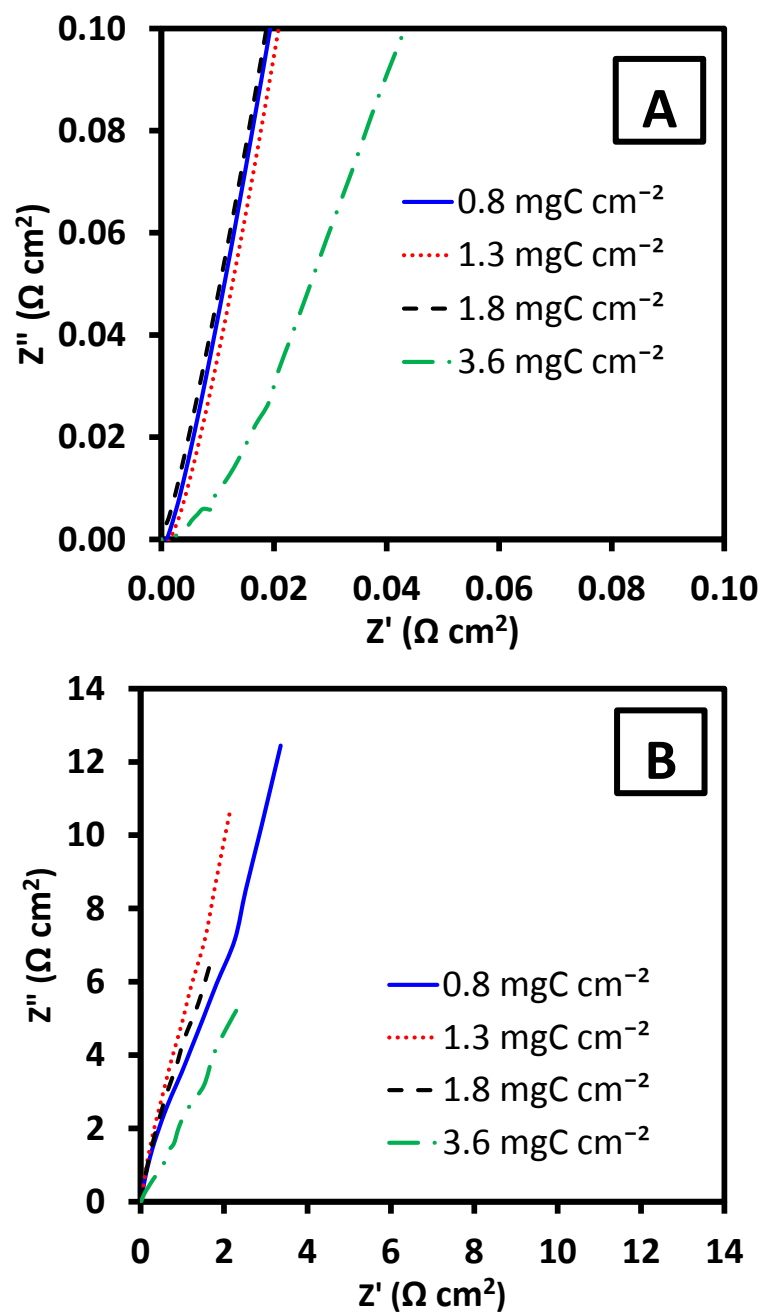


Figure 4-16: Nyquist plots of CCE's with $30\pm 3\%$ 1N silane content and varied total mass loadings. Experiments were performed in 2 M HCl anolyte under N_2 atmosphere at 60 mL min^{-1} anolyte flow rate and 25 mL min^{-1} H_2 gas provided to the cathode. (A) Nyquist plot (B) High frequency region.

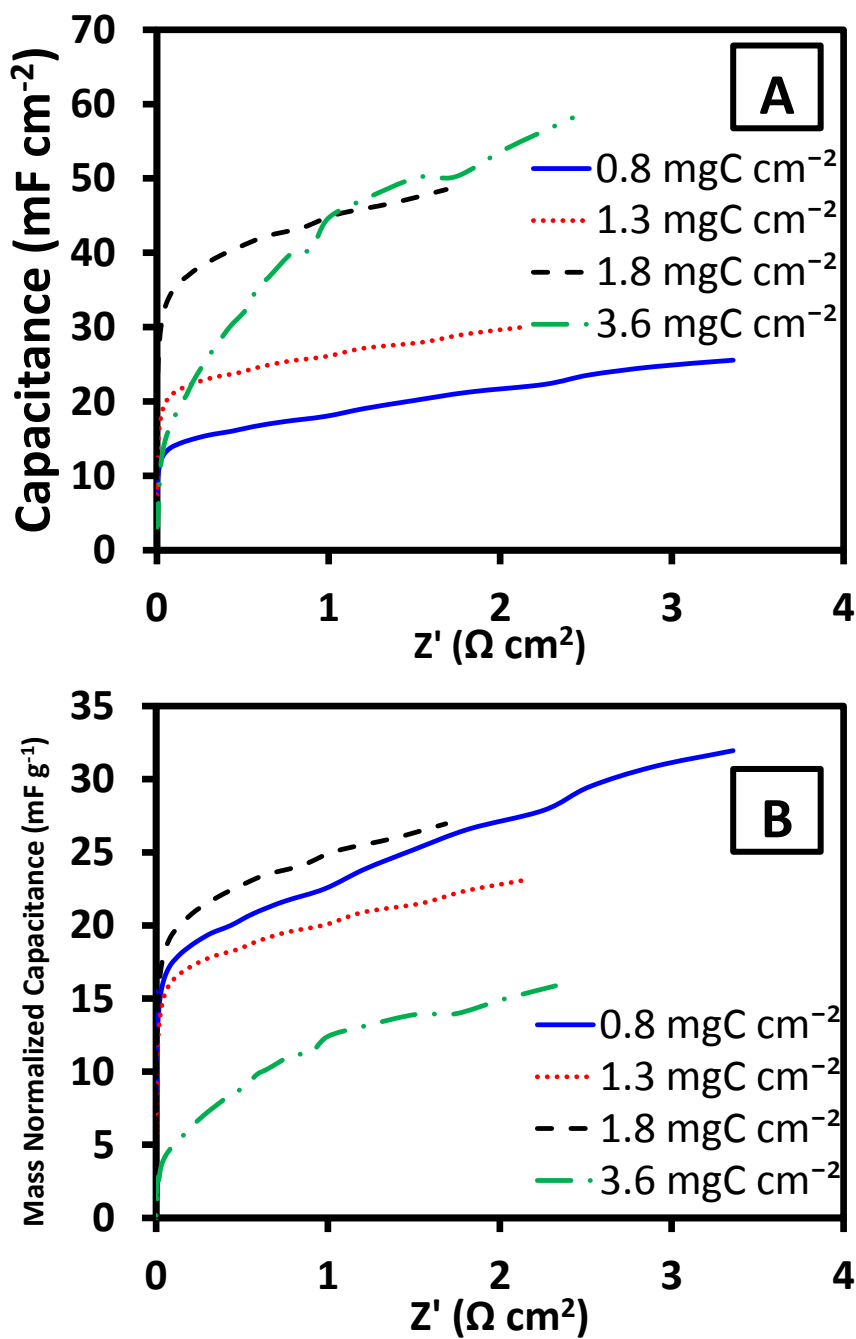


Figure 4-17: Capacitance plots of 30±3% 1N silane content CCEs with varied total mass loadings. Experiment was performed in 2 M HCl anolyte under N_2 atmosphere at 60 mL min^{-1} anolyte flow rate and 25 mL min^{-1} H_2 gas provided to the cathode. (A) Area specific capacitance (B) Mass of carbon normalized.

The samples all showed a standard behavior when potential stair step measurements were taken (Figure 4-18). In comparing the measurements taken at 60 mL min^{-1} flow rate, the samples all showed similar onset potentials though there was a difference in initial current response. Again, the three lowest loading samples showed very similar behavior while the 3.6 mg cm^{-2} sample showed a much slower current response (Figure 4-18). Other than the slower current response of the 3.6 mg cm^{-2} sample, the samples showed a smooth current response with no indication of other faradaic processes occurring.

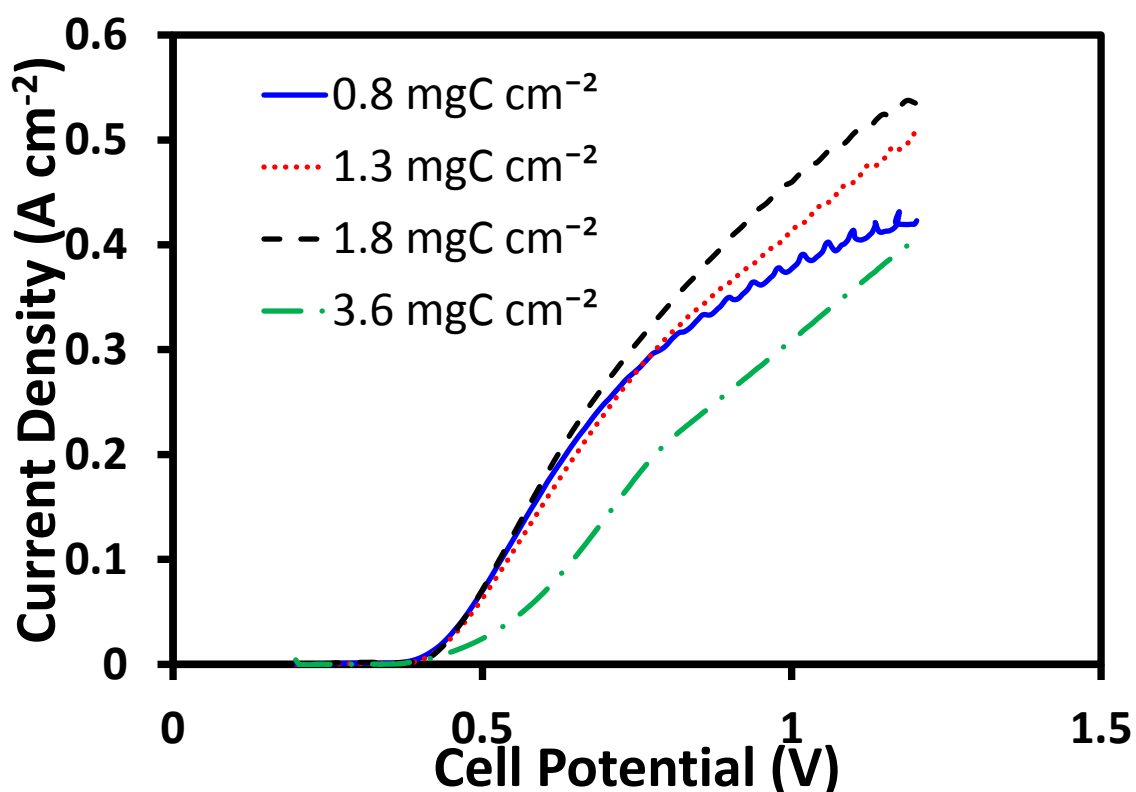


Figure 4-18: Potential stair step measurements of CCEs with $30 \pm 3\%$ 1N silane composition and varied total CCE mass loadings. Scanned from 0.2 to 1.2 V with 5 mV steps and 0.5 s dwell time per step. Experiment performed in 0.2 M CuCl in 2 M HCl anolyte and DI H₂O catholyte both under N₂ atmosphere at 60 mL min^{-1} electrolyte flow rate.

Similarly to the capacitance plots (Figure 4-17), when potential vs. flow rate is compared the three lowest mass samples performed similarly and better than the $3.6 \text{ mg}_{\text{Carbon}} \text{ cm}^{-2}$ sample. The similar current responses are much more pronounced at 0.7 V vs. RHE. In addition to this information Figure 4-18 and Figure 4-19 show that the $1.8 \text{ mg}_{\text{Carbon}} \text{ cm}^{-2}$ sample performed the best across all measurements. From the plots of current vs. flow rate

(Figure 4-19) it is apparent that all of the samples show a linear increase in current response with flow rate.

During the potentiostatic measurements both the 0.8 and 1.8 $\text{mg}_{\text{Carbon}} \text{cm}^{-2}$ samples showed evidence of copper crossover. The samples were treated in situ to remove the plated copper and the runs were continued. After the plated copper was removed there was a characteristic decrease in performance. Additionally, for the 0.8 $\text{mg}_{\text{Carbon}} \text{cm}^{-2}$ sample there was a hardware error that prevented the acquisition of data for flow rates above 60 mL min^{-1} so the points were not included in the analysis. The current recorded at 150 s into the potentiostatic hold measurements was taken to be representative of the entire measurement. At this time in the potentiostatic holds there was no indication of copper crossover occurring so the values can be considered representative of only the oxidation of CuCl and the production of H_2 gas. Both the 1.3 and 3.6 $\text{mg}_{\text{Carbon}} \text{cm}^{-2}$ samples showed a linear increase in current with the increased flow rate (Figure 4-20). This increase is consistent with the data taken from the potential stair step measurements. As with the potential stair step measurements the three lower loading samples (0.8-1.8 $\text{mg}_{\text{Carbon}} \text{cm}^{-2}$) outperformed the higher 3.6 $\text{mg}_{\text{Carbon}} \text{cm}^{-2}$ sample by a considerable margin during the 40 mL min^{-1} flow rate measurement. Beyond the 40 mL min^{-1} measurement, the 0.8 and 1.8 $\text{mg}_{\text{Carbon}} \text{cm}^{-2}$ samples showed a decrease in current due to copper crossover. The 1.3 $\text{mg}_{\text{Carbon}} \text{cm}^{-2}$ sample also showed a steeper increase with increased flow rate when compared with the 3.6 $\text{mg}_{\text{Carbon}} \text{cm}^{-2}$ sample. While there is a larger surface area associated with the 3.6 $\text{mg}_{\text{Carbon}} \text{cm}^{-2}$ sample it has been shown through the EIS measurements that there is a much lower conductivity in the sample and a lower utilization of the carbon surface area. These two shortcomings are likely what contributed to the lower overall current response from the sample.

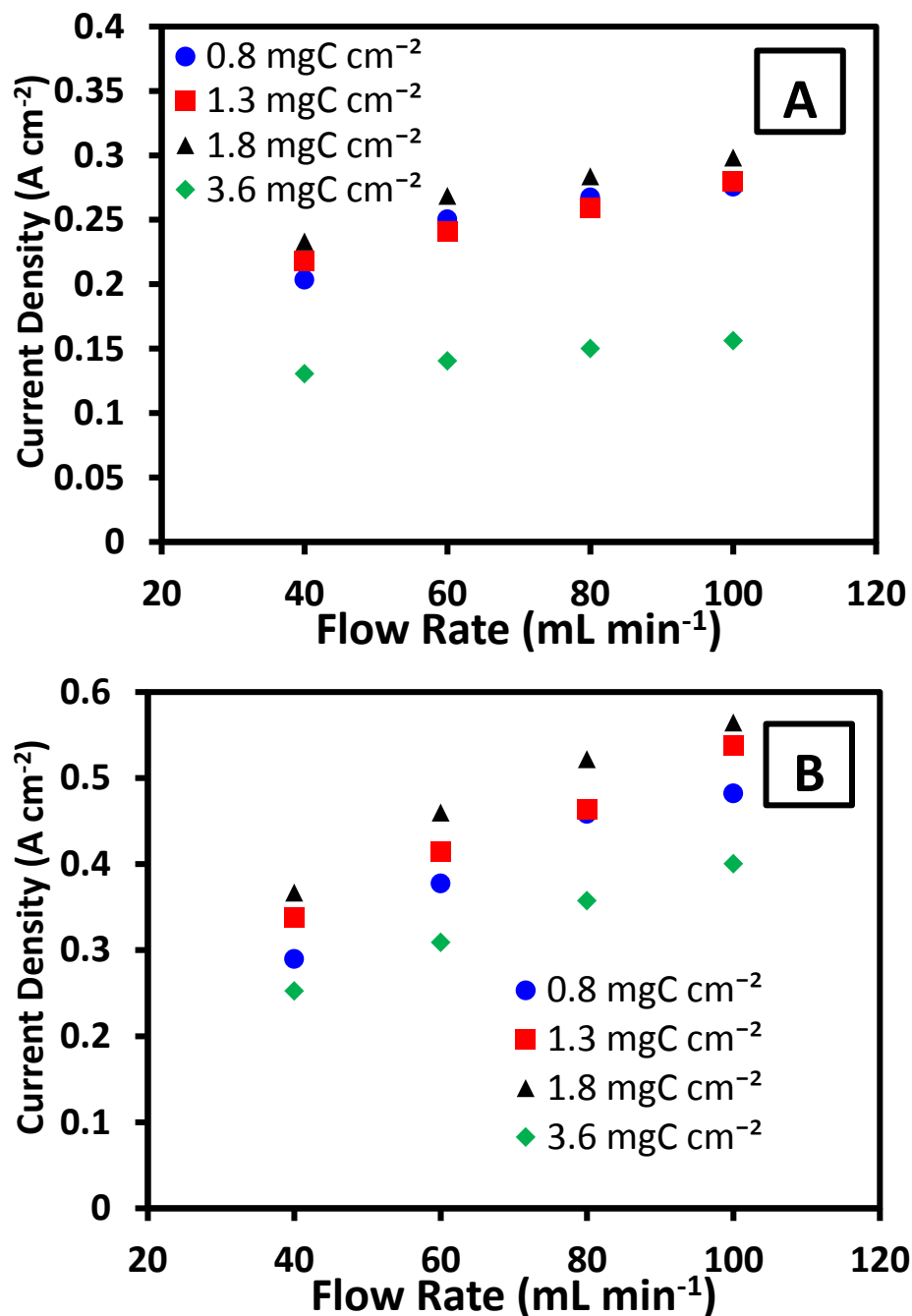


Figure 4-19: Current Trends of CCEs with 30±3% 1N silane composition and varied total CCE mass loading at 0.7 and 1.1 V and varied flow rates. Tests performed in 0.2 M CuCl in 2 M HCl anolyte and DI H₂O catholyte both under N₂ atmosphere at 40, 60, 80, and 100 mL min⁻¹ electrolyte flow rate. Scanned from 0.2-1.2 V vs. RHE with 5 mV steps and 0.5s dwell time per step. (A) Current density at 0.7 V vs. RHE (B) Current density at 1.1 V vs. RHE.

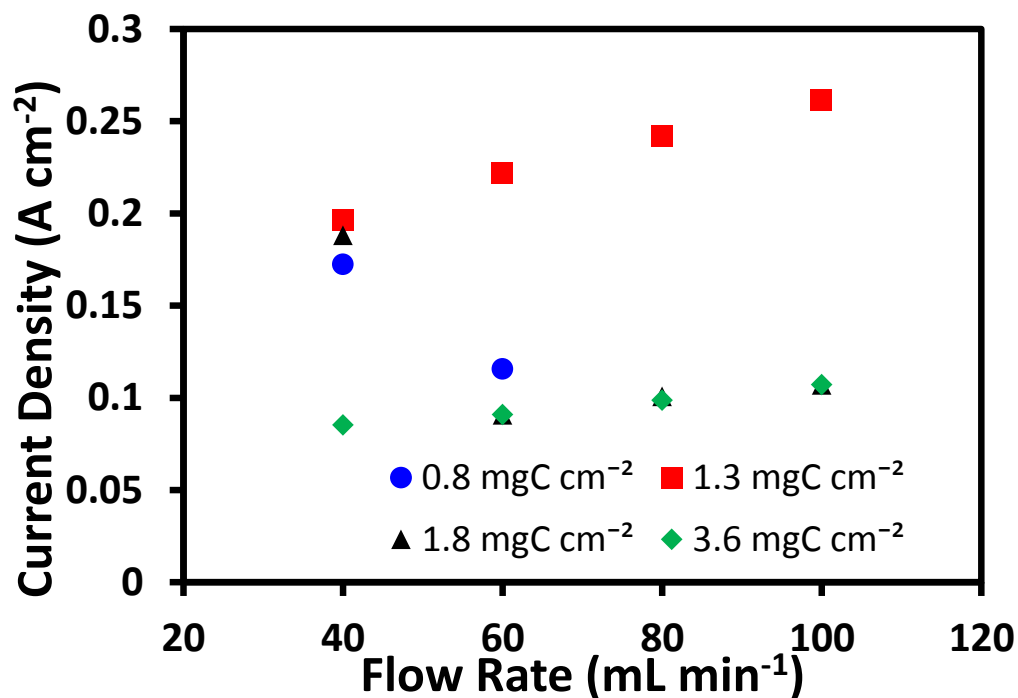


Figure 4-20: Potentiostatic hold current trends of CCEs with 30±3% 1N silane composition and varied total CCE mass loadings at 0.7 V vs. RHE and varied flow rates. Tests performed in 0.2 M CuCl in 2 M HCl anolyte and DI H₂O catholyte both under N₂ atmosphere at 40, 60, 80, and 100 mL min⁻¹ electrolyte flow rate. Potential held at 0.7 V, current value taken at 150 s.

The current response at an electrolyte flow of 40 mL min⁻¹ was used to compare the various samples. This measurement was chosen as there was no indication of copper crossover occurring while or before the measurement was taken. Figure 4-21 compares the current during the 40 mL min⁻¹ potentiostatic holds to the total mg cm⁻² loading of ceramic carbon. The three samples with the lowest loading (0.8-1.8 mg_{Carbon} cm⁻²) show little deviation in current response from one another with them all out performing the 3.6 mg_{Carbon} cm⁻² sample (Figure 4-21).

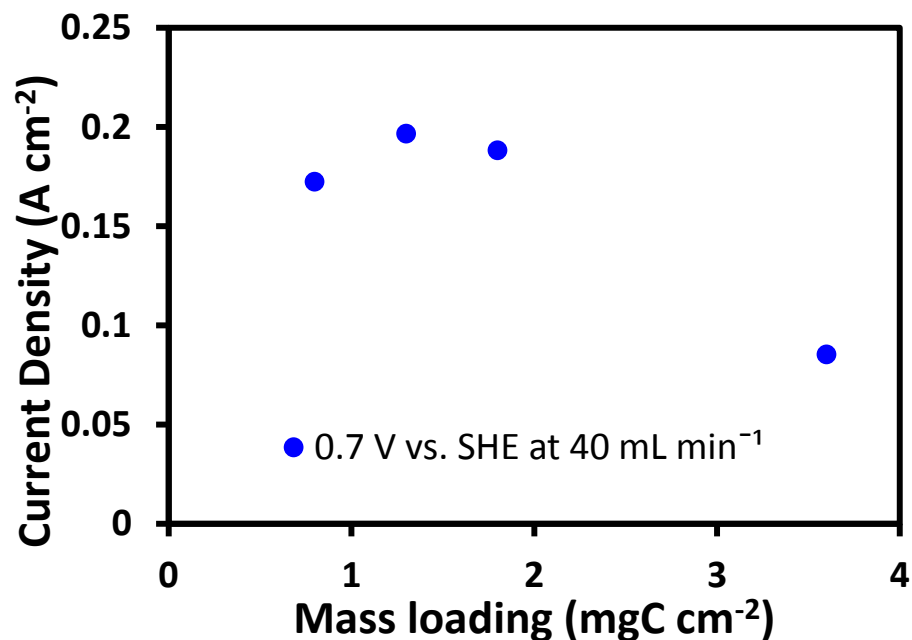


Figure 4-21: Relationship of total CCE mass loading to current response in potentiostatic holds taken at 0.7 V. Collected in 0.2 M CuCl in 2 M HCl anolyte and DI H₂O catholyte both under N₂ atmosphere at 40 mL min⁻¹ electrolyte flow rate.

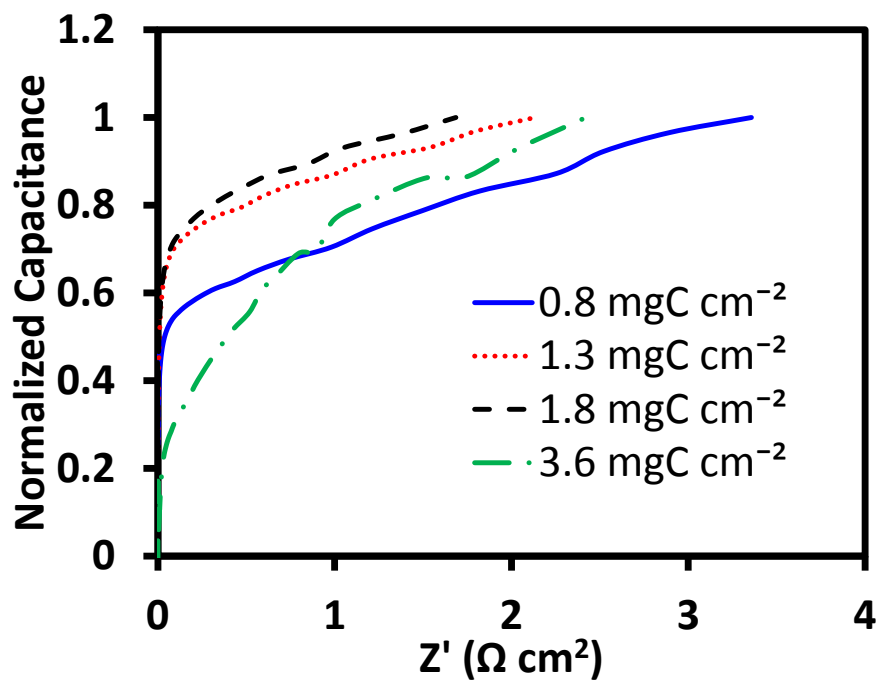


Figure 4-22: Normalized capacitance plot of 30±3% 1N silane content CCEs with varied total mass loadings. Tests performed at 0 V vs. OCV in 2 M HCl anolyte under N₂ atmosphere at 60 mL min⁻¹ anolyte flow rate and 25 mL min⁻¹ H₂ gas provided to the cathode.

4.1.3: Results for Varied Silanes

Concluding the analysis of the effects of amine functionalized ceramic carbon electrodes the effects of varying the silane type at similar molar silane loadings were examined. By using silane monomers containing additional amine functionalities the resistivity associated with the increased silane content can be standardized while still varying the amine functional group amounts. This was intended to show the increased conductivity only from the increased amine functional groups. The same 1N, 2N, and 3N silanes (Figure 1-10) as used in the initial half-cell measurements in chapter 3 were used here. This allows us to also compare our trends in half cell testing with those in the full-cell environment. The 1N silane information discussed in section 4.1 will be compared with 2N and 3N data discussed in this section to provide a comparison of the effects of varied silanes on CuCl electrolysis.

4.1.3.1: Physical Electrode Characterization Results

Both the 2N and 3N materials were prepared with the intent to create CCE materials with similar molar loadings of silane and mass loadings of carbon as were recorded for 1N CCEs in 4.1: Results three samples were produced for both the 2N and 3N CCE materials. The sol-gels were prepared in the standard method outlined in section 2.1.1 and spray coated as outlined in 2.1.3. The gels were later characterized by TGA to determine their bulk silane content.

Table 4-3: 2N and 3N CCE materials for full-cell electrolysis: compositional Information.

| Name | Silane | wt% Sample | Mass Loading | g_{Carbon} mass loading | $\text{mmol Si } g_{\text{Carbon}}^{-1}$ |
|---------|--------|------------|--------------|----------------------------------|--|
| B1P81S1 | 2N | 42.49 | 2.59 | 1.49 | 4.81 |
| B1P81S2 | 2N | 46.63 | 2.09 | 1.11 | 5.70 |
| B1P83S1 | 2N | 67.84 | 4.21 | 1.35 | 13.76 |
| B1P85S2 | 3N | 57.40 | 2.26 | 0.96 | 6.86 |
| B1P85S1 | 3N | 66.27 | 1.85 | 0.62 | 10.01 |
| B1P85S3 | 3N | 69.86 | 1.84 | 0.56 | 11.80 |

Under flowing air in the TGA the 2N and 3N CCE samples showed a similar decomposition pattern to the 1N CCE materials tested previously. The samples were determined to have silane loadings between 4.81 and 13.76 $\text{mmol } g_{\text{Carbon}}^{-1}$. This molar loading is in good agreement with the 1N samples produced which had a silane loading range of 3.28 to 15.14 $\text{mmol } g_{\text{Carbon}}^{-1}$. In keeping a similar range of silane loadings the electrical resistance from the Si-O-Si backbone can be kept approximately constant. The constant electrical resistance and silane loading allows for the analysis of the silane functionalities independent of other variables. The mass of carbon in

the CCE material was also kept in a standard range to avoid changes in the electrochemical activity as detailed in 4.2.

The 2N materials showed a similar change in morphology as the 1N materials as the molar loading of the silane was increased. With the increased silane content there appears to be a decrease in the overall homogeneity of the 2N samples at the 2500x magnification (Figure 4-24). The overall coating was quite similar at the 100x magnifications, both within the 2N samples and when compared to the 1N samples. The 3N materials began to deviate from the previously seen patterns with increased silane content (Figure 4-25). At 2500x magnification there is less of an apparent decrease in surface homogeneity with increased silane content. In regards to this, the 3N silanes all have molar loadings above the median values for the 1N and 2N samples, and are spread over a narrower range of silane loadings. This increased silane content and decreased range would make it difficult to discern changes in the surface morphology. At the 100x magnification, small amounts of the CFP backing are visible and the CCE material can be seen coating individual fibers. Similar to the 1N and 2N materials, the 3N materials still show the similar coating patterns at 100x magnification. This indicates that although there is a lighter coating on the CFP backing there is still the same relatively even distribution of the ceramic carbon material for all of the 1N, 2N, and 3N CCE samples. In addition to the SEM images taken of all 1N, 2N, and 3N electrodes TEM images were taken of the 1N and 2N materials to confirm their homogeneity of their structures on a nanometer scale (Figure 4-23). The materials imaged were largely indistinguishable from each other showing that the different silane precursors did not alter the CCEs structures on a nanometer scale.

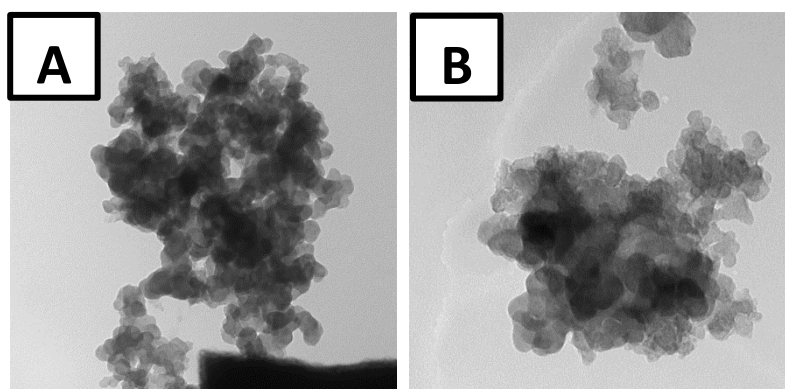


Figure 4-23: TEM Images of B1P69S1 1N material (A) and B1P83S1 2N material (B) at 92000 and 180000x magnification respectively.

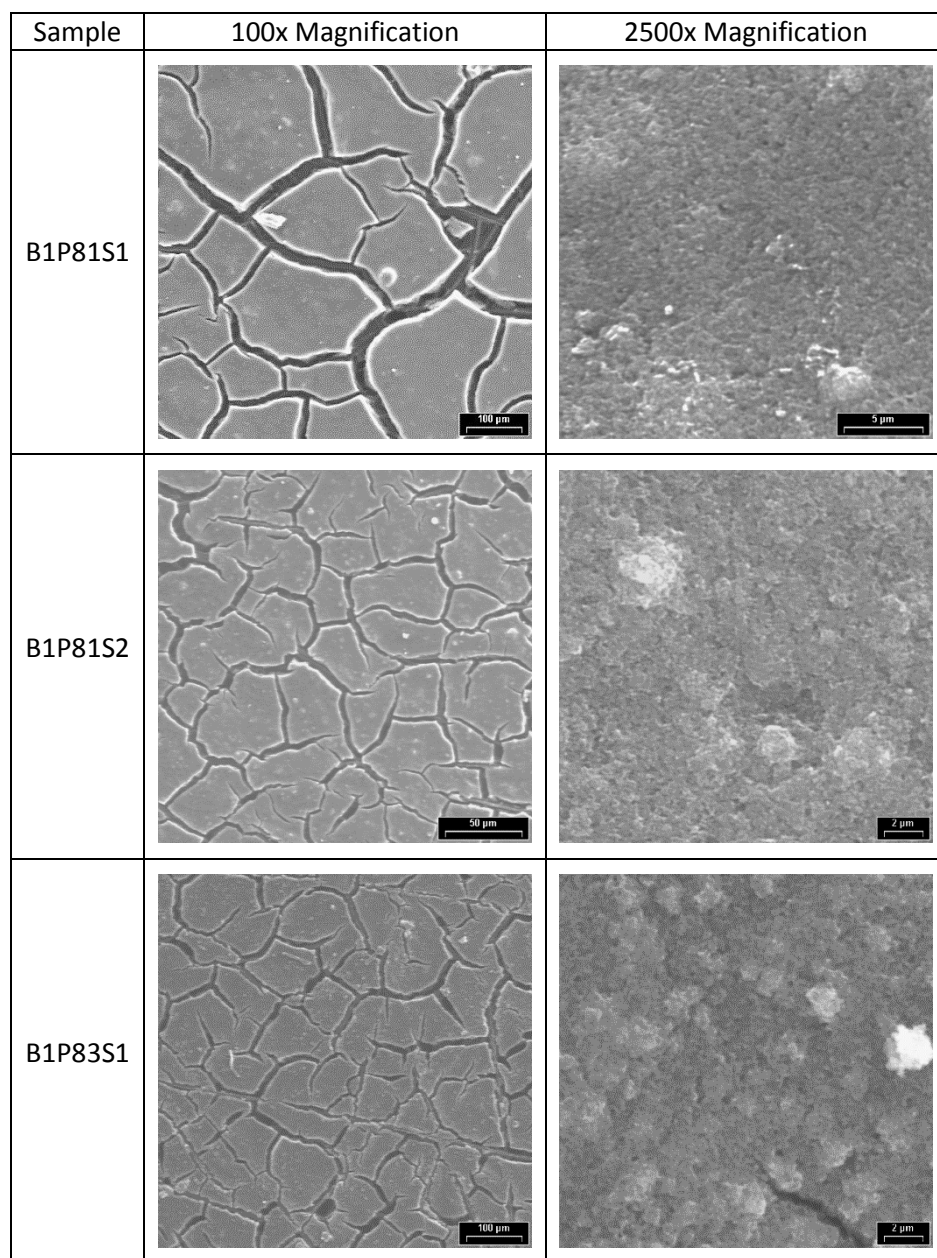


Figure 4-24: SEM images taken of CCE samples B1P81S1, B1P81S2, and B1P83S1 at 100 and 2500 x magnification

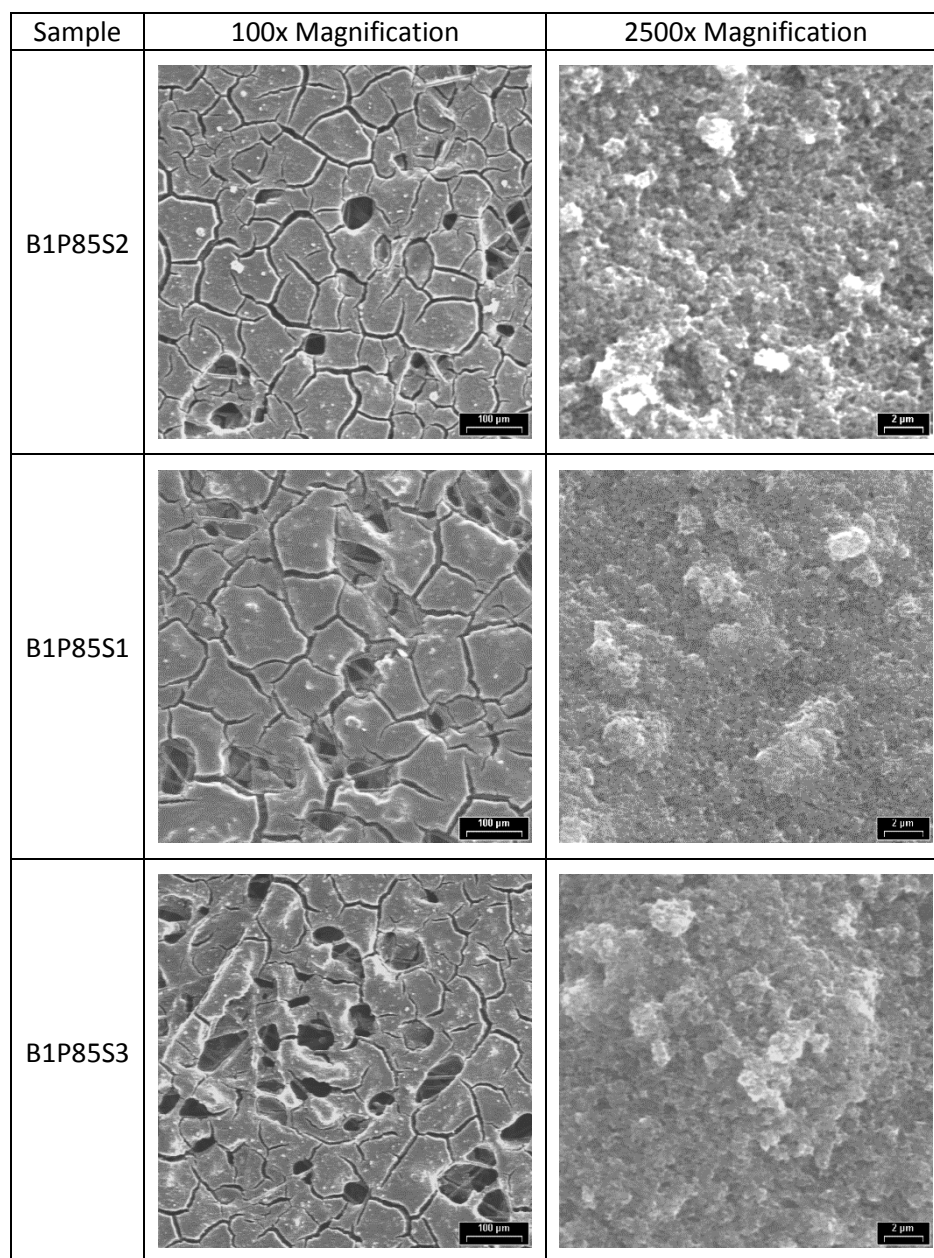


Figure 4-25: SEM images taken of CCE samples B1P85S2, B1P85S1, and B1P85S3 at 100 and 2500 x magnification.

4.1.3.2: Electrochemical Results for 2N Materials

The 2N materials were examined separately from the 3N materials to investigate the effects of the different silanes. In the 2N silane we see a longer amine functionalization on the silane backbone. This longer pendant arm can potentially affect the electrochemically active

surface area of the carbon electrode. The CCE materials were produced to have a range of silane concentrations similar to those produced with the 1N silane. The 1N materials had a range of 3.4 to 15.1 mmol Silane $\text{g}_{\text{Carbon}}^{-1}$. The 2N CCE materials were produced with a silane concentration range of 4.8 to 13.8 mmol Silane $\text{g}_{\text{Carbon}}^{-1}$.

Cyclic voltammetry was performed in the absence of CuCl to assess the capacitive surface area of the three CCE materials (Figure 4-26). There was little difference in the surface area of the 42 and 47 wt% silane CCEs. This was expected as there was little difference between their carbon and silane loadings. The 68 wt% silane sample had a much larger absolute capacitive surface area (Figure 4-26 (A)). This was also expected as the carbon loading was much larger than what was present in the 42 and 47 wt% silane samples. Normalizing for the carbon loading on each of the CCEs the utilization of the carbon was examined (Figure 4-26 (B)). A trend in the surface areas of the CCEs appeared, with increased silane content the utilization of the carbon surface area appears to increase dramatically. This indicates that the available carbon surface is being better utilized at higher silane contents. This dramatic correlation was not seen in the 1N samples tested in chapter 4.1 (Figure 4-4).

EIS was also used to examine the conductivity of the CCE materials. In this case we can expect to see generally higher conductivities from the samples given the presence of additional charged amine functionalities (Figure 4-27). The Nyquist plot of the 47 and 68 wt% silane samples shows that the 68 wt% sample has a shorter Warburg region. The shorter Warburg region of the Nyquist plot indicated that the sample has a higher overall conductivity.

Capacitance plots were also generated to re-examine the capacitive surface area as well as the conductivity of the samples (Figure 4-28). We see similar indications of the carbon surface area when compared to the capacitive CV measurements taken (Figure 4-26). In the raw capacitance plot the 68 wt% silane has a much higher plateau level indicating a higher overall surface area (Figure 4-28 (A)). When normalized for the mass of carbon present in the sample we see a smaller overall increase, but the 68 wt% 2N sample still shows a higher normalized capacitive surface area (Figure 4-28 (B)). The steepness of the initial charging area of the capacitance plot also shows that the 68 wt% 2N sample has a higher overall conductivity than the 47 wt% 2N sample. Conductivity can be shown as a steeper slope in initial charging area of capacitance plots. Normalizing the maximum capacitance values to 1 allows for a clearer picture of the initial slope of the capacitance plots and thus the conductivity (Figure 4-28 (C)). While the

68 wt% sample appears to have a lower conductivity, it can be attributed to the larger absolute conductivity altering the samples. The 42 wt% sample can be seen to have a higher conductivity than the 47 wt% sample; this is consistent with the 47 wt% samples shorter Warburg region seen in the impedance plots (Figure 4-27).

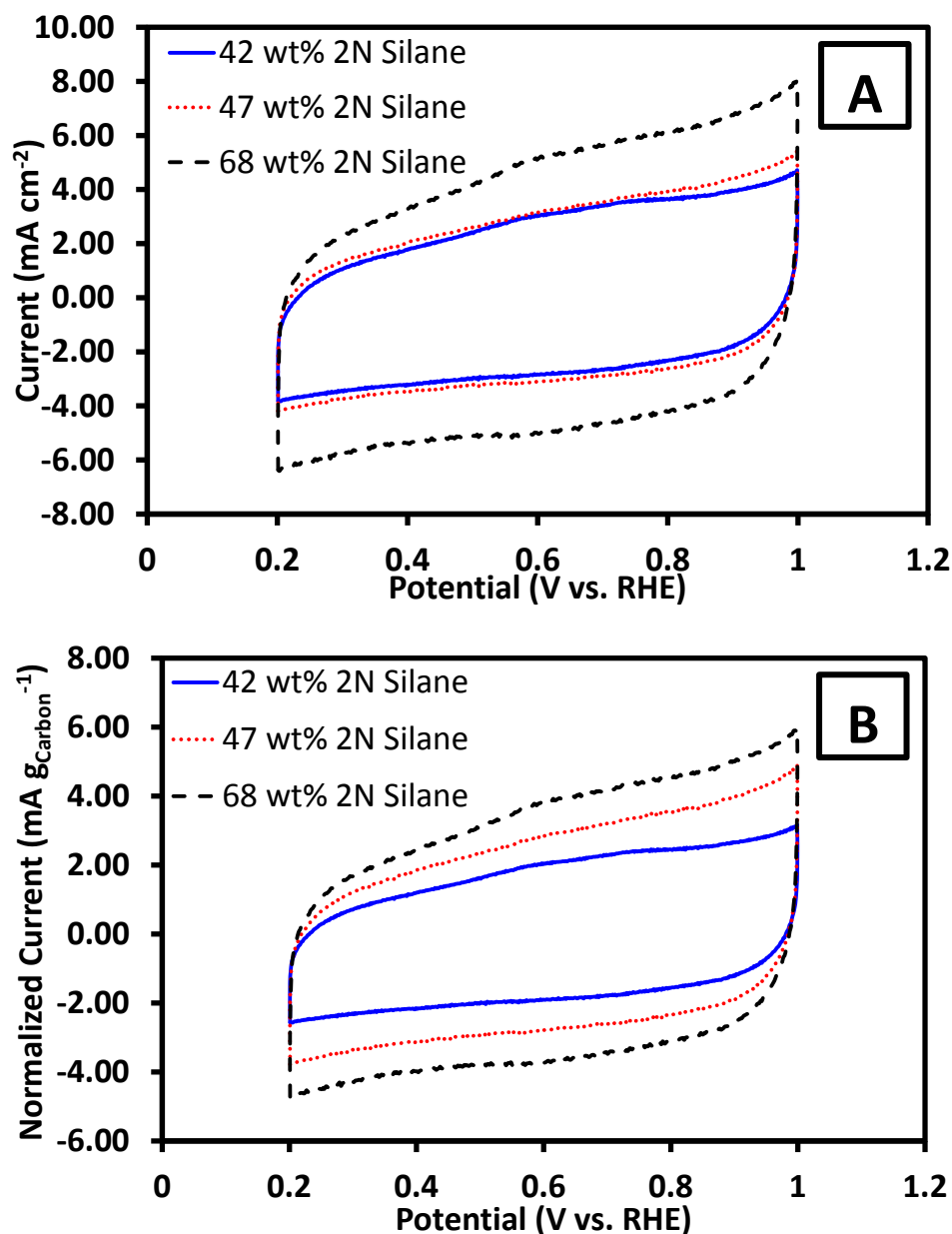


Figure 4-26: Capacitive CV of CCE materials with varied 2N silane loading. 10 mV s⁻¹ scan rate from 0.2 to 1.0 V vs. RHE. Current normalized for geometric SA and for mass of carbon. In 2 M HCl under N₂ atmosphere at 60 mL min⁻¹ anolyte flow rate. (A) Area specific (B) Carbon mass normalized.

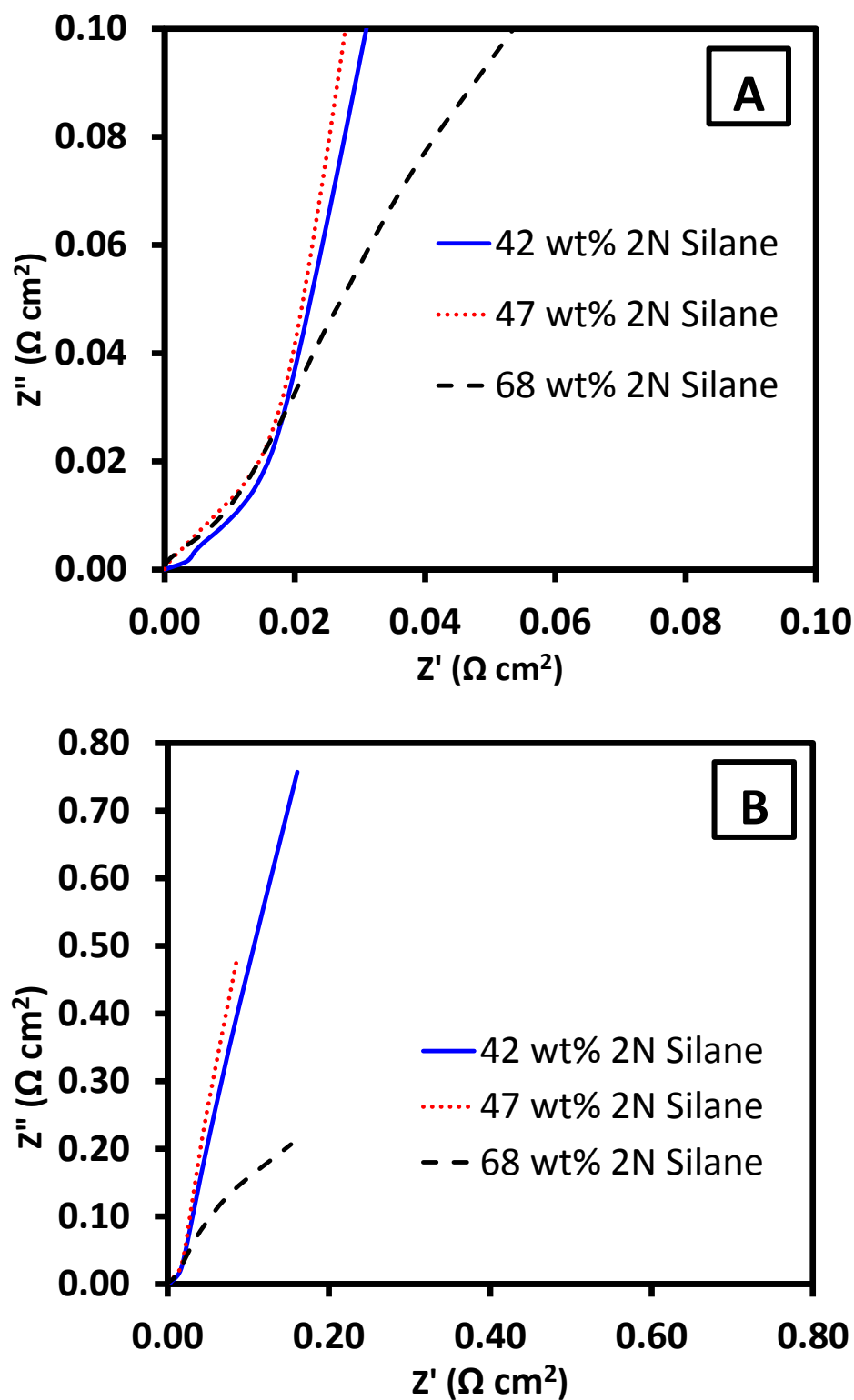


Figure 4-27: Nyquist plots of varied 2N silane content CCEs. Tests performed at 0 V vs. OCV in 2 M HCl anolyte under N_2 atmosphere at 60 mL min^{-1} anolyte flow rate and 25 mL min^{-1} H_2 gas provided to the cathode. (A) Nyquist plot (B) High frequency region.

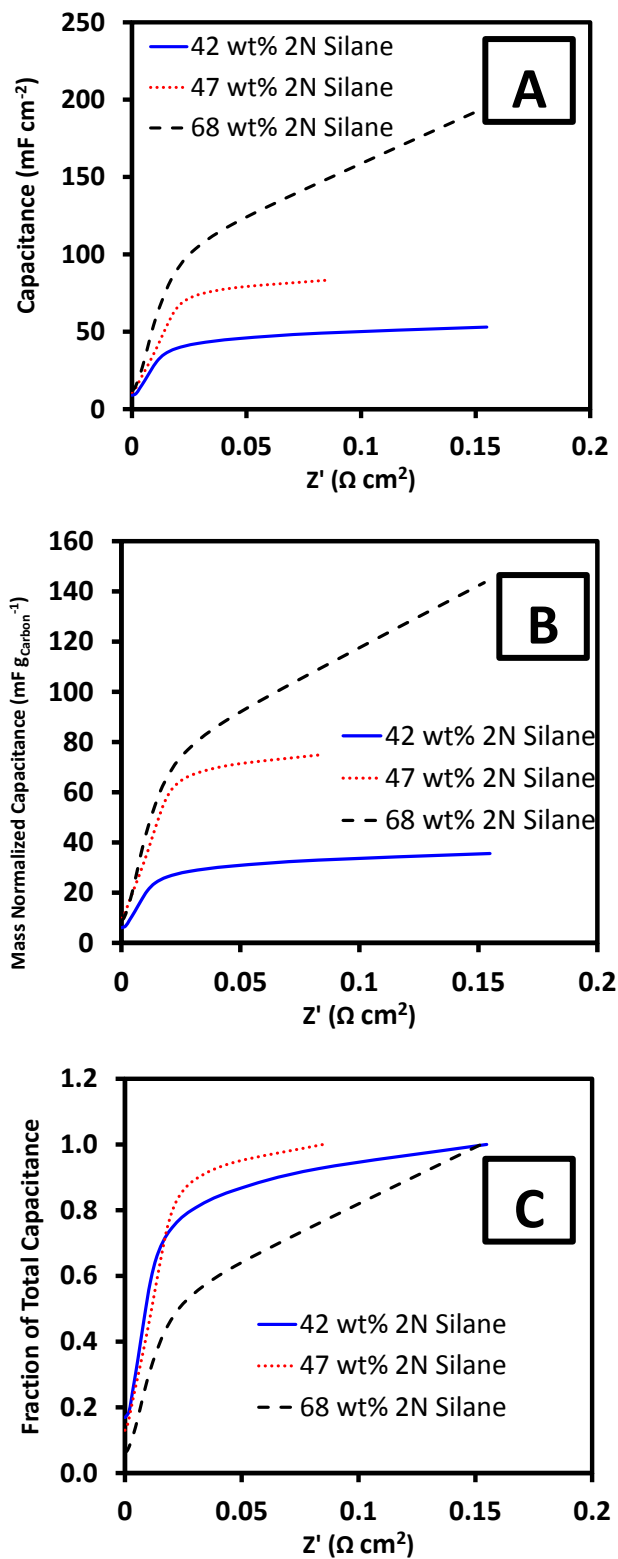


Figure 4-28: Capacitance plots of CCEs with varied 2N silane content. Experiments performed at 0 V vs. OCV in 2 M HCl analyte under N_2 atmosphere at 60 mL min^{-1} analyte flow rate and 25 mL min^{-1} H_2 gas provided to the cathode. (A) Area specific capacitance (B) Mass of carbon normalized (C) Capacitance normalized to 1.

The standard CuCl oxidation testing protocol was also used to examine the 2N CCE materials. Standard potential stair step measurements were made to observe the current response to increased potential as the cell was polarized (Figure 4-29).

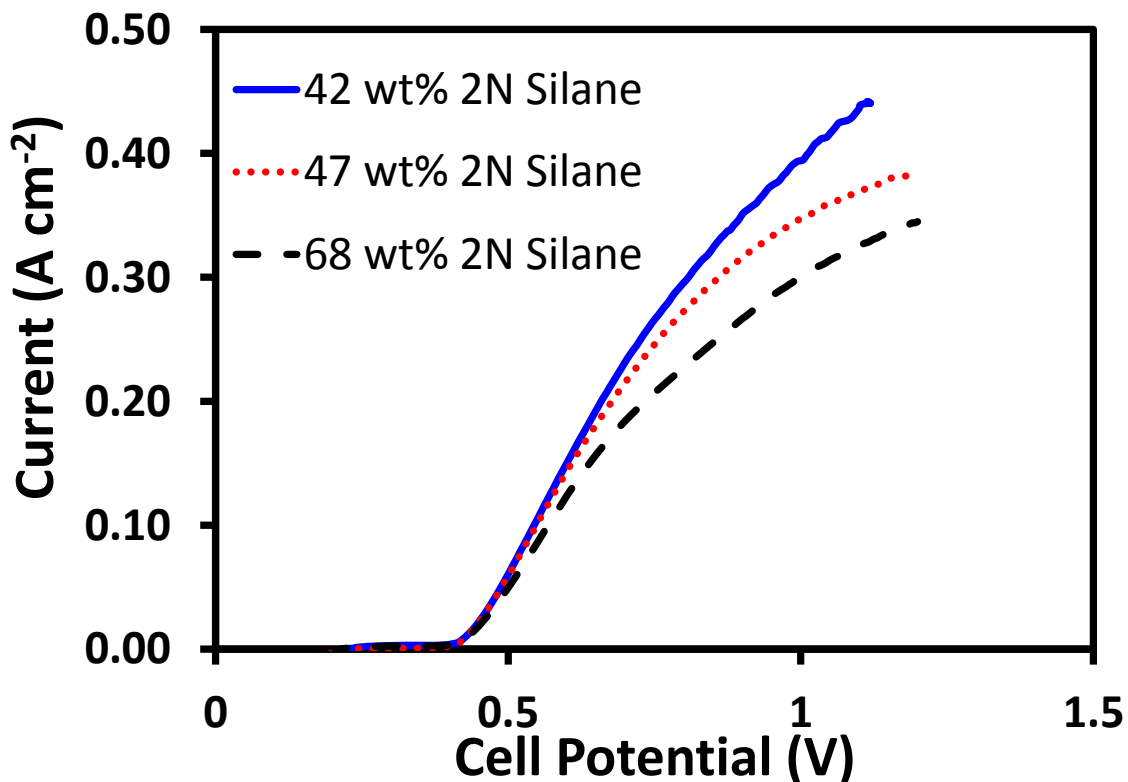


Figure 4-29: Potential stair step measurements of CCE's with varied 2N silane composition. Scanned from 0.2 to 1.2 V with 5 mV steps and 0.5 s dwell time per step. Tests performed in 0.2 M CuCl in 2 M HCl anolyte and DI H₂O catholyte both under N₂ atmosphere at 60 mL min⁻¹ electrolyte flow rate.

The three CCE materials showed similar onset potentials to one another as well as to the assumed standard value of 0.4 V vs. RHE. With this information we can see that the increased resistance from silane content is not affecting the onset of the CuCl oxidation. The three materials showed similar smooth current responses as the cell potential was increased indicating there was no separate processes occurring aside from CuCl oxidation. For better diagnostic abilities, the cell current was compared at 0.7 and 1.0 V vs. RHE and at different flow rates (Figure 4-30).

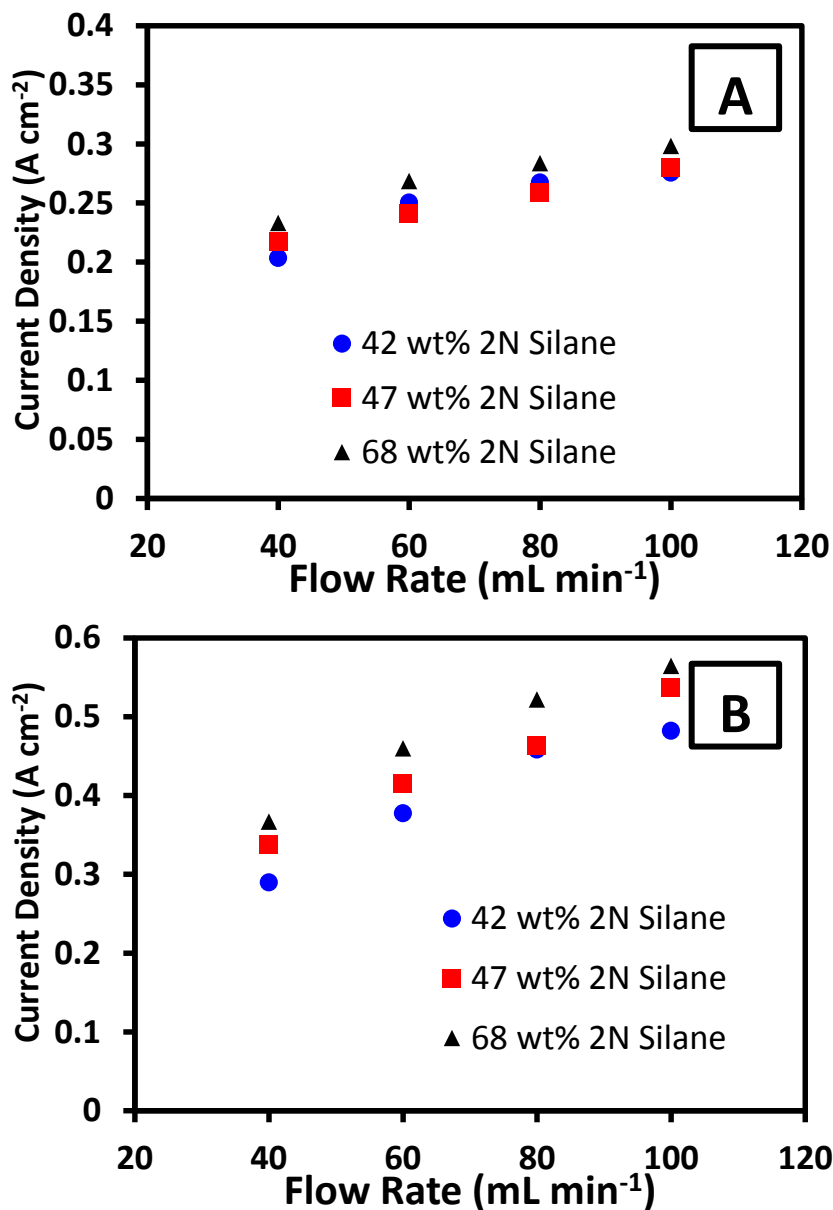


Figure 4-30: Current Trends of CCEs with varied 2N silane content at 0.7 and 1.1 V and varied flow rates. Tests performed in 0.2 M CuCl in 2 M HCl anolyte and DI H₂O catholyte both under N₂ atmosphere at 40, 60, 80, and 100 mL min⁻¹ electrolyte flow rate. Scanned from 0.2 to 1.2 V vs. RHE with 5 mV steps and 0.5 s dwell time per step. (A) Current density at 0.7 V vs. RHE (B) Current density at 1.1 V vs. RHE.

At the 0.7 V vs. RHE potential there is very little difference in current response between the three samples. A similar increasing trend in current vs. flow rate can be seen in all three samples, though this is expected when dealing with increased effective Cu⁺ concentration at the electrode. The differences in the CCE materials can be better seen when the currents at 1.0 V vs. RHE are compared. In these measurements we can see that the 68 wt% sample

responded the best to the applied potential, followed very closely by the 42 and 47 wt% samples. Ultimately there is little difference in the current responses of the three samples when compared by LSV measurement. It is still apparent that the three materials are behaving well, and as expected.

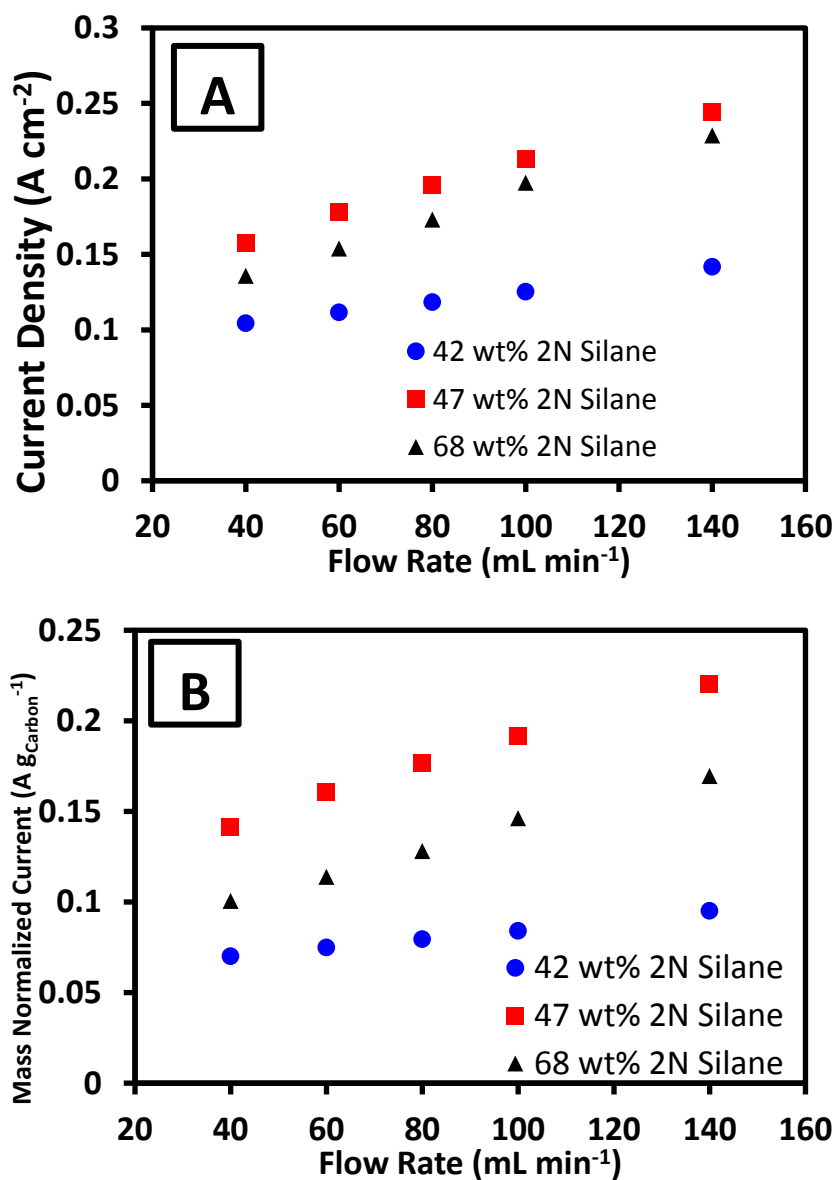


Figure 4-31: Potentiostatic hold current trends of CCEs with varied 2N silane content at 0.7 V and varied flow rates. Tests performed in 0.2 M CuCl in 2 M HCl anolyte and DI H₂O catholyte both under N₂ atmosphere at 40, 60, 80, and 100 mL min⁻¹ electrolyte flow rate. Potential held at 0.7 V vs. RHE, current value taken at 150 s. (A) Area specific (B) Carbon mass normalized.

As a final comparison, potentiostatic holds at 0.7 V vs. RHE were taken for each of the samples at flow rates up to 140 mL min^{-1} . When compared through this method we can see that there is much better separation between the three samples. In the potentiostatic hold measurements the 2N materials performed quite well, with some current densities above 200 mA cm^{-2} . In the 2N samples the CCE materials were tested up to 140 mL min^{-1} as opposed to the previous standard of 100 mL min^{-1} to examine any plateaus in the current response at higher flow rates (Figure 4-31). The three samples did not show any signs of plateauing at the higher flow rates. Each sample was able to be fit with a linear regression with an R^2 value of 0.995 or higher. This indicates that there is a positive linear correlation between the increase in flow rate of the analyte and the current response recorded for CuCl oxidation.

The 47 wt% sample was by far the best performing of the three samples with a consistently higher current response across all flow rates. When normalized for the mass of carbon present in the CCE material the 47 wt% sample increased its relative performance compared to the other CCE materials. This indicates that the 47 wt% CCE material is giving the best overall utilization of the electrode material. The 47 wt% sample also had the fastest charging rate when examined through capacitance plots. This faster charging of the electrode surface could be assisting the CCE in oxidizing the Cu^+ leading to a higher overall current response.

The overall current response in the potentiostatic tests showed a similar relationship between the wt% loading of silane and current response as was seen previously in our group²⁴. There was a much more pronounced difference in the current response for the 2N materials as opposed to the 1N materials (Figure 4-14). The overall relationship between the 1N silane content and the current response was not seen in the 2N materials. However, silanes with a composition below 42 wt% silane were not tested. Overall, for the 2N materials, it appears that there is an increase in current response as the overall wt% of silane in the CCE is increased.

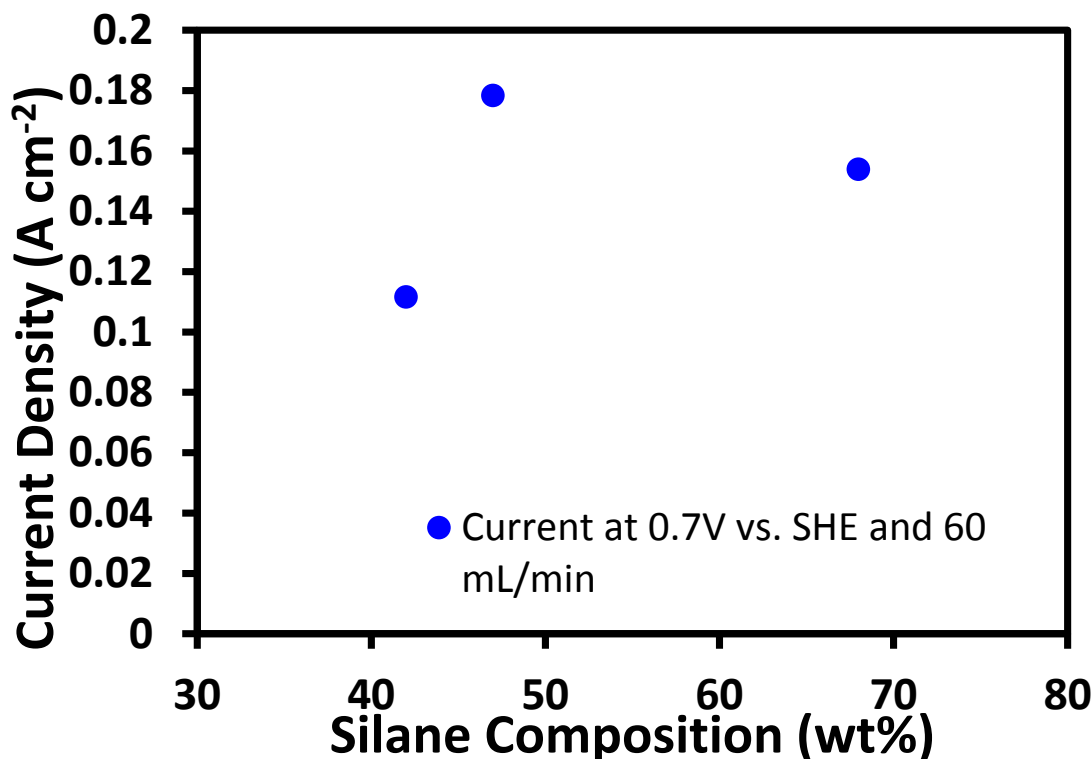


Figure 4-32: Relationship of 2N silane composition to current response in potentiostatic holds taken at 0.7 V. Experiments performed in 0.2 M CuCl in 2 M HCl anolyte and DI H₂O catholyte both under N₂ atmosphere at 40 mL min⁻¹ electrolyte flow rate.

All three materials displayed an acceptable current response across all flow rates. There was no sign of crossover or poisoning in the electrolysis cell and the current response was maintained throughout the full testing protocol. Of the three materials the 47 wt% sample had the best overall current response and the best utilization of the carbon surface for the Cu⁺ oxidation reaction. With this in mind the electrochemical surface area was found to be best utilized by the 68 wt% sample and the sample was also found to have the best conductivity and capacitance. This indicates that the decreased silane content substantially increases the overall reactivity of the CCE materials for the oxidation reaction. The improved oxidation from the lower silane content sample also supports the theory that the amino functionalities can block pores of the carbon surface, limiting the possible oxidation sites.

4.1.3.3: Electrochemical Results for 3N Materials

The 3N silane material with two secondary and one primary amine functionalities was examined. The 3N material is the silane with the largest amine pendant arm functionality

allowing for extended investigation of the effect of the longer pendant arm on the electrochemically active surface area of the carbon electrode. The 3N materials were produced with silane content ranging from 6.86 to 11.80 mmol Silane $\text{g}_{\text{Carbon}}^{-1}$ (Table 4-3).

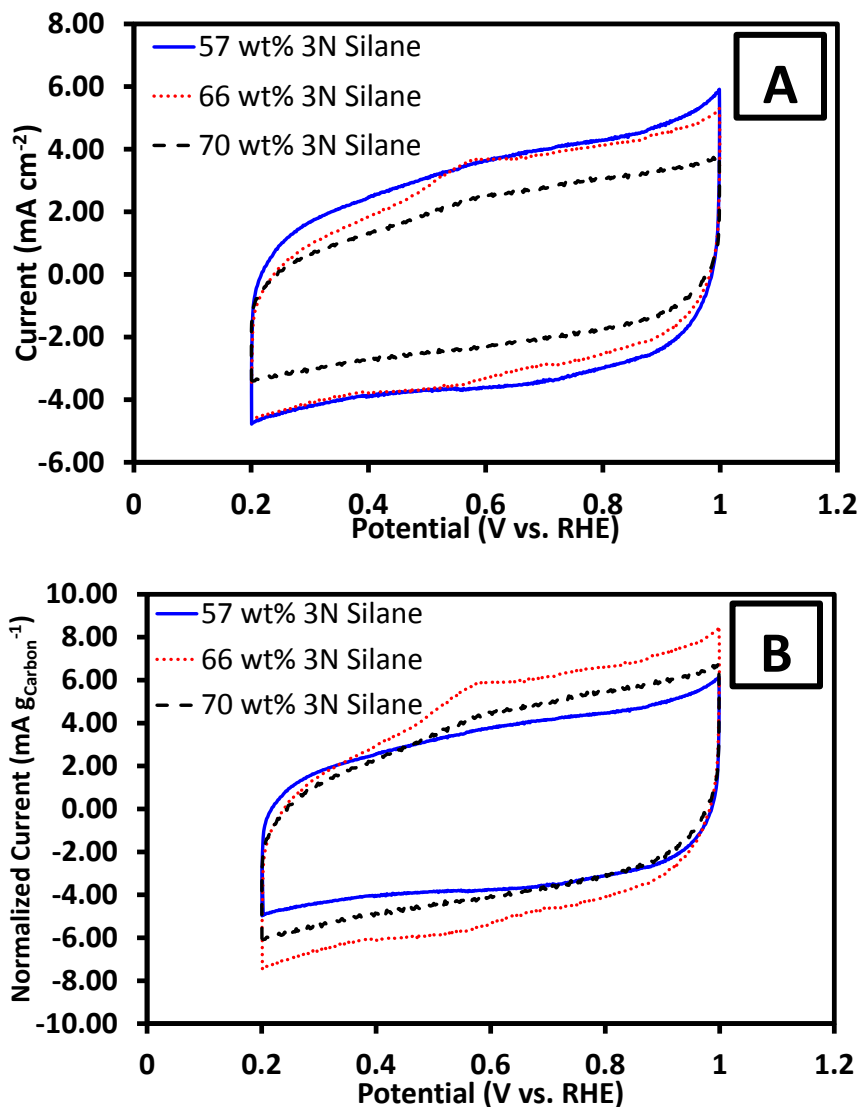


Figure 4-33: Capacitive CV of CCE materials with varied 3N silane loading. 50 mV s^{-1} scan rate from 0.2 to 1.0 V vs. RHE. Current normalized for geometric SA and for mass of carbon. In 2 M HCl under N_2 atmosphere at 60 mL min^{-1} analyte flow rate. (A) Area specific (B) Carbon mass normalized.

Again, capacitive CVs were taken in the absence of CuCl to assess the surface area of the CCE materials. The three materials all showed a stable box like shape in the CV indicating there were almost no non faradaic processes occurring during the measurements. The only apparent faradaic process occurred in the 66 wt% silane sample at approximately 0.55 mV. This was

assumed to be the result of Cu^+ deposition from copper contamination. The three samples had capacitive areas of decreasing size in the same order as the decreasing mass loading of carbon. After normalizing for the mass of carbon on the surface it was seen that the 66 wt% sample had the highest capacitive area indicating the best utilization of the carbon surface area. The 57 and 70 wt% samples had similar capacitive areas once normalized for the mass of carbon present.

The EIS measurements were also taken to assess the conductivity of the 3N materials (Figure 4-34). Again the increased amine content in the silane functionality leads us to expect greater increases in ionic conductivity with increased silane content. While the 57 wt% sample did not show a discernable Warburg region, the 66 and 70 wt% samples did show a well-defined Warburg region (0.01 and 0.02 Ω respectively) with the 66 wt% sample appearing to have a higher conductivity.

The capacitance plots (Figure 4-35) showed a similar ordering of the CCE samples based on their capacitance when compared to the capacitive CV's that were collected (Figure 4-33). The non-normalized samples showed close to the same limiting capacitance for the 57 and 66 wt% samples with a lower limiting capacitance observed for the 70 wt% sample. After normalizing for the mass of carbon present in the CCE the 66 wt% sample again shows a much higher limiting capacitance indicating the sample had the best overall utilization of the carbon surface. In addition to this, the 57 and 70 wt% samples had nearly equal limiting capacitances, although the 70 wt% sample charged to its capacitance at a lower real resistance (Z'). The information that is obtained from the mass normalized capacitance plots also closely mimics the information generated from the mass normalized capacitive CV graphs. The initial steepness of the capacitance plots is very similar even when the maximum capacitance is normalized to a maximum value of 1. From this we can conclude that the materials are charging at similar rates meaning the difference in the conductivity of the samples is quite small.

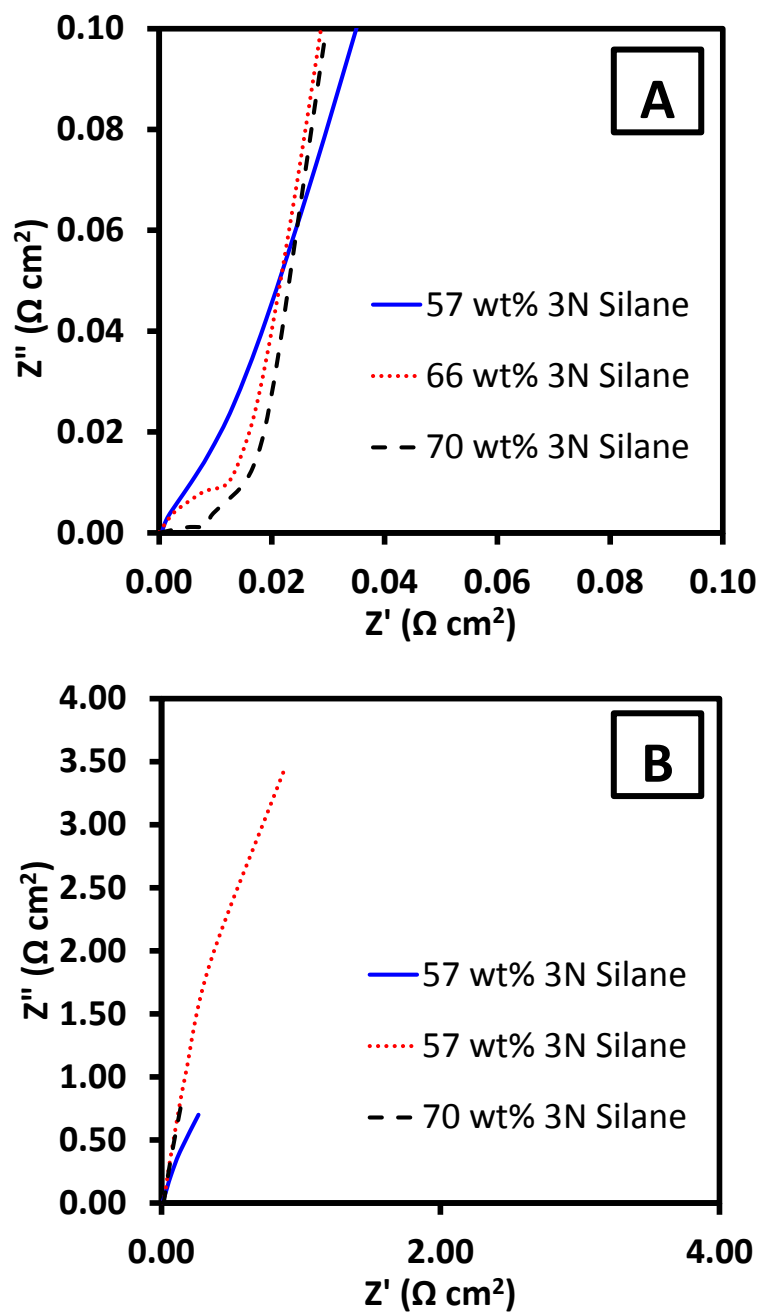


Figure 4-34: Nyquist plots of varied 3N silane content CCEs. Experiment performed at 0 V vs. OCV in 2 M HCl anolyte under N_2 atmosphere at 60 mL min^{-1} anolyte flow rate and 25 mL min^{-1} H_2 gas provided to the cathode. (A) High frequency region (B) Full nyquist plot.

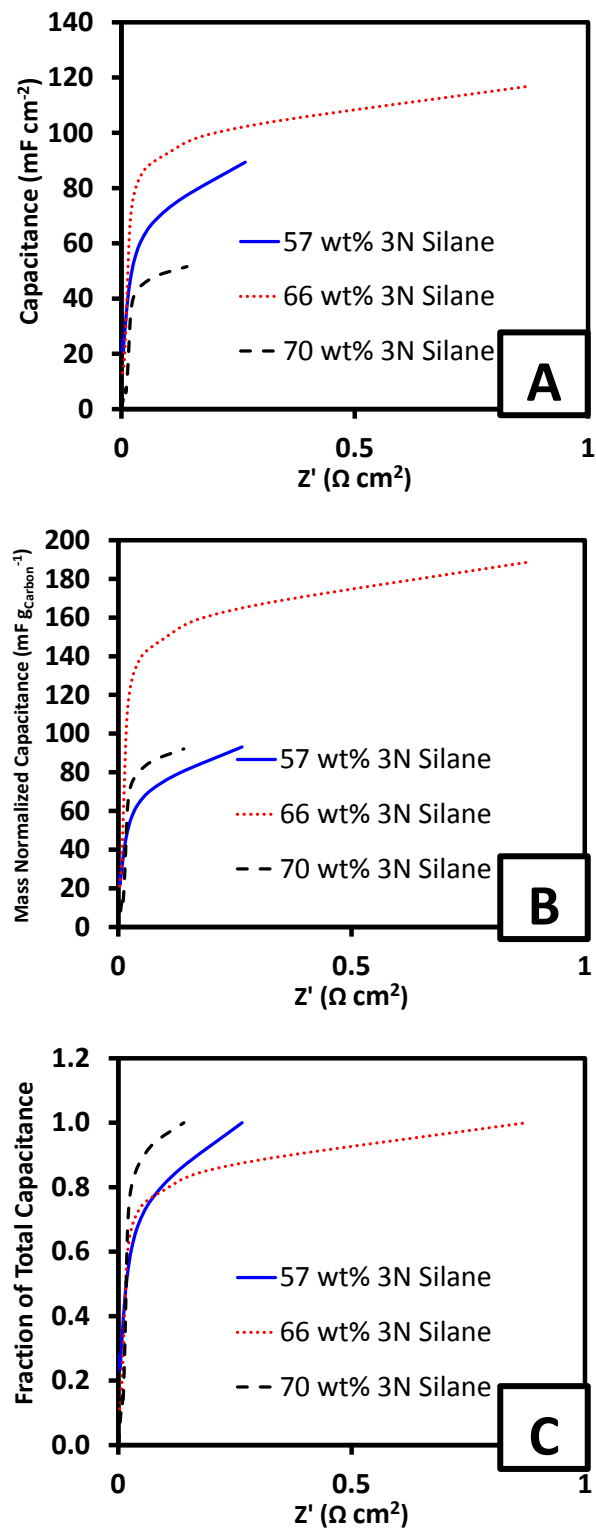


Figure 4-35: Capacitance plots of CCEs with varied 3N silane content. Experiment performed at 0 V vs. OCV in 2 M HCl anolyte under N_2 atmosphere at 60 mL min^{-1} anolyte flow rate and 25 mL min^{-1} H_2 gas provided to the cathode. (A) Area specific capacitance (B) Mass of carbon normalized (C) Capacitance normalized to 1.

There was very little variation found between the 3N materials when linear sweep measurements were taken in the presence of CuCl. The 3N CCE's all showed a similar onset potential that was in keeping with previous measurements made of both the 2N and 1N CCE's. The increase in current was smooth for all three samples with a similar reduction in the rate of current increase at approximately 0.6 V vs. RHE. All three samples performed similarly to one another with no clear best material over the whole current range.

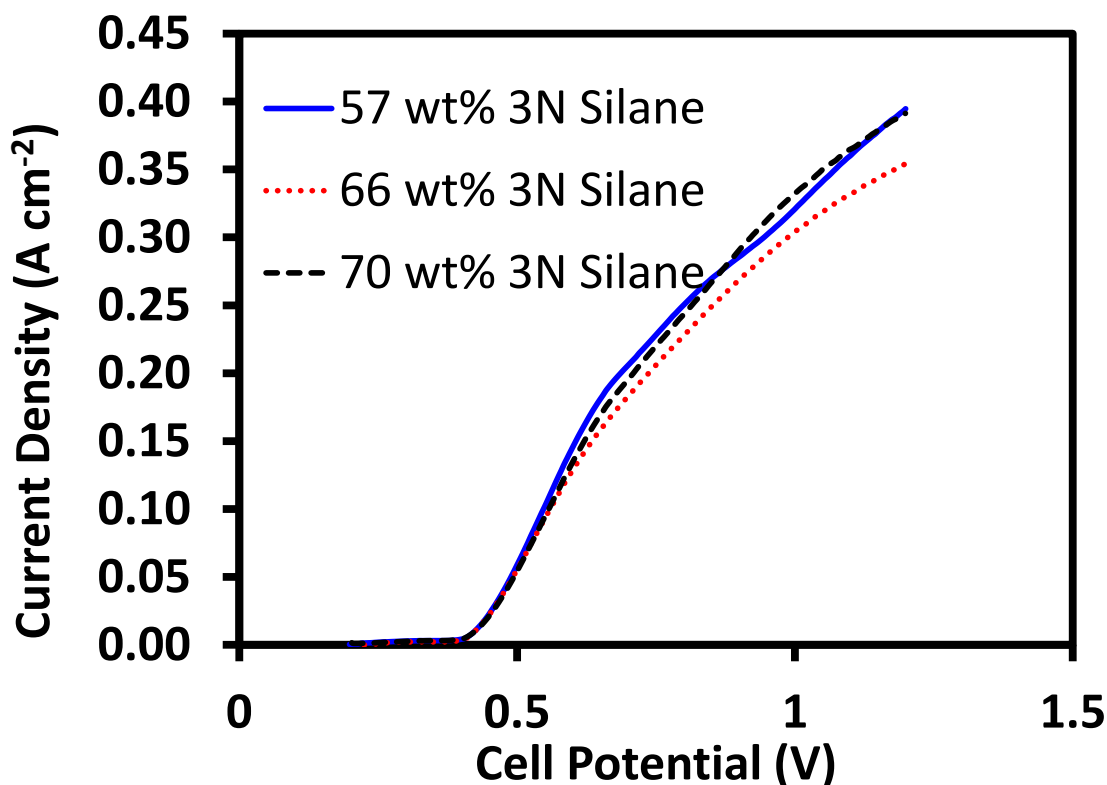


Figure 4-36: Potential stair step measurements of CCEs with varied 3N silane composition. Scanned from 0.2-1.2 V with 5 mV steps and 0.5 s dwell time per step. Collected in 0.2 M CuCl in 2 M HCl anolyte and DI H₂O catholyte both under N₂ atmosphere at 60 mL min⁻¹ electrolyte flow rate.

To better analyse the current responses, comparisons of the current of the potential stair step measurements at 0.7 and 1.0 V vs. RHE and at varied flow rates between 40 and 100 mL min⁻¹ were made (Figure 4-37). A linear increase in current response with flow rate was observed for the CCE's as expected. The only case of plateauing current was seen in the 66 wt% sample at 1.0 V vs. RHE and 100 mL min⁻¹ anolyte flow. The 57 wt% sample also appeared to have a steeper slope of current response vs. flow rate at 0.7 V vs. RHE.

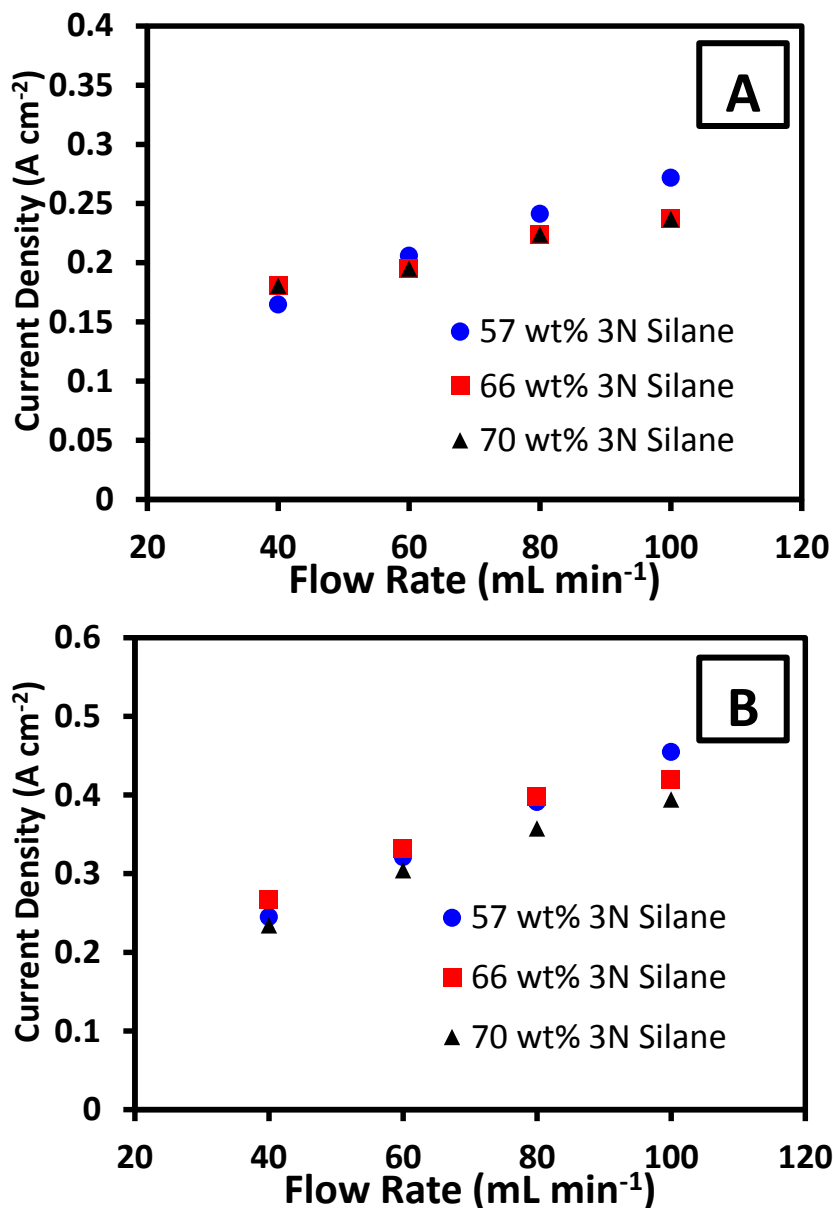


Figure 4-37: Current Trends of CCEs with varied 3N silane content at 0.7 and 1.1 V and varied flow rates. Experiments performed in 0.2 M CuCl in 2 M HCl anolyte and DI H₂O catholyte both under N₂ atmosphere at 40, 60, 80, and 100 mL min⁻¹ electrolyte flow rate. Scanned from 0.2 to 1.2 V vs. RHE with 5 mV steps and 0.5 s dwell time per step. (A) Current density at 0.7 V vs. RHE (B) Current density at 1.1 V vs. RHE.

The potentiostatic holds taken at 0.7 V vs. RHE show the best current response from the 57 wt% sample followed by the 70 wt% sample and finally the 66 wt% sample. Upon normalizing for the total mass of carbon in the CCE material the 70 wt% sample showed the best mass normalized current response. The current responses were compared with respect to the total

silane composition (Figure 4-39). There was no discernable trend in current with the silane composition.

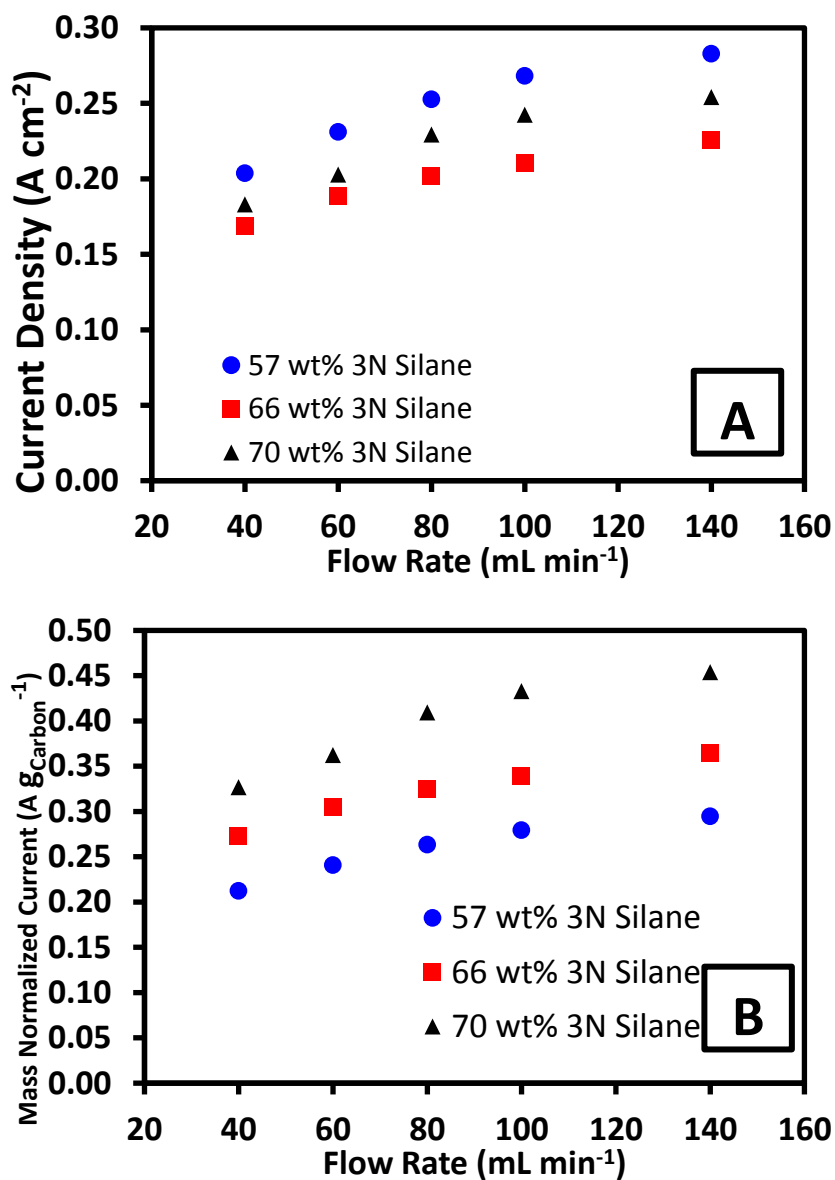


Figure 4-38: Potentiostatic hold current trends of CCEs with varied 3N silane content at 0.7 V and varied flow rates. Experiments performed in 0.2 M CuCl in 2 M HCl anolyte and DI H₂O catholyte both under N₂ atmosphere at 40, 60, 80, and 100 mL min⁻¹ electrolyte flow rate. Potential held at 0.7 V vs. RHE, current value taken at 150 s. (A) Area specific (B) Carbon mass normalized.

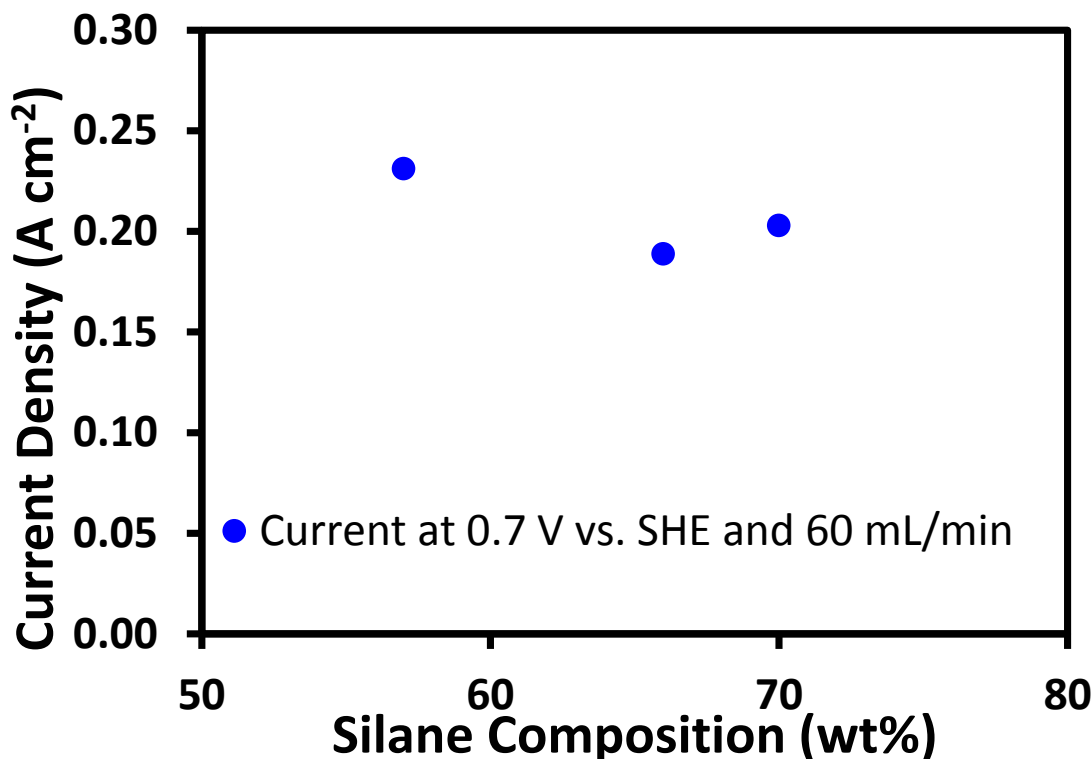


Figure 4-39: Relationship of 3N silane composition to current response in potentiostatic holds taken at 0.7 V. Collected in 0.2 M CuCl in 2 M HCl anolyte and DI H₂O catholyte both under N₂ atmosphere at 40 mL min⁻¹ electrolyte flow rate.

4.2: Discussion

To examine the effects of the silane materials in the full-cell environment two variables were investigated. First the 1N, 2N, and 3N materials were examined, expanding on the investigation of these materials in a half-cell. The second variable investigated was the total loading of the electrode material on the CCE. This investigation was specific to the full-cell environment.

4.2.1: 1N Materials

One of the reasons for producing the 1N CCE materials with silane loadings between 20 to 60 wt% was to allow for comparison to CCEs produced previously in our lab. These CCEs were tested extensively in a half-cell environment²⁴. Three CCE materials containing the 1N silane were tested with silane loadings of 22, 36, and 56 wt%. It was determined through anodic polarization that the 36 wt% silane sample was the best performing demonstrating the highest limiting current. Initially the new half-cell materials discussed in Chapter 3 were intended to be

compared to those produced previously. However, because the samples we produced all had silane loadings above the original best 36 wt% silane we were not able to compare our silane materials to those produced previously. To that end, the full-cell CCE's tested showed silane compositions between 27 and 62 wt% of silane allowing for a more direct comparison of the initial half-cell work to our materials. While there was a compositional similarity between the original half-cell and the full-cell CCE materials it is still a comparison between full and half-cell operation which possess drastically different operating conditions. With this in mind, only basic connections between the original half-cell data and the full-tests can be made.

The decrease in surface homogeneity with increasing silane content that was observed when the 1N materials were examined under SEM (Figure 4-3) was attributed to the additional sol-gel binder present in the CCEs creating macrostructures. Within the CCE structure, the sol-gel material exists as a binder holding the carbon surface together. By increasing the silane content, the binder will be more able to form cross linking creating surface defects. Ultimately the surface of the CCE structures can be assumed to be largely homogeneous. This is because the capacitive CV measurements when normalized for the mass of carbon showed little variation (Figure 4-4).

As with the half-cell experiments, EIS measurements were performed on the 1N CCEs (Figure 4-5). The very low Warburg regions were attributed to the electronic conductivity of the carbon support as well as the high ionic conductivity of the analyte liquid. As with the half-cell measurements the high silane content materials showed the highest resistance. While the samples with the higher silane content were expected to have a higher ionic conductivity this can be explained. The increased electronic resistance from the silane backbone will decrease the overall conductivity of the materials. Excess silane content could also block micro-pores within the CCE material in doing this the additional ionic conductivity of the added silane can be mitigated. Beyond the inverse dependence of conductivity on silane content there was no clear trend in the conductivity. The Warburg regions of the two CCEs containing the least silane were very similar, the same behavior was seen for the two highest silane content CCEs. The capacitance plot shows behavior similar to what was seen in the capacitive CV measurements (Figure 4-6). The lower plateau level for the capacitance plot of the 62.5 wt% sample (not included in capacitive CV measurements) showed that the porous structure was quite reduced. This is likely due to the blocking of micro-pores in the carbon by the larger amount of the silane

and the associated amine functionalities attached to the silane monomers. After normalizing for the mass of carbon, the only notable difference was that the relative capacitance values of the four CCEs with the lowest silane content increased relative to the CCE with the highest silane content. This further supports the idea that the increased silane content eventually blocks micro-pores of the carbon surfaces and not that there was simply less carbon present to be capacitive²⁴.

The initial examination of the potential stair step measurements in the full-cell environment showed the expected onset potential; however the samples showed a plateauing of current response at higher potentials. Since this phenomenon was not seen in the faster flow rate runs or in the CCEs that showed a higher capacitive surface area and greater current response (Figure 4-7 and Figure 4-8), it is likely that this is due to a mass transport plateau current being reached. At higher flow rates it can be assumed that the Cu^+ at the electrode surface is being replenished fast enough to avoid the slower mass limited current response. A noticeable feature of the CCEs is that up to 100 mL min^{-1} they do not appear to be showing signs of diminishing returns in current response for the increased flow rate of the electrolytes. As determined by Stolberg et al., there will be an increased flow rate or potential at which all of the CCEs will reach a point of diminishing returns, though it may be higher than it is feasible to operate the electrolysis cell²¹. In addition to the comparison of materials, the potential stair step measurements can also be used to predict the cell's response to higher concentrations of anolyte. When the flow rate is doubled the amount of CuCl per unit time at the electrode surface should be identical to an anolyte with twice the CuCl concentration flowing at the original flow rate.

Again, as with the half-cell experiments, the potentiostatic hold tests were used to examine the materials' activity during sustained CuCl oxidation (Figure 4-13). While these tests were shown to give the same data as potential stair step measurements (Figure 4-11), the ability to assess the sustained operation of the CCE was important along with Cu oxidation was quite valuable.

Across the 4 samples measured there was a negative correlation between current response and silane content (Figure 4-14). The differences in the relationship between the silane content and the current measured are likely because of varied microstructures within the carbon. The similar mass normalized capacitive CVs which indicated that the carbon support

was being utilized by the same amount for each sample. However, during the capacitive CV measurements the surface of the electrode is simply being charged and discharged. This is different from what is expected under normal operation. When making a potentiostatic hold, bulky copper compounds must reach the surface of the electrode as opposed to electrons which can be transferred through the carbon material. With this in mind we can draw the conclusion that the increased silane presence in the CCE structure will obstruct the migration of CuCl to the electrode surface. While it is expected that there will be better ionic conductivity from higher wt% silane samples given their amine functionalities, the amino-propyl side chain could also physically obstruct micropore sites, limiting access to the electrode's surface area. This would not affect the capacitive surface area measured as the electrolyte solution could more easily penetrate into pores obstructed by the silane side chains. The increased silane content will also increase the resistance in the electrode increasing the potential required for CuCl oxidation. This also supports the previous half-cell measurements made showing a low 36 wt% silane loading to be optimal²⁴.

4.2.2: Varied CCE Loadings (1N)

Initially there were two reasons for testing the increased loading on the CCE materials. It was shown that the mass normalized capacitance of the different samples tested (shown in Figure 4-4) were very similar. This implies that with increased carbon surface area we should see an increased activity of the samples or at least see an increase in the point at which a maximum current is reached. The second reason is that the higher mass loadings should also correlate to a thicker electrode structure. This increased thickness is potentially valuable to the cells ability to resist copper crossover. This phenomenon is discussed at length in Chapter 5: Materials Durability and Copper Crossover Resistance. In brief, the increased thickness of the CCE layer increases the distance that Cu^+ must migrate to cross through the membrane and poison the cathode catalyst.

By using samples that all contain the same silane to carbon ratio (Table 4-2), the effects of only the total CCE loading were isolated. During the capacitive CV measurements we observed the highest CCE loading sample discharging at a much slower rate (Figure 4-15), this was attributed to the thick electrode layer which created a larger resistive environment slowing the discharging from the electrode surface. In spite of this, the highest CCE loading sample showed a large capacitive surface area as expected from the large amount of carbon within the

CCE. However, after normalizing for the mass of carbon the 3.6 mg C cm^{-2} was shown to have the worst carbon utilization. The decrease was expected as the increased mass of CCE will necessarily obstruct some of the carbons surface area. This trend was also shown in the mass normalized capacitance measurements (Figure 4-17 (B)). The capacitance measurements also showed a better definition between the samples with respect to the overall capacitance, however there was no trend amongst the low CCE loading samples. The lack of a trend in the mass normalized capacitance and CV measurements further speaks to the very similar CCE structure in the three CCE's with a lower mass loading.

From the EIS measurements it was observed that only the 3.6 mg C cm^{-2} sample showed a significant Warburg region (Figure 4-16). While there could be some decreased conductivity from electronic resistance the decreased conductivity is assumed to be primarily ionic. This is because the silane content is nearly the same for all four of the samples. The similar silane loading indicates that the any resistance within the samples from the silane presence should be roughly equivalent leaving only the varied CCE structure to affect the ionic conductivity.

For both the potential stair step and potentiostatic hold measurements there does not appear to be any dependence of the current response on the silane content in these samples (Figure 4-19 and Figure 4-20). With this in mind, the current responses were compared with the ionic conductivity measured in the samples. This was accomplished by normalizing the maximum capacitance values for each of the CCEs to 1, allowing for the rate at which the materials charge to their maximum value to be examined. The normalized capacitance plot showed that the $1.8 \text{ mg}_{\text{Carbon}} \text{ cm}^{-2}$ sample had the highest conductivity from the steepness of the initial slope on the capacitance plot (Figure 4-22). The order from highest to lowest conductivity for the remaining three samples is; $1.3 \text{ mg}_{\text{Carbon}} \text{ cm}^{-2}$, $0.8 \text{ mg}_{\text{Carbon}} \text{ cm}^{-2}$, and finally the $3.6 \text{ mg}_{\text{Carbon}} \text{ cm}^{-2}$. While the $3.6 \text{ mg}_{\text{Carbon}} \text{ cm}^{-2}$ sample capacitance plot crosses the line made by the $0.8 \text{ mg}_{\text{Carbon}} \text{ cm}^{-2}$ sample and reaches its maximum capacitance sooner, the steeper initial slope of the $0.8 \text{ mg}_{\text{Carbon}} \text{ cm}^{-2}$ sample indicated it had a higher ionic conductivity. With the exception of the 1.3 mg C cm^{-2} sample, which showed the highest response, the order of increasing ionic conductivity from the normalized capacitance graph correlated with the maximum current response recorded in the potentiostatic measurements taken at 40 mL min^{-1} (Figure 4-20). From this it was inferred that the increased ionic conductivity of the electrodes led to an increased current response. This is not surprising as the diffusion of the CuCl

molecules to the electrode surface is by far the slowest step in the electrolysis reaction, increases made to this portion of the electrolysis will strongly affect the overall current response²¹.

Beyond ionic conductivity, there appears to be little dependence of the current on other factors in the composition of the four samples (Figure 4-21). In these samples, increased ionic conductivity cannot be attributed to varied silane content as all four fall within a very narrow range. As described above, the lower ionic conductivity of the $3.6 \text{ mg}_{\text{Carbon}} \text{ cm}^{-2}$ sample can be attributed to the slower mass transport through the much thicker CCE layer. For the three lower loading samples the $0.8 \text{ mg}_{\text{Carbon}} \text{ cm}^{-2}$ sample had the worst performance because of its overall lower mass loading and the $1.8 \text{ mg}_{\text{Carbon}} \text{ cm}^{-2}$ sample began suffering from the decreased reaction kinetics associated with the higher mass loadings. The $1.3 \text{ mg}_{\text{Carbon}} \text{ cm}^{-2}$ sample represents an optimal mass loading, gaining the increased reaction kinetics of the lower loading samples without losses from a smaller overall surface area.

4.2.3: 2N Materials

For the examination of the 2N materials the produced CCE materials had a range of silane concentrations completely within the 1N materials silane concentration range it allows for easy comparison between the 1N and 2N materials (Table 4-3). As with the 1N materials, the 2N CCEs showed a decrease in surface homogeneity with increased silane content. Again, this was attributed to the increased binder content increasing crosslinking and, thus, the surface defects observed. Differing from the 1N materials, the 2N materials showed increasing capacitive area with increasing silane content. In this case it is possible that the higher silane content is allowing for better utilization of the high surface area carbon. The increased amine functionalizations from higher silane content would allow for easier electron transport to the surface of the electrode increasing the capacitive charging. This phenomenon can also explain why there was a more dramatic increase in CCE surface area with silane content for the 2N CCEs when compared to the 1N CCEs.

The EIS measurements made showed that the Warburg regions of the three CCEs were almost identical (Figure 4-27). While the 68 wt% sample showed the shortest Warburg region overall, all three materials showed very low resistance. This can also be attributed to the

increased protonated amine content within the CCE. The increased conductivity is also likely not from an increase in electronic conductivity. The increase of the silane content will necessarily increase the resistance of the CCE material. For these two reasons it is assumed that the increase in conductivity is from the increased ionic conductivity of the CCE. The capacitance plots of the 2N materials also showed that the capacitance was increasing with surface area (Figure 4-28), confirming the capacitive CV measurements.

When examining the potential stair step measurements it was determined that the 68 wt% sample performed the best (Figure 4-29), while this was not the case for the measurements made in the potentiostatic holds an interesting trend can be observed. While none of the materials showed any signs of plateauing the 68 wt% sample does show a better response to the increased flow rate. The slope of the 68 wt% sample in Figure 4-31 (A) was 0.00094 compared to 0.00086 for the 47 wt% sample. These two slopes were found to be statistically different at a 95% confidence interval. This implies that the 68 wt% sample will eventually overtake the 47 wt% sample's current response at a much higher flow rate. However, this does rely on the premise that neither sample will plateau before that point is reached as predicted by Stolberg et al.²¹. The 42 wt% sample showed a much lower current response with a lower overall response to the increased flow rate. While the sample did appear to have a higher ionic conductivity, from the EIS measurements (Figure 4-27), the lower overall surface area limited the CCEs ability to oxidize Cu^+ . Beyond this, the potentiostatic measurements did not show any trend in current response to silane content (Figure 4-32). While the surface area of the materials would affect the reaction the similar ionic conductivity the three CCEs likely contributed to the overall lack of trend in the potentiostatic data.

4.2.4: 3N Materials

To complete the examination of varied silanes 3N materials were produced for the full-cell environment. Again, the CCE materials were produced with silane contents that fell within the range of silane content produced for the 1N and 2N materials allowing for the comparison between the different silanes (Table 4-3). When the SEM images of the 3N materials are compared to the 1N and 2N materials, the 3N CCEs did not show the expected decrease in surface homogeneity (Figure 4-25). This can be explained by the narrow range over which the materials were produced. This made it more difficult to discern changes in the CCE structure.

The surface was still taken to be homogeneous as the capacitive CV measurements showed very similar capacitive areas when normalized for the mass of carbon.

Once again, an increase in the Warburg region and, thus, resistance with increasing silane content was observed (Figure 4-34). The 2N materials showed decreasing resistance with increased silane content implying that the increase in ionic conductivity was greater than the increase in electronic conductivity. While an increase in ionic conductivity from the 70 wt% sample is expected, it is also possible that the very high wt% content of the silane in the CCE led to dramatic increases in resistance, lowering the electrical conductivity, and increasing the overall resistance. As with the 1N and 2N materials, the mass normalized capacitance plot showed the same trend in increasing capacitance as was seen in the capacitive CVs (Figure 4-35).

The potential stair step measurements showed very similar current responses making analysis of the CCE materials based on this technique difficult (Figure 4-37). Contrary to this, the potentiostatic hold measurements showed very clear differences in current response at all flow rates tested (Figure 4-38). There was a large change in the relative current responses between the area and mass normalized current responses. The change can be ascribed totally to the variety in carbon loadings between samples. Normally the 57 wt% sample had a higher total mass of carbon giving it the best overall performance. The low loading on both the 66 and 70 wt% samples gave them much better utilization of the carbon surface area. Ultimately all three materials performed quite well allowing excellent mass normalized current responses. This excellent utilization of the carbon surface can be partially attributed to the increase in ionic conductivity afforded by the protonated amine functionalities. In addition to the increased ionic conductivity it is also important to note that the oxidation can also occur outside of the CCE material. The smaller total mass of carbon meant that a larger percentage of the total oxidation was occurring outside of the CCE, this gave the CCE material an artificially increased utilization of the CFP surface. This increase would also have not been seen in the surface area measurements where the non-ceramic surface area can always be seen as negligible.

Overall, the 3N materials showed a good current response in the potentiostatic hold measurements, comparable to both the 1N and 2N materials discussed previously. The 3N material did not appear to follow the trend seen in the 2N and previously published data from our research (Figure 4-39)²⁴. Instead the lowest wt% sample appeared to have the best overall

current response. This decreasing current with increased silane content is likely due to the much higher silane contents tested for the 3N samples. The ratio of silane to mass of carbon is much higher for the 3N samples tested when compared to the 1N and 2N samples. Due to this, the range of 3N samples tested represents the upper portion of the 1N and 2N samples tested. This means that while the best performing 3N sample had the lowest silane content, it still corresponds with the best 1N and 2N sample compositions.

4.2.5: Comparison of Varied Silane Types

From the analysis of the CCE materials produced with the three silane materials it is possible to compare the samples based on silane type, and amount, as well as amine content. The CCEs showed similar conductivities across all of the samples. The 1N materials, on average, possessed shorter Warburg regions than the 2N and 3N CCE materials, but the overall conductivity from the CCE materials was largely the same (Figure 4-40 (A)). Additionally, the conductivity associated with the CCEs was quite low. This is in large part due to the liquid electrolyte providing excellent electronic and ionic conductivity. With the initially low ionic conductivity of the MEA it was difficult to discern differences solely based on changes in total silane content. The capacitance of the materials also gives an approximate insight into the total surface area of the materials. While the conductivity of the CCEs was quite similar, a difference in the limiting capacitance was observed when comparing the different materials (Figure 4-40 (B)). Overall there was not a dramatic change in the limiting capacitance values associated with the 1N, 2N, or 3N materials. This indicates that the overall surface morphology of the CCEs is more important to the capacitance of the CCEs than the silane binders.

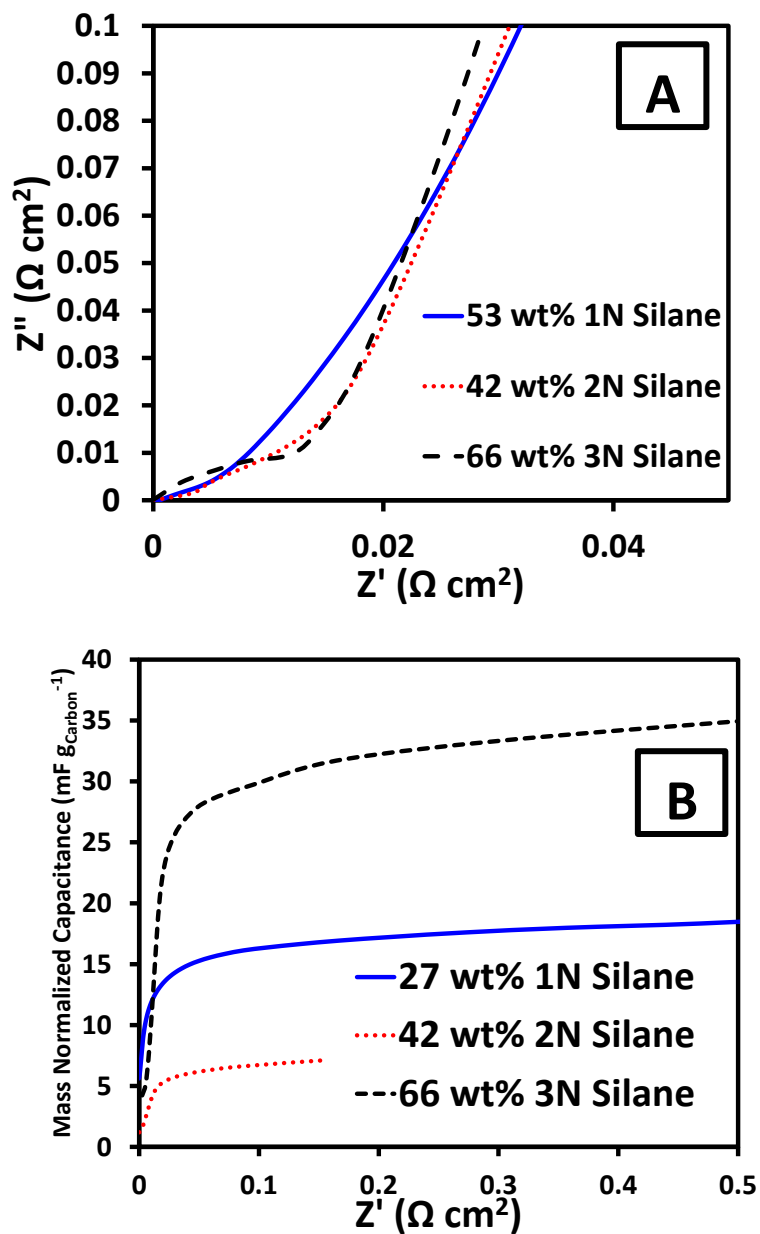


Figure 4-40: Nyquist and Capacitance plots of CCEs with representative compositions from 1N, 2N, and 3N silane precursors. Representative compositions of the silanes were used. Collected in 2 M HCl anolyte under N_2 atmosphere at 60 mL min^{-1} anolyte flow rate and 25 mL min^{-1} H_2 gas provided to the cathode. (A) High frequency region Nyquist plot (B) Mass of carbon normalized capacitance plot.

In addition to the EIS information, the capacitive CV measurements taken in the absence of CuCl provide an interesting insight into the surface area of the materials. There should be a correlation between the overall charge on the surface of the CCEs during capacitive CV measurements and the electrochemically active surface area (ECSA) of the material. The forward scans of the capacitive CV measurements were integrated with respect to time to provide a columbic charge values for each material (Figure 4-41).

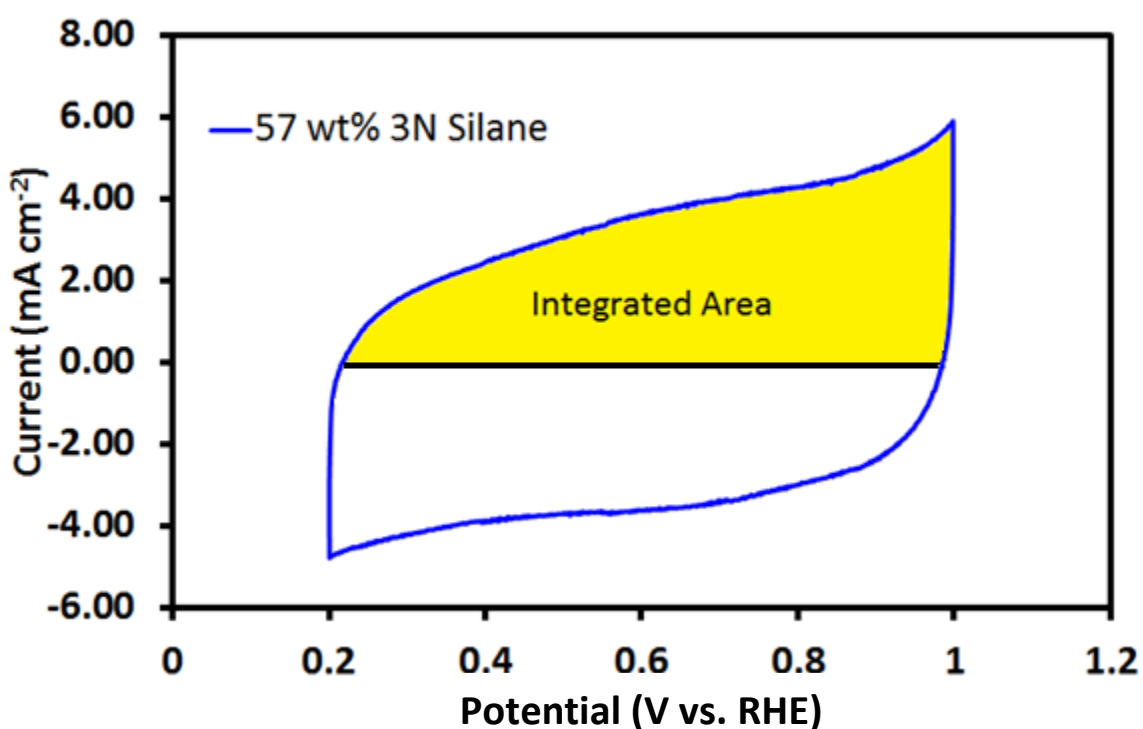


Figure 4-41: Example of the integrated area for the forward scan integration of capacitive CVs.

When comparing all of the CCE materials a slight association between the molar loading of the silane and the capacitive surface area. At higher molar loadings of silane the capacitive surface area is increased (Figure 4-42). During the charging and discharging of the CCE surface, low conductivity can potential required for the materials ability to be fully charged. From this, while the increase in charge with increased silane loading is not necessarily tied to an increased surface area it can be correlated with the electrodes overall ability to facilitate non faradaic charging.

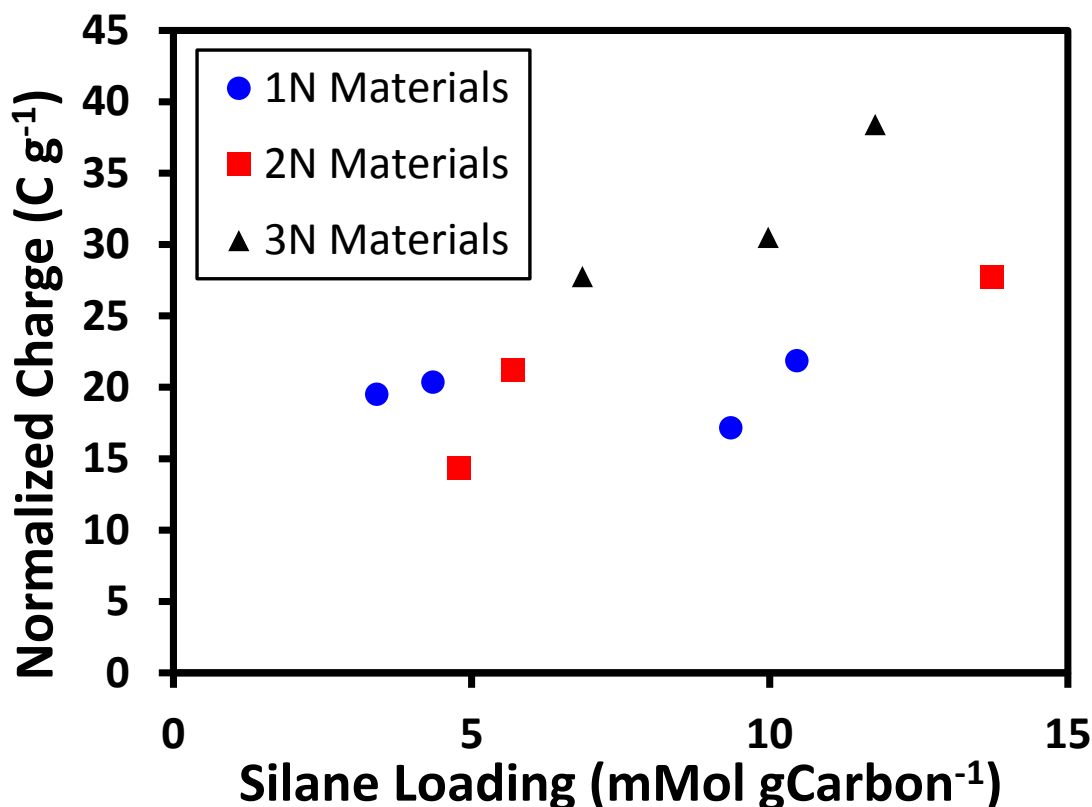


Figure 4-42: Total charge from capacitive CV measurements taken at 50 mV s^{-1} in relation to the molar loading of silane in the CCE material.

As has been mentioned, the increase in charge is likely not due to an increase in overall surface area, but more likely because of increased conductivity in the materials allowing for easier electron transport. The sol-gel network supporting the CCE will insulate the CCE structure so the positive correlation between charge and silane content must be related to the total amine content of the material. In comparing the sum of the amine functionalities (both primary and secondary) to the total charge a good linear correlation can be seen ($r^2 = 0.8165$) (Figure 4-43). From this we conclude that the increased ionic conductivity afforded by the amine content increased the electrodes ability to be charged. In all cases this increased ionic conductivity appears to outweigh the electrically resistive effects of the sol-gel binder. The increase in charge with amine content also appears to be more pronounced in the 2N and 3N materials.

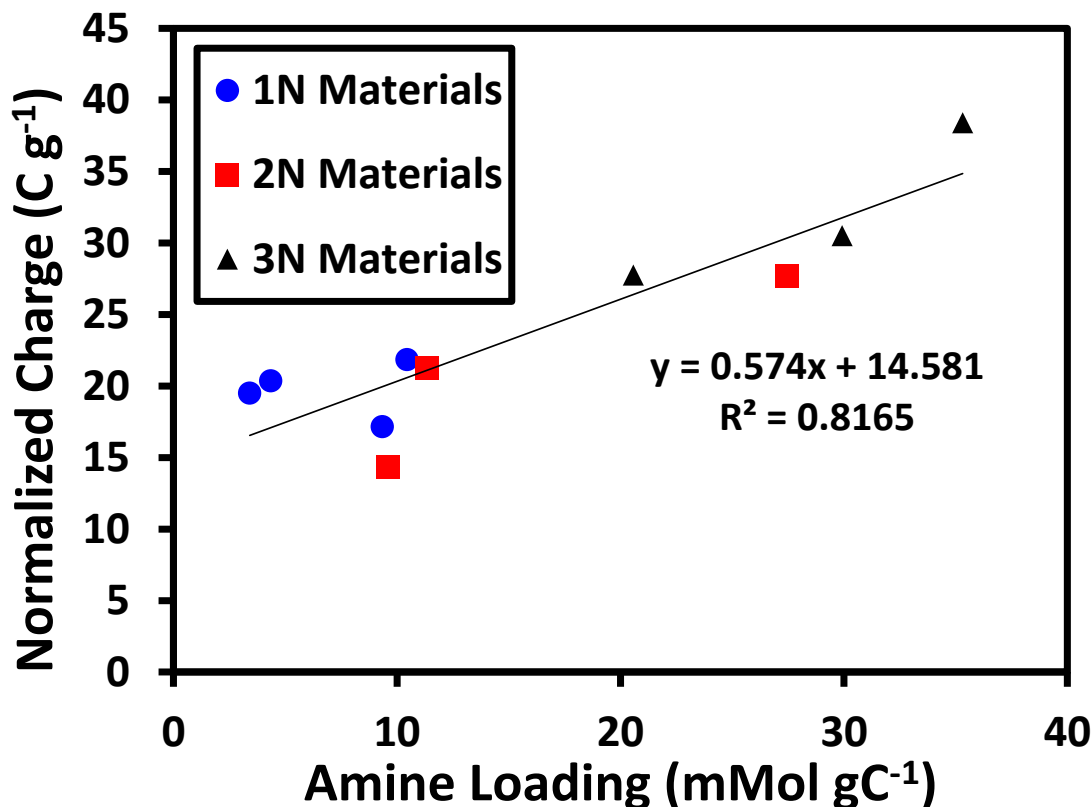


Figure 4-43: Total charge from capacitive CV measurements taken at 50 mV s⁻¹ in relation to the molar content of amines in the CCE material.

The CCE materials all showed similar behavior when compared by potential stair step measurements. The materials all had similar onset potentials and behavior as the potential was scanned to higher values. When compared to standard Pt catalyst materials and a bare CFP control it can be observed that the onset potential does not change significantly (Figure 4-44). The current response does appear to be better for the bare CFP material. This is due to a faster reaction occurring at the surface of the CFP. The increased activity of the CCE materials over the Pt catalyst material is in agreement with work previously performed by our lab and others²⁷.

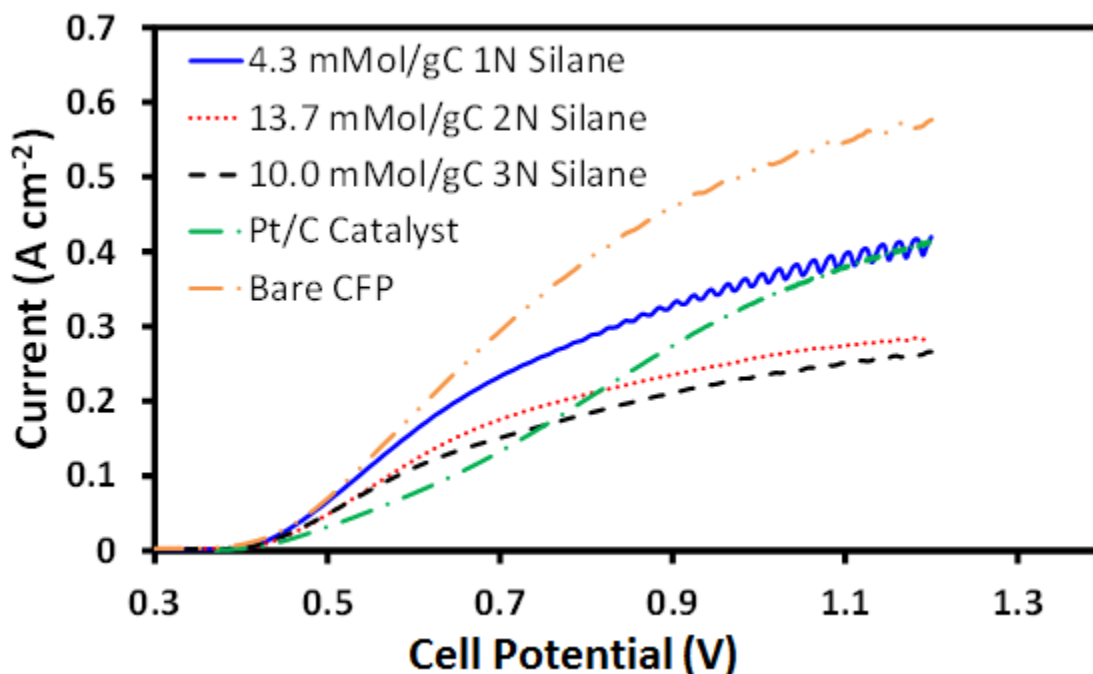


Figure 4-44: Comparison of best potential stair step measurements for 1N, 2N, and 3N CCEs as well as bare CFP and standard Pt/C catalyst materials. Scanned from 0.2 to 1.2 V with 5 mV steps and 0.5 s dwell time per step. Collected in 0.2 M CuCl in 2 M HCl anolyte and DI H₂O catholyte both under N₂ atmosphere at 60 mL min⁻¹ electrolyte flow rate.

While these measurements give insight into the operational behavior of the different electrodes, full potentiostatic measurements allow for a more realistic comparison between electrode properties and their operating current. As with the previous potentiostatic measurements, after 150 s of the cell's operation at 0.7 V vs. RHE with 60 mL min⁻¹ electrolyte flow the recorded current was taken to be representative of the material. To account for the materials varied total loadings, all measurements comparing the different CCE materials were normalized for mass of carbon present. When the mass normalized current is compared to the molar loading of the silane precursor used there is a varied current response to increased silane content (Figure 4-45). As the molar loading of the silane is increased the ionic conductivity should increase and the electronic conductivity should decrease. These two properties can be attributed to the protonated amine groups and the non-conductive sol-gel network respectively. The competition between these two phenomena should produce an optimal loading of silane. In the case of the 1N silane it is likely that the optimal loading is lower than the range of silane that was tested. This is evident from the constant decrease in activity with increasing silane

content. There appears to be little to no dependence of current response to the molar loading of the 2N silane, the optimal loading could also be within the tested range. Finally, the optimal loading of the 3N silane could be above the tested amounts given the positive correlation between 3N silane content and current response. Of the tested materials, the 3N materials best utilized their carbon supports with all of the samples performing the best of all those tested.

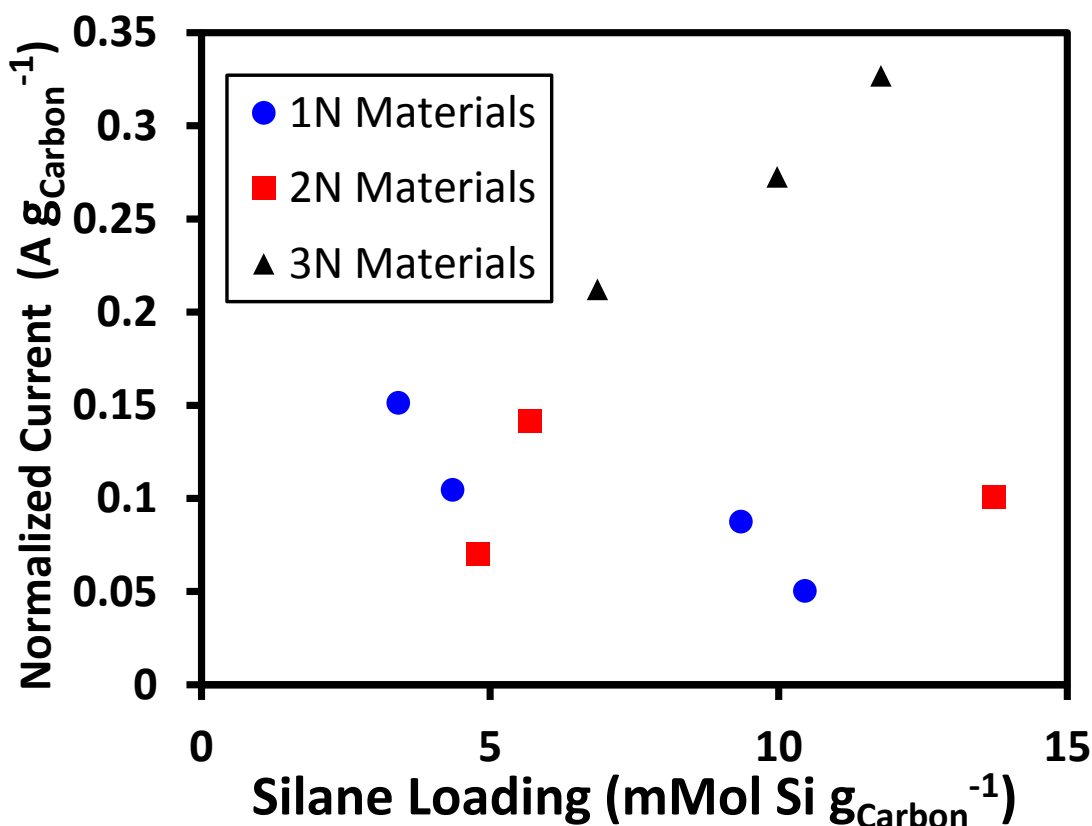


Figure 4-45: Relationship between silane loading and mass of carbon normalized limiting current taken from potentiostatic measurements.

Given that the oxidation of CuCl does not require a catalyst site it is expected that there should be a positive relationship between the surface area and the limiting current of the materials. The capacitance of the CCEs as determined by the CV measurements was plotted against the mass specific limiting current as determined from potentiostatic measurements at 0.7 V vs. RHE (Figure 4-46). A positive relationship can be seen between the normalized capacitive charge and the current response ($r^2 = 0.6006$). The positive relationship appears

independent of the type of silane used to produce the CCE. This indicates that the oxidation of CuCl does indeed depend on the capacitance of the CCE material.

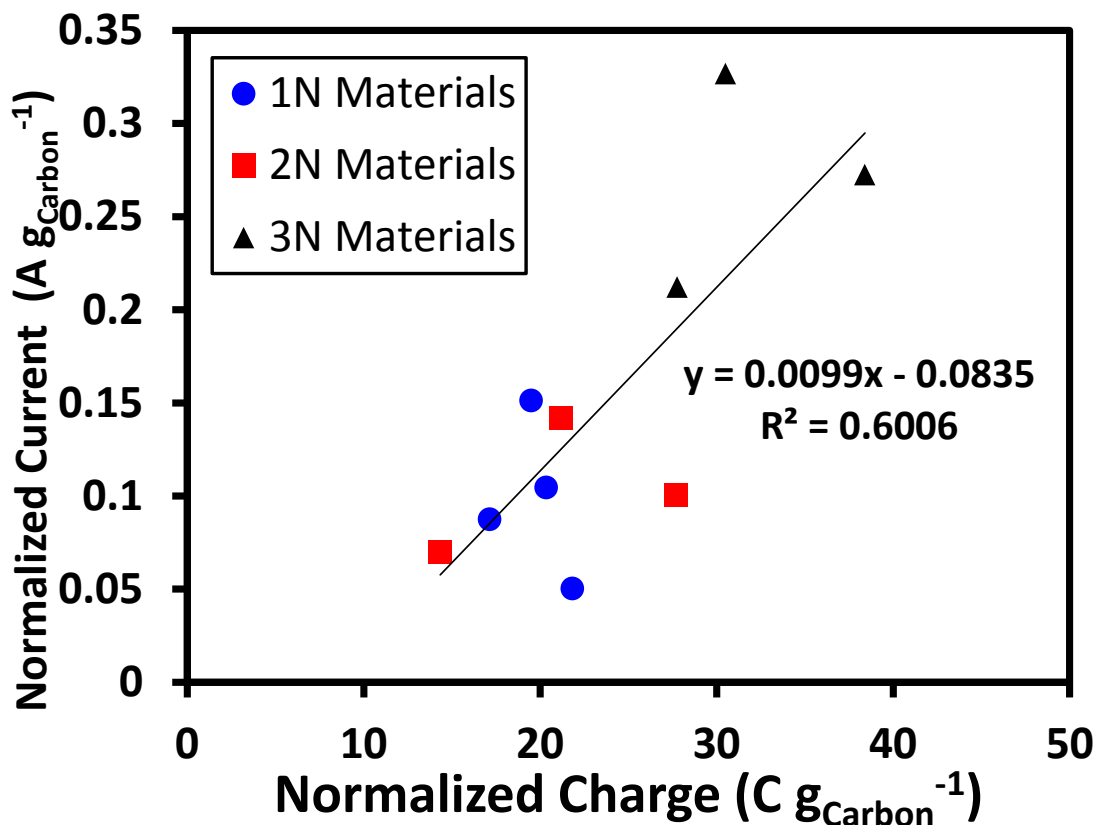


Figure 4-46: Comparison of CCE capacitance and mass of carbon specific limiting current taken from potentiostatic holds.

Ultimately, the comparison of mass specific currents does not allow for an adequate comparison of the electrodes that were specifically tested. Through only normalizing for the specific area of the electrode the absolute current response of the different CCE materials can be compared to determine the best overall performing material (Figure 4-47). There appears to be a marked decrease in the maximum current obtained for the 2N materials. This could be attributed to low overall CCE loadings as the 2N materials performed comparably to the 1N materials when normalized for the mass of carbon (Figure 4-45). The most notable change is the difference in current response of the 3N materials. While they showed good mass specific currents the 3N materials showed relatively lower absolute currents more similar to those recorded for the 1N and 2N electrodes. The low loadings of carbon at the surface of the electrode limited the overall current responses while giving much better mass normalized

performance. Of the materials tested the best performing CCE from each of the three precursors was selected for comparison to control materials (Figure 4-48). Of the materials, the best 1N and 3N materials outperformed the bare CFP control electrode and performed comparably well to the Pt/C catalyst electrode.

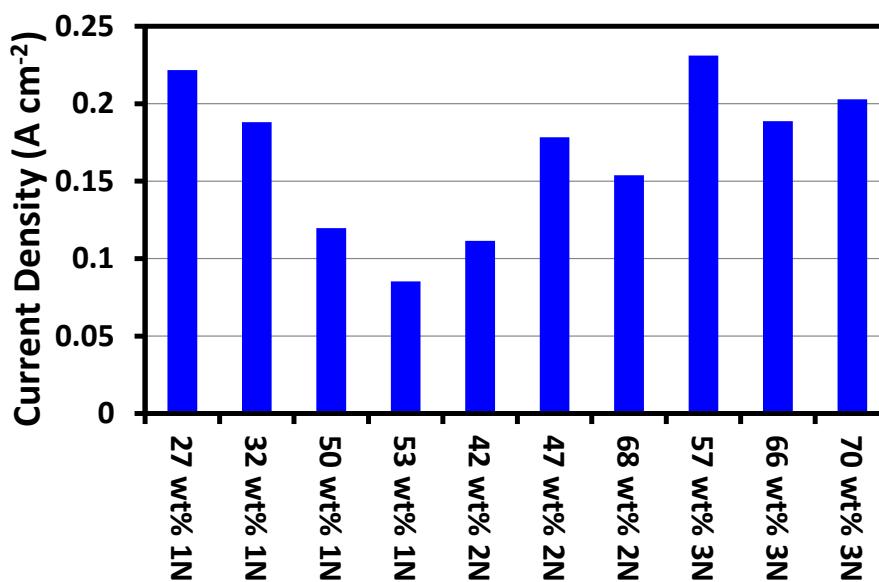


Figure 4-47: Comparison of area normalized current response to potentiostatic holds for all 1N, 2N, and 3N materials.

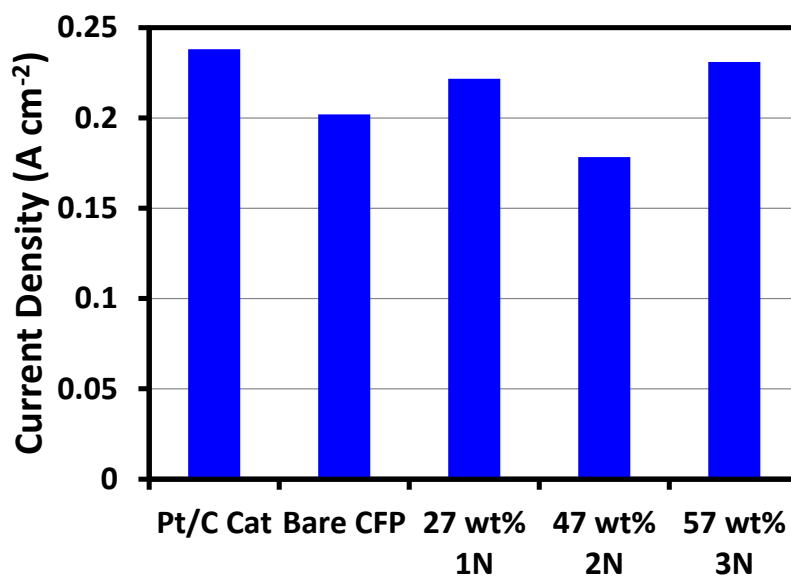


Figure 4-48: Comparison of best area normalized current responses to potentiostatic holds from 1N, 2N, and 3N CCE materials as well as control electrodes.

The CCE materials showed different responses to varying the silane compositions. The CuCl oxidation process was shown to be related to the total capacitance of the electrode surface independent of the silane precursor used (Figure 4-46). In addition to this the total capacitance was shown to be related to the silane content and much more accurately to the total amine content in the CCE (Figure 4-43). This relationship between the amine content and capacitance can be attributed to increased ionic conductivity from the charged amine groups within the CCE as well as increased wettability of the carbon surface by the surface bound hydrophilic groups. The increased ionic conductivity from the amine content should also help balance the resistive nature the sol-gel back bone imparts on the CCE structure. While there is not a clear best material of those tested, the increase in capacitance with amine content and the increase in current with capacitance leads to the 3N materials being good candidates for future investigations.

Chapter 5 : Materials Durability and Copper Crossover Resistance

Cell durability was a problem of particular importance during our experiments. Copper crossover represents either the total failure of the Nafion membrane or the plating of Cu^+ as Cu^0 at the cathode electrode⁴. This copper plating causes a shift in the potential for the hydrogen evolution reaction (HER) at the cathode⁴³. The cathode reaction is also used as the cell's internal reference electrode, so altering the reaction's chemical potential will alter at what potential the reaction is held. Beyond the change in potential for the reaction, the Cu plating has also been shown to remove or obscure existing Pt catalyst sites. This was shown through high resolution transmission electron microscopy (TEM) (Figure 5-1). The initial structure of the cathode catalyst shows a high surface area carbon structure with Pt nanoparticles evenly dispersed across the surface. The structure is visibly different after Cu crossover was identified and the MEA was considered spent. There was a significant, and sometimes complete, decrease in the prevalence of the Pt nano particles. This supports the assumption that Cu plating is either destroying or obscuring the Pt catalyst sites.

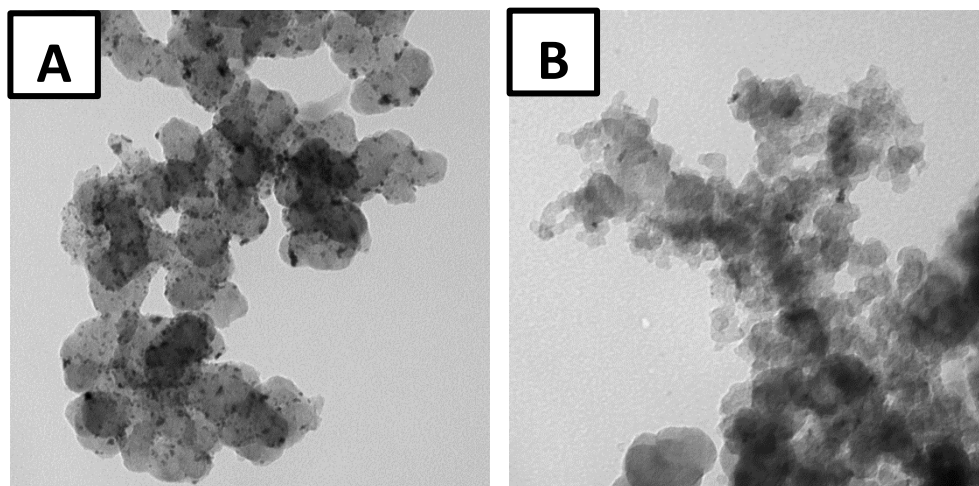


Figure 5-1: 18000x magnification TEM image of Pt/C cathode catalyst before operation (A) and after Cu plating had occurred (B).

Further proof of the Cu crossover and plating can be seen in SEM images. Images of the spent cathode and membrane were taken to examine the Cu deposition (Figure 5-2). There is clear evidence of dendritic structures forming on the surface of the electrode caused by copper crossover and plating. The membranes and electrodes were also visibly plated with copper after copper crossover was identified (Figure 5-3).

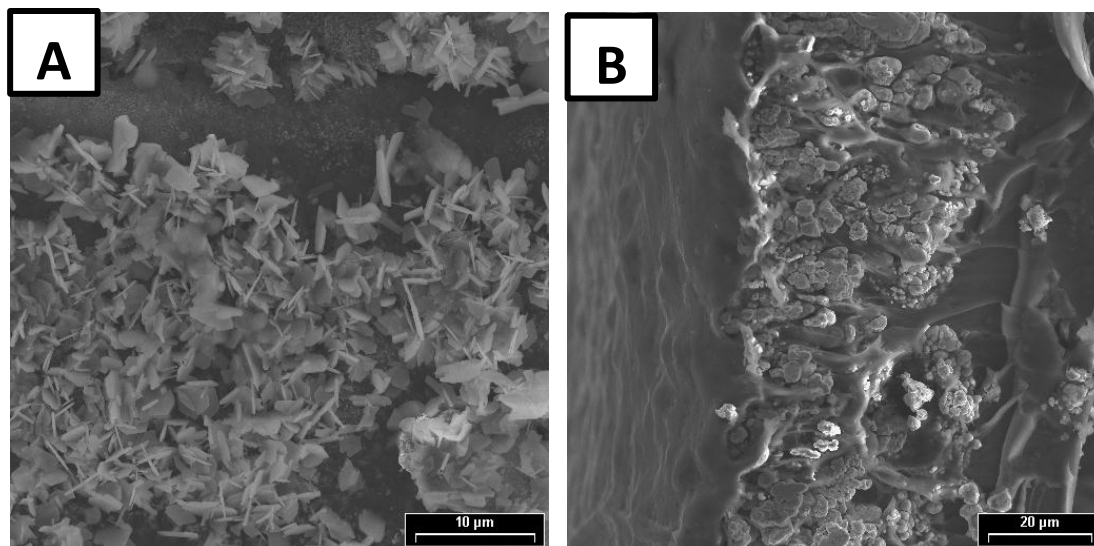


Figure 5-2: SEM Images of Cu Dendrites grown on $0.3 \text{ mg Pt cm}^{-2}$ catalyst cathode (A) and Cu metal impregnated into the Nafion 115 PEM (B) after electrolysis cell failure.

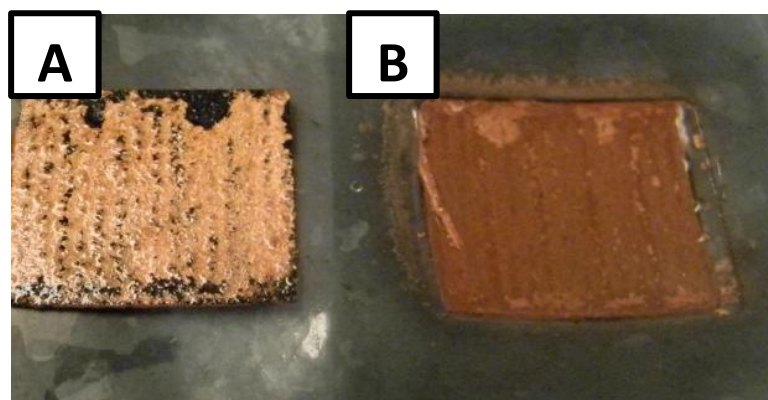


Figure 5-3: Picture of $0.3 \text{ mg Pt cm}^{-2}$ catalyst cathode (A) and cathode side of the Nafion 115 PEM (B) for the CuCl-HCl electrolysis process after significant Cu crossover and plating has occurred (Red/brown colour is Cu metal).

5.1: Copper Crossover Identification

Copper plating at the cathode creates a transient current response that can be observed during cell operation. The crossover current is more easily identified during potentiostatic holds. In an ideal case, the cell will operate at a standard current associated with both the potential applied as well as the materials used. The apparent maximum current that was observed for the cell testing was approximately $0.2 - 0.25 \text{ A cm}^{-2}$ at 0.7 V vs. RHE cell potential with standard electrolyte solutions supplied to the electrode at a rate of 60 mL min^{-1} . Sustained operation of the cell above this current was taken to be a sign of copper crossover. Additionally,

sustained increases in the current of the cell and an unstable current response during potentiostatic holds were also considered signs of copper crossover and plating at the cathode.

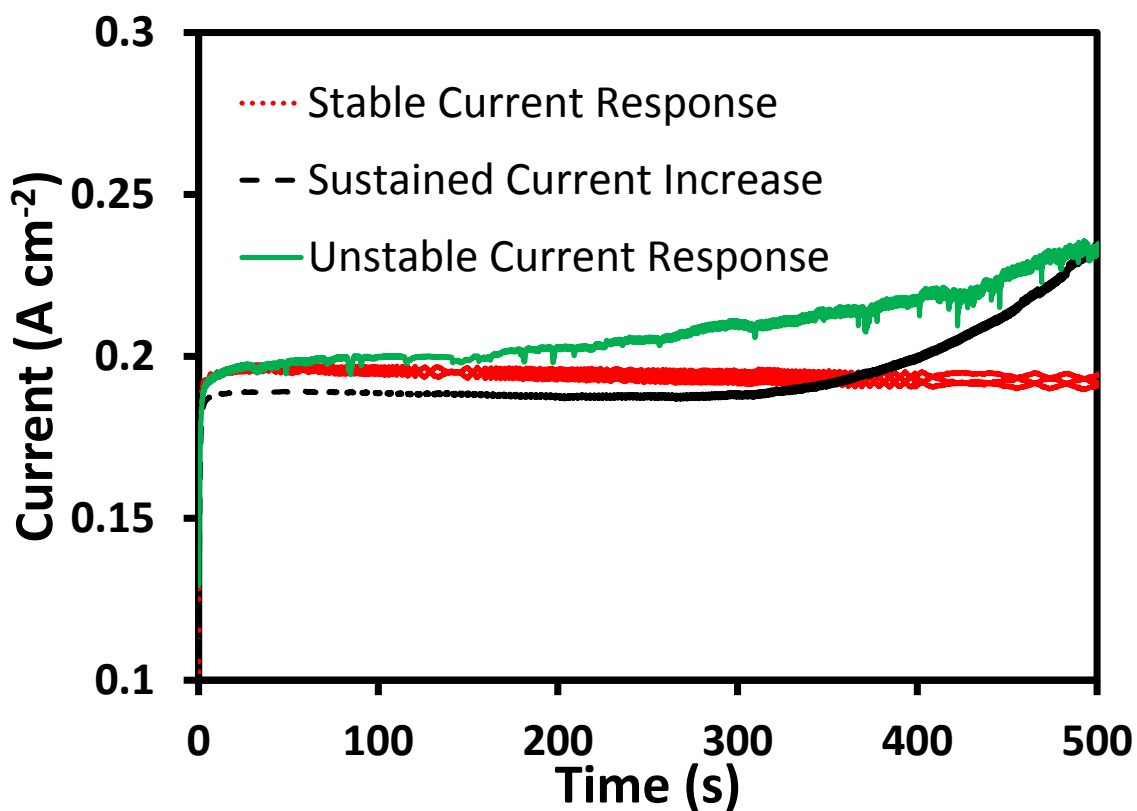


Figure 5-4 : Examples of transient currents during potentiostatic measurements.

Both forms of transient current can be observed in Figure 5-4. In Figure 5-4 sustained increases in current can be seen at approximately 350 s of operation on the black curve and unstable current responses are seen throughout the green curve. In both cases of transient currents, allowing the cell to continue operation caused dangerous increases in cell current. Postmortem analysis of the cell revealed copper visibly plated on the cathode electrode (Figure 5-3), as well as, the flow channels, and on the graphite bipolar plate. The presence of copper metal at the cathode confirms the theory that the transient current is related to the crossover of copper and its subsequent reduction.

5.2: Comparison of materials crossover resistances

As previously mentioned the constant conditions maintained during testing isolated the anode electrodes effects on reducing copper crossover within the cell. The combined effects of

the thickness of the CCE layer as well as the silane content are expected to contribute to the overall copper crossover resistance that the anode provided. When the main family of materials was compared, the constant carbon loading allowed for comparison of the materials based on their silane content while the varied CCE loading materials allowed for comparison based on their carbon loading. Observations of each material's ability to resist the crossover of copper was made during normal cell operation (Table 5-1). The time of each MEA's failure was compared to assess their relative abilities' to resist copper crossover. During the extent of the full-cell testing, there were significant changes to the overall testing protocol and additionally variations in the current response. These changes affected the environment in which the cell was operating. To normalize for this variation the total charge over the operation of the cell was integrated for comparison. Both the total operation time and total operation charge are compiled in Table 5-1.

Table 5-1: Bare CFP and CCE materials for full-cell electrolysis: Cu crossover resistance and sample compositional information.

| Sample Code | Silane Type | mMol Silane $\text{g}_{\text{Carbon}}^{-1}$ | Time Total (s) | Charge (C) |
|-------------|-------------|---|----------------|--------------|
| B1P73S2 | 1N | 3.39 | 5970 | 6632 |
| B1P69S1 | 1N | 4.36 | 3087 | 4004 |
| B1P69S2 | 1N | 9.36 | 1143 | 1876 |
| B1P69S3 | 1N | 10.44 | 3724 | 7772 |
| B1P81S1 | 2N | 4.81 | 2575 | 2961 |
| B1P81S2 | 2N | 5.70 | 2107 | 2138 |
| B1P83S1 | 2N | 13.76 | 2171 | 2489 |
| B1P85S2 | 3N | 6.86 | 3311 | 2948 |
| B1P85S1 | 3N | 10.01 | 8162 | 8509 |
| B1P85S3 | 3N | 11.80 | 2873 | 2665 |
| Bare CFP | Bare CFP | N/A | 2024 | 1850 |

The total time of the cell operation was taken as the time the cell spent operating under load with the standard CuCl/HCl anolyte supplied to the anode. Time spent while the cell operated in the absence of Cu was discarded as there was no source of cationic copper to permeate the membrane. Additionally, time spent while no current passed through the cell, specifically open circuit potential holds, were also discarded as it was assumed that there would be no significant concentration of cationic copper to drive crossover. The charge values were determined by numerical integration of the current signal with respect to time using the

trapezoidal rule. A time step of 0.5 s integrated over scale thousands of seconds ensured an accurate determination of the total charge value. As with the total cell operation time, the portions of cell operation where no current was flowing or no copper was present at the anode were discarded for the total charge integration.

When comparing the total cell operation time it can be seen in Table 5-1 that the bare carbon fiber paper control is outlasted by all of the materials tested with the exception of B1P69S2, the CCE with the second highest molar loading of 1N silane (Figure 5-5). A greater performance difference can be observed when the total charge of the materials is compared. The bare carbon fiber paper is outperformed by all of the CCE materials with respect to the total charge before failure. It is visible that the 1N materials showed the largest spread in material performances, with a much more varied performance when compared to the 2N and 3N materials. This difference is likely due to the previously mentioned changes in testing protocol. For the 1N materials a series of galvanostatic tests at 0.1 A cm^{-2} and varied flow rates were also performed. This low current density test potentially allowed for increased cell duration while more rigorous cell testing would have decreased its operational lifetime. Conversely, a more consistent testing and protocol was employed for the 2N and 3N materials as well as the bare CFP control. Between the 2N and 3N materials, there was a much closer distribution observed.

With the exception of 66 wt% 3N sample (B1P85S1) operating to a total charge above 8000 C, the 2N and 3N materials show a relatively narrow distribution. In fact, with a Q test value of 0.870 the charge at crossover value for the 66 wt% 3N sample (B1P85S1) can be discarded as an outlier with 99% confidence. With this in mind the average total charge at crossover for the 2N and 3N materials is 2640 C and the Bare CFP sample falls more than two standard deviations below this value (at 1850 C total). It is important to note that no duplicate runs of the CCE or CFP control materials were made. While it is possible to say that the 2N and 3N materials performed better than the CFP control material, variation of individual materials over multiple runs was not taken into account. Additionally, while the overall effect of CCE materials on inhibiting copper crossover can be observed, the specific effects of each material cannot be identified accurately.

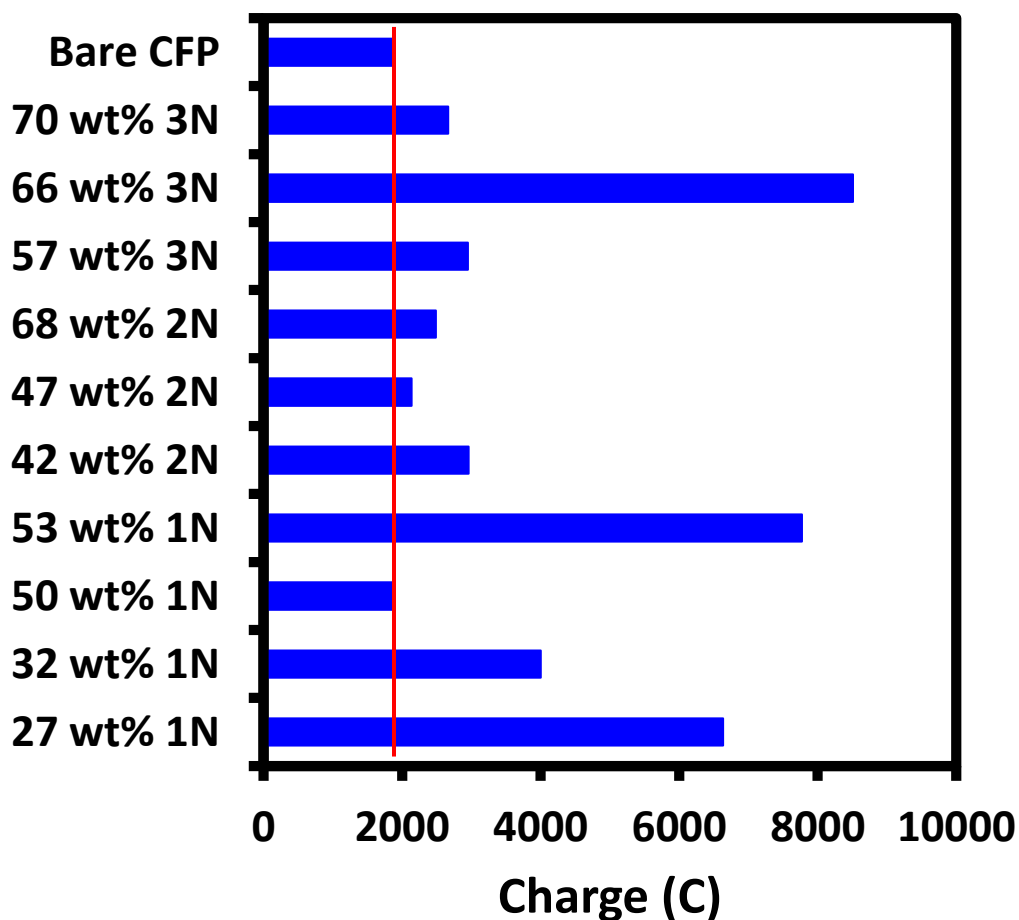


Figure 5-5: Total charge at time of cell failure for CCE materials and Bare CFP control.

5.3: Cell Regeneration

During cell operation, to prolong the testing of the cell, two “cell regeneration” techniques were developed and employed. The primary cause of cell failure as discussed in 5.1 and 5.2 is copper crossover and plating at the cathode. In future work, high concentration HCl can be used to inhibit the plating of copper at the cathode electrode. In our electrolysis cell because the aim is not to produce extended tests, but rather to compare materials, only DI H₂O was supplied to the cathode. By replacing the cathode liquid with 2 M HCl and circulating for periods of time up to 2 hrs, the plated copper was dissolved into solution regenerating the cathode electrode for further testing. In this testing the flow of the HCl solution was kept constant and the cell was purged of liquid at the cathode prior to restarting circulating deionized H₂O. These precautions allowed us to reliably dissolve and then finally remove plated Cu from the cathode of the electrode. In addition to this, to regenerate the electrode, a potential of 0 V

vs. RHE was held while current was allowed to flow from the “Cathode” to the “Anode”, allowing reduction at the CuCl containing “Anode” electrode. When this occurs the plated copper becomes oxidized and dissolves into the catholyte. This also allows for a successful regeneration of the full-cell, however, the Cu metal is simply dissolved into the catholyte allowing for potential redeposition during cell operation. The 0 V hold technique allows for much shorter regeneration times with successful runs as short as 5 minutes.

A long term experiment was performed to assess the 0 V hold technique’s ability to repeatedly regenerate the cathode electrode and with it cell function (Figure 5-6). During the cell potentiostatic conditions were employed with 60 mL min^{-1} electrolyte flow and a cell potential of 0.7 V vs. RHE. For regeneration the cell potential was adjusted to 0 V vs. RHE while the flow was kept the same conditions as during the potentiostatic holds. Initial testing was performed after the cell had experienced crossover and regeneration by chemical means. The baseline current for the cell was initially recorded at approximately 0.13 A cm^{-2} . This current already represents a decrease from the best performing current response recorded for the tested material. This decrease is assumed to be because of degradation at the cathode electrode from previous cell testing. Cell operation was held constant with switches to 0 V holds when there was evidence of copper crossover occurring within the MEA. The cell regeneration technique worked in three repeated instances, returning the cell’s current response to approximately the standard value. As the cycles were increased the operation time until crossover was detected shortened. This is likely due to an increase in total copper concentration in the catholyte liquid. After the regenerations were discontinued, sustained copper crossover was observed over the final approximately 200 min showing the sustained increases in current from copper crossover.

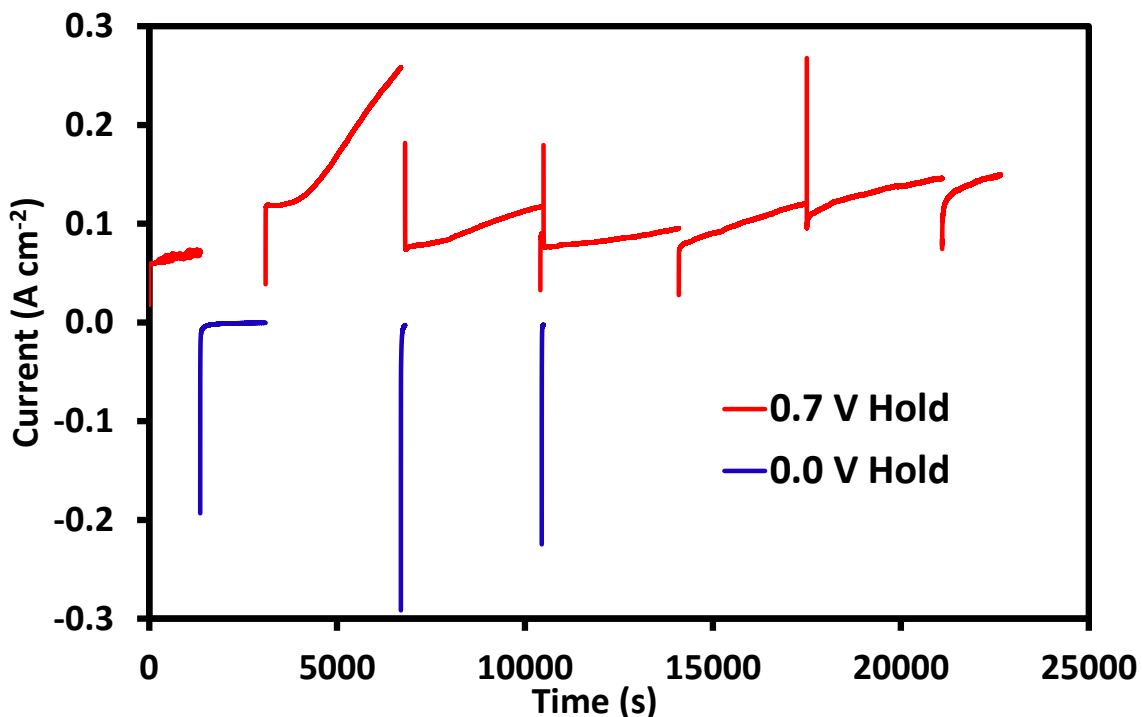


Figure 5-6: Example crossover and cell regeneration of the 50 wt% 1N CCE (B1P69S2) during 0.7 V potentiostatic holds (Red) with 0 V regeneration holds (Blue). Experiments performed in 0.2 M CuCl in 2 M HCl anolyte and DI H₂O catholyte both under N₂ atmosphere at 60 mL min⁻¹ electrolyte flow rate.

5.4: Ultra-Micro Electrode Measurements

In pursuit of a simple method to measure copper crossover the use of ultra-micro electrodes for copper concentration measurements was investigated. Initially the ultra-micro electrodes were investigated for their abilities to discern between Cu(I) and Cu(II) allowing the percent conversion of Cu(I) to Cu(II) in the anolyte solutions to be determined. The complexity of the electrochemical signal prevented this from being accurately determined, however, further work was done to examine the ability to detect total copper concentration. The hemispherical diffusion and low operating currents of the ultra-micro electrode allow for it to maintain a steady state current that is linearly related to the concentration of the analyte in solution³⁹.

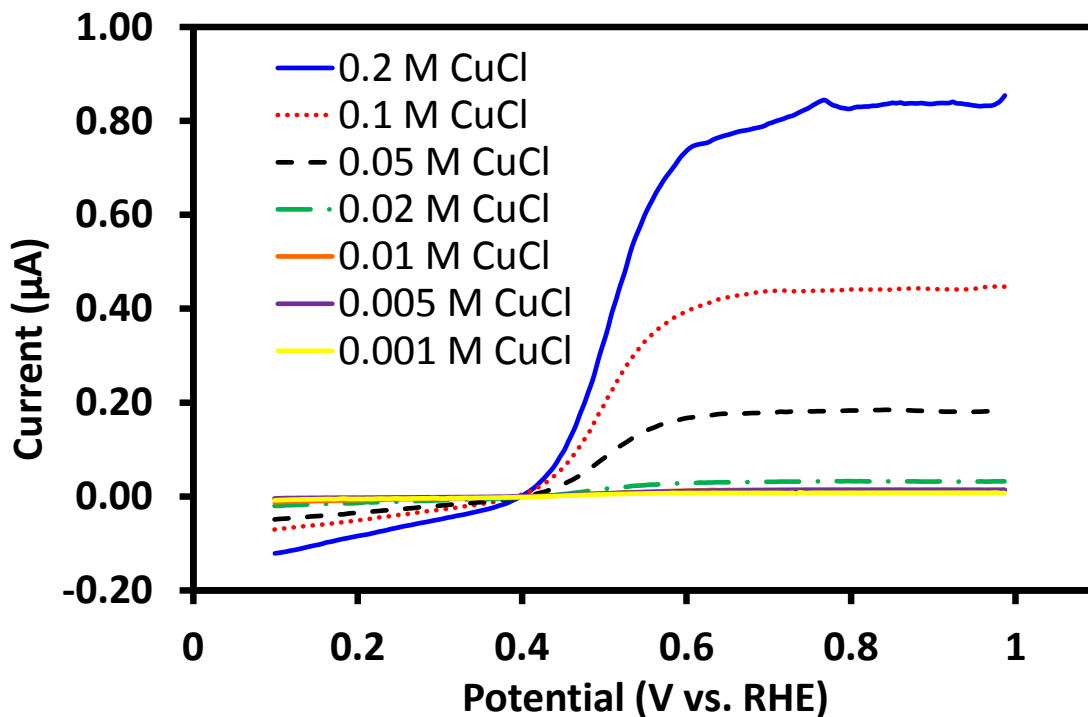


Figure 5-7: Linear sweep voltammetry from 0.1 to 1.0 V at 20 mV s^{-1} scan rate of CuCl at varied concentrations in 2 M HCl under N_2 atmosphere.

In Figure 5-7 the scan from 0.1 to 1.0 V vs. RHE was taken to include the Cu(I) oxidation at approximately 0.4 V vs. RHE. This was performed on a series of solutions with known CuCl concentrations allowing for the external calibration of the technique. Above 0.7 V vs. RHE the current response from the Cu(I) oxidation obeyed a steady state behavior. The plateau current showed a proportion to the copper concentration decreasing with the decreasing copper content. The anodic current response was determined for each solution tested and plotted relative to the concentration of copper in Figure 5-8. Overall the maximum anodic current in the LSV measurement shows a very linear relationship to the concentration of the copper in the analyte. This method allows for the overall determination of the concentration of copper with a current lower detection limit of 1 mMol Cu or 60 ppm. Notably, the current tested detection limit is orders of magnitude higher than that of a conventional absorption based analytical technique, but has the potential to be operated in situ for constant online monitoring of catholyte copper content.

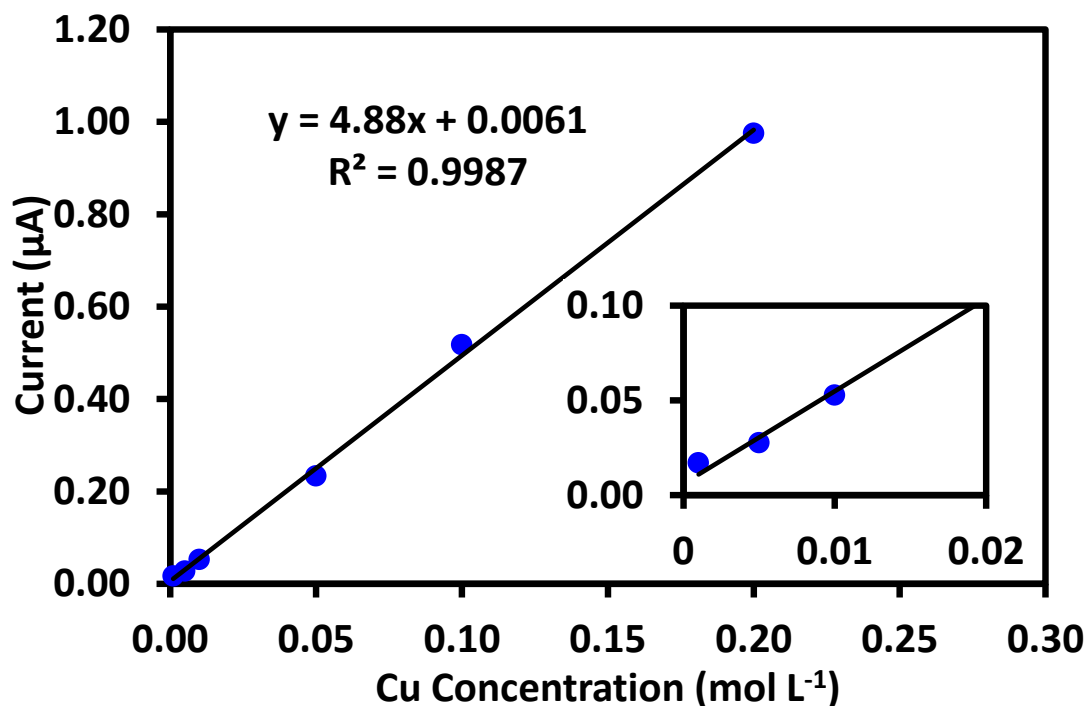


Figure 5-8: Relationship between Cu concentration in 2 M HCl and current amplitude. Low concentration values expanded and inset. Data taken from Figure 5-7.

To determine the concentration of CuCl without an external set of standards the current can be related to the total copper concentration via Equation 5-1³⁹.

$$i_D = 4nFDr_0C \quad \text{Equation 5-1}$$

In Equation 5-1 the current i_D is related to the concentration (C), the radius of the electrode (r_0), the diffusion coefficient for the species in question in the electrolyte, Faradays constant, and finally the number of electrons involved in the redox process (n). With this information the concentration can be determined without the need to prepare external standards. From this, ultra-micro electrodes show promise for the in-situ determination of Cu concentration within the full-cell system.

Chapter 6 : Conclusions and Future Directions

6.1: Conclusions

In this thesis we produced and characterized a number of CCE materials for the CuCl-HCl electrolysis step of the hybrid three step CuCl-HCl thermochemical cycle. The materials were produced using a standard amount of high surface area carbon (Vulcan XC-72) and varied amounts of three silane precursors. The silane precursors were (3-Aminopropyl) triethoxysilane, N-[3-(Trimethoxysilyl)propyl]ethylenediamine, and N¹-(3-Trimethoxysilylpropyl) diethylenetriamine listed as 1N, 2N and 3N respectively. These materials were chosen for their amine functionalities which were intended to provide increased ionic conductivity. A definite increase in ionic conductivity with increased silane content was not observed in the EIS measurements. This can be partially attributed to the finite transmission line model not allowing us to distinguish between the electronic and ionic resistance in our CCE materials. These two forms of resistance should have opposite correlations with silane content. The increase in the amine functionalities of the silane backbone did show a good linear correlation with increased overall capacitance and to a lesser degree the operational current during potentiostatic holds.

The CCE materials were physically characterized through both TGA measurements and SEM imaging. All of the materials showed general stability up to 300 °C before a mass loss attributed to the degradation of the functionalities was seen. Beyond this the materials were shown to be stable up to 600 °C in air before combusting. The full-cell materials were imaged using an SEM. The imaging showed that there was a decrease in surface homogeneity with increased silane content (Figure 4-3, Figure 4-24, and Figure 4-25). This was expected as the increased silane content provides increased binding capabilities.

The half-cell electrolysis experiments showed similar activity for CuCl electrolysis when materials produced with 1N, 2N, or 3N silane precursors were tested. Within the tests it was shown that the best performing material contained the 1N silane. While this would normally indicate that the 2N and 3N materials should be ignored for full-cell electrolysis, the loadings of the materials were all quite high so further full-cell analysis was performed with 2N and 3N materials using lower loadings of silane.

In the full-cell electrolysis cell the CCE materials all showed similar behaviors. The overall best material was shown to be produced from 3N silane precursors. When normalized for the mass of carbon present the 3N materials showed the best overall performance with the

1N and 2N materials showing similar and lower activities for CuCl electrolysis. A mixture of trends for mass normalized current and silane content were observed for the CCE materials. This is explained by the variation in the ionic conductivity provided by the amine functionalities countering a constant electronic resistance from the silicate backbone. In addition to the electrolysis measurements the CCE materials were characterized with respect to the total silane and amine content. A linear relationship between the amine content and the total capacitance was seen. There was also a linear relationship between the total capacitance and the current response recorded for CuCl-HCl electrolysis.

All but one of the CCE materials was shown to outperform the bare CFP control for the resistance of copper crossover. Beyond the increase in the resistance there was no clear trend in the materials' ability to resist copper crossover. For the resistance of copper crossover we developed a method to electrochemically regenerate the cathode surface. After an initial current drop, the regeneration was shown to return transient current signals to a consistent stable level. Finally, we also examined the use of an ultra-micro electrode for the detection of copper crossover at the anode. Signals for Cu concentrations as low as 60 ppm were recorded. This technique is still outstripped by analytical spectroscopic techniques such as flame atomic adsorption but it has the unique advantage of being an in situ method that requires no advanced sample preparation.

When compared to work done by Balashov et al. in 2011 we see that our materials show comparable and better current responses compared to the best materials produced²⁰. The best materials show comparable current densities to those listed as an interim DOE goal, though the operational time for our materials is far below the target or 168 hrs^{25,26}. Of most importance, the data we collected was in the absence of a Pt catalyst at the anode. The cited works have all used Pt catalyst anode materials.

In conclusion we produced a series of CCE materials with varied silane types and contents. The materials were tested in a full-cell liquid electrolysis test station. All of the materials showed increased activity towards CuCl oxidation when compared to the bare CFP control. In addition to this a selection of the materials also showed comparable activities to a standard Pt/C catalyst material without the use of any precious metals.

6.2: Future Directions

The further characterization of the CCE materials is an important future direction for the development of new and better electrode for CuCl oxidation in the CuCl-HCl electrolysis step. When compared to other members of the CuCl-HCl project the cell used for the discussed measurements was operated in comparatively benign conditions with regards to flow rate, temperature, and electrolyte composition. Further testing at elevated temperatures would allow for better reaction kinetics and from that a better overall current response from our materials. It was shown in the potentiostatic measurements that the current response has a positive linear relation to increased flow rate. With this modification, while it is promising, it has also been shown that the overall increases in current with electrolyte flow rate will eventually plateau. With this in mind, we the full-cell is still being operated at flow rates well below other members of the research project and the increases in flow rate should still afford increased current response. Both of these modifications to the process simply represents better reaction kinetics and a higher effective concentration of CuCl at the anode. There are still simple methods to improve the overall performance of the materials that have been have produced.

The most notable difference in the cell operation when compared to the collaborators who focus on the electrochemical step is the electrolyte composition, the catholyte was kept as pure water as opposed to acid and the anolyte was a comparatively dilute CuCl and HCl solution^{20,21}. By increasing the CuCl concentration in the anolyte there should be an increase in current response. Again, this is simply by an improvement in the effective concentration of CuCl at the anode electrode. Increasing the HCl concentration is partly required to help solvate an increased CuCl concentration. In addition to this, the HCl should provide assistance to the oxidation of the CuCl by increasing the available Cl⁻ concentration. Finally, adding HCl to the catholyte has two potential benefits. The first is that it will improve the overall current response by improving the cathode reduction reaction. The increased H⁺ concentration will allow for faster reaction kinetics. In addition to this, the HCl concentration helps maintain cell performance in the presence of contaminate Cu⁺ by keeping it in solution as CuCl. This is shown qualitatively by the operation of other CuCl electrolyzer operating with HCl at the cathode. This is also shown through a pourbaix diagram investigation of CuCl speciation by Beverskog et al⁴⁴⁻⁴⁶.

An easy direction to take in this research would be to test the effects of a cloth CCE backing. The increased wettability of the carbon cloth would potentially provide increased diffusion of the CuCl species to the electrode surface. Currently, every CCE material tested has a companion material produced on carbon cloth. With these materials it would be simple to test and compare the effects of the carbon cloth backing.

There are a number of other improvements that could be made to the CCE materials that were produced. First there is an indication that at lower silane content of the 1N material there should be an improvement in current response (Figure 4-14). This is mirrored by the trend that shows increased current response at higher 3N silane contents (Figure 4-45). These trends could be examined by producing new materials with either lower 1N content or higher 3N content. It has also been established that there appears to be an increase in capacitance with higher amine content (Figure 4-43). From this it would be interesting to further expand these tests to include novel silanes with increased amine functionalities.

Novel CCE materials have been produced containing sulfonate groups in our research group^{47,48}. It was shown that the optimal composition of those CCE materials was produced from a mix of functionalized silane precursor and unfunctionalized TEOS. From this knowledge it would be useful to synthesize a series of CCEs with a mixture of the amine functionalized silanes and TEOS as precursors to investigate the effects of the silicate backbone in combination with the protonated amine functionalities.

Ultimately the future directions of this project can be summarized in the following way. The improvement of the electrolysis testing conditions to provide a more aggressive environment for the oxidation of CuCl, and to limit Cu⁺ plating. Additionally, it would be useful to further investigate the effects of carbon cloth, silane type, and silane content on the CCE materials. Both of these suggestions could be performed simply, with little additional research required.

Chapter 7 : References

1. Holladay JD, Hu J, King DL, Wang Y. An overview of hydrogen production technologies. *Catal Today*. 2009;139(4):244-260. doi: 10.1016/j.cattod.2008.08.039.
2. Turner J, Sverdrup G, Mann MK, et al. Renewable hydrogen production. *Int J Energy Res*. 2008;32(5):379-407. doi: 10.1002/er.1372.
3. Barbir F, Gomez T. Efficiency and economics of proton exchange membrane (PEM) fuel cells. *Int J Hydrogen Energy*. 1996;21(10):891-901. doi: 10.1016/0360-3199(96)00030-4.
4. Naterer GF, Suppiah S, Stolberg L, et al. Canada's program on nuclear hydrogen production and the thermochemical cu-cl cycle. *Int J Hydrogen Energy*. 2010;35(20):10905-10926. doi: 10.1016/j.ijhydene.2010.07.087.
5. Hino R. *Nuclear hydrogen production handbook*. New York: CRC Press; 2011.
6. Carrette L, Friedrich K, Stimming U. Fuel cells: Principles, types, fuels, and applications. *Chemphyschem*. 2000;1(4):162-193. doi: 10.1002/1439-7641(20001215)1:4<162::AID-CPHC162>3.0.CO;2-Z.
7. Utgikar V, Thiesen T. Life cycle assessment of high temperature electrolysis for hydrogen production via nuclear energy. *Int J Hydrogen Energy*. 2006;31(7):939-944. doi: 10.1016/j.ijhydene.2005.07.001.
8. Hydrogenics, shift power energize your world. <http://www.hydrogenics.com/>. Accessed July/1, 2013.
9. Proton onsite: The leader in onsite gas generation. <http://www.protononsite.com/>. Accessed July/1, 2013.

10. McQuillan B, Brown L, Besenbruch G, et al. High efficiency generation of hydrogen fuels using solar thermochemical splitting of water. annual report. . 2002.
11. Lewis M, Taylor A. High temperature thermochemical processes. DOE hydrogen program. annual progress report. . 2006:182.
12. Onuki K, Kubo S, Terada A, Sakaba N, Hino R. Thermochemical water-splitting cycle using iodine and sulfur. *Energy Environ Sci.* 2009;2(5):491-497. doi: 10.1039/b821113m.
13. Staser JA, Weidner JW. Effect of water transport on the production of hydrogen and sulfuric acid in a PEM electrolyzer. *J Electrochem Soc.* 2009;156(1):B16-B21. doi: 10.1149/1.3001923.
14. Fatih K, Wilkinson DP, Moraw F, Ilicic A, Girard F. Advancements in the direct hydrogen redox fuel cell. *Electrochemical and Solid State Letters.* 2008;11(2):B11-B15. doi: 10.1149/1.2812788.
15. Ranganathan S, Easton EB. High performance ceramic carbon electrode-based anodes for use in the cu-cl thermochemical cycle for hydrogen production. *Int J Hydrogen Energy.* 2010;35(3):1001-1007. doi: 10.1016/j.ijhydene.2009.11.077.
16. Naterer GF, Suppiah S, Stolberg L, et al. Clean hydrogen production with the cu-cl cycle - progress of international consortium, II: Simulations, thermochemical data and materials. *Int J Hydrogen Energy.* 2011;36(24):15486-15501. doi: 10.1016/j.ijhydene.2011.08.013.
17. Naterer GF, Suppiah S, Stolberg L, et al. Progress of international hydrogen production network for the thermochemical cu-cl cycle. *Int J Hydrogen Energy.* 2013;38(2):740-759. doi: 10.1016/j.ijhydene.2012.10.023.

18. Ranganathan S, Edge PSR, Easton EB. Evaluation of anode electrode materials for cu-cl/HCl electrolyzers for hydrogen production. *Electrochemical Energy Summit - an International Summit in Support of Societal Energy Needs*. 2012;41(31):111-120. doi: 10.1149/1.3702861.
19. Gilbert T, Kirss R, Davies G. Appendix 6 standard reduction potentials. In: *Chemistry the science in context*. New York: Norton; 2004:A-28.
20. Balashov VN, Schatz RS, Chalkova E, Akinfiyev NN, Fedkin MV, Lvov SN. CuCl electrolysis for hydrogen production in the cu-cl thermochemical cycle. *J Electrochem Soc*. 2011;158(3):B266-B275. doi: 10.1149/1.3521253.
21. Stolberg L, Boniface H, McMahon S, Suppiah S, York S. Development of the electrolysis reactions involved in the cu-cl thermochemical cycles. . 2009:167.
22. Lewis M, Masin J, Vilim R. Development of the low temperature cu-cl thermochemical cycle. . 2005.
23. Stolberg L, Boniface H, McMahon S, Suppiah S, York S. Electrolysis of the CuCl/AHCl aqueous system for the production of nuclear hydrogen. . 2008:1.
24. Ranganathan S, Easton EB. Ceramic carbon electrode-based anodes for use in the cu-cl thermochemical cycle. *Int J Hydrogen Energy*. 2010;35(10):4871-4876. doi: 10.1016/j.ijhydene.2009.08.085.
25. Lewis M. Electrolyzer development for the cu-cl thermochemical cycle. . 2013.
26. Lvov S. Electrolyzer development for the cu-cl thermochemical cycle. . 2012.

27. Naterer G, Suppiah S, Lewis M, et al. Recent canadian advances in nuclear-based hydrogen production and the thermochemical cu-cl cycle. *Int J Hydrogen Energy*. 2009;34(7):2901-2917. doi: 10.1016/j.ijhydene.2009.01.090.
28. Ranganathan S, Easton EB. Novel ceramic carbon electrode (CCE) materials for CuCl electrolysis. . 2008.
29. Brinker C, Scherer G. *Sol-gel science: The physics and chemistry of sol-gel processing*. Sandiego, CA: Academic Press; 1989.
30. Scherer G, Brinker C. Sol-gel technology. In: Bergna H, Roberts W, eds. *Colloidal silica fundamentals and applications*. Vol 131. CRC Press; 2005:613.
31. Lev O, Wu Z, Bharathi S, et al. Sol-gel materials in electrochemistry. *Chemistry of Materials*. 1997;9(11):2354-2375. doi: 10.1021/cm970367b.
32. Ranganathan S, Easton EB. High performance ceramic carbon electrode-based anodes for use in the cu-cl thermochemical cycle for hydrogen production. *Int J Hydrogen Energy*. 2010;35(3):1001-1007. doi: 10.1016/j.ijhydene.2009.11.077.
33. Eastcott JI, Easton EB. Electrochemical studies of ceramic carbon electrodes for fuel cell systems: A catalyst layer without sulfonic acid groups. *Electrochim Acta*. 2009;54(12):3460-3466. doi: 10.1016/j.electacta.2009.01.007.
34. Qi ZG, Pickup PG. High performance conducting polymer supported oxygen reduction catalysts. *Chemical Communications*. 1998(21):2299-2300. doi: 10.1039/a805322g.

35. Maleki N, Safavi A, Tajabadi F. High-performance carbon composite electrode based on an ionic liquid as a binder. *Anal Chem*. 2006;78(11):3820-3826. doi: 10.1021/ac060070+.
36. Pedersen AW, Pauric AD, Eastcott JI, Easton EB. Proton conductivity within fuel cell electrodes containing a sulfonated carbon support. *Fuel Cell Membranes, Electrode Binders, and Mea Performance*. 2010;28(27):39-49. doi: 10.1149/1.3496611.
37. Collinson M. Sol-gel strategies for the preparation of selective materials for chemical analysis. *Crit Rev Anal Chem*. 1999;29(4):289-311. doi: 10.1080/10408349891199310.
38. Rabinovich L, Lev O. Sol-gel derived composite ceramic carbon electrodes. *Electroanalysis*. 2001;13(4):265-275. doi: 10.1002/1521-4109(200103)13:4<265::AID-ELAN265>3.3.CO;2-U.
39. Bard A, Faulkner L. *Electrochemical methods fundamentals and applications*. Hoboken, NJ: John Wiley and Sons Inc; 2001:833.
40. Loveday D, Peterson P, Rodgers B. *Evaluation of organic coatings with electrochemical impedance spectroscopy part 1: Fundamentals of EIS*. ; 2004:46.
41. Li G, Pickup P. Ionic conductivity of PEMFC electrodes - effect of nafion loading. *J Electrochem Soc*. 2003;150(11):C745-C752. doi: 10.1149/1.1611493.
42. Lefebvre M, Qi ZG, Rana D, Pickup PG. Chemical synthesis, characterization, and electrochemical studies of poly(3,4-ethylenedioxythiophene)/poly(styrene-4-sulfonate) composites. *Chemistry of Materials*. 1999;11(2):262-268. doi: 10.1021/cm9804618.

43. Nishihara C, Nozoye H. Underpotential deposition of copper on pt(s)-[N(111)x(100)] electrodes in sulfuric-acid-solution. *J Electroanal Chem.* 1995;386(1-2):75-82. doi: 10.1016/0022-0728(94)03803-B.
44. Beverskog B, Puigdomenech I. Pourbaix diagrams for the system copper-chlorine at 5–100 °C. . 1998;98:19.
45. Beverskog B, Pettersson S. Pourbaix diagrams for copper in 5 m chloride solution. . 2002;23.
46. Beverskog B, Puigdomenech I. Revised pourbaix diagrams for copper at 25 to 300 degrees C. *J Electrochem Soc.* 1997;144(10):3476-3483. doi: 10.1149/1.1838036.
47. Eastcott JI, Yarrow KM, Pedersen AW, Easton EB. Fuel cell electrode structures containing sulfonated organosilane-based proton conductors. *J Power Sources.* 2012;197:102-106. doi: 10.1016/j.jpowsour.2011.09.023.
48. Eastcott JI, Powell JA, Vreugdenhil AJ, Easton EB. Electrochemical and morphological studies of ceramic carbon electrodes for fuel cell systems. *Polymer Electrolyte Fuel Cells* 11. 2011;41(1):853-864. doi: 10.1149/1.3635619.

Chapter 8 : Appendices

[Colloidal silica : fundamentals and applications](#)

Billing Status:

N/A

- **Order detail ID:**64432158
- **ISBN:**978-0-8247-0967-9
- **Publication Type:**Book
- **Publisher:**TAYLOR & FRANCIS GROUP LLC
- **Author/Editor:**BERGNA, HORACIO E.
- **Permission Status:**  **Granted**
- **Permission type:**Republish or display content
- **Type of use:**Republish in a thesis/dissertation
-

Order License Id: 3325621403378

- [Hide details](#)

○

| | |
|--|--|
| Requestor type | Academic institution |
| Format | Print, Electronic |
| Portion | chart/graph/table/figure |
| Number of charts/graphs/tables/figures | 1 |
| Title or numeric reference of the portion(s) | FIGURE 47.1 Illustration of the various stages of the sol-gel process. |
| Title of the article or chapter the portion is from | Sol-Gel Processing of Silica |
| Editor of portion(s) | N/A |
| Author of portion(s) | George W. Scherer, C. Jeffrey Brinker |
| Volume of serial or monograph | N/A |
| Page range of portion | 616 |
| Publication date of portion | 2006 |
| Rights for | Main product |
| Duration of use | Life of current edition |
| Creation of copies for the disabled | no |
| With minor editing privileges | no |
| For distribution to | Worldwide |
| In the following language(s) | Original language of publication |
| With incidental promotional use | no |
| Lifetime unit quantity of new product | 0 to 499 |
| Made available in the following markets | Academic |
| The requesting person/organization | Patrick Edge, University of Ontario Institute of Technology |
| Order reference number | |

| | |
|----------------------------------|---|
| Author/Editor | Patrick Edge |
| The standard identifier | None Available |
| Title | The Production and Characterization of Ceramic Carbon Electrode Materials for CuCl-HCl Electrolysis |
| Publisher | University of Ontario Institute of Technology |
| Expected publication date | Feb 2014 |
| Estimated size (pages) | 165 |